THE CCRS/SURSAT ACTIVE-PASSIVE EXPERIMENT

1978 - 1980

THE MICROWAVE SIGNATURES OF SEA ICE

by

C.E. Livingstone, R.K. Hawkins, A.L. Gray

L. Drapier Arsenault, K. Okamoto

T.L. Wilkinson and D. Pearson

Canada

Data Acquisition Division
Canada Centre for Remote Sensing
Dept. of Energy, Mines & Resources
Ottawa, Canada
June 1983

FEATURE - SPACE FOR THE CLASSIFICATION OF SEA ICE
CCRS/SURSAT ACTIVE - PASSIVE EXPERIMENT 1979 - 1980

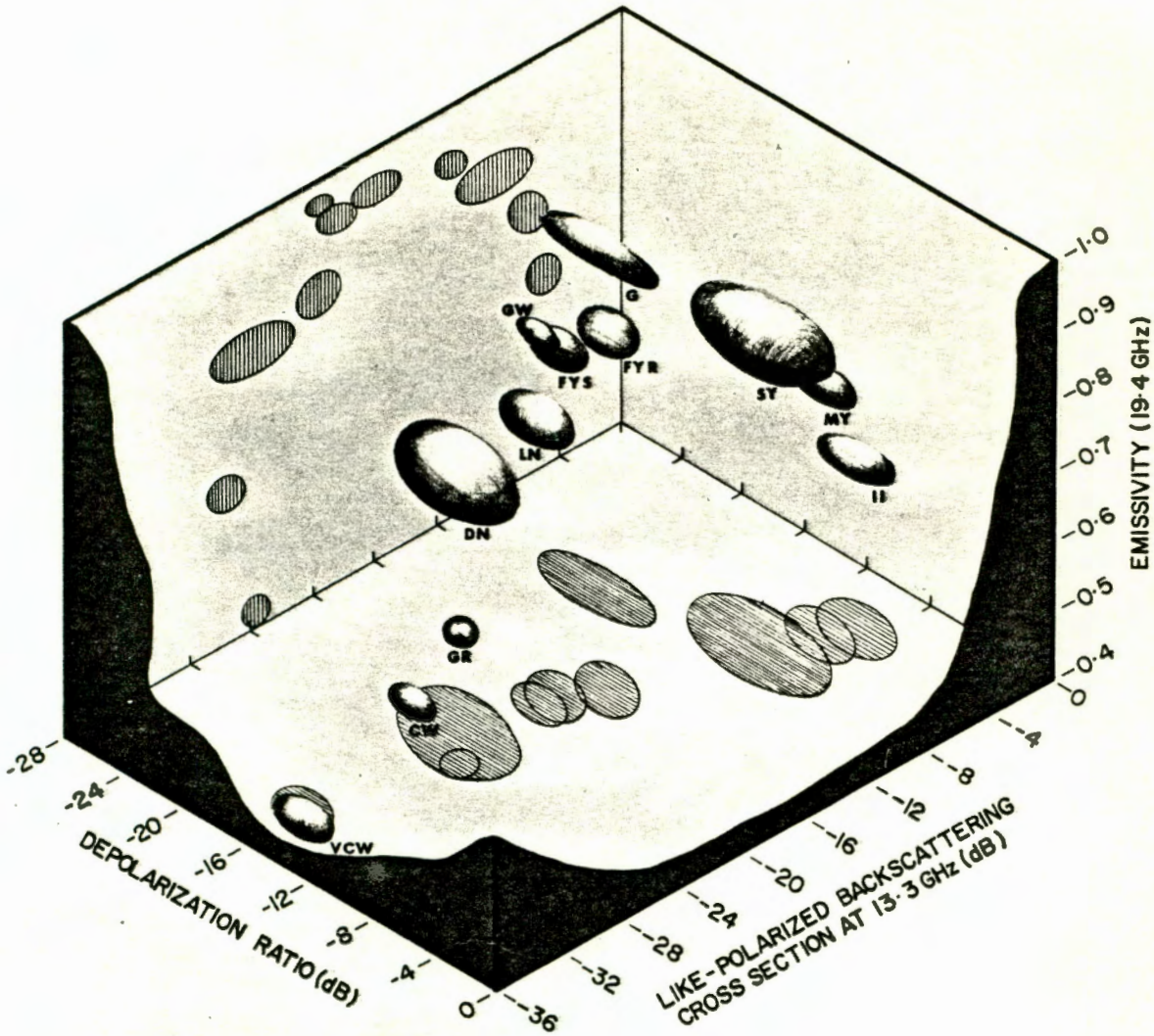

The CCRS/SURSAT Active-Passive Experiment 1978-1980

The Microwave Signatures of Sea Ice

by

C.E. Livingstone, R.K. Hawkins, and A.L. Gray
Canada Centre for Remote Sensing

L. Drapier Arsenault
Cold Regions Remote Sensing

K. Okamoto
Radio Research Laboratories, Tokyo

T.L. Wilkinson
University of Waterloo

and

D. Pearson
Intera Environmental Consultants Ltd.

February 1981

ACKNOWLEDGEMENTS

A project of this magnitude requires much more support than the immediate team of experimenters can provide. It is a pleasure to acknowledge the contributions of a number of individuals and groups whose efforts have been instrumental to the completion of this experiment, many of whom have worked selflessly to ensure its success.

Among the many individuals who have contributed directly to this experiment we would like to thank:

- Aircraft maintenance: M. Bullock, A. McKinnon, R. Sorenson.
- Computer programming assistance: K. Dagg, H. Edel, J. Gibson, V. Thomson.
- Draughting: P. Sharp, R. Staples.
- Pilots: E. Gardiner, C. Gleddie, W. Graves, B. Healey, A. MacDonald.
- Report typing: V. McInnes, B. Sigaty, P. Stewart, B. Terry.
- SAR analysis: B. Guindon, R. Lowry.
- Scientific and technical liaison: M. Kirby, R. Ramseier.
- Sensor operation: H. Code, B. Detillio, G. Doucette, B. Fretts, S. Leung, H. McKay, F. Smith, L. Wheatley.
- Sensor preparation, testing and installation: J. Allen, J. Granot, K. Holthusen, M. Lalonde, J. René de Cotret, D. Percy, J. Waddell.
- Supporting airborne data used in this project: H. Hengeveld, L. Jones, D. Ketchum, R. Shertler.

We would also like to express our appreciation to other members of the following organizations for their assistance in various phases of this project:

- DOME CANMAR
- ESSO Exploration
- Gulf Exploration
- NORDA
- C-CORE
- CCRS Airborne Operations Division
- CCRS Data Processing Division

- Intera Environmental Consultants
- Innotech Aviation
- SURSAT Project Office
- The Technical University of Denmark
- NASA Lewis Research Centre

A special thanks is due to the group of L. Jones at NASA Langley Research Centre for the loan of the microwave radiometer used in this experiment and for their assistance in bringing this instrument on line.

Finally, we acknowledge the helpful criticism and comments of R. O. Ramseier as external reviewer and H. Zwick and R. O'Neil as internal reviewers.

ABSTRACT

This document reports sea-ice microwave signature results from a detailed analysis of the CCRS Active-Passive Sea Ice Experiment conducted in March and April 1979 as part of the Canadian Surveillance Satellite (SURSAT) Project.

Measurements were taken under cold winter conditions in the Beaufort Sea and in spring conditions in the Eastern Arctic using the Convair-580 aircraft equipped with the following principal sensors: the X/L, imaging synthetic aperture radar (SAR), Ku-band scatterometer; K-band radiometer and RC-10 mapping camera.

Twelve sea-ice classes and subclasses (based on age and roughness), ranging from open water to multi-year and icebergs, were identified from the photography and their scatterometer and radiometer profiles were used to extract the covariant statistics of these active and passive signatures for each class and ice condition. These results demonstrate considerable classification potential for a combined active and passive sea-ice sensor. The results also show that the microwave signatures are significantly influenced by the thermal and mechanical history of ice and change rapidly near the freezing point.

Radar contrasts are given from scatterometer measurements for ridges and icebergs in multi-year and first-year ice backgrounds as a function of incidence angle. For incidence angles between 15 and 60°, these contrasts appear to be weakly influenced by incidence angle, but 4 to 6 dB contrast advantages are available with cross-polarized radar configurations.

It is recommended that future experiments continue to explore and develop the combination of complementary active and passive sensors in ice-classification work in the context of the regional and seasonal variation of microwave sea-ice signatures.

Résumé

Le rapport présente les signatures dans la bande micro-ondes de la glace de mer; ces signatures ont été obtenues lors d'une étude, au moyen d'un radar en mode passif et actif, sur la glace de mer. L'étude a été effectuée en mars et avril 1979 par le Centre canadien de télédétection, dans le cadre du Programme canadien de surveillance par satellite (SURSAT).

La collecte de données par survol a eu lieu en hiver, au-dessus de la mer de Beaufort, et au printemps, au-dessus de l'Arctique de l'est. L'avion utilisé, un Convair 580, portait à son bord les capteurs principaux suivants: un radar à ouverture synthétique (SAR) X/L, un diffusiomètre à bande Ku, un radiomètre à bande K et une chambre métrique de prises de vues RC-10.

Les photographies aériennes permettent de diviser en 12 classes et sous-classes la glace de mer, selon son âge et sa rugosité. Ces classes englobent tant l'eau libre et les icebergs que la glace du plusieurs années. Les profils obtenus par diffusiométrie et par radiométrie permettent de déterminer la convariance relative aux signatures pour chaque classe et condition de glace. Les résultats démontrent qu'un capteur combinant le mode passif et actif pourrait être utilisé pour classifier la glace du mer. Ils indiquent aussi que les signatures sont influencées par les contraintes thermiques et mécaniques qu'a eu à subir las glace. Ils indiquent de même que les signatures changent rapidement prés du point de congélation.

Les contrastes sur l'image radar dus aux crêtes et icebergs sur fond de glace de premiére année ou de plusieurs années s'obtiennent, à partir des données acquises par un diffusiométre, en fonction de l'angle d'incidence du faisceau. Les angles d'incidence entre 15° et 60° semblent influencer faiblement ces contrastes; toutefois, l'utilisation de radar à polarisation croisée permettrait d'obtenir les avantages provenant d'un contraste dont la valeur varie entre 4 et 6 décibels.

Enfin, il est souhaitable que les prochaines expériences continuent d'étudier et de mettre au point des capteurs combinant le mode actif et passif; ces capteurs seraient applicables à la classification des glaces. Cette tâche doit s'accomplir dans le contexte de la variation régionale et saisonnière des signatures de la glace de mer dans la bande des fréquences micro-ondes.

TABLE OF CONTENTS

LIST OF FIGURES

LIST OF TABLES

LIST OF ABBEVIATIONS, SYMBOLS AND ACRONYMS

α_m - Mainlobe efficiency of antenna

δ - Skin depth

$\delta(x)$ - Dirac delta function

ε - Emissivity

ε_v - Vertically polarized emissivity

ε_h - Horizontally polarized emissivity

ε_r - Relative dimensionless dielectric constant

$\varepsilon_{r'}$ - Real part of dielectric constant

$\varepsilon_{r''}$ - Imaginary part of dielectric constant

$\Gamma(z)$ - Attenuation coefficient of atmosphere

Ω - Solid angle

Ω_m - Solid angle subtended by the mainlobe of the antenna

$\gamma_{jk}(s, i)$ - Bistatic scattering coefficient

σ^{o}_{hh} - HH-polarized backscattering coefficient

σ^{o}_{hv} - HV-polarized backscattering coefficient

θ - Incidence angle

θ_o - Nominal incidence angle of the radiometer

θ_p - Pitch angle

$\rho_j(\theta)$ - Fresnel reflection coefficient

Δ - Approximate beam width of the radiometer

Δt_d - Time delay between nadir and the footprint of the radiometer

ADAS - Airborne Data Acquisition System

AIDJEX - Arctic Ice Dynamics Joint Experiment

AIR - Airborne data processing system

APU - Auxillary Power Unit

AR - Airborne Roll

ASCII - American Standard Code of Information Interchange

C-CORE - Centre for Cold Ocean Resources Engineering

CCRS - Canada Centre for Remote Sensing

CCT - Computer Compatible Tape

CPU - Central Processing Unit

CRT - Cathode Ray Tube

CV-580 - Convair - 580 aircraft

DAD - Data Acquisition Division

DPD - Data Processing Division

EDF - Event Data File

ESF - Event Summary File

FFT - Fast Fourier Transform

FY - First-year ice

G - Grey ice

$G(\Omega)$ - Antenna gain factor at solid angle (Ω)

GDI - Generalized Digital Interface

GMT - Greenwich Mean Time

GRAMS - Ground Recovery and Monitoring System

h - Elevation of the aircraft

HDDT - High Density Digital Tape

HH - Horizontal transmit, Horizontal receive polarization

HP - Hewlett Packard

HV - Horizontal transmit, Vertical receive polarization

II - Ice Island

INS - Inertial Navigation System

IPS - Inches Per Second

L	- Grey-white ice
L_{atm}	- Atmospheric loss factor
L_{POL}	- Like polarization configuration: either HH or VV
MAP	- Maximum a posteriori classifier
MUX	- Multiplexed data stored on ADAS track 13
MY	- Multi-year ice
ND	- Dark Nilas
NL	- Light Nilas
NRC	- National Research Council (Canada)
R	- Grease ice
RMS	- Root Mean Square
S	- Salinity
SAR	- Synthetic Aperture Radar
SIRE	- Sea-ice Radar Experiment
SLAR	- Side-Looking Airborne Radar
SMMR	- Scanning Multi-Frequency Microwave Radiometer
SURSAT	- Surveillance Satellite Project
SY	- Second-year ice
T	- Temperature
T_B	- Brightness temperature
T_B'	- Smoothed brightness temperature
$T_D(i)$	- Downward emission of atmosphere
T_M	- Measured input temperature to radiometer
$T_A(\Omega)$	- Apparent radiometric temperature
$T_R(\Omega)$	- Component of downward welling radiation from atmosphere reflected by surface

$T_{s\ell}$	- Apparent temperature in side lobe of antenna
T_{SKY}	- Radiometric temperature of sky
T_{SURF}	- Physical temperature of surface
$T_U(\Omega)$	- Upward emission from atmosphere
t(z)	- Physical temperature of the atmosphere at height z
V	- Brine volume fraction
V_g	- Ground speed
VH	- Vertical transmit, Horizontal receive polarization
VV	- Vertical transmit, Vertical receive polarization
W	- Water
WMO	- World Meteorological Organization
X_{POL}	- Cross-polarization configuration: either HV or VH
Z	- Frazil

1.0 INTRODUCTION

1.1 Background

In recent years, imaging radars and radiometers in the microwave region of the electromagnetic spectrum have become practical tools for operational ice reconnaissance. Studies directed towards the improvement of these tools and the development of automatic sea-ice classification techniques, have used profiling scatterometers and radiometers extensively for primary research sensors to determine the radiometric and scatterometric signatures of many sea-ice classes.

An extensive literature exists on the correlations between sea-ice classification and both radar backscattering coefficient, σ^{o}, and microwave emissivity, ε. This is reviewed briefly below.

1.1.1 Radiometric studies of sea ice

Wilheit et al. (1972) reported the results of an airborne, arctic study in which radiometric measurements of sea ice were made at eight wavelengths in the range 0.51 cm to 2.81 cm (58.8 GHz to 10.7 GHz). The ice was classified as 'new' and 'old' with the new ice forms having a higher emissivity than the old. At 19.4 GHz and 45° incidence angle, θ, emissivities of 0.87 were reported for new ice and 0.77 for old ice, from measurements made with a horizontally polarized radiometer. At nadir, the 19.4 GHz emissivities were 0.95 and 0.8 respectively.

Gloerson et al. (1973) reported measurements of sea-ice emissivities at frequencies between 1.4 GHz and 94 GHz and confirmed the use of emissivity measurements for gross sea-ice classification. At 19.4 GHz, at 45° incidence angle, a horizontally polarized radiometer gave brightness temperatures of 247 K for first-year (FY) ice and 220 K for multi-year (MY) ice. The surface temperature reported by this group, 258 K, may be used to infer emissivities of (ε) 0.95 for first-year ice and 0.84 for multi-year ice, in agreement with Wilheit et al.

The AIDJEX (Arctic Ice Dynamics Joint Experiment) report of Meeks et al. (1974), contains radiometer results for both V (vertical) and H (horizontal) polarization at three incidence angles (25, 40 and 55°) for five sea-ice classifications: open water, first-year, second-year, multi-year and refrozen melt ponds. The V-polarized radiometer results yielded excellent ice-type discrimination but the H-polarized results showed some class boundary overlap.

Little work appears to have been done on the very young ice forms such as grey ice, nilas, grease and frazil. The stability of their emissivities, in space and time, requires further study, as does the variation of emissivity with ice melting.

1.1.2 Scatterometer measurements of sea ice

In his early study, Rouse (1969) used 13.3 GHz (2.25 cm) VV* scatterometer measurements off Point Barrow, Alaska, to separate first-year rough, first-year smooth, multi-year ice and open water

effectively. He also determined an empirical roughness parameter through the angular dependence of $\sigma^o(\theta)$ which could be used to characterize these ice classes. Rouse took simultaneous radiometer measurements but no results are reported.

This work was extended by Parashar et al. (1974) to include 400 MHz (75 cm) with HH, HV, VV and VH polarizations, to complement 13.3 GHz VV scatterometer measurements taken at the same time (1970). Seven ice categories (water, nilas, grey, grey-white, first-year smooth, first-year rough, and multi-year) were identified from stereo pair photography. By using the angular dependence of $\sigma^o(\theta)$, an 87% success rate was obtained in an automatic ice-type classification scheme using the 13.3 GHz sensor and a 75% success rate was obtained at 400 MHz. The full angular signatures were required because of inherent ambiguities between ice classes at particular incidence angles.

Following this, Gray et al. (1977a,b) acquired dual-polarized 13.3 GHz scatterometer data from the Beaufort Sea (1977a) and from the east coast of Canada (1977b). The results from the Beaufort Sea showed similar trends in backscatter contrasts to the earlier Arctic work and also showed that the cross-polarized contrasts between first-year and multi-year ice were significantly larger than with the like-polarized data. The authors also show an anticorrelation between T_B and σ^o for first-year and multi-year ice in the Beaufort Sea data. In the eastern Canadian seaboard data variations of 10 dB were seen in σ^o from thin ice forms and 25 dB from shorefast ice, at all incidence angles, verifying the difficulties that arise when radar grey scale information alone is used to determine ice type. In this data the cross-polarized data also showed increased contrast between ice types but the effect was much smaller than with multi-year ice.

Recently, Onstott et al. (1979) have reported their analysis of multifrequency, ground based scatterometer data collected at several sites near Point Barrow, Alaska, in 1977. This data set includes the angular dependence of thick first-year, multi-year, lake and pressure ridge ice forms for all polarizations over two ranges of frequency, 1-2 GHz and 9-18 GHz. Each measured ice form could be discriminated easily on the basis of σ^o differences but cross-polarization was shown to be better than like-polarization. In the higher frequency range, absolute cross sections appear to increase linearly with microwave frequency, for all their ice classes.

Jackson et al. (1979) have shown good correlation between scatterometer and laser profilometer in a preliminary analysis of 13.9 GHz (2.16 cm) data.

1.2 Objectives of the Active-Passive Experiment

From the foregoing, it is evident that most previous work was based on data from a single sensor class in each experiment; however, the data of Gray et al. (1977 a,b) indicated that radiometric and

---

* In this notation VV means vertical transmit, vertical receive; VH means vertical transmit, horizontal receive and so on.

scatterometric data might be complimentary for some ice types. Although the World Meteorological Organization (WMO) sea-ice classification scheme (Atmospheric Environment Service, Environment Canada, 1978) is based on the visible characteristics of the ice, previous microwave data have indicated that it might have a broader quantitative base than has been reported.

The SURSAT active-passive sea-ice experiment (Active-Passive Experiment) was designed to obtain simultaneous radiometric, scatterometric and photographic sea-ice data and overlapping Synthetic Aperture Radar (SAR) imagery for a large variety of sea-ice classes.

The primary objectives of the experiment were defined as follows:

(1) To determine the quantitative microwave signatures of as many WMO sea-ice classes, under as many environmental conditions, as were reasonably accessible;
(2) To investigate the feasibility of classifying sea ice directly from quantitative microwave data;
(3) To determine the detectability of sea-ice features, such as ridges and icebergs, in a frozen ocean background.

A secondary experiment objective was to determine gain stability of the Canada Centre for Remote Sensing (CCRS) SAR along flight lines and thus determine the feasibility of using the radar as a quantitative scatterometric tool.

To achieve the experiment objectives it was planned to divide the final-stage analysis into three studies:

(1) A sea-ice classification study;
(2) An ice feature study;
(3) A SAR grey scale stability study.

1.3 Data Requirements and Acquisition Overview

The data sets required to meet the primary objectives of the Active-Passive Experiment consisted of outputs from the following five sensors along low altitude (400 m) flight lines:

(1) the aircraft inertial navigation system (INS),
(2) the aircraft radar altimeter,
(3) the nadir-looking RC-10 mapping camera,
(4) the 13.3 GHz dual-polarized fan-beam scatterometer,
(5) the 19.4 GHz H-polarized radiometer.

The data sets required to meet the secondary objectives of the experiment consisted of SAR images overlapping the profiling sensor lines, and although at higher altitudes, obtained in close time proximity so that ice movement was insignificant.

Three deployment regions were initially planned for the Active-Passive Experiment: the Beaufort Sea; the Gulf of St. Lawrence; and the Eastern Arctic seaboard. The Gulf of St. Lawrence site was deleted from the program due to equipment and logistical problems.

The CCRS Convair-580 (CV-580) gathered data in the Beaufort Sea during the period of March 11 to March 19, 1979*, mainly for older ice classes under cold conditions (-26°C). Particular attention was paid to those flight line segments within the polar pack ice and the shear zone between the landfast and polar pack. An opportunity to measure the microwave properties of an ice island, T3, was fortuitous.

The deployment to the Eastern Arctic occurred one month later during the period of April 7 to April 12, 1979. Data obtained there were for much warmer conditions and mainly young ice forms and icebergs were encountered. The primary SURSAT site in the Eastern Arctic deployment was the Danish experiment area, over which five aircraft including the CCRS Convair-580 participated, Gray et al., (1979).

Figure 1 shows the CV-580 flight lines used in the Beaufort Sea deployment. The dashed lines indicate SAR flights and the full lines depict profiling sensor flight lines. These lines are further detailed in Table 1, Section 2.3.1. The majority of the SURSAT surface-based measurements for this deployment were in the vicinity of the north/south line, marked 030803, and the line across T3, marked 030603. Appendix 1 gives a catalogue of ground truth information and site locations as well as data on flights by other participating aircraft for this deployment.

Figure 2 and Table 4, Section 2.3.2, detail the CV-580 flight lines from the Eastern Arctic deployment. Surface-based measurements were made in the Danish experiment area (lines marked G and H in Figure 2) and in the Pond Inlet/Eclipse Sound area (line N). Appendix 2 gives details about these ground truth stations and information about other participating aircraft in the Eastern Arctic deployment.

As indicated in Figure 2, active-passive profiling sensor data were collected along lines marked D, F, G, H, L and N but subsequent analysis was mainly confined to the Frobisher Bay line, D, the Danish cross lines, G and H, and the Melville Bay line, L, to obtain representative samples of young ice types. Heavy cloud cover in the Davis Strait and Labrador Coast precluded the collection of full data sets in these regions; and much of the Pond Inlet/Eclipse Sound line, N, is marginally useful due to cloud cover.

1.4 General Outline of the Active-Passive Experiment Data Analysis Program

During the initial data reduction phase of the Active-Passive Experiment, data sets were preselected by flight line and all flight line segments for which no major sensor or recording system failures occurred were used in the preliminary data analysis.

---

* Flights occurred on three days, 12, 16 and 18 March; however, time is recorded on the aircraft monitors in G.M.T. so that late flights on each day crossed the date boundary. This accounts for labelling in this report of lines on 12 March local time as 13 March G.M.T., see Figure 1 and Table 1.

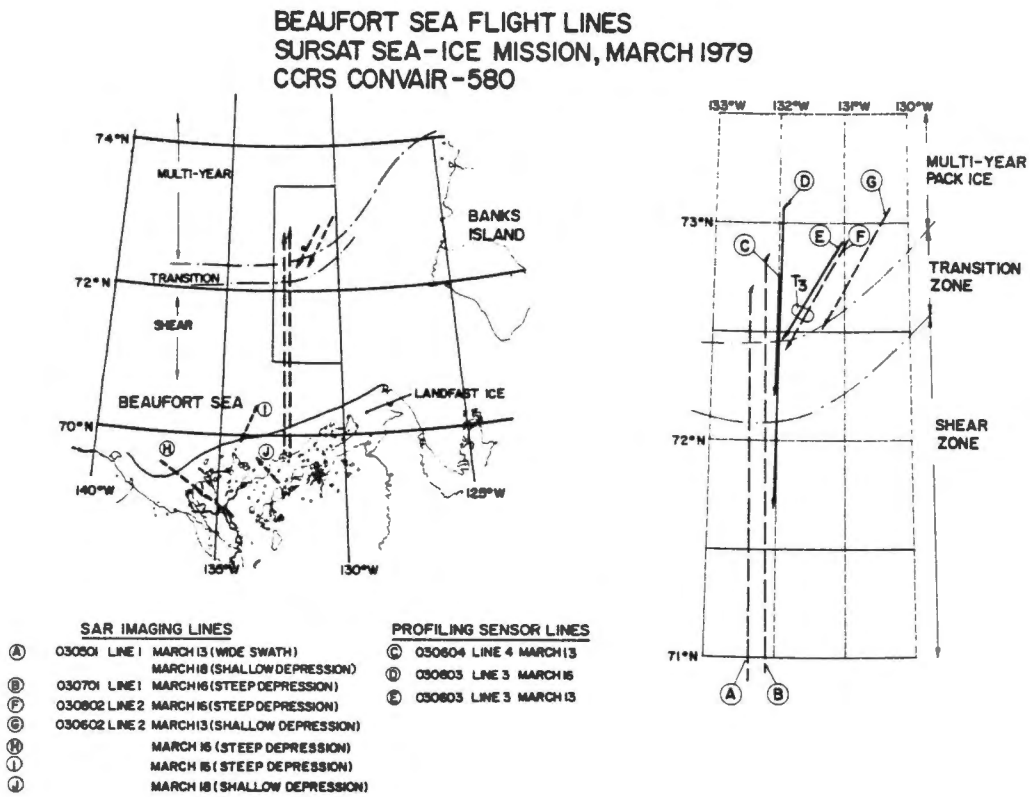

Figure 1. Flight lines in the Beaufort Sea Deployment.

Seven SAR lines and three profiling sensor lines are indicated in relation to the general ice location and type in the Beaufort Sea. Detailed analysis lines: 030603 (marked E) across T3 and the north/south line 030803 (marked D).

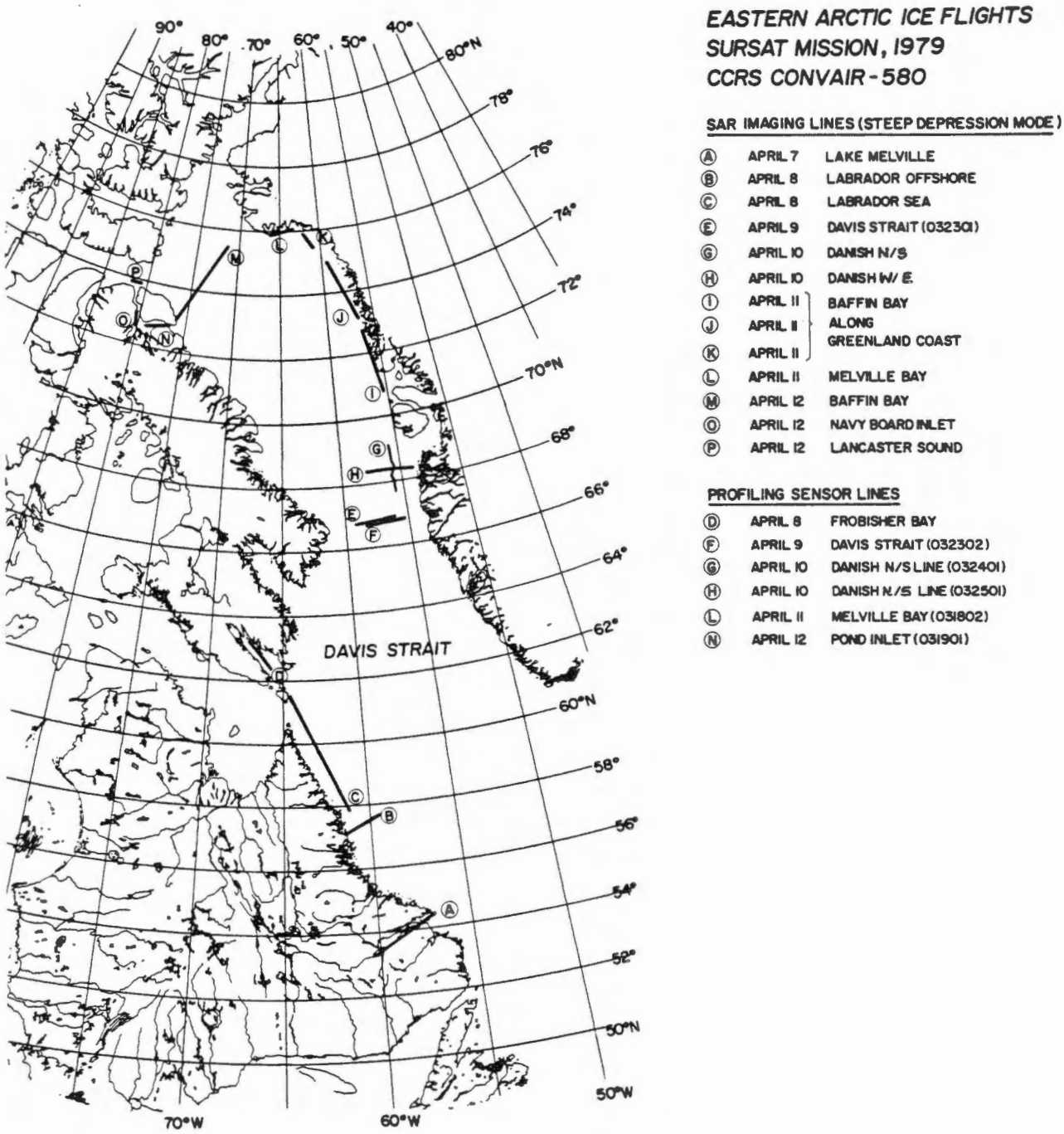

Figure 2. Flight Lines in the Eastern Arctic Deployment

Thirteen SAR lines from the SURSAT mission and six profiling sensor lines are indicated. Detailed analysis of the Frobisher Bay line 032201 (marked D) and the Danish W/E line 032501 (marked H) are reported in this document, as well as iceberg results from the Melville Bay line 031802 (marked L).

The preliminary analysis phase of this experiment consisted of reducing the raw data from the selected flight line segments to physically meaningful parameters. Scattering coefficient time histories were calculated at six incidence angles between 8 and 55°, for both like-polarized (H transmit, H receive) and cross-polarized (H transmit, V receive) scatterometer channels; microwave brightness temperatures were calculated from the raw radiometer data; photo mosaics were constructed for each profiling sensor flight line and the profiling sensor tracks were overlaid on the photo mosaics and on the overlapping SAR imagery.

The photo mosaics were then interpreted along the profiling sensor tracks to classify the sea ice using visual classification techniques. The resulting sea-ice class boundaries were transferred to the scattering cross-section time history plots, as were significant ice surface features such as ridges, icebergs, leads, etc.

The backscattering coefficient, brightness temperature and SAR data were then partitioned by ice type to form 'events', with each event being a section of the time history corresponding to a single ice type classification or a single feature (ridge, iceberg, etc.) of interest.

A data set* consisting of:

(1) a scatter plot of σ^o_{hh} vs. σ^o_{hv} parametric in angle,
(2) a scatter plot of σ^o_{hh} vs. T_B,
(3) a scatter plot of σ^o_{hv} vs. T_B,
(4) a time history of σ^o_{hh} at six incidence angles,
(5) a time history of σ^o_{hv} at six incidence angles,
(6) a time history of T_B,

was assembled for all events two seconds or longer (along-track distance greater than 160 m) in the sea-ice classification study. A similar data set, containing ice features whose along track extent was greater than 20 m, was assembled in the ice feature study.

The events of the classification study were edited to remove event boundary contamination and to remove those events which represented ice-class mixture. Microwave parameter statistics (means, variances and correlation coefficients) were computed for each event and then compiled for each sea-ice class.

The resulting quantitative microwave class signatures were used to define feature spaces suitable for automatic sea-ice classification. Two sea-ice classification algorithms were developed and tested using these spaces.

Events for the ice feature study were edited to select those features for which beam-filling conditions existed and to remove those events that represent mixtures. The events were then analysed to determine ice feature contrasts at all incidence angles, with backgrounds of various ice types.

---

* Examples of this graphics data set may be found in Appendix 7, Figures A7.2, A7.4 etc.

Selected sections of X-band SAR data were digitized along profiling sensor flight lines in the Beaufort Sea for the SAR grey-scale contrast studies. These studies were, however, only partially completed due to limitations in time and manpower.

2.0 DESCRIPTION OF THE ACTIVE-PASSIVE EXPERIMENT

2.1 The Data Acquisition System

The profiling sensor data acquisition system used on board the CCRS CV-580 is shown schematically in Figure 3. A plan view of the sensor locations is given in Figure 4.

Data from all profiling sensors and the inertial navigation system were recorded on magnetic tape, using the CCRS Airborne Data Acquisition System (ADAS) to multiplex and format low rate data. A time code from the aircraft time code generator was recorded on one tape track for use in accessing tape records. Tape recorder channel characteristics and ADAS data frame codes may be found in Appendix 3.

The RC-10 mapping camera recorded time and navigation data on the film space between each frame, in the format given in Appendix 4.

SAR data was recorded on signal film with time and position information recorded on the SAR log sheets. Real-time processor SAR output was produced for 'quick-look' use during the data acquisition period.

2.2 Sensor Characteristics and Operating Parameters

The sensor characteristics and operating parameters of principle interest to this experiment are given in the subsections below.

2.2.1 Ku-band scatterometer (Chan and Gray, 1979)

Frequency	- 13.3 GHz (2.25 cm)
Antennas	- Two linearly-polarized array antennas (one horizontal and one vertical polarization) for transmitting - Two similar linearly-polarized arrays for receiving. During the Active-Passive Experiment only the H transmit antenna was used
Beam shape	- $\pm 60^{\circ}$ fore-aft fanbeam (centred at nadir) with 3° transverse beam width
RMS power	- 2 W
Transmitter type	- CW Klystron
Transmitter polarization	- Horizontal
Receiver polarization	- Horizontal and vertical (simultaneous)
Resolution	- Approximately 18 m along track at an altitude of 1500 feet (460 m), as processed for this equipment

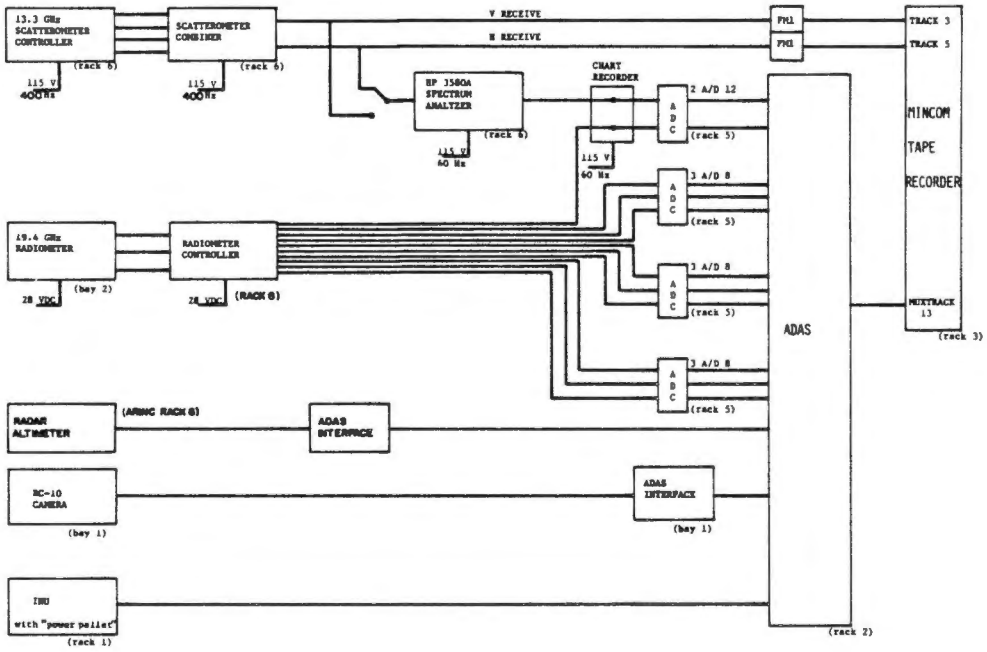

CONVAIR-580
PROFILING SENSOR CONFIGURATION AND RECORDING
SCHEME ACTIVE PASSIVE EXPERIMENT
MARCH/APRIL 1979

Figure 3. Data Acquisition System Schematic for the Profiling Sensors Used in the Active-Passive Experiment.

Data is shown to flow in four sensor streams to be recorded on the Mincom tape. The scatterometer combiner output is recorded analogue, while other sensor data is recorded digitally using ADAS.

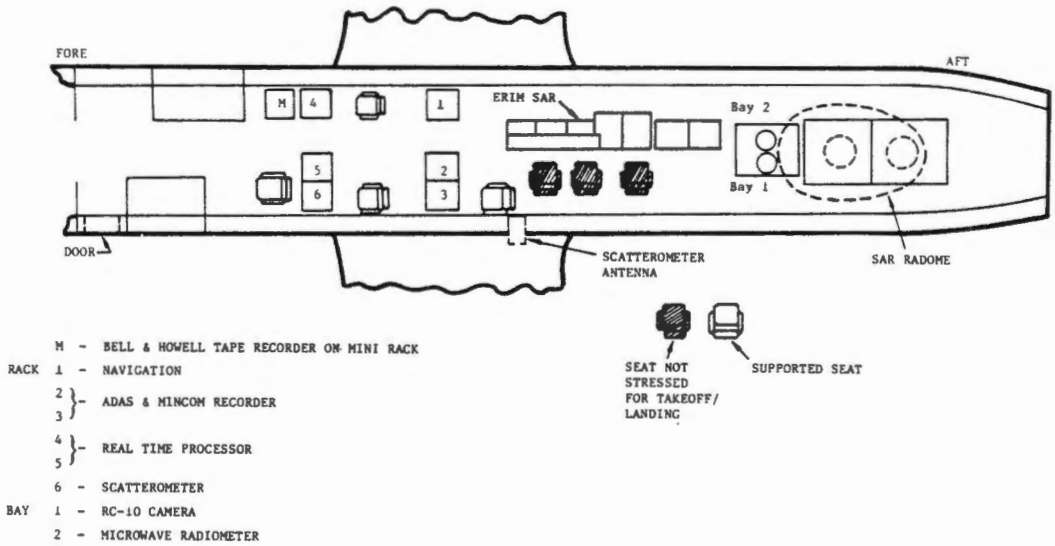

CONVAIR-580
SENSOR LOCATIONS.
ACTIVE PASSIVE EXPERIMENT
MARCH/APRIL 1979

Figure 4. Sensor and Equipment Configuration for the CCRS Convair-580 During the Active-Passive Experiment.

Incidence angle	-	Nadir to 60° available, data processed to yield six angles from 8° to 55°
Outputs	-	Like-polarized (H transmit, H receive) Double-side band,suppressed carrier, analogue signal centred at 10 kHz. Upper sideband is fore beam and lower sideband is aft beam
	-	Cross-polarized (H transmit, V receive) Double side-band suppressed carrier, identical to like-polarized
	-	100 Hz bandwidth filtered corresponding to approximately 45° forward
Recorded signal level	-	Nominal maximum 1V RMS
Level calibration	-	Fixed side tones on DSB signal
	-	Horizontal receiver 8.7 kHz
	-	Vertical receiver 9.3 kHz

Figure 5 shows the geometry and disposition of the scatterometer fanbeam.

2.2.2 K-band radiometer (see Operations and Maintenance Manual, K-band Microwave Radiometer, Aerojet-General Corp.)

Frequency	-	19.35 GHz (1.55 cm)
RF bandwidth	-	200 MHz
Integration time	-	0.1 s
Incidence angle	-	44.3° forward
Antenna	-	Rectangular horn
	-	E plane (across track) beam width 4.63°
	-	H plane (along track) beam width 5.54°
Polarization	-	Horizontal
Resolution	-	Approximately 80 m along track at 1500 ft. (460 m)
	-	Approximately 50 m across track at 1500 ft. (460 m)
Radiometer type	-	Dicke
Calibration	-	Two reference loads at different temperatures
	-	Hot load 393.2 K
	-	Warm load 331.4 K
	-	Eight thermistor wave guide and component temperature monitors
Outputs	-	Radiometer output 10 V max, 10 Hz bandwidth
	-	Eight thermistor outputs 10 VDC maximum
	-	One thermistor reference supply output 2.5 VDC

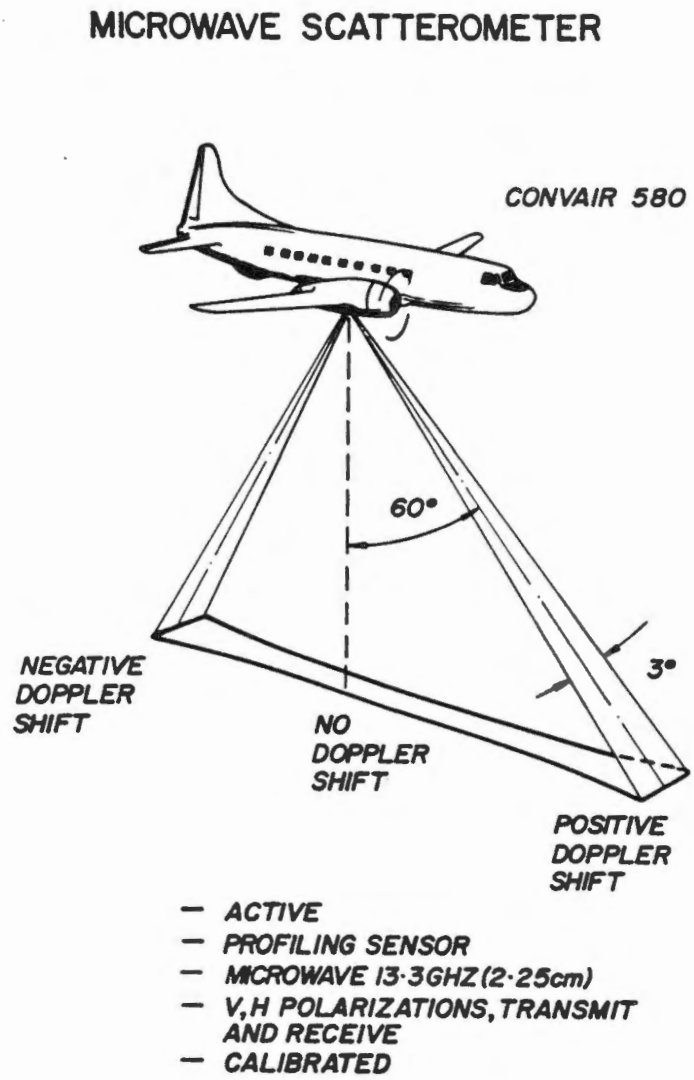

Figure 5. Geometry of the CCRS, 13.3 GHz Fanbeam Scatterometer.

The scatterometer is mounted within the Convair-580 wing root and transmits a continuous wave fanbeam at 13.3 GHz. Only the H-polarized transmitter was used in the experiment, but both polarizations were received. The beam width is 18 m at nadir for typical flight line altitudes.

Recording mode	- Digital using ADAS analogue to digital converters

Figure 6 shows the geometry of the radiometer beam in flight.

2.2.3 RC-10 mapping camera (see RC-10 Universal Film Camera Manual, 1970)

Lens	- 88 mm focal length super wide angle Superaviogon II, 120°, 75.6
Film	- Kodak, Plus X, 2402 Aerographic, black and white
Output	- 9x9 inch negatives with 20% or 60% frame overlap
Annotation	- ADAS annotation block on interframe space see Figure A4.1 - Frame number on frame border on the aft edge of the negatives - A complete index of RC-10 data is given in Appendix 4
Drift angle correction	- None

2.2.4 Inertial navigation unit (see Technical Description, Litton LTN-51 INS, 1972) (Track recovery)

Type	- LTN 51 with Pooling Program
Ports used	- Side port with ADAS interface - Navigation ports including attitude synchros and resolvers
Recording mode	- Digital, ADAS MUX track channel

2.2.5 X/L-band synthetic aperture radar (see the SAR-580 Production System, Intera, 1978 and Rawson et al., 1975)

Frequencies	- X-band 9.3 GHz (3.2 cm) - L-band 1.2 GHz (25 cm)
Video bandwidth	- 50 MHz
Pulse repetition rate	- Coupled to ground speed
Pulse width	- 33 MHz/μs chirp - X-band 3μs - L-band 2μs
Transmit polarizations	- Horizontal

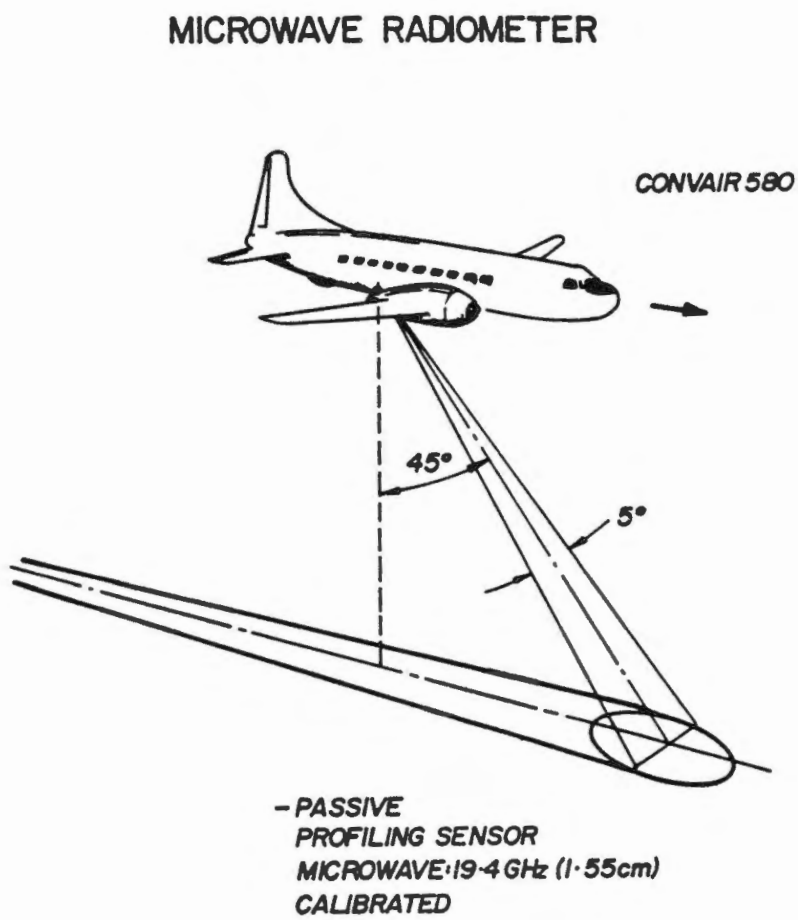

Figure 6. Geometry of the NASA, 19.4 GHz Radiometer Mounted in the Convair-580.

The pencil beam received by the radiometer pyramidal horn is ~ 5° in width and points ~ 45° from nadir along the aircraft heading.

Receiver polarization	- Horizontal and vertical - Horizontal transmit, horizontal receive - X-band only for wide swath lines
Depression angle	- Steep depression (37° to 90°) - Shallow depression (21° to 30.5^{o}) - Wide swath (16° to 90°)
Recording	- 70 mm signal film with drive speed controlled by radar PRF - Dry silver paper (one channel only) real time processor output
Control	- Aircraft navigation INS LTN 51 with ERIM program
Range delay	- Dependent on operating altitude and antenna depression angle
Maximum slant range	- 5.4 km X/L mode - 20 km wide-swath mode

2.2.6 Radar altimeter (see Honeywell Component Maintenance Manual Radar Altimeter, 1975)

Model	- Honeywell YG7500
Frequency	- 4.3 GHz
Pulse repetition rate	- 7 kHz
Pulse width	- 60 ± 20 ns
Power	- 100 W
Range	- 0 to 5000 ft. (0 to 1524 m)
Resolution	- 3 ft. ± 2% (1 m ± 2%) (leading edge detection)
Beam width	- $\pm 40^{o}$

2.3 Mission Flight Lines and Data Acquired

2.3.1 The Beaufort Sea deployment - March 11 to March 19, 1979

During the Beaufort Sea deployment a number of experiments were conducted that required different SAR antenna configurations and depression angles. Three missions were flown on three different days as follows:

(1) March 12, 1979 - SAR mode X-band only, wide swath, horizontal polarization.

(2) March 16, 1979 - SAR mode X/L, steep depression angle (44°), dual polarization.

(3) March 18, 1979 - SAR mode X/L, shallow depression angle (10°), dual polarization.

Data were collected for the Active-Passive Experiment during each of these missions along two experiment lines; a North/South line (latitude $69^{o}30'$N, longitude 132°W to latitude 73°N, longitude 132°W) and a Cross line (latitude $72^{o}52.7'$N, longitude $131^{o}02.7'$W to latitude $72^{o}27.5'$N, longitude $131^{o}54.1'$W).

For the SAR passes, the aircraft flight tracks were offset to centre the experiment lines in the SAR image; for the profiling sensor passes, an attempt was made to position the aircraft directly over the experiment lines.

Table 1 summarizes the Active-Passive Experiment flight lines shown in Figure 1 and gives the sensor status during the lines. The times are given in GMT. In all cases, the SAR lines were flown before the profiling sensor lines and for the Beaufort North/South (N/S) SAR lines, the aircraft was always flying north and the SAR line aircraft tracks were to the west of the experiment lines. The profiling sensors and camera were operated during the SAR flight lines to obtain low resolution profiling sensor data for use in sensor resolution studies.

During the March 12 sortie a failure of the aircraft auxillary power unit (APU) forced a prolonged refuelling stop at Inuvik which seriously shortened the period of daylight for photography. As a result, all photographs for this mission were taken at lower sun angles than in subsequent missions and the first attempt at a N/S line profiling sensor pass lacked photography due to low light level. Although the SAR was operated during all three SAR lines, a failure in the SAR optical recording system during the early part of the mission limited the N/S line wide swath SAR coverage to the latitude interval $71^{o}45'$N to $72^{o}52.4'$N. During the Cross line profiling sensor pass, the SAR was operated at low altitude to obtain super shallow depression angle imagery.

On March 16, all sensors behaved well and steep depression angle data were collected for the entire N/S line and Cross line. The N/S line profiling sensor pass ended in the shear zone (latitude $71^{o}44.6'$N) to allow the diversion of the aircraft to other experiment sites. Some camera annotation unit failures occurred.

On March 18, the ADAS system failed at the start of the N/S SAR line. The profiling sensors were operated in any case and a hand-written log of the aircraft flight parameters was kept. The profiling sensor line was completed for the full length of the N/S line.

During the southern portion of this line, the CV-580 was joined by the NASA (Johnson Research Centre) C-130 carrying a pencil-beam 13 GHz scatterometer and a nadir-looking 6 GHz radiometer. This was part of our co-operative work with Dr. L. Jones, NASA Langley Research Center and it was hoped to compare in detail the NASA sensor data with our data. The two aircraft flew in formation from approximately latitude $71^{o}41'$ to

Table 1. Summary of Convair-580 Flight Lines and Sensor Status From the Beaufort Sea Deployment, 1979.

		Start of Flight Line			End of Flight Line						Sensor Status		
Date (Location)	Run (Line)	Time (HH:MM:SS)	Latitude (DD:MM.M)	Longitude (DDD:MM.M)	Time (HH:MM:SS)	Latitude (DD:MM.M)	Longitude (DDD:MM.M)	Altitude (ft)	Heading (°)	SAR Mode	RC-10	Scatt.	Rad.
March 13 (Beaufort Sea)	1 (030501)	00:10:57.0	69:32.0	132:18.2	01:00:22.0	72:52.4	132:25.8	12500	360	wide swath	ON	ON	ON
	2 (030602)	01:14:30.0	73:02.6	130:18.2	01:22:45.0	72:30.4	131:18.7	12500	210	wide swath	ON	ON	ON
	3 (030603)	01:34:32.0	72:52.7	131:02.7	01:46:48.0	72:27.5	131:54.1	1400	210	wide swath	ON	ON	ON
	4 (030604)	01:54:35.0	72:41.5	132:00.5	02:12:10.0	~71:30.	132:00.0	1500	180	OFF	OFF	ON	ON
March 16 (Tuktoyaktuk)	5	21:28:14.9	69:16.2	132:38.0	21:31:35.3	69:28.2	133:09.9	20000	303/309	steep dep.	ON	OFF	OFF
(Beaufort Sea)	6 (030701)	21:41:40.0	69:36.0	132:08.7	22:20:32.0	72:47.0	132:12.0	20000	360	steep dep.	ON	ON	ON
	7 (030802)	22:31:46.0	72:54.3	130:56.0	22:39:25.0	72:28.5	131:44.6	20000	205	steep dep.	ON	ON	ON
	8 (030803)	23:09:33.0	73:05.2	131:52.6	23:41:38.8	71:44.6	132:02.3	1500	181	OFF	ON	ON	ON
	9	00:08:00.0	70:16.6	133:50.4	00:14:00.0	69:50.9	134:18.2	20000	200	steep dep.	OFF	OFF	OFF
(Mackenzie Delta)	10	01:03:00.0	69:27.3	137:23.2	01:17:00.0	59:51.8	134:17.0	20000	117	steep dep.	OFF	OFF	OFF
March 18 (Tuktoyaktuk)	11	21:32:36.2	69:20.0	132:38.0	21:39:44.0	69:28.0	133:09.0	3000	303/309	shallow dep.	ON	OFF	OFF
(Beaufort)	12	22:10:17.8	69:26.9	132:10.7	23:12:54.0	72:41.0	132:11.0	3000	360	shallow dep.	ON	ON	ON
	13	23:20:00.0	72:35.6	132:00.0	00:31:04.0	69:41.1	131:56.1	1500	182	OFF	ON/OFF	ON	ON

latitude 69°41.1'N. The CV-580, RC-10 camera failed intermittently during the profiling line and failed completely at approximately 69°57.9'N.

In the western Arctic just two profiling sensor lines had complete data sets (SAR, scatterometer, radiometer and RC-10 with annotation). Therefore data reduction of the scatterometer and radiometer data was performed for these lines only (i) Beaufort Cross line, 13 March 1979, 030603 (line 3, Table 1) and (ii) Beaufort N/S line, 16 March 1979, 030803 (line 8, Table 1).

Ice conditions along these two lines were quite similar and appear to be characteristic of cold, western Arctic sea ice during the January-March time frame. The snow cover was dry, wind packed, quite fine grained and was rarely uniform in depth. Drifting occurred around ridges and often small snow dunes were formed around smaller features on the ice. Because of the very low temperatures the top layers of the sea ice had very little free liquid water and what did exist was in the form of a concentrated brine solution.

2.3.1.1 Beaufort Cross line, 030603

The location of the profiling sensor line, 030603, is shown in Figure 1 with the corresponding SAR line, 030602, which both begins and ends before the 030603 line. The line lies entirely within the polar pack, with multi-year floes intersected by first-year leads (oriented in a mainly north/south direction). Since the Cross line ran northeast to southwest the leads usually intersected the line obliquely.

The line ran directly over the ice island T3, across its shorter axis, as indicated in Figure 1, and includes also some very old multi-year ice adhering to both edges of T3. Rough percentages of the major ice types represented along the line are shown in Table 2.

2.3.1.2 Beaufort N/S line, 030803

The Beaufort N/S SAR line began at the Tuktoyaktuk Peninsula coast line (69°32'N, 135°W) and passed northwards across 30 km of landfast ice (all first-year ice with varying degrees of rubbling), then across approximately 220 km of shear zone (again almost entirely first-year ice crossed by major and minor ridges) before traversing 50 km into the polar pack (a mixture of multi-year ice in a first-year matrix). This is illustrated in Figure 1.

The usable length of SAR, scatterometer and radiometer data encompassed only the latter third of this line, shown in Figure 1 as the 030803 line for the low altitude pass and the 030501 line for the SAR pass. The data reduced and processed has shear zone, (ridged and smooth first-year ice with some younger leads), a transitional zone (first-year ice and mainly small multi-year fragments), then multi-year pack ice. Rough percentage concentrations of the major ice types along the line, for both SAR imagery and scatterometer lines, are shown in Table 3.

Table 2. Ice Distribution on the Beaufort Cross Line, 030603.

Ice Class	Ice Distribution (%)	
	SAR Imagery	Scatterometer Line
Multi-year	78	67
Second-year	2	4
First-year	10	10
Grey-white and grey	*	1
Ice island	10	18

* These classes cannot always be identified in the SAR imagery

Table 3. Ice Distribution on the Beaufort N/S Line, 030803.

Ice Class	Ice Distribution %		
	Shear Zone	Transition Zone	Polar Pack
Multi-year ice	-	35	70
Second-year ice	-	Trace	Trace
First-year ice	100	65	30
Grey-white and grey ice	-	-	Trace

In the pack ice there was more first-year ice on the N/S line than on the Cross line, since the line ran roughly parallel to the orientation of the refrozen leads. In addition there was a cementing matrix of older first-year ice between very large and smaller multi-year floes.

The transition between polar pack and shear zone ice was not instantaneous: beyond the main 'edge' of multi-year floes were several major outliers (including a vast floe designated by events 222 to 224 in this study) and groups of small multi-year fragments. The latter had been crushed and broken against each other and the intervening first-year ice.

2.3.2 The Eastern Arctic Deployment - April 7 to April 12, 1979

Unlike the Beaufort Sea deployment in which all experimental areas were directly accessible from a single base of operation, the Eastern Arctic deployment, April 7 to 12, 1979, progressed from base to base to obtain wide areal coverage. To simplify the experiment logistics, the SAR was operated in a single mode (X-, L-band, dual-polarization, steep (43°) depression angle) throughout the entire mission. Most of the experimental flight lines were covered only once.

The CV-580 base of operation for this deployment was moved from Goose Bay, Labrador; to Frobisher Bay, Baffin Island; to Søndre Strømfjord, and to Thule, Greenland; in order to acquire ice data from the regions of interest:

(1) The north Labrador coast
(2) Davis Strait
(3) Baffin Bay off the west Greenland coast
(4) Melville Bay
(5) North Baffin Bay
(6) Pond Inlet/Eclipse Sound
(7) Lancaster Sound

Particular emphasis was placed on obtaining iceberg and broken pack ice data, including young ice forms. Several flight lines were needed in this deployment to collect data sets representative of ice regimes in different ambient temperatures for the Active-Passive Experiment.

The Active-Passive Experiment flight lines shown in Figure 2 and sensor status for the Eastern Arctic deployment are summarized in Table 4.

2.3.2.1 Frobisher Bay line, 032201

A break in the cloud cover as the aircraft was in transit to Frobisher Bay provided a target-of-opportunity profiling sensor line (line 032201, run 5, Table 4). No overlapping SAR coverage was obtained, however, because of insufficient aircraft fuel reserves. This line is shown in Figure 7.

Table 4. Summary of Convair-580 Flight Lines and Sensor Status From the Eastern Arctic Deployment, 1979

		Start of Flight Line			End of Flight Line						Sensor Status		
Date (Location)	Run (Line)	Time (HH:MM:SS)	Latitude (DD:MM.M)	Longitude (DDD:MM.M)	Time (HH:MM:SS)	Latitude (DD:MM.M)	Longitude (DDD:MM.M)	Altitude (ft)	Heading (°)	SAR Mode	RC-10	Scatt.	Rad.
April 7	1	20:12:00	53:29.5	069:19.6	21:09:00	54:55.3	056:17.2	18000	057.3	steep	ON	ON	ON
(Lake Melville)	2	21:40:00	54:37.4	056:25.7	22:13:00	53:21.7	060:19.9	18000	242.9	steep	OFF	OFF	ON/OFF
April 8	3	18:42:00	57:07.7	061:30.6	19:03:00	57:25.3	059:11.6	17000	076.0	steep	OFF	OFF	OFF
(Labrador Sea)	4	19:15:00	57:52.9	060:27.1	20:17:00	61:32.9	064:37.6	17000	320	steep	OFF	OFF	OFF
(Frobisher Bay)	5	20:42:54	62:30.8	065:50.0	21:12:43	63:18.5	067:26.0	1500	323	OFF	ON	ON	ON
	(032201)												
April 9	6	16:52:00	67:08.0	066:42.3	17:01:00	67:14.8	065:00.7	12500	079.5	steep	OFF	OFF	OFF
(Davis Strait)	7	17:20:00	66:32.6	062:42.7	17:56:33	66:53.6	056:21.6	17000	079.3	steep	OFF	OFF/ON	OFF/ON
	8	18:08:34	66:50.2	055:47.7	18:35:42	66:49.9	058:26.5	2500-1000	264	OFF	ON	ON	ON
April 10	9	13:59:00	68:15.7	053:44.2	14:23:00	68:15.2	058:42.5	18000	272	steep	PART	OFF	OFF
(Davis Strait)	10	14:55:00	67:47.9	056:09.8	15:16:48	69:20.6	056:10.0	18000	000	steep	OFF	PART	PART
	11	15:30:49	69:07.4	055:54.2	16:03:38	67:38.8	055:50.0	1500	180	OFF	ON	ON	ON
	(032401)												
	12	16:30:50	68:24.7	058:06.8	16:56:54	68:23.1	054:51.0	1500	90	OFF	ON	ON	ON
	(032501)												
	13	17:01:00	68:20.1	054:08.0	17:06:07	68:20.0	054:07.0	1500	171	OFF	ON	ON	ON
	14	17:09:42	68:19.9	054:08.0	-	-	-	-	341.4	OFF	ON	ON	ON
April 11	15	14:24:00	69:20.0	055:59.3	14:38:00	70:18.8	055:29.2	18000	010	steep	OFF	OFF	OFF
(Baffin Bay)	16	14:45:00	70:47.8	055:34.7	15:13:46	72:42.1	056:43.1	18000	350	steep	ON	OFF	OFF/ON
	17	15:19:00	73:07.5	057:15.5	15:48:53	75:10.9	059:21.3	18000	345	steep	ON	OFF	OFF
	18	15:55:10	75:31.8	060:52.9	16:02:20	75:50.2	062:19.6	18000	311	steep	ON	OFF	OFF
	19	16:10:00	76:01.8	063:50.6	16:23:00	75:50.7	067:45.8	19000	260	steep	OFF	OFF	OFF
(Melville Bay)	20	17:04:44	76:03.4	063:26.2	17:21:05	75:53	066:26.1	1500	260	OFF	ON	ON	ON
	(031802)												
April 12	21	14:29:00	75:37.9	071:38.0	14:40:00	-	-	20200	211	steep	OFF	OFF	OFF
(Baffin Bay)	22	14:47:00	74:38.0	074:06.3	15:03:00	73:45.5	076:05.5	20200	212	steep	OFF	OFF	OFF
(Pond Inlet)	23	15:28:00	72:43.7	077:12.0	15:42:00	72:27.9	080:51.7	20200	258	steep	OFF	OFF	OFF
	24	16:28:00	72:19.6	079:02.9	16:36:00	72:56.7	080:48.4	20200	320	steep	OFF	OFF	OFF
(Lancaster Sound)	25	16:57:00	73:51.8	081:50.9	17:02:00	73:52.0	080:43.8	20200	089	steep	OFF	OFF	OFF
(Pond Inlet)	26	20:35:00	72:48.0	076:52.6	20:53:23	72:40.6	079:35.3	1500	250	OFF	ON	ON	ON
	(031901)												

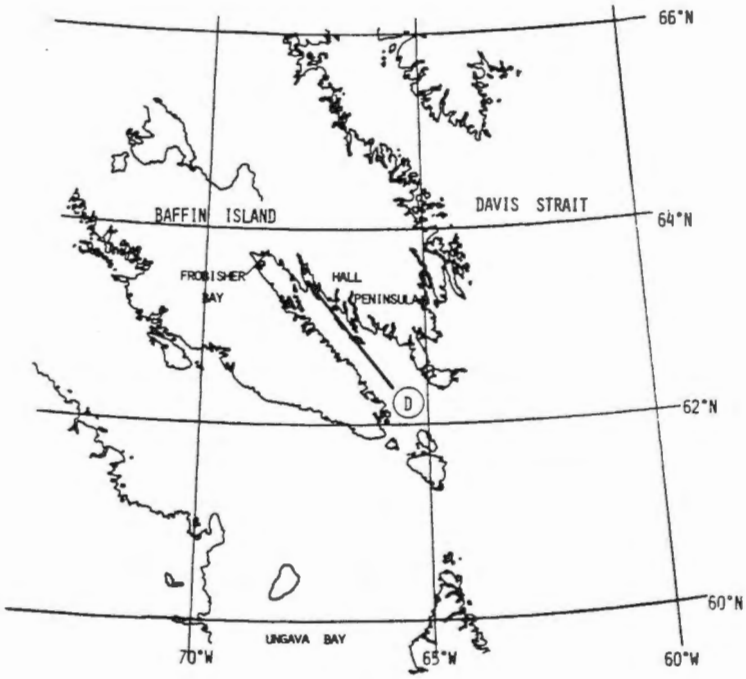

FROBISHER BAY FLIGHT LINE

Ⓓ 032201 APRIL 8,1979

Figure 7. The Frobisher Bay Profiling Sensor Line, April 8, 1979.

This was a line of opportunity and was unscheduled in the original experimental plan, but has been analysed in detail. The ambient temperature of the ice is estimated to be $-5^{o}C$ during the flight (from Frobisher Bay observations).

None of the ice in Frobisher Bay line was older than first-year; there were newer categories present and a little open water, in the approximate percentages shown in Table 5.

The ambient temperature was about -5°C (estimated from Frobisher Bay Weather Observation), so that only recently opened leads remained free of ice, and many less recent leads had frazil and/or nilas forming on each side. The first-year ice of many floes showed evidence of being fairly thin, but whether it was younger first-year or thicker first-year ice that had already undergone melting is not known.

2.3.2.2 Davis Strait

An attempt was made to fly a profiling sensor line across Davis Strait on April 9 during the CV-580 transit from Frobisher to Søndre Strøm, but this was defeated by thick, low-lying clouds. Nevertheless, SAR data was collected at high altitude.

2.3.2.3 Danish West Greenland Experiment lines, 032401 and 032501

On April 10, the CV-580 flew out of Søndre Strøm to participate in a joint Danish, U.K., Canadian, and U.S. experiment off the west coast of Greenland. Two SAR lines and two profiling sensor lines (the Danish West/East (W/E) line and the Danish North/South (N/S) line) were flown in the form of a cross over the eastern edge of the pack ice. These are designated as the 032501 and 032401 lines in Figure 8 (runs 11 and 12, Table 4). Attempts were made to obtain surface truth data (Gray et al., 1979) but because the ice was relatively thin and decaying, only measurements of snow and ice thickness plus some salinity measurements were taken.

The CV-580 flying sequence of runs 9, 10, 11 and 12 in Table 4 is significant because the ice drift was sufficiently rapid to shift the ice seen in the east to west SAR line swath away from the W/E profiling sensor line in the 2½ hours required to fly the other three lines.

The Danish W/E profiling sensor line (032501) contained a mixture of ice types similar to the Frobisher Bay line, and an additional transition area from heavy ice concentrations to open water (referred to as 'marginal' ice in Gray et al., 1979), where the floes had undergone melting and break-up due to swell and wave action. Floe sizes decreased continuously, first as close pack ice, then the floes became separated with large polynya, and finally they formed several plumes in open water. A few small icebergs and bergy bits were imaged but were not intersected by the profiling sensor lines.

The ambient temperature was between -1° and -3°C with many floes being both very wet and quite thin. The snow layer was unsaturated, but the snow/ice interface was wet and the ice waterlogged, (Gray et al., 1979).

The preceding comments also apply to the Danish N/S line (032401). This line, however, included profiles of several icebergs, mostly pinnacle type.

Table 5. Ice Distribution on the Frobisher Bay Line, 032201.

Class	Ice Distribution (%)
Water	3.5
Frazil	4.5
Nilas	15
Grey	8
Grey-white	2
First-year	67

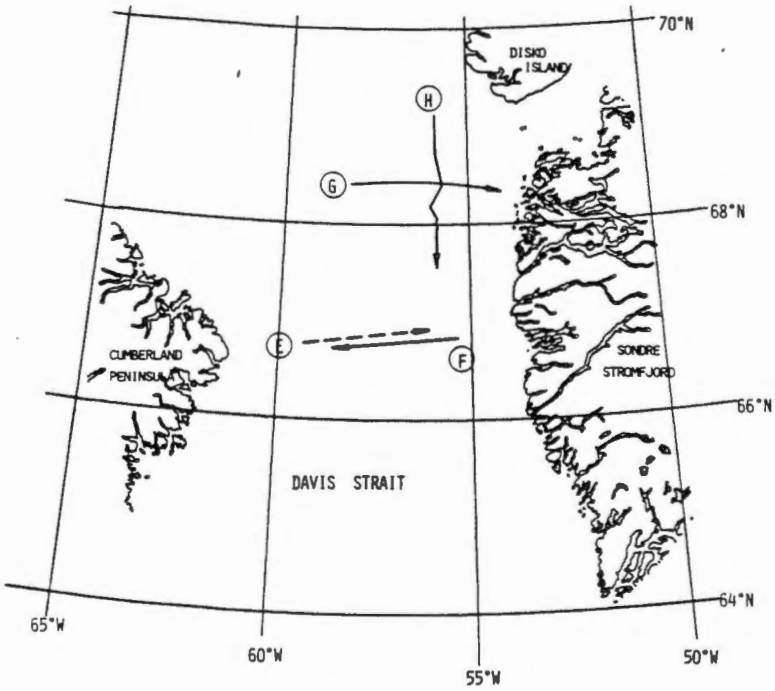

DAVIS STRAIT FLIGHT LINES

Ⓗ 032401 } DANISH EXPERIMENT
Ⓖ 032501 } APRIL 10, 1979

Ⓔ 032301 } APRIL 9, 1979
Ⓕ 032302 }

Figure 8. Flight Lines in the Davis Strait.

The 032401, and 032501 lines (marked H and G) were part of the Danish West Greenland Experiment in which the CCRS, Convair-580 participated. The W/E line (marked G) was analysed in detail to give results for ice melting conditions.

2.3.2.4 Melville Bay line, 031802

During the CV-580 transit from Søndre Strøm to Thule on April 11, two lines, were flown for the Active-Passive Experiment in the north western section of Melville Bay. At the time of the flights, a cloud layer existed between the high altitude (19000 ft.) SAR line and the lower altitude (1500 ft.) profiling sensor line (031802, Figure 2; run 20, Table 4) with the result that high-level photography was impossible and the surface lighting for the profiling sensor line was less than optimal for sea-ice classification from the photography. Sufficient surface texture is, however, present in the photography for some ice classification work and icebergs are clearly discernable.

The ice surveyed in the Melville Bay line was predominantly landfast. This level, thick first-year ice in many areas was scattered with icebergs, thousands of small fragments and many huge bergs, mostly tabular type, some old and sculptured, some grounded.

Parts of the line included close pack ice also containing bergs, and the end of the line reached the more mobile ice off Kap York, with ridged first-year ice and some thinner ice (grey) with few bergs present.

2.3.2.5 Pond Inlet/Eclipse Sound line, 031901

A sortie was flown from Thule to the Pond Inlet/Eclipse Sound areas near Bylot Island on April 12. During this mission, two flight lines provided data for the Active-Passive Experiment. These were the Pond Inlet SAR line (run 23, Table 4), and the Pond Inlet profiling sensor line (line 031901, Figure 2; run 26, Table 4).

Weather conditions were similar to those found on the previous day in Melville Bay, with the result that the profiling sensor line photography is difficult to interpret in places due to low light levels. The cloud ceiling descended over Eclipse Sound and the profiling sensor line was terminated prematurely.

Ice conditions along the profiling sensor line were very uniform. Almost all of the ice seen was first-year landfast, which varied in texture from very smooth to fairly rough or rubbled. Few ridges were observed and no new ice was seen; however, the rough areas included a few small bergs and multi-year floes.

Extensive ground truth is available for the portion of the line near Pond Inlet, as indicated in Appendix 2.

2.4 Data Processing and Analysis

Raw data from the Active-Passive Experiment consisted of high-density magnetic tapes of profiling sensor data, keyed to time along the flight lines, RC-10 photography and SAR imagery. The integration of the profiling sensor data with the photographs and SAR imagery was an interactive process, involving the matching of features observed in the imagery with a graphical display of scattering coefficient and brightness temperature along the flight line, as described in Section 2.4.3.

Airborne flight logs were used to determine run time and location for each sensor and this information, together with annotation block provided on each RC-10 frame*, allowed a registration of ice photography and profiling sensor footprint. Coincident features of the SAR imagery** and aerial photography were identified using visual pattern recognition*** and the profiling sensor flight lines were transferred to overlay the SAR data. A classification done on the basis of any of the three kinds of data (profiling scatterometer and radiometric, RC-10 photography, or SAR imagery) was then easily cross referenced.

A linear photomosaic was made by cutting and overlaying RC-10 roll prints to form a continuous image of the ice along the aircraft flight line. The aircraft track was marked on this mosaic, with ice classes and features being identified using key letters as listed in Table 6, Section 2.4.1. In most cases, ice types were readily interpretable from the photography alone as described in Section 2.4.1; but, in ambiguous cases, data from other sensors: SAR, scatterometer and radiometer, were used to resolve the classification. These interpreted photomosaics formed the principle index to the Active-Passive Experiment sea-ice classification and ice feature studies and remain archived at CCRS.

Extensive computer processing was required to reduce the profiling sensor data and a considerable body of software was developed to complement already existing programs. The software analysis is discussed in Section 2.4.2.

2.4.1 Photographic interpretation and description of sea ice

General ice conditions along each line have been described in Section 2.3 including the basic proportions of each ice type. In this section each ice type will be described briefly, together with its appearance in the imagery, in tabular format. An example of each ice type is given in Appendix 7 and is illustrated by an RC-10 image with radiometer and scatterometer time histories for comparison.

---

* The annotation block is described in Appendix 4, Figure A4.1 and includes, in addition to time code, several navigation parameters: latitude, longitude, heading, track, etc. Unfortunately this annotation was not transferred from the negative to the roll prints used for interpretation and cross referencing was done by hand.

** SAR imagery from the optical processor is annotated after processing into equal-spaced divisions and arbitrarily sequence numbered.

*** This process was especially tedious because the RC-10 film and SAR film scales differ by a factor of 30.

Ice nomenclature has become increasingly standardized into an internationally accepted code, under the auspices of the World Meteorological Organization (Atmospheric Environment Service, Environment Canada, 1978). This classification scheme was used in this study. Twelve main categories were distinguished, with several subcategories for some ice types in special circumstances, such as rough or smooth ice for first-, second- and multi-year ice in the western Arctic and wet or wave-broken for first-year ice in the eastern Arctic. Table 6 describes the twelve ice types. Sub-categories are described in the following paragraphs.

In the Beaufort Sea the majority of ice was first-year or older. There was a wide variation in appearance within these classes depending upon the frequency of ridges, rubble blocks or hummocks. Broadly, the classes could be subdivided (depending on these surface features) into rough or smooth events, which were analysed further as independent classes. A small subclass of broken bits, usually multi-year fragments in a first-year matrix, was identified but not analysed later, since the category was a mixture of ice types.

First-year ice in the eastern Arctic was somewhat different in nature from the western examples, mainly because of higher ambient temperatures. In addition, the overcast conditions resulted in an absence of shadows, obscuring the contrast between rough and smooth ice conditions. The warmest and wettest ice was found on the Danish West/East (032501) and North/South (032401) lines; much of the first-year ice was designated into a wet first-year subclass. The ice appeared puddled (dappled) or had patches of darker grey tone within the floes due to greater snow melt in these areas. In some cases, all the ice surface appeared wet except for the snow drifts.

A further subclass, wave-broken ice, occurred on the Danish lines; the margin of the pack is subjected to swell and wave action so that the floes break into increasingly smaller fragments, in a progressive development towards the open water, with water, brash ice or younger ice forms between the floes.

2.4.2 Computer processing of profiling sensor data

The airborne data required for the analysis of this experiment included:

(1) Time (from the aircraft time code generator);

(2) Aircraft flight parameters (from the aircraft inertial navigation system)
   (a) latitude,
   (b) longitude,
   (c) pitch,
   (d) roll,
   (e) track angle,
   (f) ground speed;

Table 6. Sea-Ice Classification

Ice Type (Notation)	Thickness (cm)	Description	Behaviour Under Pressure	Appearance in RC-10 Photography	Present in Line
Open Water (W)	-	Navigable water, ice absent or nearly so (fragments smaller than sensor resolutions).	-	Black, may be waves visible as ripples	032201, 032401 032501
Frazil (Z)	0-5	Fine spicules or plates of ice, suspended in water.	Moves freely	Black, waves less likely	032201, 032401 032501
Grease (R)	0-5	Ice crystals coagulated to form soupy layer on surface.	Moves freely	Almost black, matte surface	032401, 032501
Dark Nilas (ND)	<5	Thin elastic crust of new ice, easily bending on waves. Quite saline.	Interlocking finger rafting	Very dark grey	032201, 032401 032501
Light Nilas (LN)	5-10	As above, a little thicker.	As above	Dark grey	032201, 032401 032501
Grey (G)	10-15	Young ice, less elastic than nilas, breaks under swell. Highly saline near surface.	Forms rafts	Mid-grey	All but 031901
Grey-white (L)	15-30	Thicker young ice. Highly saline near surface	More likely to ridge than raft	Light grey	All but 031901
First-year (F)	30-200	Sea ice of not more than one winter's growth. Saline.	Forms ridges	White, except shadows	All
Second-year (S)	>200	Old ice which has survived only one summer's melt. Less dense and less saline and smoother topography than above, less weathered than following.	Forms ridges	White, except shadows	030603, 030803
Multi-year (MY)	>200	Old ice which has survived at least two summer's melt. Smoothed topography and low salinity especially at surface.	Forms ridges	White, except shadows	030603, 030803
Ice Island (II)	>2500	Large piece of ice, glacial or land marginal in orgin, non-saline, having a regularly undulating surface and thickness of 25-50 m.	-	White, except shadows	030603
Iceberg (B)	Various	Floating or aground piece of ice of glacial origin. Varying in shape - tabular, pinnacled, sloping, dome-shaped or weathered.	-	White, except shadows	032401, 031801 031901

(3) Aircraft altitude (from the radar altimeter);

(4) Microwave radiometer output
  (a) receiver output,
  (b) thermistor outputs,
  (c) reference voltage;

(5) Scatterometer output
  (a) horizontal receiver output,
  (b) vertical receiver output,
  (c) narrow band (filtered) horizontal receiver output (filtered by the HP3580A spectrum analyser).

The aircraft data acquisition system (ADAS) was used to store items 1 to 4 and 5c in a high density, multiplexed digital channel (called the MUX track) on magnetic tape (Mincom recorder). Items 5a and 5b were stored on adjacent analogue tracks.

The MUX track digital channel data and the analogue channel data were processed in separate streams as shown in Figure 9. The MUX track data are first stripped from the high density Mincom tapes onto computer compatible tapes (CCT), by the CCRS Data Processing Division (DPD), on the airborne data processing system (AIR) computer. The CCT data were then processed on the DPD time-sharing system and data from each sensor were stored in CCRS non-imagery disk files*. Conversion of raw sensor data into meaningful parameters** was accomplished in the MUX to CCT to non-imagery disk file procedure.

Each analogue data channel is read and moved onto CCT's with the AIR system using a digitization rate of 50,000 points/s on the DPD analogue-to-digital converter described by Edel (1979). These CCT's are read and a 12288 point Fast Fourier Transform (FFT) is performed, separating the scatterometer incidence angles by their Doppler frequencies in time segments of 0.2458s. The spatial resolution was determined by this time period and the aircraft ground speed. An accurate knowledge of both ground speed and altitude is required for the proper assignment of incidence angles; these were recovered manually from a display of recorded navigation MUX track data using the procedures outlined in the right-hand column of Figure 9. The preceding processing steps were performed using the program SCATT. The program ARRR, which follows SCATT in the analysis sequence, shifts the time of the data so that all time references refer to the nadir-looking footprint.

---

* The CCRS non-imagery disk file system is described by Edel and Gough, 1979 and the airborne processing and description of MUX data is given by Bridgeman, 1978 and Bridgeman and Gough 1979.

** The 10 radiometer output voltages - receiver output, 8 thermister outputs and a reference voltage - are converted to thermocouple temperatures and an estimate of microwave brightness temperature. See Appendix 5 for details.

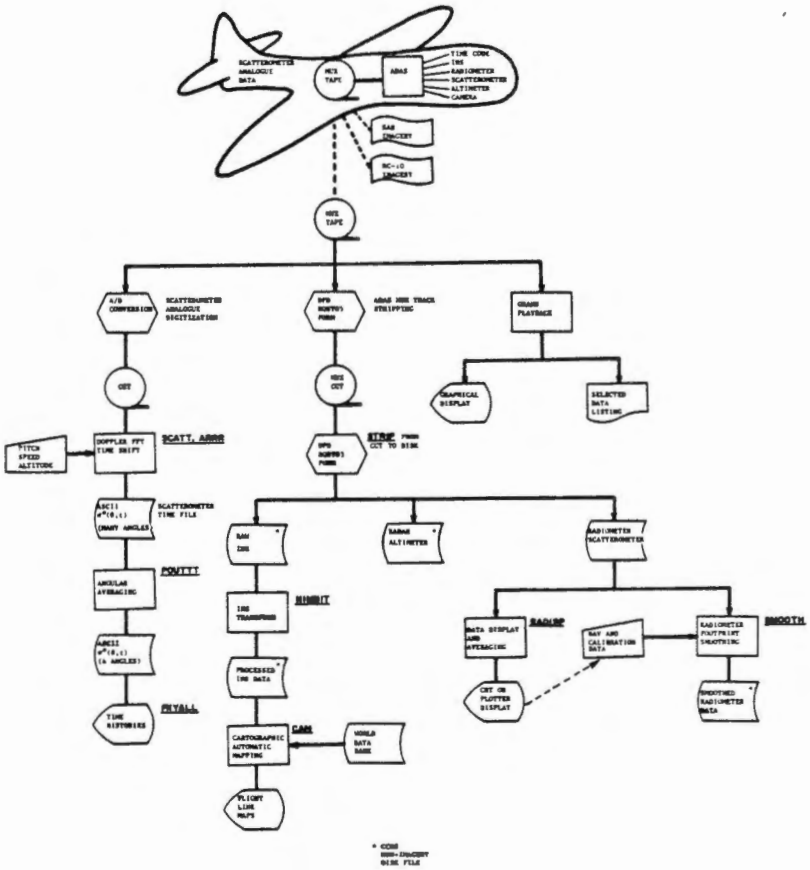

SCATTEROMETER - RADIOMETER
DATA PROCESSING

Figure 9. Data Processing Schematic for Active-Passive Experiment.

Data from the analogue and digital channels of the Mincom tapes are processed in separate and parallel streams. Both kinds of data may be reviewed on the quick-look ground recovery and monitoring system (GRAMS).

Scatterometer processing was done in one-minute flight line segments to combine ease of data handling and limits of current software capabilities with allowable variation of flight parameters. The raw data processing required approximately 93 hours of PDP-10 KA Central Processing Unit (CPU) time for the 186 line-minutes of data analysed. This initial processing represents the major computer expenditure on the project and although the software required for further data analysis was substantial, its operation costs were minimal.

Reduced scatterometer data* for each line were computed, stored and displayed as a time history of six scattering angles, between 0 and 60° (aft) for each scatterometer polarization, using POUTTT. These detailed time histories could be correlated easily with ice type through comparison with the mosaic of RC-10 photographs and were used to define the time boundaries of each 'event'**.

To facilitate the quantitative classification of the data, a software package (schematically depicted in Figure 10) was designed to create and process event files containing all relevant information for each event. The ice description, its time boundaries and associated data file sources were entered through the routine EVMAKE, which creates the initial entries in the Event Summary File, ESF***. The ESF file was usually the only input to succeeding steps in the package. Navigation data were added to the ESF by time averaging the INS and altimeter files over the period of the event using the routine EVNAV. The program EVFILL searches the HH and HV scatterometer time history files and creates a new non-imagery disk file known as the Event Data File (EDF). This file initially contains the event time history, with scattering coefficients for six incidence angles formed by averaging the raw processed scatterometer data in the decades $0\text{-}10^{o}$, $10\text{-}20^{o}$, $20\text{-}30^{o}$,...., $50\text{-}60^{o}$. Using the ESF navigation data, the routine EVRDM calculated the time offset required in the radiometer footprint to synchronize this result with scatterometer nadir footprint****, and interpolated the already smoothed radiometer data, adding these results to the EDF. At this point,

---

* The scattering coefficients determined from the scatterometer processor have a systematic error due to uncertainty in the two-way antenna gain function. This means that the incidence angle behaviour of the results may be in error; however, relative measurements (radar contrasts) at the same incidence angle are unaffected by this uncertainty, cancelling when a ratio is taken. An improved calibration is now under investigation and will be reported separately.

** Event classification procedures are discussed in Section 2.4.3.

*** Examples of complete ESF's may be seen in Appendix 7, Tables A7.1 to A7.16.

**** Note that the initial processing of the scatterometer data implicitly includes a similar time shift of all non-nadir looking scattering coefficients so that each off-nadir data point is shifted to the time when the observed footprint was at nadir. EVRDM produces this same result for the radiometer.

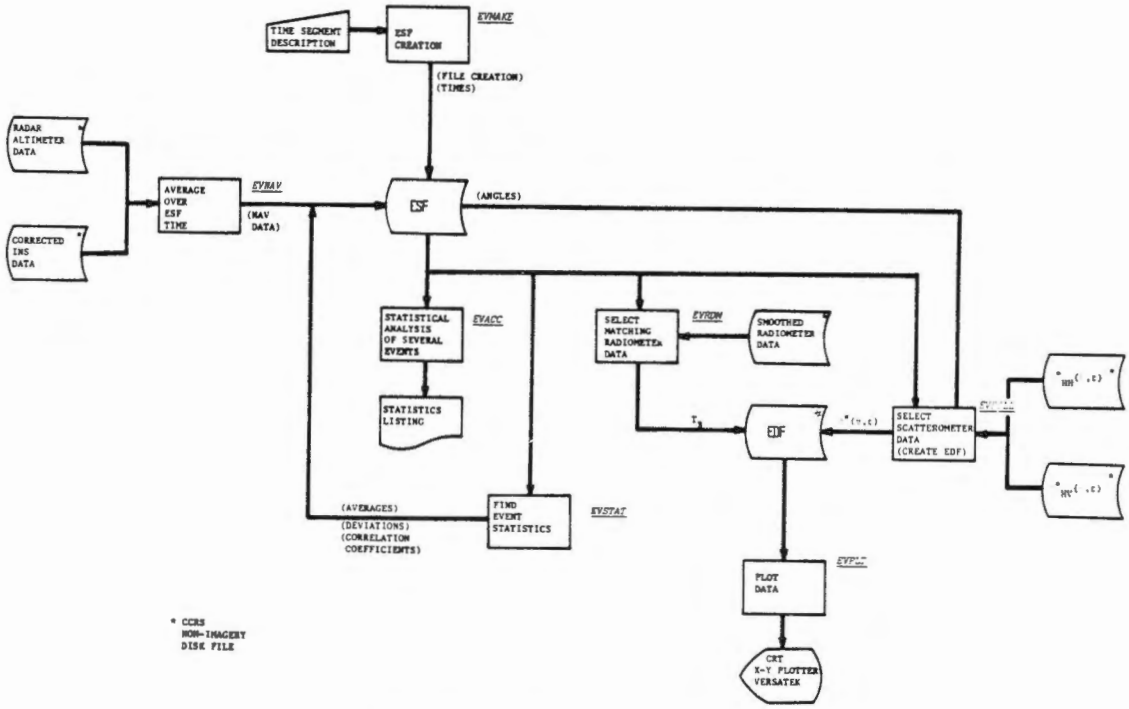

SCATTEROMETER – RADIOMETER
EVENT FILE SOFTWARE

Figure 10. Software Schematic of the Radiometer-Scatterometer Event File System.

This system allows data to be indexed in the event summary file (ESF) and efficiently stored and retrieved in a random access file called the event data file (EDF). Corresponding data from the INS, radar altimeter, time code generator, radiometer and scatterometer are merged.

the EDF was complete and statistics for the event were determined and added to the ESF using the routine EVSTAT. The statistics set consisted of averages and variances for the six angle backscatter time histories at each polarization, linear correlation coefficients between the cross-polarized scattering coefficients, and between the cross-polarized scattering coefficients, and between the cross-polarized scattering coefficients and the radiometer brightness temperatures.

The correlation between radiometer and scatterometer results was complicated by their different footprint sizes (cf. Section 2.2). to compensate partially for the mismatch, the scatterometer data was integrated over the effective along track radiometer footprint, and the correlation coefficient was calculated using the relation:

$$C_{R-S} \approx \frac{\sum_{i=1}^{N} \sigma^o - \langle \sigma^o \rangle \quad (T_B)_i - \langle T_B \rangle}{N\,(\Delta T_B)\,(\Delta \sigma^o)} \qquad (1)$$

The summation in the index, representing the i th sample in the event, extends over all N samples in the event. Here C_{R-S} is the correlation coefficient, T_B is the brightness temperature, σ^o is the scattering coefficient, with $\Delta\sigma^o$ and ΔT_B the variance in σ^o and T_B. < > indicates an averaging over the integration period of the radiometer footprint. It must be noted that this expression only matches the along track resolution cell dimensions (approximately 20m scatterometer, 50m radiometer).

The data from each event can be displayed on computer graphics peripherals using any of the standard CCRS non-imagery disk file graphics programs (PARSRT, PLTALL, PLTLUK, TRNSLT), however, for convenience in handling large volumes of data a separate event display program, EVPLT, was developed. This routine offers the user a choice of scales, output device (Tektronix model 4662 plotter, Versatek matrix plotter or CRT display plot). In practice, it was found expedient to plot all functions, as described in Section 1.4, on the Versatek plotter and review this multiple graphic package for the set of all events of the same ice class.

The time boundaries of individual events often required revision to eliminate event boundary contamination. This was done by editing the ESF* and rerunning the program sequence: EVFILL, EVNAV, EVRDM, EVSTAT, as a batch sequence.

The event description contained in the ESF enabled routine EVSORT to sort the events automatically by category, keying on the short form for ice type given in Table 8, Section 3.1, (W,Z,R,ND, etc.)

---

* The ESF files are ASCII and their review and editing is straightforward using one of the standard time-sharing editors.

Once meaningful groups of data were assembled, the routine EVACC was used to assemble the accumulated statistics for each class using standard formulae. Master Event Summary Files (MESF) of brightness temperature, scattering coefficients and their variances were assembled using program MESF. Also included in the MESF summaries output were the calculated emissivities, ε, of the ice. The formula:

$$\varepsilon = \frac{T_B - T_{SKY}}{T_{SURF} - T_{SKY}} \qquad (2)$$

was used in the calculations. Some theoretical aspects and assumptions of this calculation are discussed in Appendix 6. Here T_B is measured brightness temperature, T_{SKY} is the sky temperature, and T_{SURF} is the physical surface temperature. T_{SKY} was assumed to be 18 ± 4 K (Copeland et al., 1966, see also Appendix 6) and a gross surface temperature was obtained for each flight line from ground truth data. Finally, summary data was displayed from this file using routine RETESF.

2.4.3 Data integration and data selection

The one-minute time histories* of σ^o_{hv} were joined to form a continuous record of each flight line and these were marked with the ice classification code from the photography, relating the time markers from the RC-10 and scatterometer. For cases where the RC-10 time code was missing, time was obtained from the scatterometer time histories by matching features found in the photography and SAR imagery.

A segment of data in the time history of one ice class was called an event. Each 'event' was assigned a three digit sequential number suffixed to the flight line number (e.g. E30803.021: Beaufort Sea N/S line, event 21), as an index to the ESF file system described in Section 2.4.2. Precise flight time boundaries for each event were obtained from the scatterometer time histories. All events of the same ice type were gathered together and compared in order to identify those which were 'typical', and to reject those which were either contaminated by other ice types or had incomplete data sets. For cases where ice-class contamination occurred on the event boundary**, the boundary times were redefined and the event plots reproduced. These selected events were used in all further data analysis. Table 7 indicates how many usable events of each ice type occurred on each of the flight lines studied in detail.

---

* Cross-polarized data were used here because they were shown to give more contrast between ice types and accented the boundary and roughness features identified on the RC-10 imagery.

** This was caused usually by the differing footprints of the radiometer and scatterometer. The scatterometer time histories show much shorter response time, therefore event boundaries, defined using the scatterometer data as described, needed to be adjusted to match the radiometer response.

Table 7. Ice type Distribution by Flight Line

Ice Type	Distribution by Flight Line								Experiment Summary		
	32210		32501		30603		30803		Total	Total	Records
	Events	Records	Events	Records	Events	Records	Events	Records	Events	Records	/Event
Open Water	1	13	3	194					4	209	52.3
Frazil	1	10							1	10	10
Grease			1	9					1	9	9
Nilas, Dark	5	161							5	161	32.2
Nilas, Light	4	119	2	45					6	164	27.3
Grey	3	103	3	58	1	7	1	15	8	183	22.9
Grey-white	1	10	3	221	1	20	1	74	6	325	54.2
First-year, Smooth	8	418			1	9	7	187	15	605	40.3
First-year, Rough							9	368	9	368	40.9
First-year, Wet			19	1161					19	1161	61.1
First-year, Wave-broken			7	685					7	685	97.9
Second-year, Smooth					1	3	2	29	3	32	10.7
Second-year, Rough							2	49	2	49	24.5
Multi-year, Smooth					6	150	12	521	18	671	37.3
Multi-year, Rough					6	228	12	443	18	671	37.1
Ice Island					1	140			1	140	140.0

The event designation scheme was also employed for the ice feature analysis. In this case, each event was chosen to include a well defined feature (ridge or iceberg) and sufficient of the surrounding ice to allow a contrast measurement to be made for the feature.

The event selection process for ridge and iceberg studies proceeded as follows:

(1) Ridges and icebergs intersected by the profiling sensor lines were measured on the photographic imagery to estimate the feature width.

(2) Those features that were unambiguously crossed by the profiling sensor ground swath and occupied more than 20m for ridges and 150m for icebergs in the along track direction were selected as event candidates.

(3) The background ice was examined for uniformity in the backscatter time histories and the event length was selected so that the feature was embedded in locally normal background ice.

(4) A subset of these events for which the feature dimensions exceeded the profiling sensor footprint (i.e. the features were beam-filling) were selected for future contrast analysis.

(5) Some nonbeam-filling features were retained to estimate the variation of the detectability of such features with feature dimension to footprint size ratio.

(6) Ridge heights were estimated from photographic shadow length and sun angle where possible.

Selected features were identified on the SAR imagery, containing the profiling sensor line, for SAR grey scale analysis.

2.4.4 The sea-ice classification study

For the sea-ice classification study, the total data set was analyzed at three levels of detail; by region, flight line and event;

(1) to determine the ice class population typical of the region and season.

(2) to identify effects incorporated into the data set by the choice of flight line location and date flown.

(3) to ensure that events combined for statistical analysis were sample of only one WMO ice class or subclass.

The following features (available from photo-interpretation) were considered as potential subclass indentifiers:

(1) macro scale (< 20cm) surface texture,

(2) percentage snow cover,

(3) surface puddling.

Where overlapping SAR imagery was available, this was studied to determine the typical ice-type distribution along each flight line and to clarify any anomalies detected by the profiling sensors.

Verified events containing 'pure' samples of individual sea-ice classes were grouped to form ice type data sets and these were subdivided by potential subclass in some cases.

A statistical analysis was performed on each event to determine the event mean and variance of T_B, σ^o_{hh} and σ^o_{hv} at six depression angles and to determine the event cross correlations between T_B, σ^o_{hh} and σ^o_{hv}. All events representing the same ice class were then grouped and the analysis was repeated to determine overall statistics for each class.

The event means and standard deviations of T_B were plotted against the event means and standard deviations of σ^o_{hh} and σ^o_{hv} for each of the six incidence angles used to form mass plots encompassing all ice types. The resulting ice class clusters were tested for separability. Depolarization ratios were computed for each ice class and used in conjuction with emissivity statistics and backscattering coefficient statistics to examine regional/seasonal effects. The potential subclasses were again tested for separability.

A simple three-dimensional Euclidian classifier was constructed using class means with normalization factors derived from the class variances of T_B, σ^o_{hh} and σ^o_{hv} at 45° incidence angle. This was applied on a sample-by-sample basis to unclassified segments of data. The effects of ice features and ice surface structures on a classification algorithm with no memory were examined. More advanced classifiers, which made use of the three-dimensional ice type cluster orientation and the ice class probability density functions, were also investigated.

In a separate branch of this study, each event in the cold condition ice classification data set was parameterized as follows:

(1) The angular dependance of σ^o_{hh} and σ^o_{hv} was modelled as a linear function over the scatterometer incidence angle range, by using a chi-squared fitting algorithm to select the best line.

(2) The slope and nadir intercept of each event were used then as independent parameters to form scatter plots of the total data set.

(3) The resulting clusters were correlated by ice classification and the σ^{o}_{hh} scattering coefficient, at 0° incidence angle, was combined with the data to construct sea-ice classification vectors.

(4) The statistics of these parameters were compiled for each sea-ice class.

2.4.5 Ice feature study

The ice feature event data sets were partitioned into ice ridge and iceberg subsets. The beam-filling ridge events were further partitioned by background ice type and location of the ridge with respect to the background floes. The ridge-to-background contrasts (event signal-to-clutter ratios) were measured for each event and grouped to estimate the event detectability by event and background class.

The nonbeam-filling, ridge signal-to-clutter ratios were measured to determine the absolute feature detectability and then a mixing formula was applied to the feature to provide a comparison between the scaled return and beam-filling features of similar class.

To provide semi-quantitative measurements of ice ridge parameters from SAR data, a portion of the Beaufort Sea HH-polarized, X-band shallow depression angle SAR imagery from the polar pack edge was digitized to 15m resolution and 256 grey levels using the CCRS scanning microdensitometer*. Some radar scenes containing ice ridges were extracted from the digitized SAR using the CIAS (CCRS Image Analysis System) display and were converted to numeric grey-scale maps for analysis of local ridge-to-background contrasts and radar texture.

Other sections of the Beaufort shallow depression angle imagery were digitized by Intera** using the direct output from the ERIM SAR processor and were used to examine the correlation between ridge dimensions (extracted from the photography) and relative ridge brightness.

Iceberg signal-to-clutter ratios were measured for all iceberg events. For very large bergs the sea-ice classification analysis techniques, developed in the ice classification study, were applied.

---

* We are indebted to Dr Bert Guindon for his assistance in this work.

** We are indebted to Dr Ray Lowry of Intera for his assistance in this work.

3.0 RESULTS AND DISCUSSION

Table 8 summarizes the sea-ice classes and subclasses present in the data set that were tested for separability by their microwave signatures. Shorefast first-year ice and icebergs were also present in the data set but were not included in this part of the analysis. Although some frazil was found in the Frobisher Bay (032201) line, no usable unmixed event was found. Mixed classes, such as multi-year bits in first-year matrix or grey ice in first-year, were not included in the classification study.

Detailed analysis was performed for all events of each sea-ice class to examine their microwave signatures. This detailed set of analyses are catalogued and held at CCRS. In Appendix 7, a complete analysis and discussion of an example from each sea-ice class and subclass is given.

3.1 The Microwave Signatures of Sea-ice Classes

Statistics for ε, $\sigma\rho_{hh}(\theta)$ and $\sigma\rho_{hv}(\theta)$ were determined* for each event and combined to produce class statistics by region and flight line. The significance of these class results varies with the number of events found in each class and the number of independent samples found in each event. This information is included with the signature descriptions in this section, as an index of significance of the signature. The number of events and independent samples is found in Table 9.

Sections 3.1.1, 3.1.2, and 3.1.3 give the results for the Beaufort Sea (030603 and 030803 lines) deployment, the Frobisher Bay (032201) line, and Danish W/E (032501) line respectively.

3.1.1 Beaufort Sea mission

The Beaufort Sea data were collected at the southern edge of the polar pack in late winter. Air temperatures varied from -34°C to -27°C during the data collection period, warming from -40°C five days prior to the start of the mission. Clear weather conditions and low sun angles, typical of mid-March in this area, made available excellent ice surface texture data. With the exception of ice identified positively as grey and grey-white, the majority of the ice was snow covered.

A total of 224 events were identified in the Beaufort Sea N/S line (Table 7 in Section 2.3.1) and 105 events were identified on the Beaufort Cross line. Of these, 63 were selected as being suitable for sea-ice classification studies and the remainder (81% of all events) were rejected as being not required or unsuitable for use (see Section 2.4.3). The frequency of class occurrence on this mission is indicated in Table 7. During this season ice forms and grows very rapidly in open leads so that young ice types were rare, thus the number of examples of grey and grey-white ice was small and most events were too short to use.

---

* $\sigma\rho_{hh}(\theta)$ and $\sigma\rho_{hv}(\theta)$ define the incidence angle dependence of radar backscattering coefficient for HH and HV polarization respectively.

Table 8. Summary of Sea-ice Classes and Conditions Analysed for the Active-Passive Experiment

WMO Sea-ice class (notation)	Region	Air Temperature (°C)	Subclass
Calm open water (W)	Frobisher Bay	-5	-none
	West Greenland Pack	-2	-none
Grease ice (R)	Frobisher Bay	-5	-none
Dark nilas (ND)	Frobisher Bay	-5	-none
	West Greenland Pack	-2	-none
Light nilas (NL)	Frobisher Bay	-5	-none
Grey (G)	Beaufort Sea	-30	-dry, cold
	Frobisher Bay	-5	-damp
	West Greenland Pack	-2	-wet
	Frobisher Bay	-5	-puddled
	West Greenland Pack	-2	-fractional snow cover
Grey-white (L)	Beaufort Sea	-30	-none
	Frobisher Bay	-5	-none
	West Greenland Pack	-2	-none
First-year (FY)	Beaufort Sea	-30	-rough -smooth
	Frobisher Bay	-5	-puddled
	West Greenland Pack	-2	-dry -fractional snow cover
Second-year (SY)	Beaufort Sea	-30	-rough -smooth
Multi-year (MY)	Beaufort Sea	-30	-rough -smooth -very old
Ice island (II)	Beaufort Sea	-30	-none

Table 9. Summary of Beaufort Sea-ice Types by Event

Ice Type	Date Base	Subclass	Subclass Data Base	Ice Classfication Data Set		Events Not Used	
	Events		Events	Events	Samples	Total	Classified
Ice island	1	none	N/A*	1	140	0	N/A
Multi-year	104	rough	25	18	671	68	7
		smooth	28	18	586		10
Second-year	24	rough	5	2	49	20	3
		smooth	7	2	29		5
First-year	110	rough	18	9	368	95	9
		smooth	11	6	187		5
Grey-white	4	none	N/A	2	94	2	N/A
Grey	10	none	N/A	2	22	8	N/A
Mixtures	80	N/A	N/A	none	none	80	N/A

* Not available.

The microwave signatures of the Beaufort Sea ice types are presented in statistical form in Table 10. The means and standard deviations presented in Table 10 were computed on a sample-by-sample basis, combining all data within each class. Generally the variation between events exceeded the variation within an event.

At the event level, the standard deviation of a backscattering coefficient is a measure of the radar 'texture' of the event*. In the Beaufort Sea data set, second-year rough ice, second-year smooth ice and grey-white ice are rare and although Table 10 accurately describes these events, caution should be exercised in generalizing the results for these ice classes.

The following observations can be made from Table 10 and Figure 11a and b:

(1) σ^{o}_{hh} provides a relatively uniform separation of ice types although the total dynamic range is less than that for σ^{o}_{hv}. Ice types separated by at least one standard deviation are ice-island, multi-year, second-year grey, rough first-year and smooth first-year ice. Rough multi-year ice is statistically inseparable from smooth multi-year ice; rough second-year ice is statistically inseparable from smooth second-year ice and grey-white ice is statistically inseparable from smooth first-year ice. The probability of misclassification of adjacent separable ice types, using like-polarized backscattering alone, is in the order of 35% based on the data from one incidence angle.

(2) σ^{o}_{hv} enhances the separation between first-year and younger ice types and old ice (second-year and older) at all incidence angles but particularly at incidence angles greater than 35°. Comparison of Figure 11a and 11b shows a separate grouping of old ice and young ice in σ^{o}_{hh}. This probably reflects the volume scattering in older ice by subsurface inhomogeneities, such as brine drainage channels and air pockets which cause depolarization. Younger ice has higher salinity and surface scattering is more important in determining the radar return at these frequencies. The cross-polarized scattering coefficients also show more contrast between all rough and smooth subclasses and also more radar texture than the corresponding like-polarized data.

---

* The radar 'texture' of a floe seen in microwave sea-ice SAR is determined by the number of independent measurements making up the backscatter estimate and by variations in average backscattering cross section over the floe surface, whose physical dimensions are greater than or equal to the radar resolution cell. Physically, the image texture may be an indication of the presence of ice deformations (roughness, local incidence angle changes, ridging, rafting), inclusion of other ice types and/or internal ice conditions (variations of ice surface temperature, brine concentration, density, air pockets).

Table 10. Microwave Signatures for Sea Ice from the Beaufort Sea.

Sensor	Function	Incidence Angle	Statistic	Ice Class								
				Ice Island	Multi-year Rough	Multi-year Smooth	Second-year Rough	Second-year Smooth	First-year Rough	First-year Smooth	Grey-white	Grey
19.35 GHz Radiometer	T_B	45°	M*	163.4	190.7	192.1	210.0	205.5	227.1	225.4	229.7	222.6
			SD	5.3	7.8	6.0	4.6	5.3	3.3	4.0	2.6	3.7
	ε	45°	M	0.646	0.768	0.774	0.853	0.833	0.929	0.922	0.941	0.910
			SD	0.023	0.035	0.027	0.020	0.024	0.075	0.018	0.012	0.016
13.3 GHz Scatterometer	σ^o_{hh} in dB	8°	M	5.24	3.60	3.50	0.97	0.87	-1.84	-3.10	-1.99	0.01
			SD	0.71	1.27	1.05	1.53	0.95	1.53	1.75	1.41	0.62
		15°	M	3.55	1.92	1.55	-1.20	-1.20	-5.79	-7.05	-5.15	-0.98
			SD	0.95	1.14	0.92	1.96	1.14	1.61	1.58	1.32	0.85
		25°	M	1.95	0.52	0.02	-2.65	-2.83	-9.16	-10.83	-8.09	-4.73
			SD	1.11	1.20	1.04	2.36	1.43	1.97	1.50	1.62	1.14
		35°	M	-1.49	-2.19	-2.76	-5.16	-5.32	-12.55	-14.53	-11.80	-9.08
			SD	1.14	1.15	1.09	2.54	1.73	2.18	1.50	1.67	1.20
		45°	M	-4.98	-6.22	-6.87	-9.17	-9.34	-16.74	-18.78	15.94	-13.74
			SD	1.20	1.12	1.08	2.46	1.76	2.29	1.46	1.65	1.18
		55°	M	-5.23	-6.51	-7.39	-9.46	-9.48	-17.68	-19.08	-16.04	-14.41
			SD	1.01	1.15	1.15	2.42	1.95	2.22	1.47	1.57	0.81
	σ^o_{hv} in dB	8°	M	-6.26	-8.16	-8.84	-12.32	-12.58	-19.13	-21.26	-19.41	-19.00
			SD	1.74	1.77	1.56	3.05	1.63	2.23	2.70	1.73	0.62
		15°	M	-5.93	-8.19	-8.96	-12.76	-13.13	-22.50	-25.05	-22.76	-21.14
			SD	1.87	1.89	1.65	3.35	1.93	3.08	3.32	2.76	1.58
		25°	M	-5.61	-7.69	-8.46	-12.23	-12.66	-22.46	-25.26	-22.46	-21.80
			SD	1.01	1.83	1.64	3.45	1.95	3.27	3.40	2.86	2.46
		35°	M	-7.98	-9.76	-10.47	-13.94	-14.48	-24.42	-27.15	-24.38	-24.17
			SD	1.78	1.80	1.61	3.41	2.11	3.32	3.62	2.95	2.16
		45°	M	-8.59	-10.65	-11.45	-14.79	-15.29	-25.01	-27.56	-24.78	-24.70
			SD	1.64	1.69	1.62	3.26	2.09	3.25	3.65	2.68	2.12
		55°	M	-8.94	-10.55	-11.84	-14.63	-13.45	-25.45	-27.24	-24.25	-24.43
			SD	1.52	2.53	1.51	3.10	2.07	2.96	3.66	2.43	1.67
	$\sigma^o_{hv}/\sigma^o_{hh}$ in dB	8°	M	-11.49	-11.76	-12.34	-13.29	-13.45	-17.29	-18.06	-17.42	-19.01
			SD	1.43	1.65	1.64	1.88	1.29	1.36	2.24	1.54	0.62
		15°	M	-9.48	-10.11	-10.51	-11.55	-11.93	-16.71	-18.07	-17.61	-20.15
			SD	1.09	1.29	1.15	1.53	0.97	2.09	2.84	2.11	1.18
		25°	M	-7.55	-8.21	-8.44	-9.58	-9.83	-13.30	-14.43	-14.37	-17.07
			SD	0.89	1.13	0.97	1.20	0.64	1.78	2.80	1.70	1.83
		35°	M	-6.50	-7.56	-7.72	-8.78	-9.16	-11.87	-12.61	-12.58	-15.09
			SD	0.82	1.05	0.96	1.07	0.61	1.53	3.02	1.63	1.26
		45°	M	-3.61	-4.43	-4.64	-5.63	-5.94	-8.27	-8.78	-8.84	-10.97
			SD	0.72	1.05	0.98	1.02	0.62	1.33	3.06	1.26	1.14
		55°	M	-3.71	-4.04	-4.44	-5.17	-5.81	-7.76	-8.16	-8.21	-10.02
			SD	0.71	1.30	0.84	1.03	0.50	1.21	3.04	1.07	1.13

* M - Mean
SD - Standard deviation

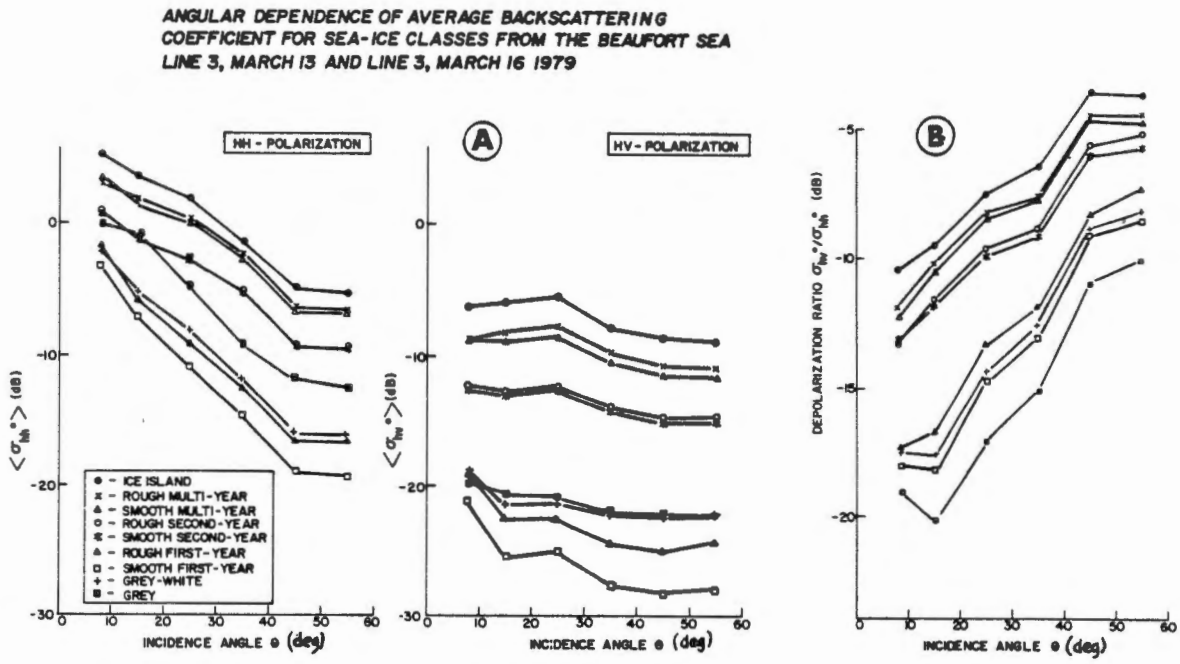

Figure 11. Angular Dependence of σ^o_{hh} and σ^o_{hv} and Depolarization Ratio for Sea-ice Classes from Beaufort 030803 and 030603 Lines.

For these classes and these cold ambient temperatures, greater class separation can be seen in the σ^o_{hh} data at large incidence angles than at the smaller incidence angles. No corresponding effect can be seen in the cross-polarized data, however. The overall separation is greater with cross-polarization. The cross-polarized results are, in general, also less dependent on incidence angle than the like-polarized data. The depolarization ratio has less overall separation with class than σ^o_{hh} or σ^o_{hv} and the shape of all the curves, but not the separation, may be in error due to antenna pattern errors.

Because σ^o_{hv} is less dependent on incidence angle than σ^o_{hh}, the opposite curvature observed in Figure 11b, is seen in the depolarization ratio $\sigma^o_{hv}/\sigma^o_{hh}$.

Ice types separated by at least one standard deviation are ice island, multi-year, second-year, first-year rough and first-year smooth. Grey ice is separated from first-year smooth ice by approximately one standard deviation at all measured incidence angles but could be confused with first-year rough ice if given σ^o_{hv} measurements only. At all incidence angles, multi-year rough ice is statistically inseparable from multi-year smooth; second-year rough ice is statistically inseparable from first-year rough ice and grey-white ice is statistically inseparable from first-year smooth ice if given measurements of σ^o_{hv} only.

(3) The horizontally polarized 19.35 GHz emissivity, ε, measured at 45° incidence angle, allows direct classification of some ice types; ice islands become absolutely separable (to the three standard deviation limit) from the other winter Beaufort Sea ice types; multi-year ice is separable from second-year ice to the two standard deviation level and grey-white ice is separable from first-year smooth ice to the one standard deviation level. Grey ice is not separable from first-year ice, and ice subclasses are not separable to the one standard deviation level, given ε measurements at 45° only.

(4) Given simultaneous measurements of σ^o_{hh} and σ^o_{hv} at incidence angles between 45° and 60° (60° is the limit of the scatterometer incidence angle range) and horizontally polarized ε at 45° incidence angle, the following ice types are separable to at least the two standard deviation level:

(a) ice island,
(b) multi-year ice,
(c) second-year ice,
(d) first-year rough ice,
(e) first-year smooth ice,
(f) grey ice.

Grey-white ice is separable from first-year smooth ice to a lesser degree (approximately one standard deviation) and the presence of second-year rough ice or second-year smooth ice may be inferred for floes greater than 360m in length which fully contain the profiling sensor beam.

It should be emphasized that the preceding results reflect the data set collected and that the number of grey and grey-white events was very small.

Figures 12a, b, c and 13a, b, c show cluster plots of σ^o_{hv} vs σ^o_{hh}, σ^o_{hh} vs ε and σ^o_{hv} vs ε at six incidence angles, for the Beaufort Sea Cross line, 030603 and the Beaufort Sea N/S line, 030803, respectively. Each point on these plots represents one event and gives one standard deviation limit. The general observations made above may be obtained from a perusal of these figures, although because of the unequal event sizes and separation of the two flight lines, these figures more accurately reflect the distribution of the data than does the preceding discussion.

Figure 12. Event Classification Clusters from the Beaufort Sea 030603 Line Across T3.

Cluster plots of all variables are represented for each of 6 incidence angles. Separate symbols are used to denote ice type and error bars are included to show the standard deviation of the data within each event.

CLASSIFICATION OF ICE FROM THE BEAUFORT SEA BY
19·4GHz EMISSIVITY AND 13·3GHz BACKSCATTERING COEFFICIENT
12 MARCH 1979, FLIGHT LINE 3 $T_{SURFACE}$~-30°C

SCATTEROMETER LOOK ANGLE - 8°

SCATTEROMETER LOOK ANGLE-15°

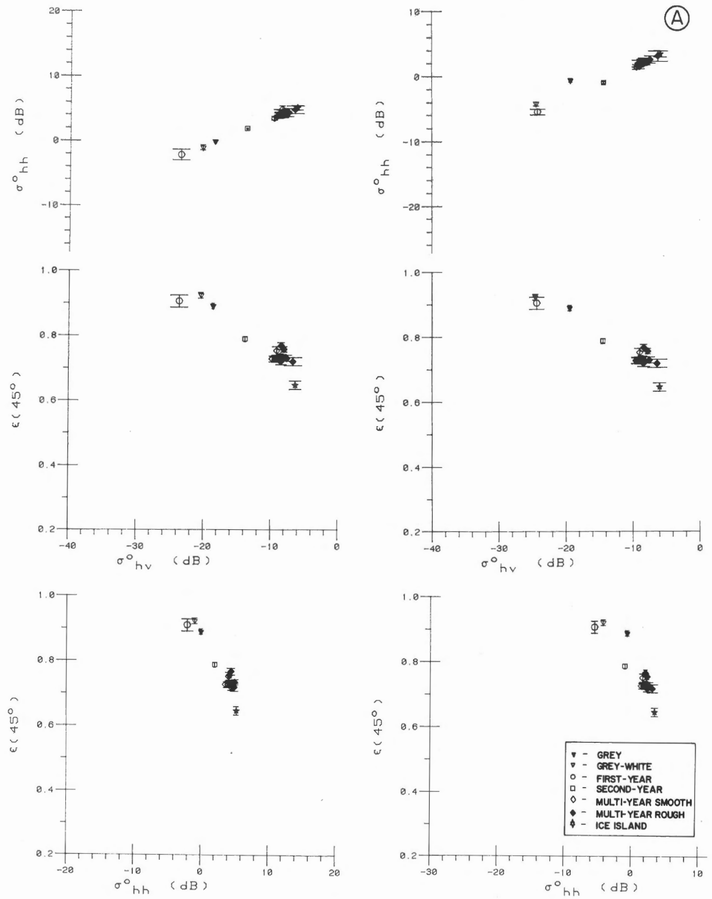

CLASSIFICATION OF ICE FROM THE BEAUFORT SEA BY
19·4GHz EMISSIVITY AND 13·3GHz BACKSCATTERING COEFFICIENT
12 MARCH 1979, FLIGHT LINE 3 $T_{SURFACE}$~-30°C

SCATTEROMETER LOOK ANGLE-25°

SCATTEROMETER LOOK ANGLE-35°

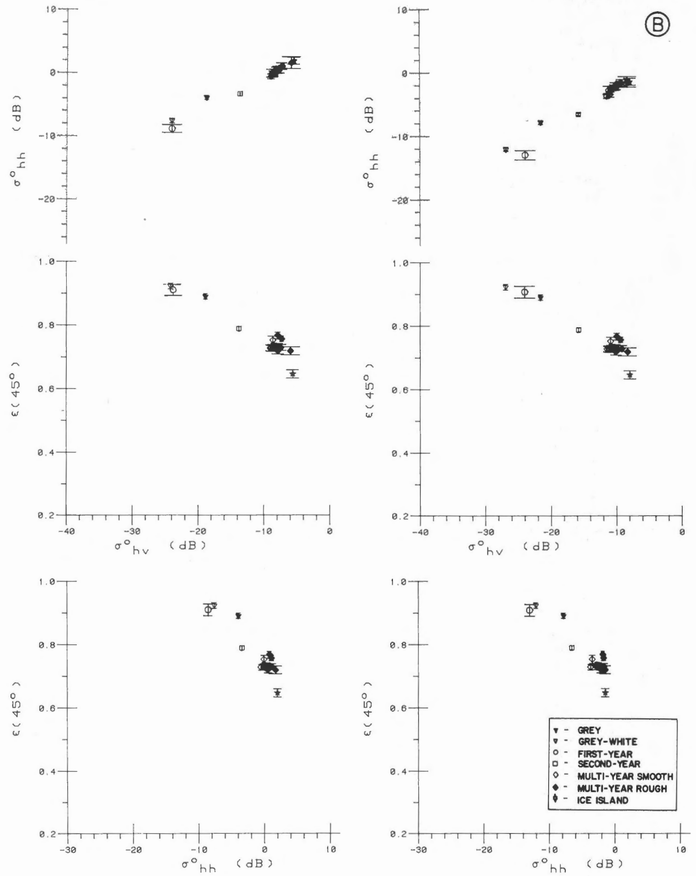

CLASSIFICATION OF ICE FROM THE BEAUFORT SEA BY
19·4GHz EMISSIVITY AND 13·3GHz BACKSCATTERING COEFFICIENT
12 MARCH 1979, FLIGHT LINE 3 $T_{SURFACE}$~-30°C

SCATTEROMETER LOOK ANGLE-45°

SCATTEROMETER LOOK ANGLE-55°

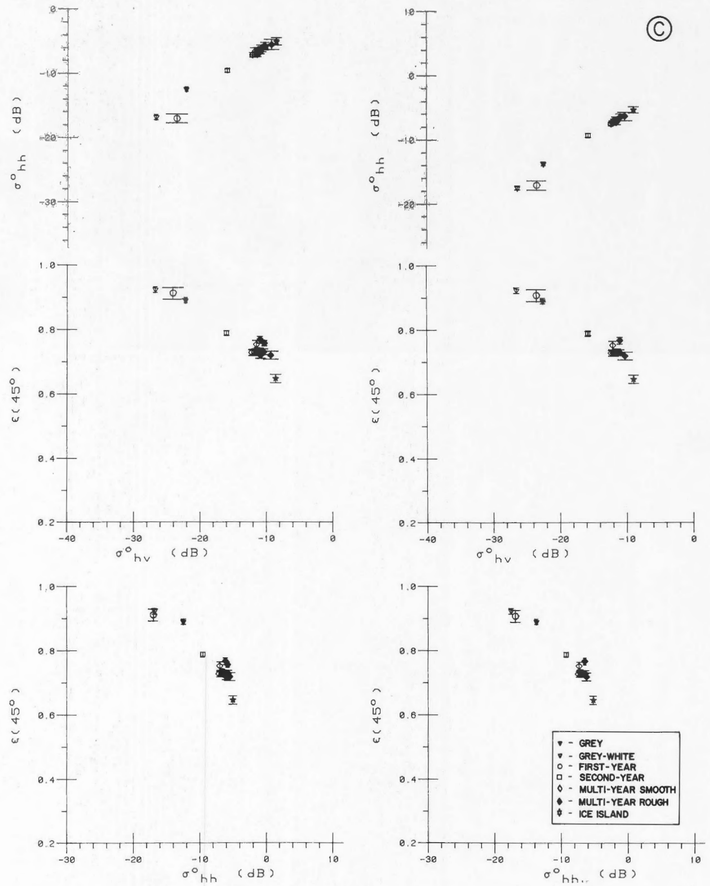

Figure 13. Event Classification Clusters From the Beaufort Sea N/S 030803 Line.

CLASSIFICATION OF ICE FROM THE BEAUFORT SEA BY
19·4GHz EMISSIVITY AND 13·3GHz BACKSCATTERING COEFFICIENT
16 MARCH 1979, FLIGHT LINE 3 $T_{SURFACE}$ = -26°C

SCATTEROMETER LOOK ANGLE - 8° SCATTEROMETER LOOK ANGLE - 15°

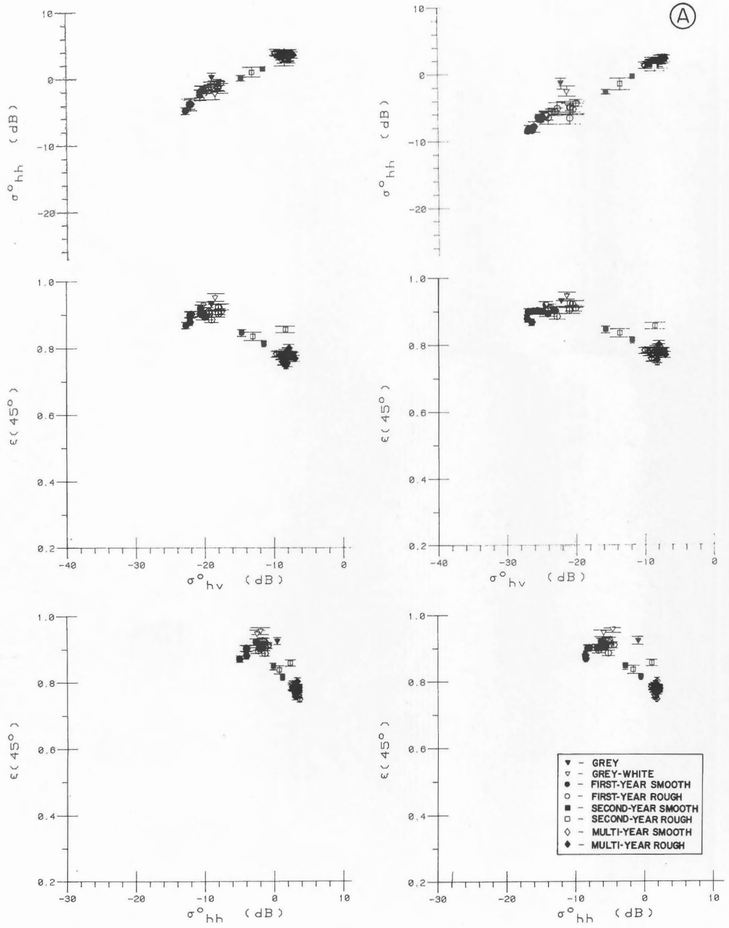

CLASSIFICATION OF ICE FROM THE BEAUFORT SEA BY
19·4GHz EMISSIVITY AND 13·3 GHz BACKSCATTERING COEFFICIENT
16 MARCH 1979, FLIGHT LINE 3 $T_{SURFACE}$ = -26°C

SCATTEROMETER LOOK ANGLE - 25° SCATTEROMETER LOOK ANGLE - 35°

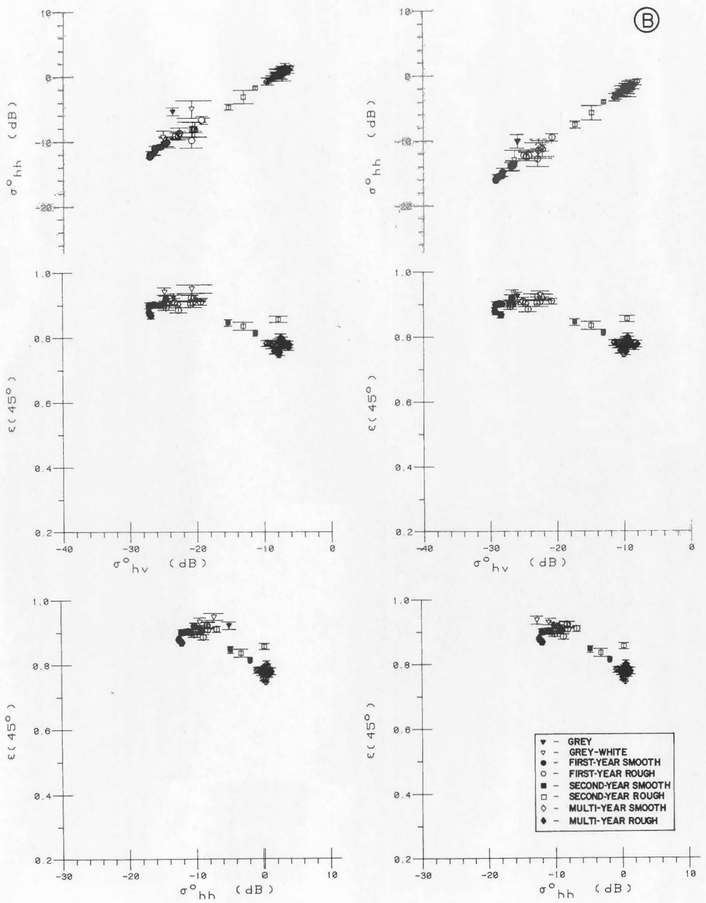

CLASSIFICATION OF ICE FROM THE BEAUFORT SEA BY
19·4GHz EMISSIVITY AND 13·3GHz BACKSCATTERING COEFFICIENT
16 MARCH 1979, FLIGHT LINE 3 $T_{SURFACE}$ = -26°C

SCATTEROMETER LOOK ANGLE - 45° SCATTEROMETER LOOK ANGLE - 55°

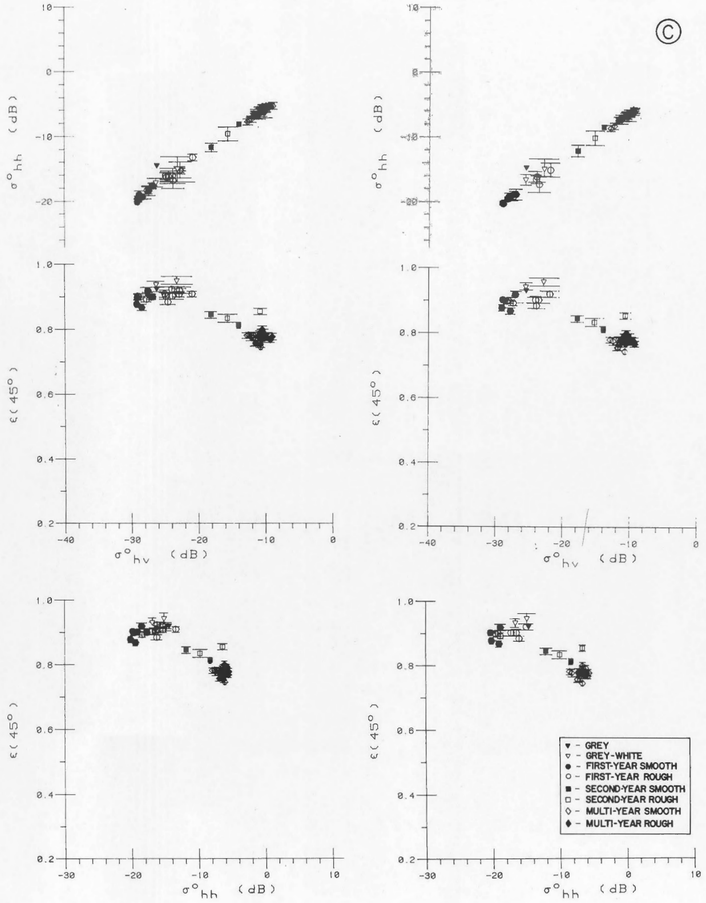

The major class overlap between these two flight lines is in the multi-year rough and smooth ice data. Careful examination of Figures 12 and 13 indicates that the emissivity of multi-year ice changes marginally between the two flight lines. The origin of this difference is not known, although it is possible that it is related to the different ambient temperatures. The lack of a corresponding change in the scatterometer data makes this explanation tenuous but not inconceivable.

3.1.2 Frobisher Bay line

The Frobisher Bay data set was taken in relatively sheltered waters in the eastern Arctic, in early spring. The atmosphere below 1000m was clear but some cloud was present at higher levels, making roughness estimations from shadow analysis impossible from the RC-10 imagery. The ice was composed of first-year floes interspersed with brash ice; and some new and young ice. Both snow-covered and bare ice were observed and some floes showed signs of recent melting and decay.

Ambient temperature was estimated to be approximately $-5^{o}C$ for the Frobisher Bay data set from the Frobisher Bay surface weather record at the time of the flight. The temperature high on the previous day was $-7.5^{o}C$ and the new ice observed may have formed during the cold nights preceding the experiment. The seaward end of the flight line appeared to be warmer than the landward end, as more examples of wet ice were visible in that area.

Table 11 summarizes the ice distribution by class along the Frobisher Bay line. A total of 144 events were identified, of which 23 were selected as being suitable and the remainder (84% of all events) were rejected (see Section 2.4.3). Problems were encountered in transferring some of the data, in the first half of the flight line, from the Mincom high density digital tape (HDDT) to CCT's and approximately 30% of the line data was not usable. This data is recoverable but time and manpower limitations during this study precluded its use. Most of the rejected data contained events that were either too short (less than 72m along track) or were too narrow so that a mixture of ice classes existed within the profiling sensor swath.

Long unmixed events of water, grease ice and grey-white ice were the rarest in the Frobisher Bay line and only a few short events were available for the sea-ice classification study. Caution should be used in generalizing the analysis results for these ice types.

The Frobisher Bay line microwave sea-ice signatures are presented in statistical form in Table 12, with the angular dependence of the backscattering coefficient and depolarization ratio presented in Figure 14a and b. The following observations can be made:

(1) Dark nilas, grey, grey-white, first-year all have parallel σ^{o}_{hh} curves as a function of incidence angle. Grease ice and calm water exhibit σ^{o}_{hh} (θ) curves which are steeper than the other curves and indicate a more specular surface. For the wind and ice conditions encountered during the experiment, contrast reversals with water occurred at:

Table 11. Summary of the Frobisher Bay Sea-ice Classification Data Set

Ice Type	Data Base	Ice Classification Data Set		Events Not Used
	Events	Events	Samples	
Calm Water (W)	20	1	13	18
Grease Ice (R)	2	1	6	1
Dark Nilas (ND)	7	5	101	2
Light Nilas (NL)	4	4	119	0
Grey (G)	15	3	103	12
Grey-white (L)	7	1	10	6
First-year (FY)	40	8	418	32
Mixtures	43	N/A*	N/A	43
Class uncertain	16	N/A	N/A	16

* Not applicable

Table 12. Frobisher Bay Sea-ice Signature

Sensor	Function	Incidence Angle	Statistic	Ice Class: First-year	Grey-white	Grey	Light Nilas	Dark Nilas	Calm Water
19.35 GHz Radiometer	T_B	45°	M*	255.0	253.4	213.0	216.0	214.3	119.50
			SD	4.7	1.90	11.4	5.4	7.4	1.4
	ε	45°	M	.948	.942	.780	.792	.785	0.406
			SD	.019	.008	.046	.022	.030	0.005
13.3 GHz Scatterometer	σ^o_{hh} in dB	8°	M	-0.45	3.12	7.30	3.11	-5.46	15.35
			SD	1.77	0.64	1.03	2.50	3.44	0.40
		15°	M	-3.03	0.17	2.93	-2.38	-9.78	9.03
			SD	1.95	0.38	0.68	2.03	2.80	0.33
		25°	M	-6.77	-4.15	-2.21	-8.07	-14.56	-3.04
			SD	2.03	0.48	0.98	1.62	2.53	0.51
		35°	M	-11.37	-9.84	-6.90	-12.86	-18.78	-14.56
			SD	2.28	0.60	1.16	1.57	2.35	0.55
		45°	M	-16.39	-14.84	-12.36	-18.87	-24.40	-24.01
			SD	1.95	0.49	1.44	1.52	2.25	0.87
		55°	M	-17.30	-16.04	-13.91	-20.08	-25.69	-27.41
			SD	2.06	0.59	1.30	1.77	2.19	0.4
	σ^o_{hv} in dB	8°	M	-20.16	-17.03	-12.50	-17.09	-24.94	-4.64
			SD	2.49	0.89	0.73	2.31	2.89	0.55
		15°	M	-22.45	-19.10	-16.64	-23.24	-29.90	-14.16
			SD	2.22	0.53	1.1	1.68	2.45	0.39
		25°	M	-25.60	-19.41	-17.97	-25.28	-31.35	-21.60
			SD	2.20	0.60	1.55	1.46	2.36	0.45
		35°	M	-25.12	-22.39	-20.63	-27.84	-33.49	-28.16
			SD	2.34	0.72	1.60	1.48	2.31	0.48
		45°	M	-25.96	-23.43	-21.94	-29.47	-34.71	-30.70
			SD	2.03	1.06	1.68	1.38	2.20	0.69
		55°	M	-25.81	-23.46	-22.26	-28.79	-33.59	-29.55
			SD	2.14	0.86	0.85	1.52	2.12	0.31
	$\sigma^o_{hv}/\sigma^o_{hh}$ in dB	8°	M	-19.71	-20.15	-19.81	-20.21	-19.47	-19.99
			SD	1.44	0.54	0.70	0.50	0.84	0.22
		15°	M	19.43	-19.27	-19.57	-20.86	-20.13	-23.19
			SD	0.99	0.31	0.72	0.58	1.08	0.15
		25°	M	-15.84	-15.26	-15.75	-17.21	-16.79	-18.56
			SD	0.89	0.32	0.80	0.68	0.93	0.19
		35°	M	-13.75	-12.54	-13.73	-14.97	-14.72	-13.60
			SD	0.83	0.38	0.79	0.700	0.76	0.29
		45°	M	-9.57	-8.59	-9.58	-10.60	-10.32	-6.69
			SD	0.81	0.75	0.70	0.59	0.66	0.38
		55°	M	-8.50	-7.41	-8.35	-8.71	-7.90	-2.14
			SD	0.67	0.45	0.67	0.60	0.96	0.36

* M - Mean
SD - Standard deviation

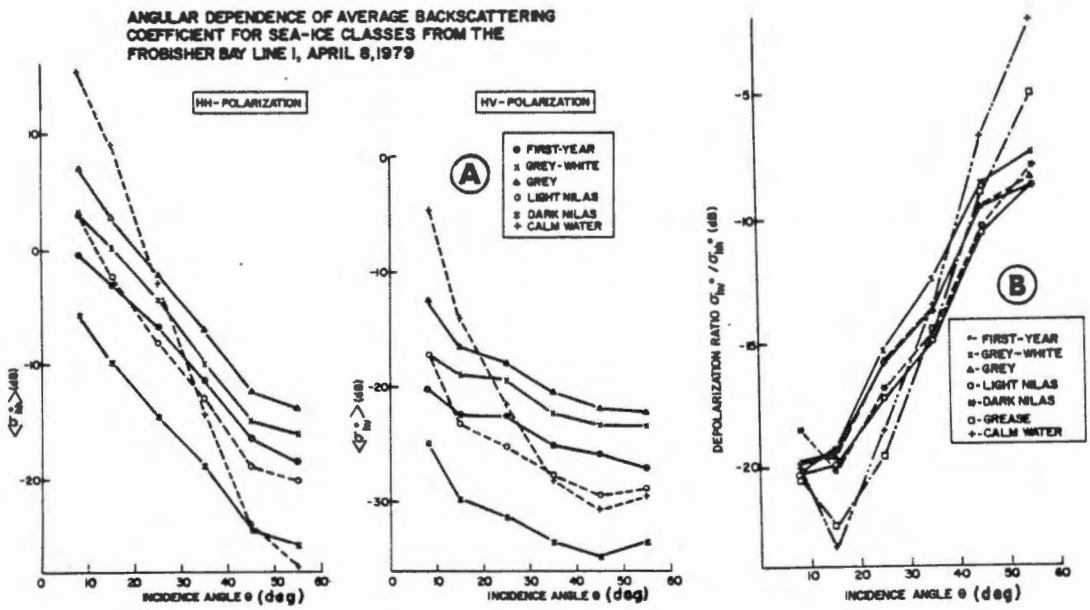

Figure 14. Angular Dependence of σ^o_{hh} and σ^o_{hv} and Depolarization Ratio for Sea-ice Classes from the Frobisher Bay 032201 Line.

In these data, ambient temperatures were approximately -5°C so that freezing conditions prevailed but the ice was much warmer than the Beaufort Sea data. The curves remain parallel for each class, except for water which intersects the other curves, and light nilas which crosses first-year and grey-white ice at incidence angles less that 20°. More pronounced dependence of the backscattering coefficient on incidence angle is seen for σ^o_{hh} and σ^o_{hv}. No advantage is seen in either polarization.

(a) 20-25° for grey ice,
(b) 20-30° for grey-white ice,
(c) 27-32° for first-year ice,
(d) 30-35° for light nilas,
(e) 40-42° for dark nilas.

Light nilas is more specular than dark nilas, grey ice, grey-white ice and first-year ice but less specular than calm water and grease ice. A contrast reversal is seen between light nilas and first-year ice.

(2) When the σ^{o}_{hh} data of ice classes common to both the Frobisher Bay (Table 12) and Beaufort Sea (Table 10) lines are compared, it is seen that first-year smooth ice, grey ice and grey-white ice are brighter in the Frobisher Bay data at small incidence angles, but are comparable in brightness at larger incidence angles. In particular, Frobisher Bay grey ice is within one standard deviation of Beaufort Sea grey ice over the incidence angle range 25° to 55°; Frobisher Bay first-year ice is within one standard deviation of Beaufort Sea first-year smooth ice over the incidence angle range 30° to 55° and Frobisher Bay grey-white ice is within a standard deviation of Beaufort Sea grey-white ice over the incidence angle range 45° to 55°.

(3) Using one standard deviation as a criterion for separability with σ^{o}_{hh} data on this line:

(a) Dark nilas is separable from all other ice types over the incidence angle range 8°-37° and is separable from all other ice types except calm water and grease ice over the incidence angle range 37° to 55°.

(b) First-year ice is separable from grey-white ice over the incidence angle ranges 8° to 25° and 42° to 55°.

(c) Grey-white ice is separable from grey ice at all angles.

(d) Light nilas is not separable from grey-white ice from 8° to 20°; is not separable from grey ice from 10° to 17° and is not separable from first-year ice from 20° to 40°.

(e) Grease ice is separable from all other ice classes, but not from water from 8° to 15° and from 35° to 37° and is separable from water from 10° to 22° and from 40° to 50°.

(4) The $\sigma^{o}_{hv}(\theta)$ data show a similar ordering to the $\sigma^{o}_{hh}(\theta)$ data, but are less dependent on incidence angle.

Contrast reversals with calm water are as follows:

(a) 15-20° for grey ice,
(b) 18-22° for grey-white ice,
(c) 23-28° for first-year ice,
(d) 24-33° for light nilas.

A contrast reversal between grey-white ice and first-year ice occurs in the incidence angle range 20° to 25°.

(5) When Frobisher Bay σ^o_{hv} data are compared with Beaufort Sea σ^o_{hv} data from Table 10, the Frobisher Bay first-year ice mean is within one standard deviation of the Beaufort Sea first-year rough ice mean.

The Frobisher Bay grey-white and grey ice types are approximately 4.5 dB brighter than their Beaufort Sea counterparts.

(6) Using one standard deviation as a criterion for separability with σ^o_{hv} data:

(a) Dark nilas is separable from first-year ice over the incidence angle range 15° to 55°.

(b) First-year ice is inseparable from grey-white ice and light nilas at all angles.

(c) Grey ice is separable from grey-white ice over the incidence angle range 8° to 15°.

(d) Light nilas is inseparable from first-year ice, is inseparable from grey-white ice over the incidence angle range 8° to 15° and is separable from grey ice over the incidence angle range 15° to 55°.

(e) Calm water is separable from all ice types, except grease ice, over the incidence angle range 8° to 14°

(f) Grease ice is separable from calm water over the incidence angle range 35° to 55°.

(7) Using both σ^o_{hh} and σ^o_{hv}, all ice types are separable to at least one standard deviation, over the incidence angle range 35° to 55°, except dark nilas and grease ice. All ice types except light nilas and grey-white ice are separable over the incidence angle range 8° to 12°.

(8) Using ε alone, first-year ice and grey-white ice are inseparable but they are separable from all other ice types; grey ice, light nilas and dark nilas are inseparable, but are separable from all other ice types. Grease ice and calm water are separable from all other ice types.

(9) When ε is combined with σ^o_{hh} and σ^o_{hv}, all ice types are separated by at least one standard deviation, at all radar incidence angles.

The event cluster plots corresponding to the data just discussed are presented in Figure 15a, b, c. In these plots each data point represents an event, bounded by its standard deviations. The utility of the radiometric measurement to distinguish grey and nilas from first-year is clear from the σ^o vs. ε clusters. Again, the small number of events for some of the ice classes and the generality of the results must be questioned.

3.1.3 Danish W/E Line

The Danish W/E line data were taken in the eastern part of the Davis Strait early in the spring breakup period. Similar ice conditions are found in the marginal ice zone in this area all winter. The ambient air temperature was below 0^oC and the snow-ice interface temperature was measured as -2^oC, so that the ice was rotting and very wet. The bottom of the snow layer was slushy and some puddled, bare ice was observed. At the eastern end of the flight line an open pack situation was observed with much of the ice in the form of wave-broken floes becoming smaller in size toward the pack edge. Weather conditions were clear and good RC-10 photography was obtained. The southward drift of the pack ice in this area precluded profiling the ice within the SAR image.

A total of 139 events were identified, of which 36 were selected as being suitable for analysis and the remainder (74% of all events) were rejected as being unsuitable for use in the sea-ice classification study. Table 13 summarizes ice distribution in the Danish W/E line.

Young ice types occurred typically in the leads between floes and were seldom unmixed with other ice classes over distances greater than 72m. This was especially true for grease ice, nilas and grey ice. Some icebergs were found in the vicinity of the profiling sensor line but none were crossed by the line. Under the surface conditions present when this data set was collected, nilas could not be subclassified accurately as light or dark and so all nilas data were assembled to form a single class. Wave-broken first-year ice was analysed as a separate ice class. No attempt was made to indicate the class by cake or bit size, however, all events in the class had ice fragments smaller than 20m and larger than 2m.

Because of the small usable sample sizes found for nilas, grey and grease ice, generalizations made for these ice types are tenuous.

The Danish W/E line microwave sea-ice signatures are presented in statistical form in Table 14 and the angular dependence of σ^o_{hh}, σ^o_{hv} and depolarization ratio in Figure 16a, b, c. The following observations may be made from these results:

Figure 15. Event Classification Clusters From the Frobisher Bay 032201 Line.

The shape of each cluster remains similar for each of the incidence angles shown, due to the parallel nature of the curves depicted in Figure 14. In the case of water (and frazil which, in this example, is a very loose mixture of ice spicules with water), which has a very distinctive dependence on incidence angle, its position is seen to migrate through the diagrams as a function of incidence angle. The utility of the radiometer to separate both grey and nilas from smooth first-year data is clearly evident.

CLASSIFICATION OF ICE FROM FROBISHER BAY BY
19·4 GHz EMISSIVITY AND 13·3 GHz BACKSCATTERING COEFFICIENT
8 APRIL 1979, FLIGHT LINE I $T_{SURFACE} \sim -5°C$

SCATTEROMETER LOOK ANGLE - 8° SCATTEROMETER LOOK ANGLE - 15°

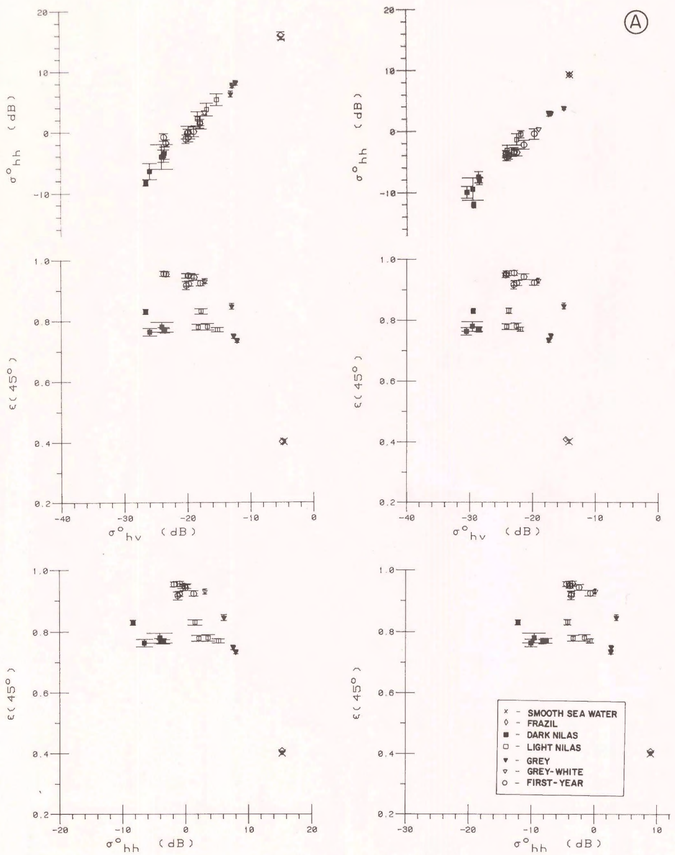

CLASSIFICATION OF ICE FROM FROBISHER BAY BY
19·4 GHz EMISSIVITY AND 13·3 GHz BACKSCATTERING COEFFICIENT
8 APRIL 1979, FLIGHT LINE I $T_{SURFACE} \sim -5°C$

SCATTEROMETER LOOK ANGLE - 25° SCATTEROMETER LOOK ANGLE - 35°

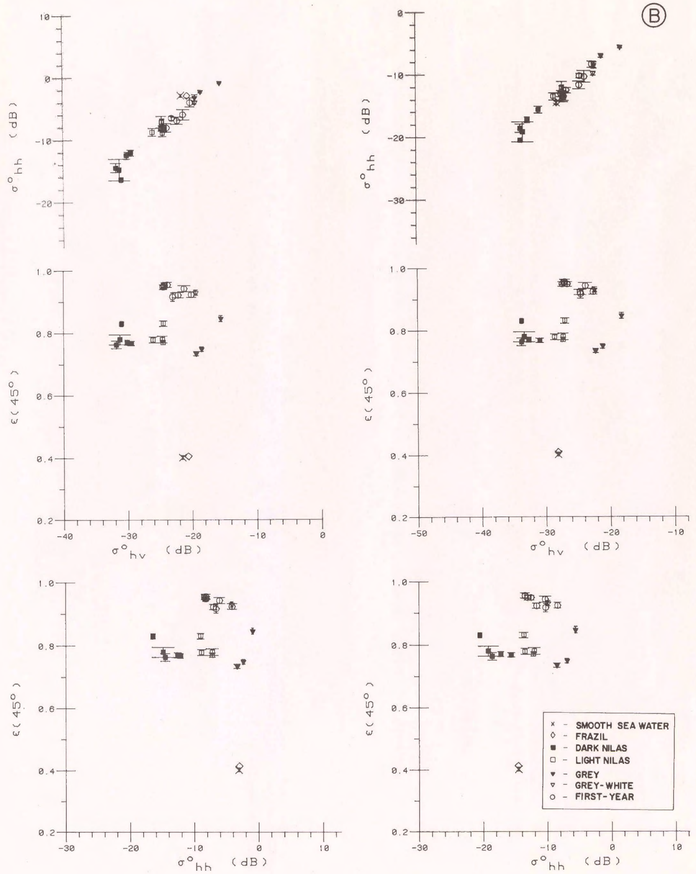

CLASSIFICATION OF ICE FROM FROBISHER BAY BY
19·4 GHz EMISSIVITY AND 13·3 GHz BACKSCATTERING COEFFICIENT
8 APRIL 1979, FLIGHT LINE I $T_{SURFACE} \sim -5°C$

SCATTEROMETER LOOK ANGLE - 45° SCATTEROMETER LOOK ANGLE - 55°

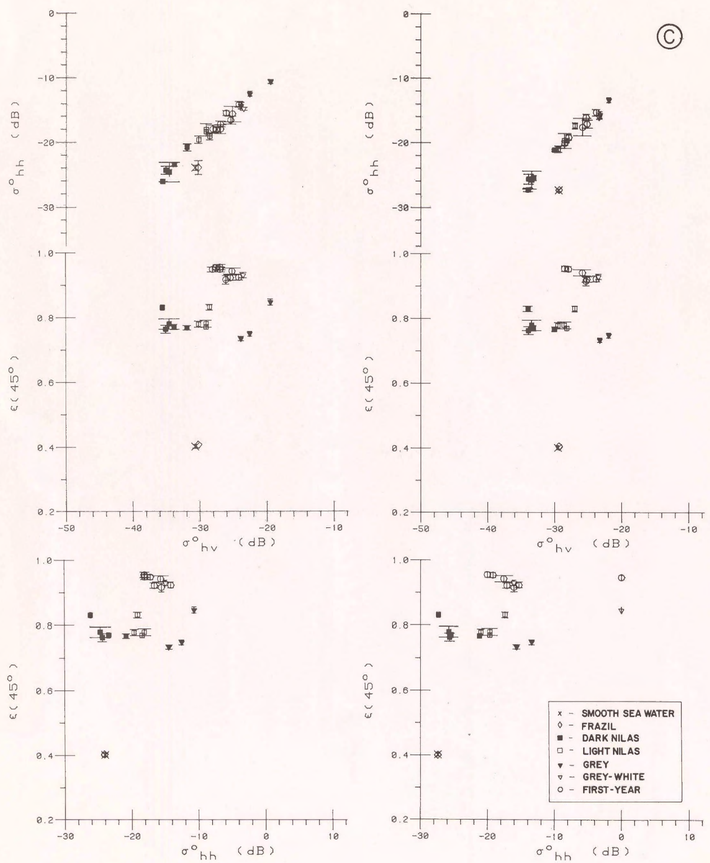

Table 13. Summary of the Danish W/E Line Sea-ice Classification Data Set

Ice Types	Data Base	Ice Classification Data Set		Events
	Events	Events	Samples	Not Used
Calm Water	7	3	194	4
Grease Ice (R)	14	1		14
Nilas (N)	9	2	45	7
Grey (G)	29	3	58	26
Grey-white (L)	6	3	82	3
First-year (FY)	30	18	1079	12
First-year (FK) (wave-broken)	7	7	685	0
Mixtures	31	0	N/A*	31
Class Uncertain	5	0	N/A	5

* Not applicable

Table 14. Danish W/E Line Sea-Ice Signature

Sensor	Function	Incidence Angle	Statistic	Ice Class: Wave-broken First-year	First-year	Grey-white	Grey	Nilas	Water
19.5 GHz Radiometer	T_B	45°	M*	230.1	239.9	204.5	214.0	191.4	106.8
			SD	9.4	8.5	6.0	6.2	3.9	3.1
	ε	45°	M	0.838	0.877	0.737	0.775	0.685	0.351
			SD	0.037	0.034	0.024	0.024	0.015	0.012
13.3 GHz Scatterometer	σ^o_{hh} in dB	8°	M	3.68	3.29	7.23	6.28	0.91	13.56
			SD	0.93	2.06	1.41	1.33	1.83	1.50
		15°	M	-0.26	-2.29	1.14	2.69	-2.44	2.40
			SD	1.04	1.59	2.21	0.95	1.49	1.62
		25°	M	-4.71	-8.16	-6.39	-2.43	-7.02	-15.27
			SD	1.37	1.88	2.50	0.86	1.16	1.29
		35°	M	-9.34	-13.76	-13.00	-8.37	-12.62	-28.63
			SD	1.64	2.00	2.48	0.90	1.24	0.88
		45°	M	-14.29	-19.57	-19.17	-14.95	-18.86	-35.26
			SD	1.74	2.06	2.52	0.65	1.50	1.10
		55°	M	-15.61	-21.38	-19.14	-18.19	-22.05	-33.14
			SD	1.98	5.10	1.08	0.98	1.77	1.44
	σ^o_{hv} in dB	8°	M	-15.89	-17.10	-13.47	13.22	-18.69	-7.84
			SD	1.03	1.64	1.44	0.98	1.74	1.54
		15°	M	-19.25	-22.55	-19.92	-16.92	-21.85	-22.13
			SD	1.22	1.40	1.96	0.62	1.67	1.52
		25°	M	-19.53	-23.30	-21.43	-17.21	-21.84	-35.42
			SD	1.31	1.84	2.11	0.84	1.56	0.85
		35°	M	-22.47	-26.63	-25.07	-20.62	-24.70	-44.01
			SD	1.43	2.00	2.18	0.88	1.43	1.22
		45°	M	-23.24	-27.56	-25.92	-22.10	-25.17	-45.66
			SD	1.43	1.95	2.02	0.64	1.27	1.58
		55°	M	-24.06	-27.69	-25.41	-24.09	-25.53	-40.46
			SD	1.69	6.32	0.81	0.92	1.00	0.88
	$\sigma^o_{hv}/\sigma^o_{hh}$ in dB	8°	M	-19.57	-20.39	-20.71	-19.50	-19.61	-21.40
			SD	0.60	0.79	0.35	0.67	0.61	0.22
		15°	M	-18.99	-20.26	-21.07	-19.61	-19.41	-24.53
			SD	0.67	1.52	0.78	0.97	0.91	0.19
		25°	M	-14.82	-15.15	-15.05	-14.78	-14.81	-20.15
			SD	0.57	1.32	0.78	0.55	0.59	0.76
		35°	M	-13.14	-12.87	-12.07	-12.25	-12.08	-15.30
			SD	0.64	1.09	0.63	0.42	0.43	0.99
		45°	M	-9.05	-7.99	-6.75	-7.15	-6.31	-10.41
			SD	0.67	0.93	0.78	0.45	0.70	1.23
		55°	M	-8.45	-6.32	-6.27	-5.91	-3.40	-7.31
			SD	0.67	1.65	5.91	0.77	1.08	0.71

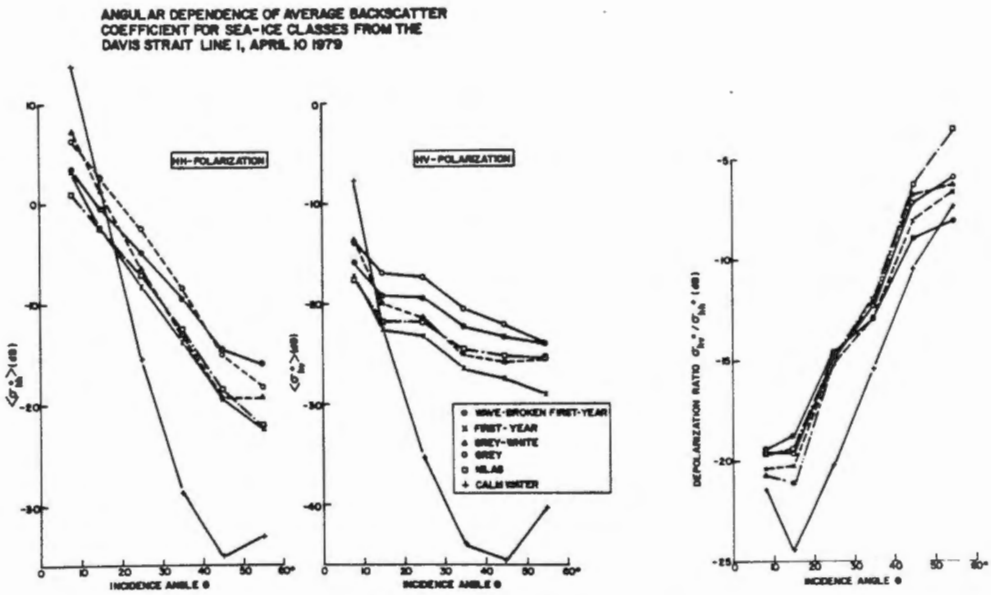

Figure 16. Angular Dependence of σ^o_{hh}, σ^o_{hv} and the Depolarization Ratio $\sigma^o_{hv}/\sigma^o_{hh}$ for the Davis Strait Line 032501.

All of the ice signatures shown are from ambient air temperatures of ~-2° (melting conditions) and are from younger ice forms. Greater angular variation is seen in the σ^o_{hh} results than for σ^o_{hv} but no advantage in dB separation classes may be seen for either polarization.

(1) For σ^{o}_{hh}, ignoring calm water, grey-white ice is somewhat more specular than the other ice types present and first-year wave-broken ice is somewhat less specular than the other ice types present. Contrast inversions are found between grey-white and grey ice in the 8° to 15° incidence angle interval and between grey-white and first-year wave-broken ice in the 17° to 23° incidence angle interval.

The water found in this data set is very calm and exhibits specular reflection. Contrast inversions with water occur in the following incidence angle intervals:

(a) 13° to 16° for grey ice
(b) 14° to 17° for grey-white ice
(c) 16° to 18° for first-year wave-broken ice
(d) 12° to 20° for nilas and first-year ice.

(2) A comparison of the Danish W/E line σ^{o}_{hh} data (Table 14) with the Frobisher Bay σ^{o}_{hh} data (Table 12) and the Beaufort Sea σ^{o}_{hh} data (Table 10) for common ice types reveals the following:

(a) The Danish W/E line first-year ice data is slightly more specular than the Frobisher Bay data and much more specular than the Beaufort Sea data. The open water found on the Danish W/E line was much more specular than that found in Frobisher Bay reflecting the lower wind speed.

(b) The σ^{o}_{hh} vs incidence angle curves for the Danish W/E line first-year ice and grey-white ice intersect their Beaufort Sea counterparts at 45° and 47° respectively. The corresponding curves for grey ice cross at 25° and are within one standard deviation of each other over the incidence angle interval 15° to 30°.

(c) Over the incidence angle range 25° to 55° the σ^{o}_{hh} values for the Danish W/E line ice type are smaller than their Frobisher Bay counterparts. Danish W/E line first-year ice lies within one standard deviation of Frobisher Bay light nilas at all incidence angles; Danish W/E line first-year ice lies within one standard deviation of Frobisher Bay grey-white ice over the incidence angle range 35° to 47°.

(3) Using one standard deviation as a criterion for separability for the σ^{o}_{hh} data:

(a) Nilas and first-year ice are separable only at 8°.

(b) First-year and grey-white ice are separable only over the incidence angle range 8° to 18° and at 55°.

(c) First-year ice is separable from first-year wave broken ice at all incidence angles greater than 15°.

(d) Grey ice is separable from first-year and nilas at all incidence angles, from grey-white ice over the incidence angle range 15° to 55° and from first-year wave-broken ice over the incidence angle ranges 8° to 30° and 54° to 55°.

(e) Calm water is separable from all ice types except for the contrast reversal intervals.

(4) When the σ^{o}_{hv} data is examined as a function of incidence angle, the same general comments on relative ice type specularity apply as for the σ^{o}_{hh} data. Contrast reversals between calm water and all ice types appear in the incidence angle range 11° to 16° and a contrast reversal between grey-white ice and first-year wave-broken appears at the 13° incidence angle.

(5) When the Danish W/E line σ^{o}_{hv} data from Table 14 are compared with the Frobisher Bay σ^{o}_{hv} data from Table 12:

(a) σ^{o}_{hv} values for the Danish W/E line ice types are generally smaller than σ^{o}_{hv} values for the corresponding Frobisher Bay ice types, with the exception of grey ice.

(b) Danish W/E line grey ice lies within one standard deviation of σ^{o}_{hv} for Frobisher Bay grey ice, over the incidence angle range 8° to 53°.

(c) Danish W/E line first-year wave-broken ice lies within one standard deviation of Frobisher Bay grey-white ice at all incidence angles.

(d) Danish W/E line grey-white ice lies within one standard deviation of Frobisher Bay first-year ice at all incidence angles greater than 15°.

(e) Danish W/E line nilas lies within one standard deviation of Frobisher Bay first-year at all incidence angles greater than 10°.

(f) Danish W/E line first-year is lower than Frobisher Bay first-year and is a marginally separable class for incidence angles greater than 50°.

(6) Using one standard deviation as a criterion for separability σ^{o}_{hv} in the Danish W/E line:

(a) Grey ice is separable from first-year wave-broken ice over the incidence angle range 8° to 43° and is separable from grey-white ice at all angles greater than 10°.

(b) First-year wave-broken ice is separable from grey-white ice for all incidence angles greater than 25°.

(c) First-year wave-broken ice is separable from nilas for all incidence angles greater than 10°.

(d) Nilas is separable from first-year for incidence angles greater than 40°.

(e) Grey-white ice is separable from first-year from 47° to 55° and from 8° to 15°.

(f) Calm water is separable from all ice types for incidence angles greater than 16° and less than 10°.

(7) When both σ^{o}_{hh} and σ^{o}_{hv} are considered, all ice types are separable to at least one standard deviation for incidence angles greater than 47° except:

(a) Grey ice and first-year wave-broken ice (separable only at angles greater than 54°).

(b) Nilas and grey-white ice (separable only at angles less than 10°).

(8) When the horizontally polarized 19.35 GHz emissivity is considered alone all ice types are separable by at least one standard deviation.

The event cluster plots corresponding to the data just discussed are presented in Figure 17a, b, c. It is clear from the distribution of events that misclassification of grey with first-year wave-broken, and grey with grey-white ice may result for some ice events on the edge of the class distribution in these spaces.

3.2 A Simple Automatic Sea-ice Classifier

A computer algorithm was developed to evaluate the validity of the microwave sea-ice class signatures on a point-by-point basis. A three-dimensional feature space was defined by σ^{o}_{hh} and σ^{o}_{hv} at 45° incidence angle and by the horizontally polarized radiometric brightness temperature, T_B, at 45° incidence angle. Each of the sea-ice classes was positioned in this space in terms of the class mean values of each of the feature space parameters.

A section of the Beaufort Sea data set containing examples of many different ice types was used to test the classifier. The test data was inserted into the feature space on a point-by-point basis and the weighted Euclidean distance between each test point and all class means was computed. The sample point was assigned to the ice class found to be closest, ignoring preceding points (a classifier without memory) and ignoring the cluster density. The accuracy of the classifier was evaluated from available photography and SAR data as follows:

Grey-white ice	67%
First-year smooth ice	80%
First-year rough ice	82%
Second-year smooth ice	74%
Second-year rough ice	80%
Multi-year smooth ice	70%
Multi-year rough ice	80%

The majority of the classifier errors were caused by rough ice features (ridges or rubble fields). When a major ridge was encountered by the classifier, it almost invariably assigned it to the next rougher/older ice category. Many of these errors could be eliminated by allowing the classifier to use the memory of the last few events to weight its decisions. Further improvement is possible by including the probability density functions and class orientation.

Some work was done with the classifier on the Frobisher Bay data set and results of a similar accuracy were obtained.

For the Beaufort Sea data, the dimension of the feature space was varied to examine the significance of each of the parameters. Backscattering cross-section data alone were adequate to distinguish the broad ice categories (first-year, second-year, multi-year) to reasonable accuracy (70%), but the full feature space yielded the greatest classification accuracies.

A second, less simplistic classification algorithm was subsequently developed (Young and Wilkinson, 1980) and tested. This MAP algorithm (Jernigan, 1979) uses the event point density functions to provide decision weighting. It uses the ice class cluster shape and orientation and defines feature space scale transformations, for distance computations between data inputs and defined ice classes.

The refined algorithm produced the following classification accuracies when tested with Beaufort Sea data:

(1) Major classes (multi-year, first-year, second-year, grey-white, grey) could be classified to 94% accuracy.

(2) Subclasses could be separated with accuracy as follows:

(a)	first-year rough	80%
(b)	first-year smooth	81%
(c)	second-year rough	69%
(d)	second-year smooth	89%
(e)	multi-year rough	66%
(f)	multi-year smooth	91%

(3) Errors in the subclass associated with smooth subclasses were usually toward rough subclass and thus were conservative.

Figure 17. Event Classification Clusters From the Davis Strait W/E Line 032501.

The shape of the data cluster changes considerably in the sequence of angles from 8 to 25°, as expected from Figure 16, but for greater incidence angles the dominant change is a monotonically decreasing signal with no advantage in class separation.

CLASSIFICATION OF ICE FROM THE DAVIS STRAIT BY
19·4 GHz EMISSIVITY AND 13·3 GHz BACKSCATTERING COEFFICIENT
10 APRIL 1979, FLIGHT LINE I $T_{SURFACE} \sim -2°C$

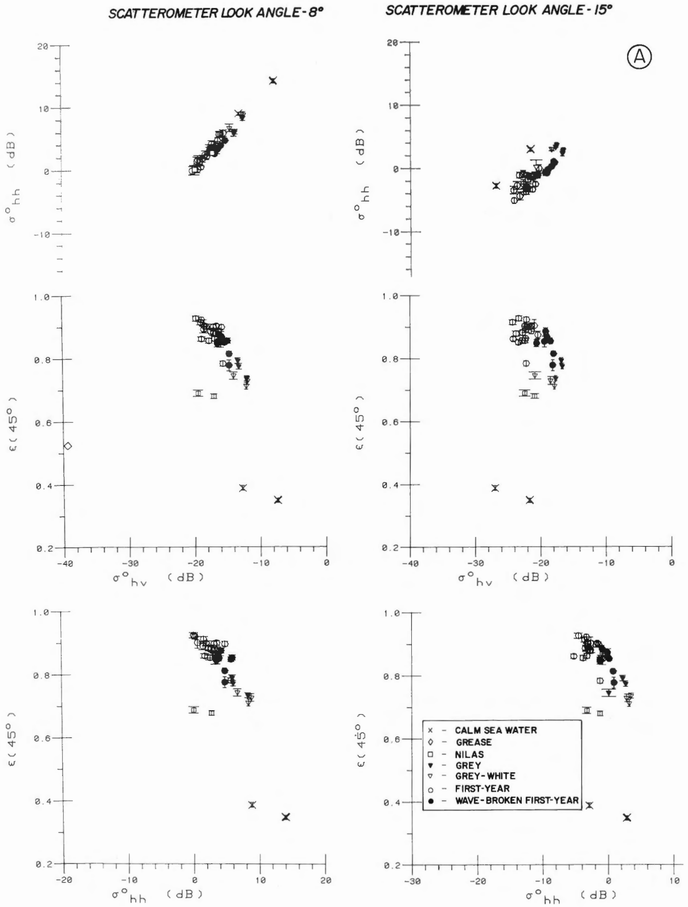

CLASSIFICATION OF ICE FROM THE DAVIS STRAIT BY
19·4 GHz EMISSIVITY AND 13·3 GHz BACKSCATTERING COEFFICIENT
10 APRIL 1979, FLIGHT LINE I $T_{SURFACE} \sim -2°C$

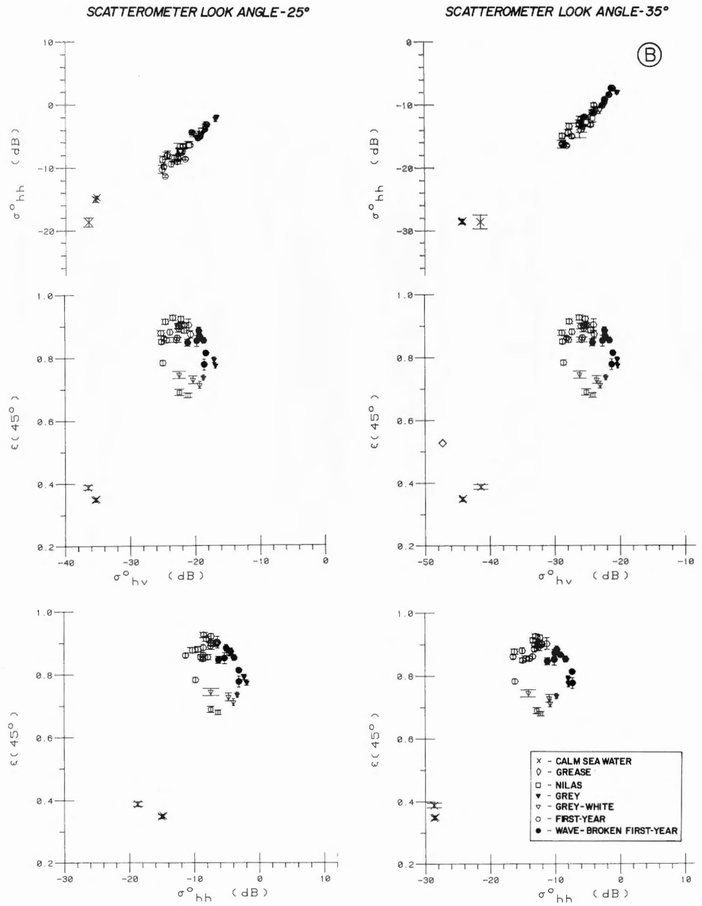

CLASSIFICATION OF ICE FROM THE DAVIS STRAIT BY
19·4 GHz EMISSIVITY AND 13·3 GHz BACKSCATTERING COEFFICIENT
10 APRIL 1979 FLIGHT LINE I $T_{SURFACE} \sim -2°C$

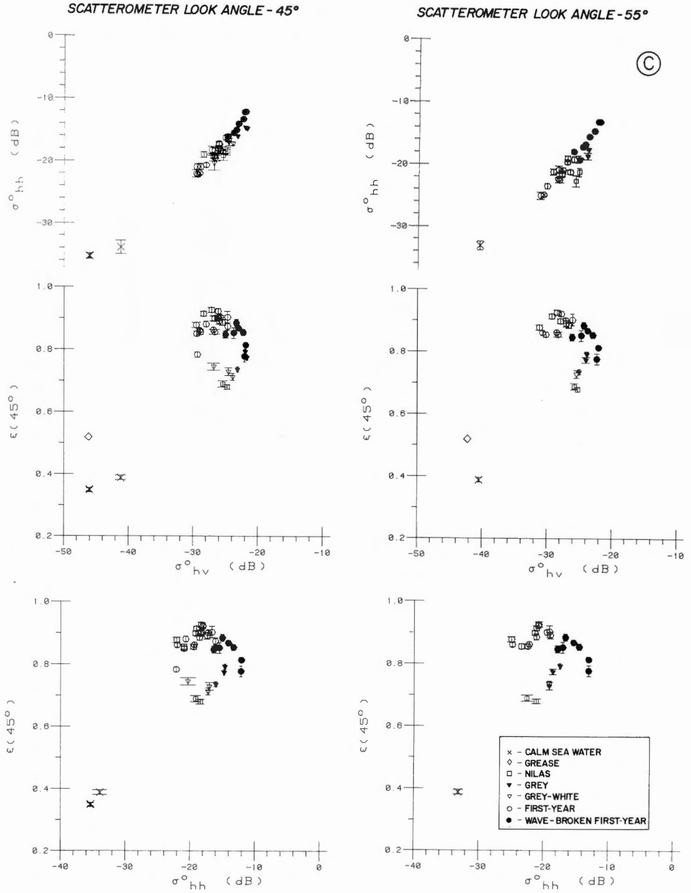

3.3 Variation of Scattering Coefficient with Incidence Angle

The variation of σ^o_{hh} and σ^o_{hv} with incidence angle depends mainly on the microwave roughness and the complex dielectric constant, at the ice surface and down to approximately one skin depth; which are each functions of ice type, the thermal history of the ice, the mechanical history of the ice and the ice surface temperature. Microwave roughness is a measure of density and distribution of inhomogeneities within the surface layer, (ice granules, brine pockets, air pockets, etc.) whose scale lengths are of the order of one radar wavelength.

In the previous section, the incidence angle dependence of σ^o_{hh} and σ^o_{hv} were discussed for each ice class, under the assumption that each sample point is independent (Section 3.1.1 to 3.1.3). Variations in sea-ice signatures in each event due to the thermal and mechanical history of the ice, are thus folded into the ice class variance along with the radar texture information. In the ε, σ^o_{hv}, σ^o_{hh} cluster plots, each event is treated as an independent entity and the effects of the event evolution and surface coverage are preserved within the statistics of each event.

σ^o_{hh} and σ^o_{hv} were modelled on an event-by-event basis using the best χ^2 fit straight lines of the form $\sigma^o_{hh} = A\theta+B$ and $\sigma^o_{hv} = C\theta+D$. Typical examples may be found in Figures 18, 19, 20 and 21 for each ice class and flight line. The fitted parameters for each event (the slope A and C and its nadir intercepts B and D) were plotted and are given in Figures 22, 23 and 24, 25 for σ^o_{hh} and σ^o_{hv} respectively. Corresponding event emissivities are displayed on these graphs as the grey scale of each data plot. Again only those events that were large enough to contain several radiometer footprints and were homogeneous examples of the specific ice types were analysed by this technique. Examination of Figures 22 and 23 shows:

(1) Within each flight line, ice types can be identified reliably by their incidence angle dependence as A, B plane clusters.

(2) As first-year and grey ice become warmer and approach melt conditions both the slope and nadir intercept of $\sigma^o_{hh}(\theta)$ increase.

(3) For the very cold ice found in the Beaufort Sea the slope of σ^o_{hh} decreases and the nadir intercept, B, increases with increasing ice age. There does not appear to be any significant difference between the multi-year ice on the two flight lines as observed by the low altitude photography and it is possible that the difference between multi-year clusters for the two lines may arise through the different ambient temperatures.

(4) For young sea ice under freezing conditions (Frobisher Bay line) as the ice ages and develops, from dark nilas to light nilas to grey ice, the slope of $\sigma^o_{hh}(\theta)$ increases slowly with ice type (age) but the nadir intercept increases rapidly. Similar results are seen under warmer conditions in the Danish W/E line data.

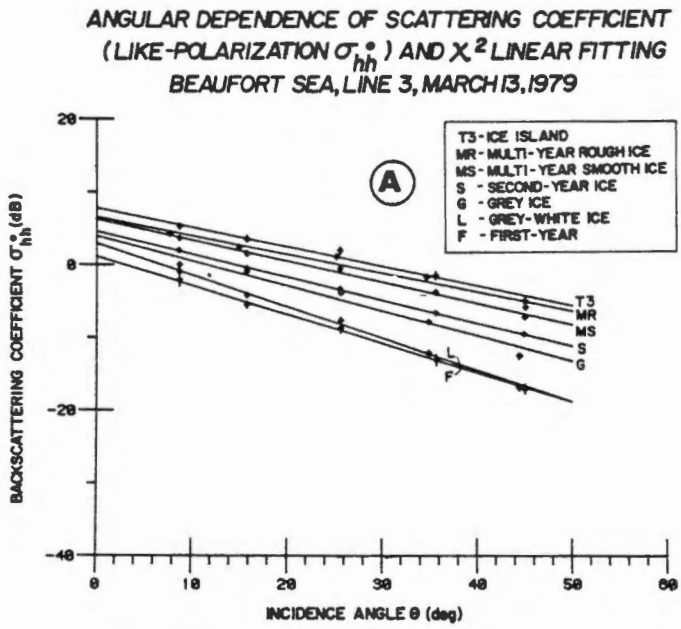

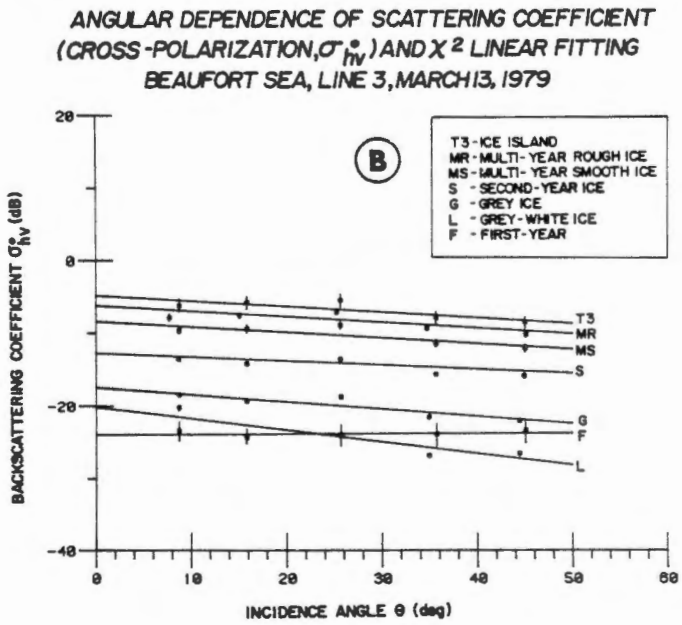

Figure 18a,b. χ^2 Line Fitting of the Angular Dependence of σ^{o}_{hh} and σ^{o}_{hv} for the Beaufort 030603 Line, March 13, 1979.

In these figures, the points represent the backscattering coefficient measurement from the experiment. The vertical lines through the points give their standard deviations. Each of the lines given are from 'typical' events within the flight line.

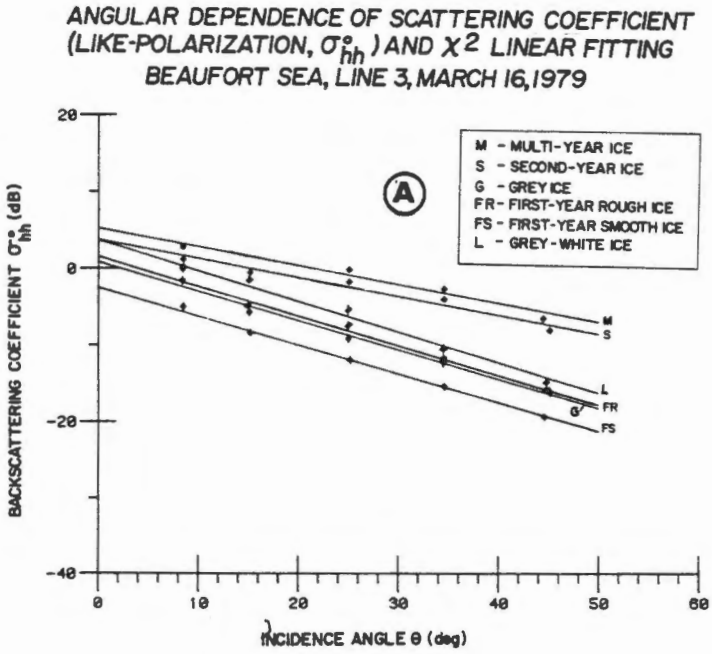

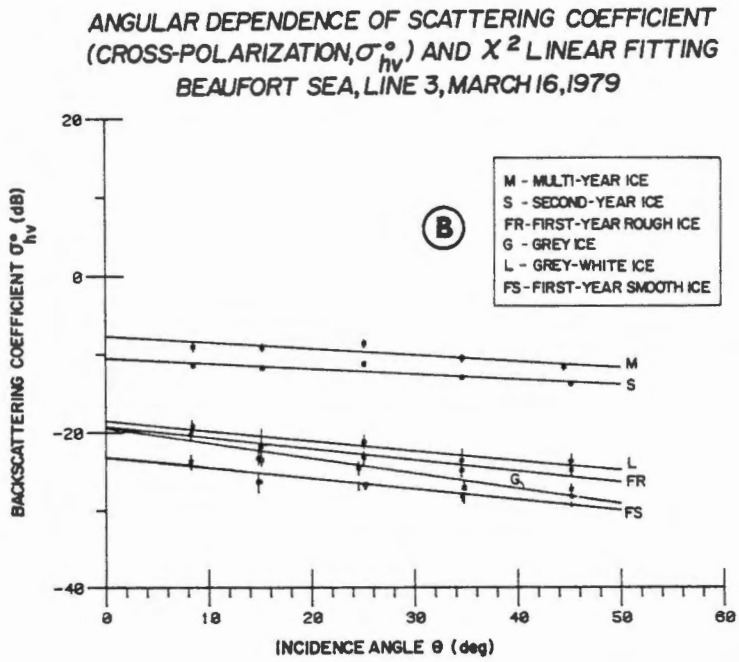

Figure 19a,b. χ^2 Line Fitting of the Angular Dependence of σ^{o}_{hh} and σ^{o}_{hv} for the Beaufort 030803 Line, March 16, 1979.

As in Figure 18a, b, each of the lines has been fitted to a typical example from each class represented in the flight line.

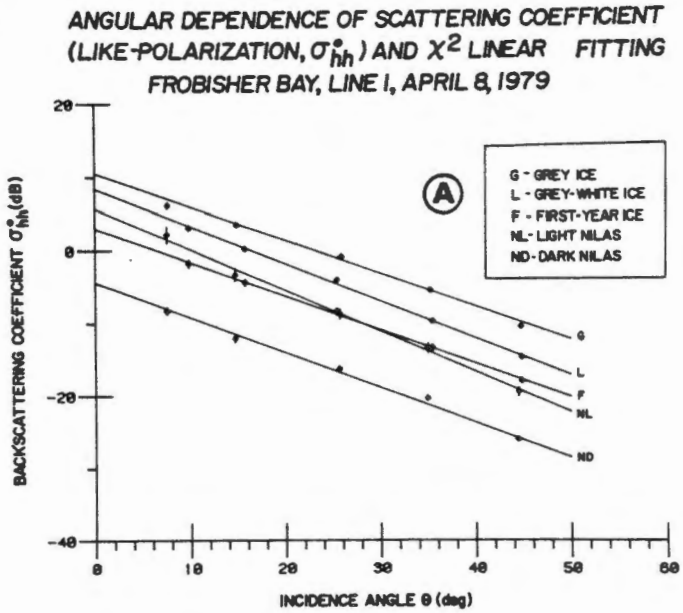

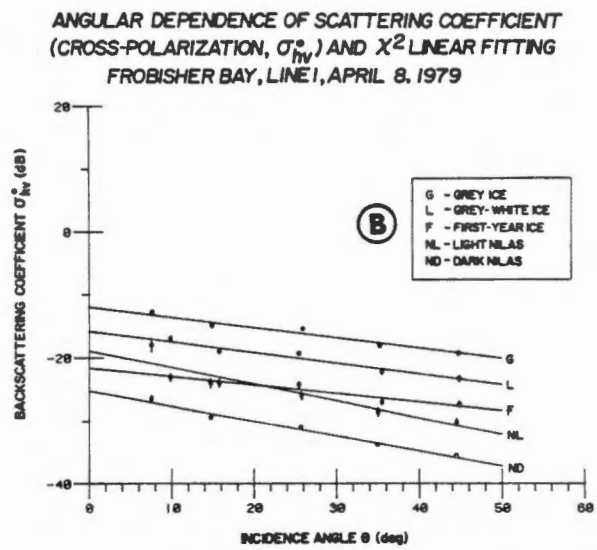

Figure 20a,b. χ^2 Line Fitting of the Angular Dependence of σ°_{hh} and σ°_{hv} for the Frobisher Bay 032201 Line, April 8, 1979.

Typical example results from events of each ice class are presented. The points with error bars show the event mean and standard deviation. The lines are the best estimates of a linear fit through the points.

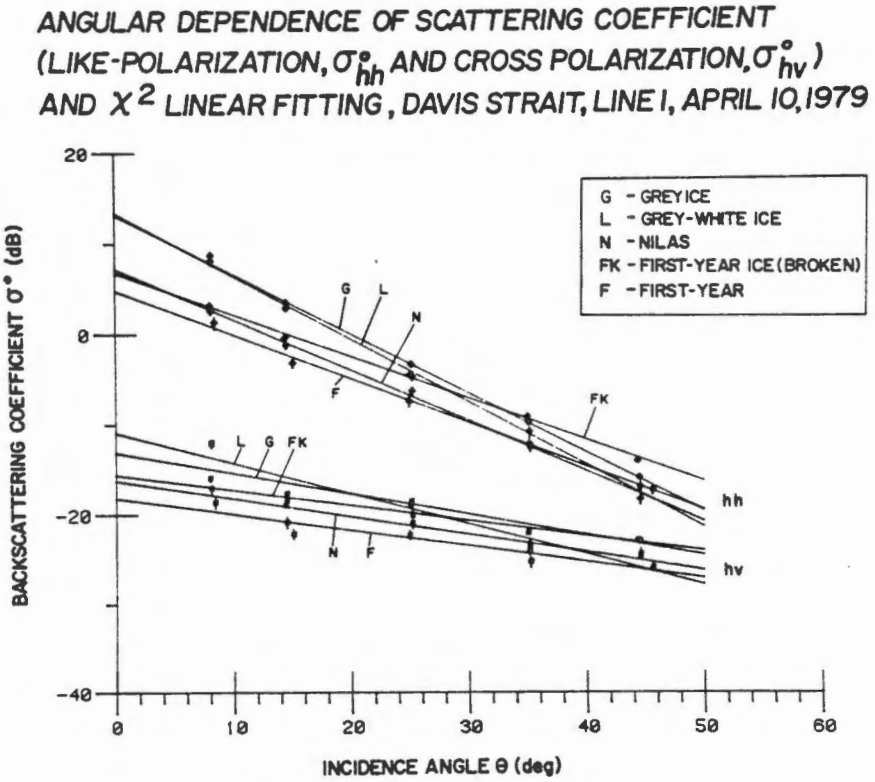

Figure 21. χ^2 Line Fitting of the Angular Dependence of σ^{o}_{hh} and σ^{o}_{hv} for the Davis Strait 032501 Line, April 10, 1979.

HH- and HV-polarizations are presented together because they are well separated. It is clear from this representation however, that these young ice classes are not well separated by their backscattering properties alone. This is further illustrated by an examination of Figure 23.

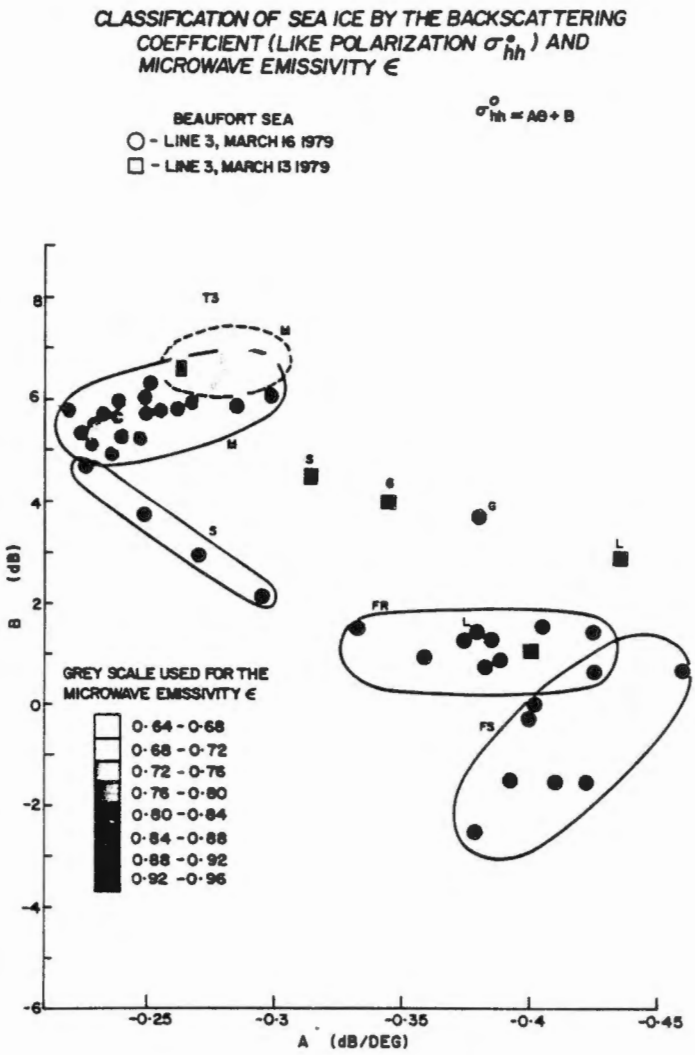

Figure 22. Classification of Sea Ice from the Beaufort Sea Using Fitted Parameters from the Angular Dependence of σ^o_{hh} together with ε.

Data from the 030603 line of March 13 are represented by squares, and circles are used for the 030803 line. For those cases where data clustering is evident, lines have been added to indicate boundaries associated with each class. Little class overlap is evident in the Beaufort data and the additional discrimination provided by the emissivity grey scale is of supplimentary value only. The symbols are as per Table 10. To help show the data clustering, solid lines have been used to surround the points from the March 16 line and a dashed line, for the March 13 line.

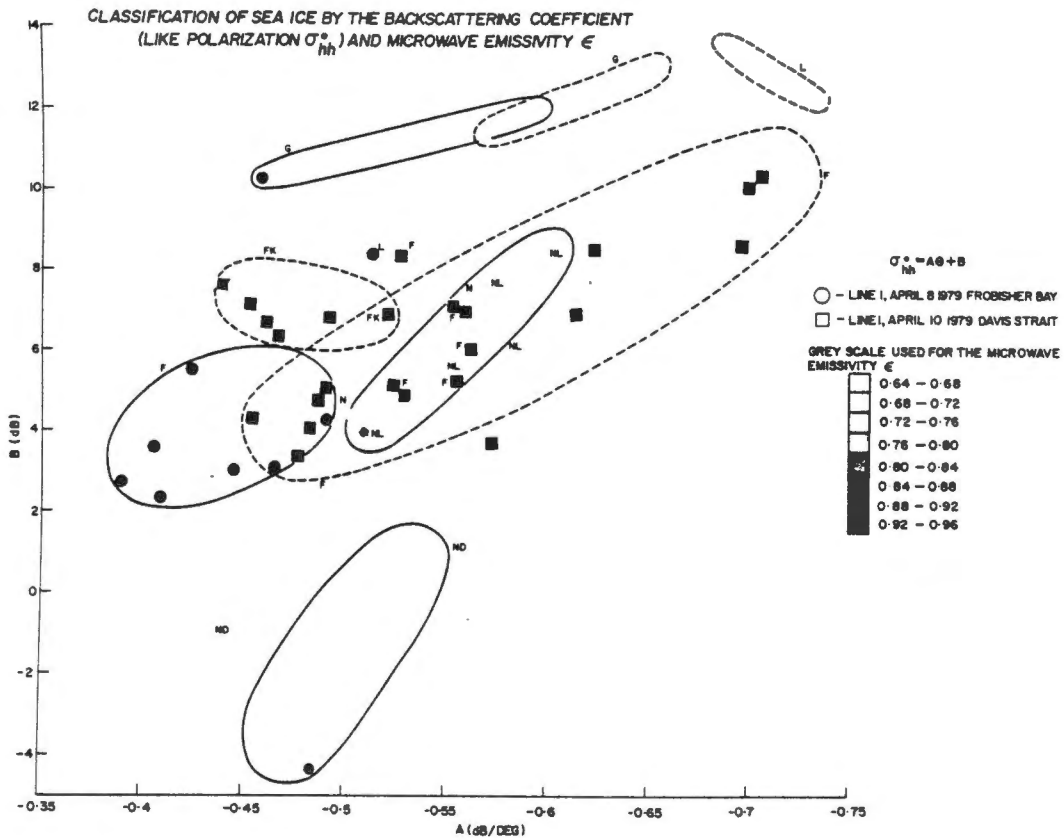

Figure 23. Classification of Sea Ice from the Eastern Arctic Using Fitted Parameters from the Angular Dependence of σ^{o}_{hh} together with ε.

As with Figure 22, the slope and intercept (A and B) of $\sigma^{o}_{hh}(\theta)$ are used for each axis. The grey scale of each point is used to indicate the average emissivity for the ice event. In this case considerable class overlap is evident and the added dimension of emissivity is more important for these classes. The data from the two lines may be separated by the circles and squares used to represent them and also by the dashed line used to form the boundaries of the Danish line and the full line used for the Frobisher line. Clear trends may be seen in going from the melting conditions of the Davis line to the colder Frobisher Bay line for grey and first-year ice. In this diagram, the symbols are as per Table 12 and 14.

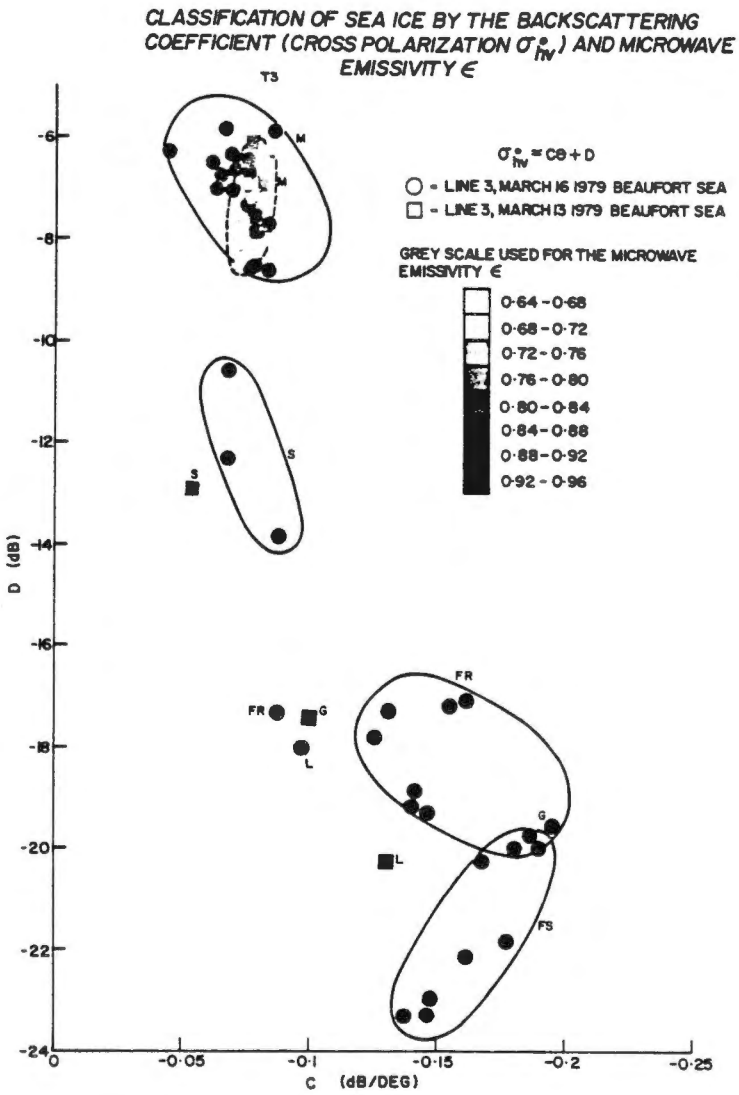

Figure 24. Classification of Sea Ice from the Beaufort Sea Using Fitted Parameters from the Angular Dependence of σ^o_{hv} together with ε.

This figure shows the HV-polarization companion to Figure 22. Generally the class separation, given by the line fitting parameters, is better with HV-polarization than HH-polarization when the intercept information is considered. HH-polarization appears to be superior, when slope is considered. Full and dashed lines are used as in Figure 22 and the symbols are as per Table 10.

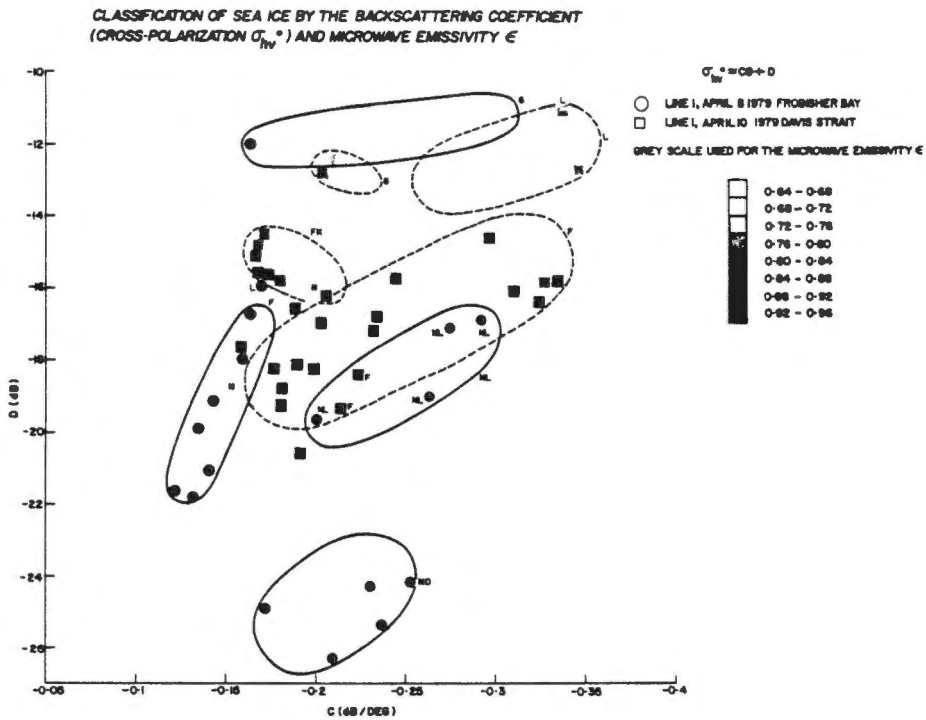

Figure 25. Classification of Sea Ice from the Eastern Arctic Using Fitted Parameters from the Angular Dependence of σ^o_{hv} together with ε.

The trends seen in the parallel representation of the HH data given in Figure 23 are again present in this figure. The overlap and shape of the clusters have however changed somewhat. No clear advantage may be seen in either polarization. Full and dashed lines are as used in Figure 23 with the symbols defined in Tables 12 and 14.

(5) As the ice ages further to form grey-white ice, the slope of $\sigma^o_{hh}(\theta)$ increases with little change in nadir intercept.

(6) The transition from grey-white ice to first-year ice is marked by a decrease in both the slope of σ^o_{hh} and nadir intercept.

Figures 24 and 25 show the parametric representation of σ^o_{hv} with a considerable reduction in slope and nadir intercept from the corresponding σ^o_{hh} cases.

The cluster separation increases for old, cold ice and decreases for young, warm ice. For each flight line, ice classes may be identified by their C, D plane event cluster. Some differences between the A, B plane and the C, D plane event clusters are as follows:

(1) The multi-year ice data from both Beaufort Sea lines fully overlap in the C, D plane.

(2) The effects of temperature/season, represented by the different flight lines, are less marked in the C, D plane than in the A, B plane and only become significant as the ice approaches melt conditions (Danish W/E line data).

Figures 26, 27 and 28, 29 show the explicit relationships between the parametric model nadir intercepts and the microwave emissivity for σ^o_{hh} and σ^o_{hv} respectively, displaying the results from the two Beaufort Sea and two Eastern Arctic lines. As in the previous diagrams, envelopes have been drawn to show the parameter boundaries for each class and subclass. Figure 26 explicitly indicates that in the Beaufort data set, emissivity enhances the class separation already present in $\sigma^o_{hh}(\theta)$. A particular advantage may be seen for the cases of ice island T_3 and multi-year ice; second-year and multi-year; and rough first-year and second-year by the combination of ε and $\sigma^o_{hh}(\theta)$. The same observation may be made for the cross-polarized representation in Figure 28 with the clear advantage in cross-polarized results in separating the major classes of the Beaufort data set. For the Eastern Arctic result, ε measurements are very important in resolving nilas, wave-broken first-year and first-year ice, as shown in Figures 27 and 29. Here, neither polarization is superior in separating classes, but the 15-20 dB increase in received signal for like-polarization makes it more desirable for these conditions.

The old multi-year ice from the 030603 line has higher $\sigma^o_{hh}(\theta)$ and lower ε than the multi-year ice from the 030803 lines. Comparison of other classes at different temperatures gives the opposite trend: warmer temperatures give higher nadir-looking σ^o_{hh} values and lower emissivities than the same ice classes at colder temperatures. No systematic trend can be seen in the cross-polarized results with temperature.

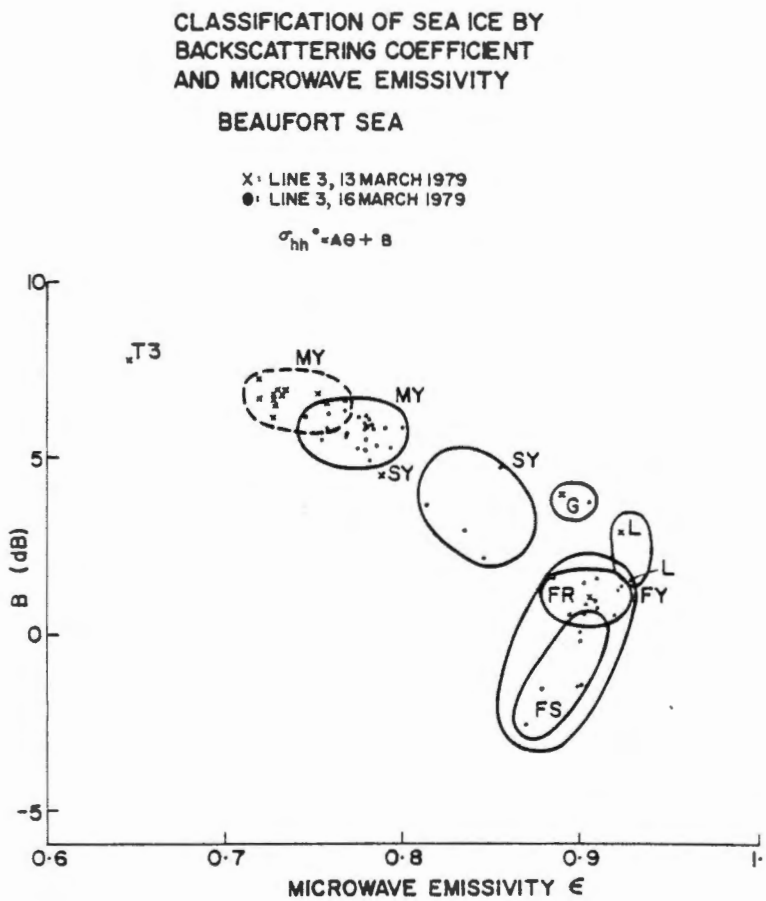

Figure 26. Classification of Sea Ice from the Beaufort Sea Using $\sigma^{o}_{hh}(\theta = 0^{o})$ and ε .

In this figure, crosses represent averages from the March 13 line and full and dashed lines have been drawn to indicate the cluster boundaries for the two different flying days. The symbols are defined in Table 10.

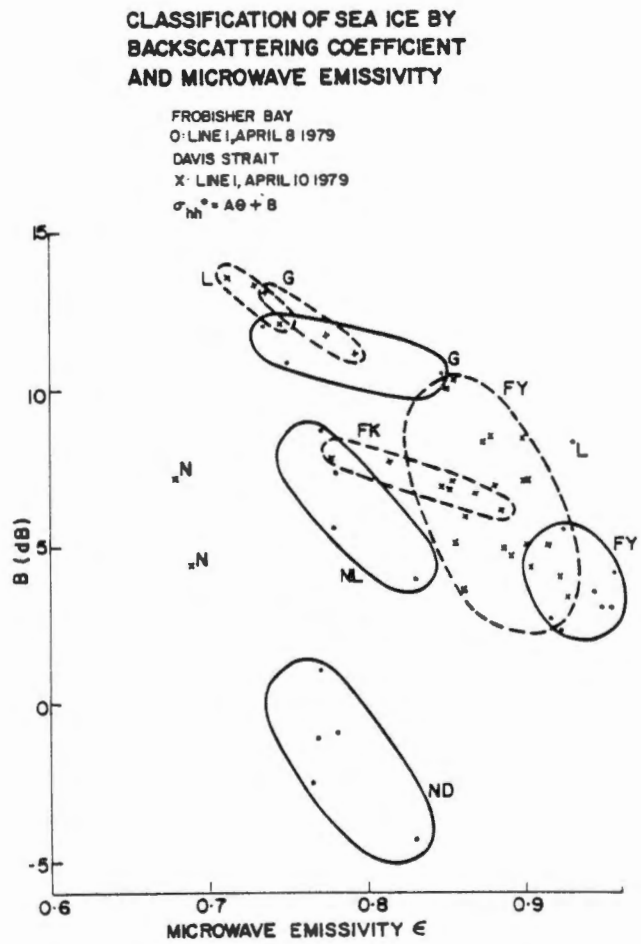

Figure 27. Classification of Sea Ice from the Eastern Arctic Using σ^{o}_{hh} (θ=0) and ε.

Data from the Frobisher Bay line is represented by dots; crosses are used for the Davis Strait line. As in Figures 23 and 25, data clusters from the Frobisher Bay are enclosed with solid lines while dashed lines are used for the results from Davis Strait. Symbols are as defined in Tables 12 and 14.

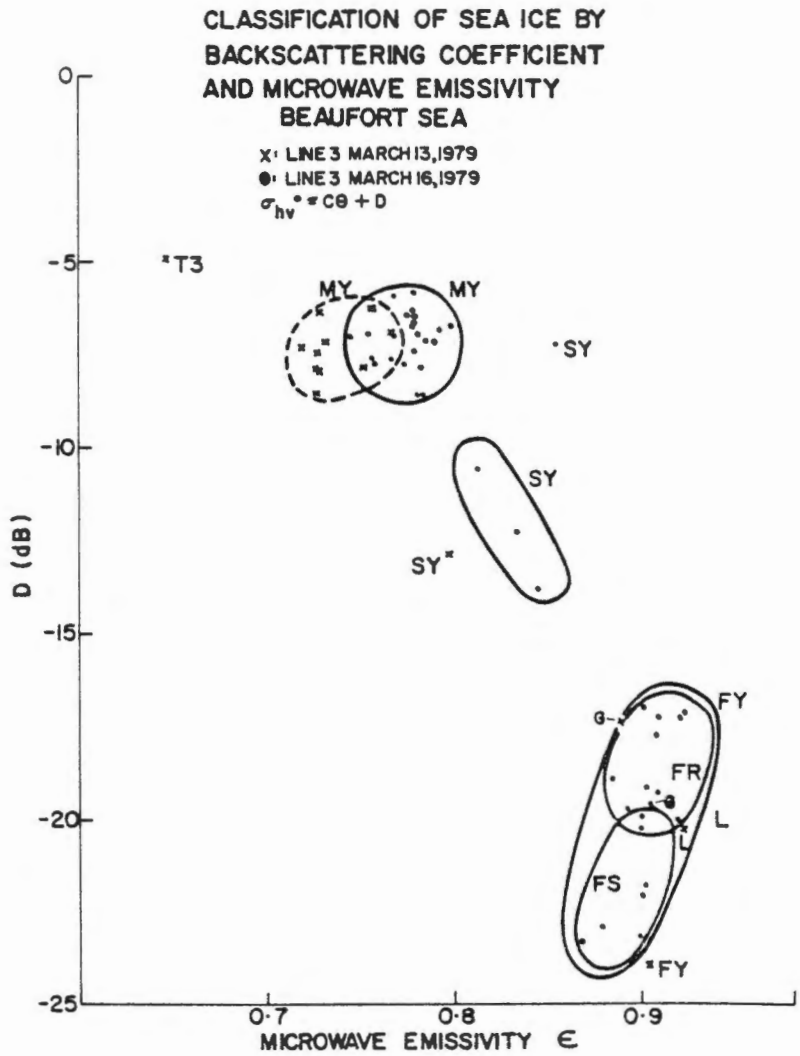

Figure 28. Classification of Sea Ice from the Beaufort Sea Using $\sigma^{o}_{hv}(\theta=0)$ and ε.

This comparison to Figure 26 shows that the cross-polarized channel has greater separation between these old ice forms and yields greater contrast and texture than the corresponding like-polarized channel. Data clusters from the March 13 line are enclosed in a dashed line and those from March 16, with a solid line. Symbols are as per Table 10.

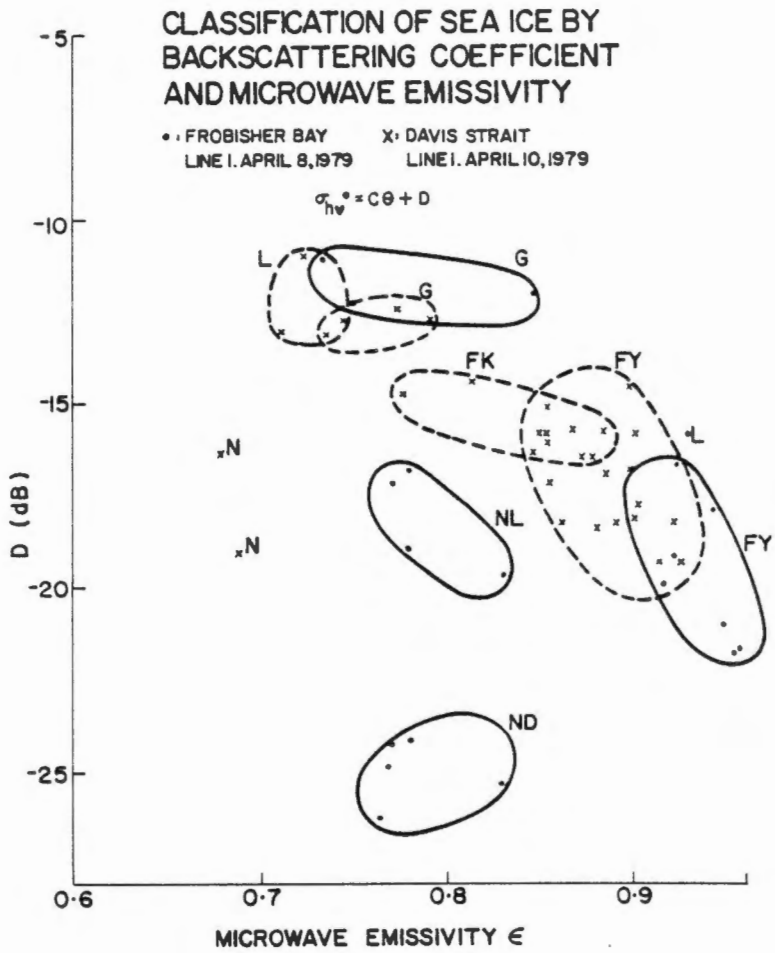

Figure 29. Classification of Sea Ice from the Eastern Arctic Using σ_{hv}^{o} (θ=0) and ε.

As with Figure 27, the data from each flight line are shown with crosses and dots; clusters are enclosed with different lines. No significant advantage may be seen in the data from either polarization. Labels are as per Tables 12 and 14.

3.4 Variation of Microwave Emissivity with Ice Thickness

Figure 30 shows the relationship between the microwave emissivity, ε , measured at 19.4 GHz of various ice classes, as a function of ice thickness. The ice types found in this experiment were matched as closely as possible to the ice thickness category of the WMO classification. The figure shows that ε appears to increase with ice thickness and has a maximum value when the ice thickness reaches that of medium first-year ice. When the ice becomes thicker than approximately 1m, ε decreases with increasing ice thickness. These two contradictory tendencies are shown in the figure by straight lines and data from different flight lines are shown by different symbols. It is clear from the figure that ice thickness (or type of ice) cannot be determined uniquely from single frequency microwave radiometer data alone.

For younger ice types in Figure 30, the ε increases with increasing ice thickness in an approximately linear manner. It should be emphasized that the 19.4 GHz emissivity is a strong function of the surface condition, e.g. wetness and roughness, of the ice which is not always related to the type or ice thickness. The majority of the young ice in this experiment was rather smooth and close to the melting point, with the exception of a few grey and grey-white ice samples from the Beaufort Sea. These young ice types are much more saline than first-year ice and thus have a larger imaginary dielectric constant and smaller skin depth.

The physical properties of the ice thicker than 1m can be described as old, rather rough and very cold (around $-30^{o}C$ in the case of the Beaufort Sea). This older ice is much less saline, which results in the low imaginary dielectric constant and larger values for skin depth.

Using formulae given in Appendix 6, the microwave emissivity (Section A6.3) and skin depth (Section A6.4), can be calculated with some assumptions. Unfortunately the complex dielectric constant data of natural sea ice at 19.35 GHz are unavailable; however, measurements at 10 GHz were made by Vant et al. (1974, 1975) for Bering Sea ice. Vant (1976) also measured complex dielectric constants of natural sea ice at 7.5 GHz as part of the AIDJEX project. Using these data, H-polarized ε, at the incidence angle $\theta = 45^{o}$, skin depths have been calculated and are given in Table 15. Brine volume fractions, V, in the table were calculated using the formula by Frankenstein and Garner (1967) who evaluated fitted curves to the brine volume data of Assur (1958). These relations are:

$$V = -(2.28 + \frac{52.56}{T})\ 10^{-3} \cdot S \qquad \left[-2.06^{o}C < T < -.5^{o}C\right]$$

$$V = (.930 - \frac{45.917}{T})\ 10^{-3} \cdot S \qquad \left[-8.2 \leq T < -2.06^{o}C\right]$$

$$V = (1.189 - \frac{43.795}{T})\ 10^{-3} \cdot S \qquad \left[-22.9 \leq T < -8.2^{o}C\right]$$

Table 15. Dielectric Properties of Sea Ice.

Sample	Experimental Value						Calculated Results			
	Frequency (GHz)	Salinity (°/oo)	Density (g/cm³)	Temperature (°C)	Complex Dielectric Constant ε_r'	Complex Dielectric Constant ε_r''	Brine Volume Fraction(V)	Microwave Emissivity ε	Skin Depth δ (cm)	Attenuation Coefficient α (db /m)
Frazil Ice† Bering Sea	10	4.4	0.836	-30	3.12	0.073	0.0039	0.8463	23.11	37.62
				-5	3.88	0.436	0.0445	0.8000	4.32	201.2
Columnar Ice† Bering Sea	10	4.6	0.896	-30	2.93	0.045	0.0041	0.8587	36.33	23.93
				-5	3.26	0.150	0.0465	0.8373	11.5	75.60
Multi-year Ice† Bering Sea	10	0.61	0.771	-30	2.59	0.015	0.0005	0.8823	102.42	8.486
				-5	2.71	0.070	0.0062	0.8736	22.46	38.70
FY1-18* AIDJEX First-year Ice	7.5	7.5 ±0.2	0.91 ±0.03	-24.08	2.99 ±0.07	0.039 ±0.022	0.0164	0.8547	56.4	15.4
				-3.99	3.27 ±0.07	0.322 ±0.022	0.0933	0.8351	7.2	121.3
FY1-19* AIDJEX First-year Ice	7.5	5.5 ±0.2	0.91 ±0.03	-29.37	2.92 ±0.07	0.007 ±0.022	0.0051	0.8594	310.7	2.8
				-3.94	2.98 ±0.07	0.234 ±0.022	0.0692	0.8541	9.4	92.4
FY1-20* AIDJEX First-year Ice	7.5	4.1 ±0.2	0.91 ±0.03	-24.51	3.13 ±0.07	0.021 ±0.022	0.0139	0.8457	107.2	8.1
				-4.06	3.29 ±0.07	0.290 ±0.022	0.0505	0.8343	8.0	108.6
FY1-21* AIDJEX First-year Ice	7.5	4.1 ±0.2	0.91 ±0.03	-24.47	2.92 ±0.07	0.032 ±0.022	0.0082	0.8594	68.0	12.8
				-3.92	2.89 ±0.07	0.297 ±0.022	0.0518	0.8592	7.3	119.0
Nilas Bering Sea∫ (thickness 4 cm)	10	8.31	0.848	-2	9.97	3.72	0.1994	0.5868	0.8241	1055
Grey Ice∫ Bering Sea (data from 0 ~ 10 cm)	10	7.95	0.891	-2	4.74	1.06	0.1908	0.7519	1.973	440.4
Grey-white Ice∫ Bering Sea (data from 0 ~ 10 cm)	10	4.04	0.795	-5	4.00	0.788	0.0409	0.7888	2.435	356.9

† Vant et al. (1974, 1975)

* Vant (1976)

∫ Bogorodsky and Khokhlov (1975)

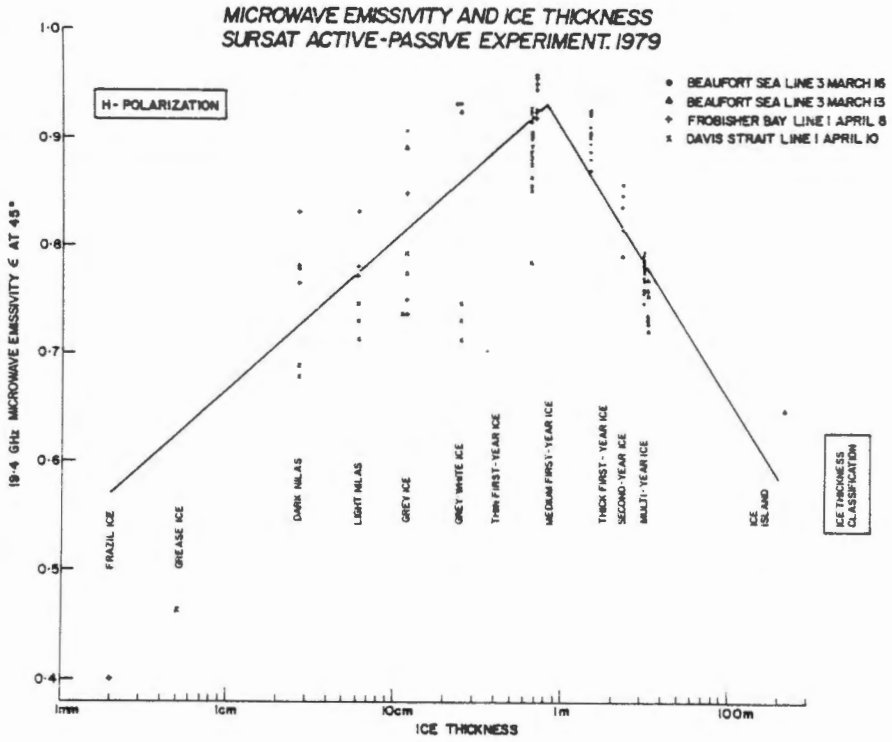

Figure 30. The Relationship Between Emissivity and Ice Thickness.

The ice thickness information presented in this diagram is inferred from the general behaviour of each class and was not measured. Although there is a considerable spread in the data, partly due to variations within each flight line and between lines (marked by different symbols), two trends can be seen. Emissivity increases with the thickness for younger ice forms and decreases with ice thickness for older ice. These general tendencies are indicated by the lines through the data.

$$V = \left(22.8478 + \frac{3.07984 \cdot 10^3}{T} + \frac{1.58402 \cdot 10^5}{T^2} + \frac{3.61615 \cdot 10^6}{T^3} + \frac{3.12862 \cdot 10^7}{T^4}\right) 10^{-3} \cdot S \qquad \left[-37.8 \leq T < -22.9^{\circ}C\right]$$

$$V = \left(14.145 + \frac{1.6426 \cdot 10^3}{T} + \frac{6.4947 \cdot 10^4}{T^2} + \frac{8.3945 \cdot 10^5}{T^3}\right) 10^{-3} \cdot S \qquad \left[-43.2 \leq T < -37.8^{\circ}C\right] \qquad (3)$$

where S is salinity in parts per thousand and T is the temperature measured in $^{\circ}C$. V plays a major role in determining the dielectric properties of sea ice and as such controls the penetration and emission characteristics.

As shown in Table 15, when the temperature is close to the melting condition (-4 to $-5^{\circ}C$) and salinity is high, the calculated brine volume fraction becomes large. This causes the large values of the imaginary part of the dielectric constant and correspondingly small skin depth for new and young ice. From these results and scaling for the frequency dependence, according to (42) of A6.4, the skin depth of ice younger than first-year at 19.35 GHz under melting conditions is estimated to be $<$ 5cm*. Since ice younger than first-year is rather smooth and homogeneous and since most of the emitted microwave radiation originates close to the ice surface, then the increase of emissivity with thickness may be explained qualitatively by the variation of the complex dielectric constant with the brine volume fraction included in the ice, using the Fresnel reflection coefficients as expressed in (32) and (33) in A6.3. When the brine volume is reduced under very cold conditions ($-30^{\circ}C$) the imaginary part of the dielectric constant becomes small and the skin depth becomes large, as shown in Table 15. Under these conditions, not only the radiation from the surface but also the radiation from the inside of the ice must be considered and the physical restrictions required for the Fresnel formulae are no longer satisfied.

The radiation from the inside of ice will be affected by the volume scattering effect. The interior of multi-year ice is porous because of the drainage of brine pockets and these vacancies form scattering sites. For these conditions, the formula by Peake (1959), detailed in Appendix 6.7, equation (9), which relates the microwave emissivity and the bistatic scattering coefficients, could be used to calculate microwave emissivity but it is necessary to assume a theoretical, or empirical, expression of bistatic scattering coefficients to account for the volume scattering effect.

---

* Because there is a maximum of loss tangent of brine around 20 GHz, the skin depth of sea ice at 19.35 GHz may be smaller than this value.

3.5 Discussion of Sea-ice Classification Study Results

Although the data collected for the Active-Passive Experiment cover a wide range of ice types and surface conditions (the polar pack and shear zone in late winter, sheltered bay ice in early spring and eastern marginal pack ice in early spring) and appear to be representative of the regions, seasons and temperatures covered, the data sets are not comprehensive: young ice types were not found in sufficient quantitities in the winter polar pack to be used in the ice classification studies; old ice types were not present in the early spring data sets. Nevertheless, the behaviour of the microwave signatures of ice types common to all regions and seasons measured does provide clues to the expected behaviour of the microwave signatures of the other ice types under other conditions.

Within each of the sea-ice classification data sets, the sea-ice types present can be identified uniquely by three-dimensional microwave signature vectors whose coordinates are ε, σ^o_{hh}, σ^o_{hv}. The relative weighting of each coordinate for ice-type classification is dependent on incidence angle and on the ice surface temperature.

In the data set from the Beaufort Sea where the ice was cold, most of the sea ice present in the scene can be classified in the σ^o_{hh} vs. σ^o_{hv} plane. The σ^o_{hh} provides a uniform separation of ice types; for incidence angles greater than 40° it provides a significant separation of all ice classes except for first-year smooth ice and grey-white ice. The σ^o_{hv} is superior for separating classes and subclasses of first-year and older sea ice but is inferior to σ^o_{hh} for separating grey ice from first-year rough ice. The σ^o_{hh} and σ^o_{hv} together permit unique classification, at all incidence angles, of all sea-ice types in the scene, except first-year smooth ice and grey-white ice. The ε allows the separation of the major sea-ice classes but not the subclasses. When used in conjunction with σ^o_{hh} and σ^o_{hv}, it allows all the sea ice in the scene to be classified by its microwave signature.

The Frobisher Bay ice was warmer than the Beaufort Sea ice, but was colder than the freezing point of sea water. No ice in Frobisher Bay was older than first-year and all ice types show stronger angular dependence than those found in the Beaufort Sea. With the exception of differentiating grease ice and calm water, all ice types present could be classified in the σ^o_{hh}, σ^o_{hv} plane at all incidence angles greater than 20°. σ^o_{hv} is marginally better than σ^o_{hh} for sea-ice classification. The ε is required to identify grease ice and water; when used in conjunction with σ^o_{hh} and σ^o_{hv} it allows each ice type to be classified uniquely.

Sea ice on the Danish W/E line was warmer than that on the Frobisher Bay line by approximately -2^oC. All ice types except grey-white ice, nilas, grey ice and wave-broken first-year ice are separable in the σ^o_{hh}, σ^o_{hv} plane at incidence angles greater than 47°. σ^o_{hv} is marginally better than σ^o_{hh} for ice type identification. All ice types in this data set can be classified using ε alone.

The sea-ice class separability is summarized in Figures 31-36, which have been compiled from selected cluster plot data and in the frontispiece figure, which has been completed from selected statistical data. When the three data sets are compared, it is seen that the microwave signatures for common ice types are not constant. These changes may be related to different roughness and surface conditions arising from a different thermal and mechanical history for the ice. However, because of the significant changes in dielectric properties with temperature, it is also important to examine how the microwave signatures change with temperature.

A comparison of ε between the data sets is given in Table 16. The following observations on the behaviour of ε with temperature may be made from our data:

(1) First-year emissivities show the least change with temperature. Beaufort Sea first-year ice has slightly lower emissivities than Frobisher Bay first-year ice and the Danish W/E line first-year ice emissivity is comparable to Beaufort Sea smooth first-year ice. The lower emissivity of the wave-broken first-year ice may be due to breccia and water between the floes.

(2) Grey-white ice emissivity remains unchanged from the Beaufort Sea and the Frobisher Bay conditions but decreases significantly from the Frobisher Bay line to the Danish W/E line.

(3) Grey ice emissivity decreases significantly from the Beaufort Sea data set to Frobisher Bay data set but is unchanged from the Frobisher Bay data set to the Danish W/E line data set.

(4) Nilas emissivity changes significantly from the Frobisher Bay data set to the Danish W/E line data set.

(5) When the multi-year ice emissivity data from the two Beaufort Sea lines is compared, a consistent difference is seen between the lines; however, this difference is less than the standard deviation of the multi-year ice data set from either line. Since the ambient temperature was different by 3 to 5°C on the days the lines were flown, this could be a temperature effect. An instrumentation drift is improbable and a fully satisfactory explanation of this difference has not been found.

To examine the effects of temperature on the backscattering cross-sections, Figures 37, 38, and 39 were constructed, combining data from this experiment with published σ^{o}_{hh} and σ^{o}_{hv} data (Gray et al., 1977a, b) for examples of ice with similar known ambient temperatures, for 15°, 25° and 45° incidence angles. Variations in backscattering coefficients caused by changes in the instrumentation (the scatterometer was mounted in a DC-3 when the published data was gathered and was mounted in a CV-580 for the Active-Passive Experiment) and a change in the software algorithm

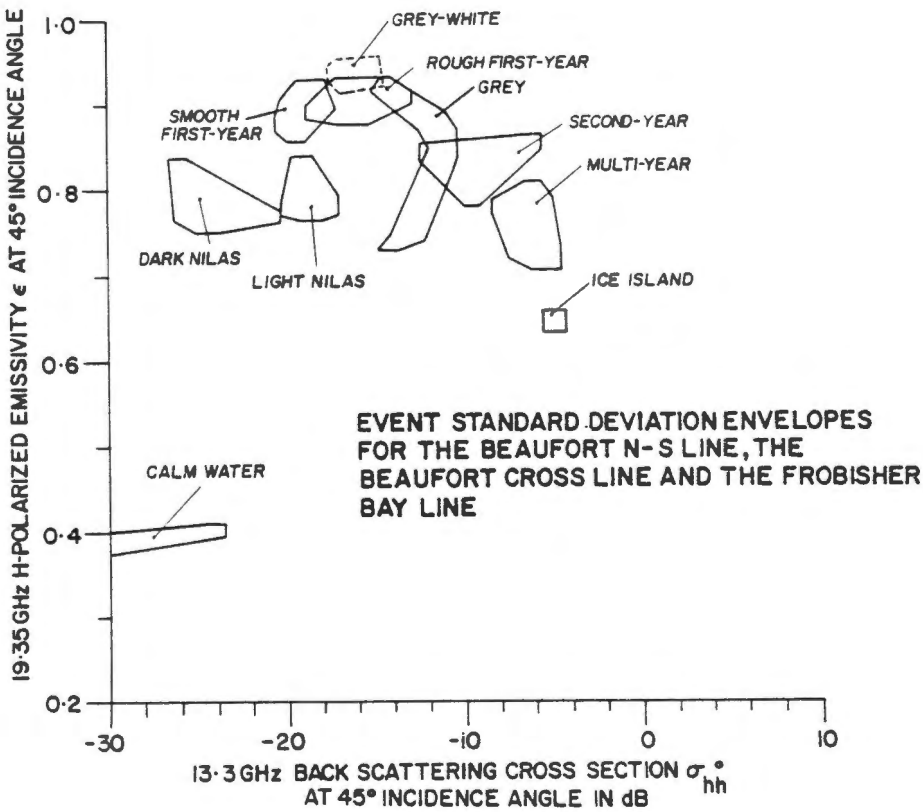

Figure 31. Cluster Envelopes From Ice Classes From the Beaufort Sea and Frobisher Bay Lines Using $\sigma^{o}_{hh}(\theta \simeq 45^{o})$ and ε.

The envelopes show the cluster boundaries for each class and have been constructed from overlays of Figures 12, 13 and 15. The utility of using results from two sensors is evident.

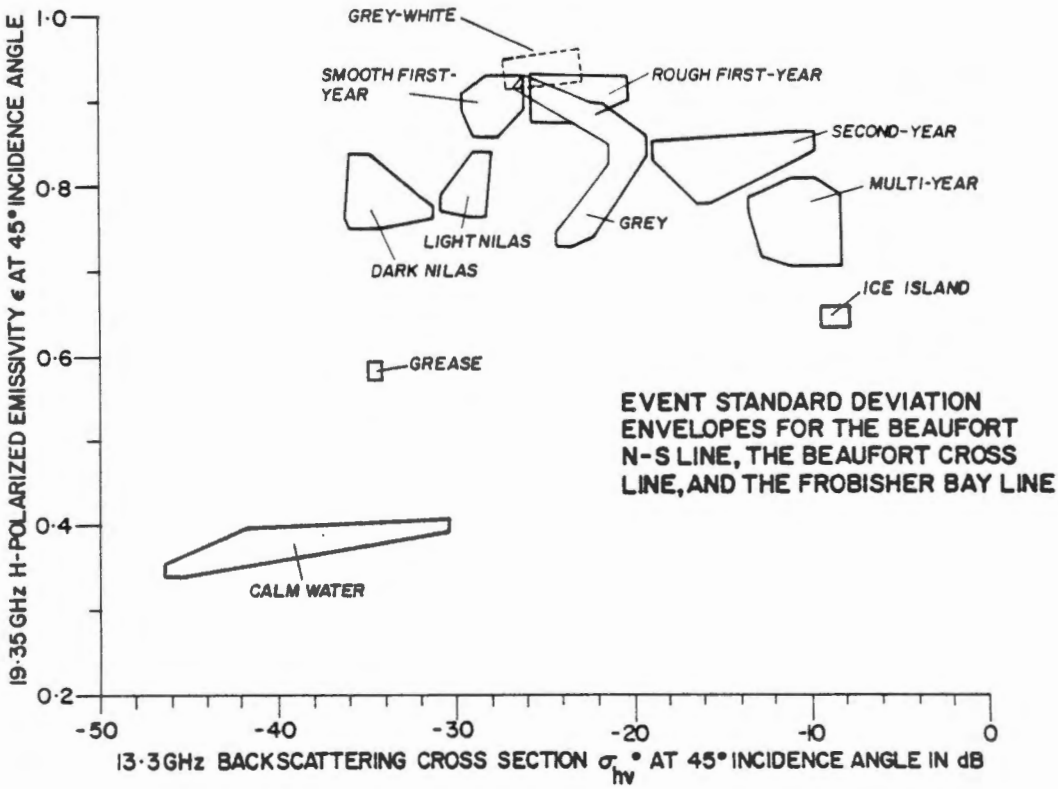

Figure 32. Cluster Envelopes for Ice Classes from the Beaufort Sea and Frobisher Bay Lines Using $\sigma^{o}_{hv}(\theta \simeq 45^{o})$ and ε.

Comparison with Figure 31 shows that HV-polarization has advantages in dividing light and dark nilas, first-year rough and smooth, and grey and second-year ice.

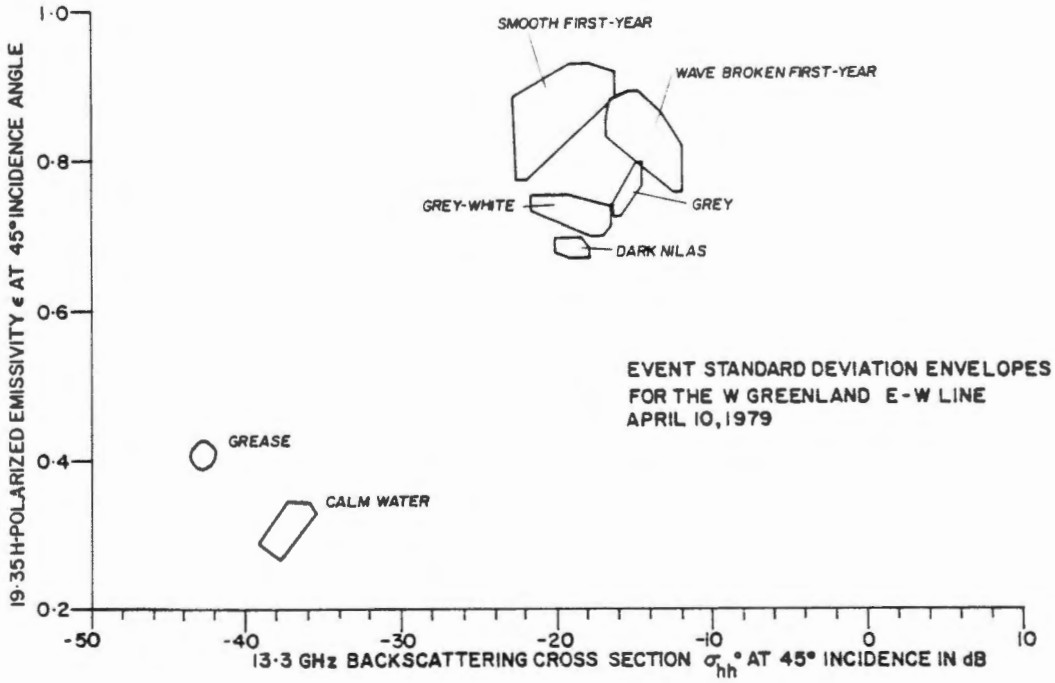

Figure 33. Cluster Envelopes for Ice Classes from the Davis Strait E/W Line Using $\sigma^o_{hh}(\theta \simeq 45^o)$ and ε.

The class envelopes show the cluster boundaries for each class as constructed from Figure 17.

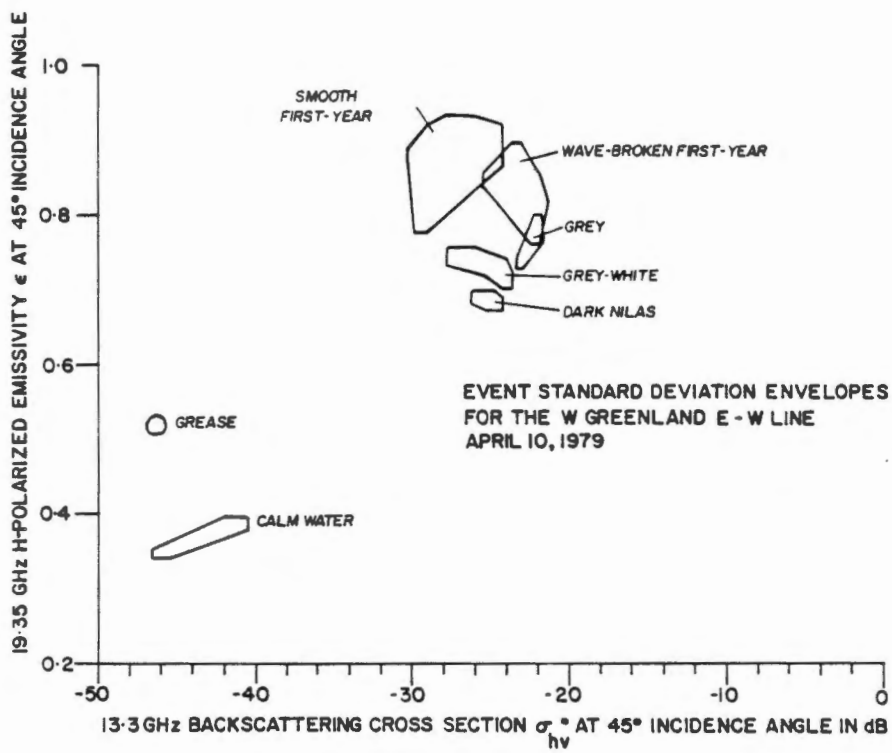

Figure 34. Cluster Envelopes for Ice Classes from the Davis Strait E/W Line Using $\sigma^{o}_{hv}(\theta \simeq 45^{o})$ and ε.

Less cluster overlap may be seen using $\sigma^{o}_{hh}(\theta \simeq 45^{o})$ shown in Figure 33 than is seen in the data of $\sigma^{o}_{hv}(\theta \simeq 45^{o})$ and ε given here.

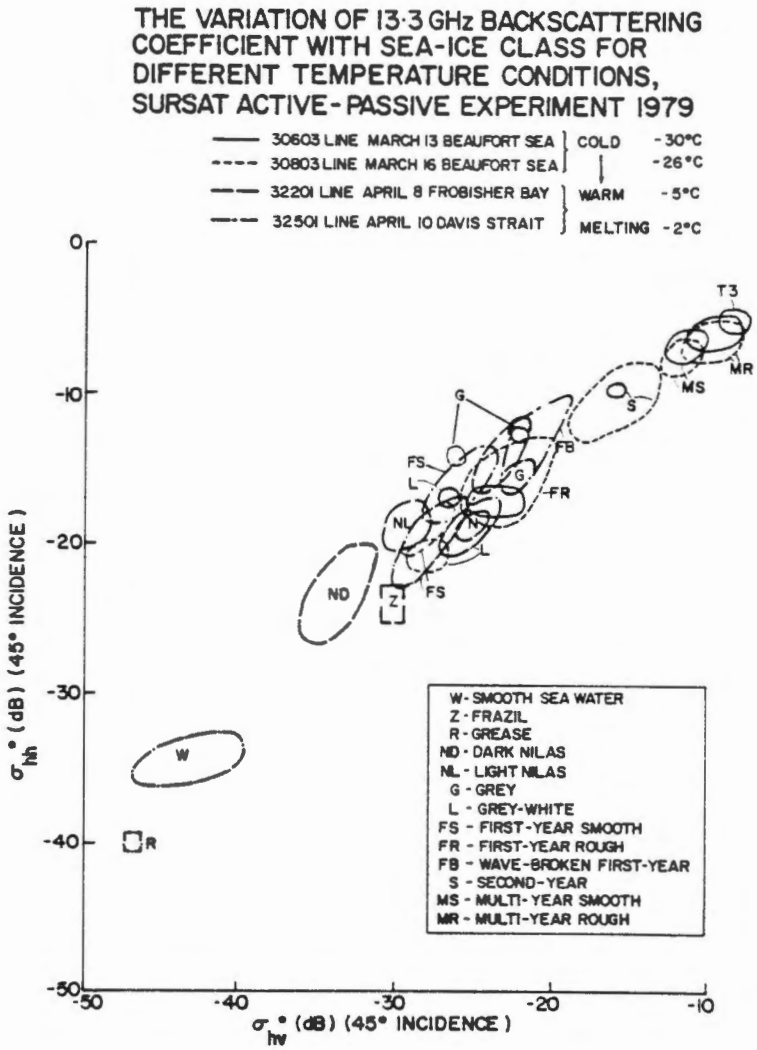

Figure 35. Cluster Envelopes for Sea Ice Class from All Flight Lines showing $\sigma^o_{hh}(\theta \simeq 45^o)$ and $\sigma^o_{hv}(\theta \simeq 45^o)$.

Data envelopes from each line are shown with differing line types as indicated. The central portion of this diagram is a tangle of ice classes. Much of the class confusion may be removed by concentrating on the isotherms represented by each flight line.

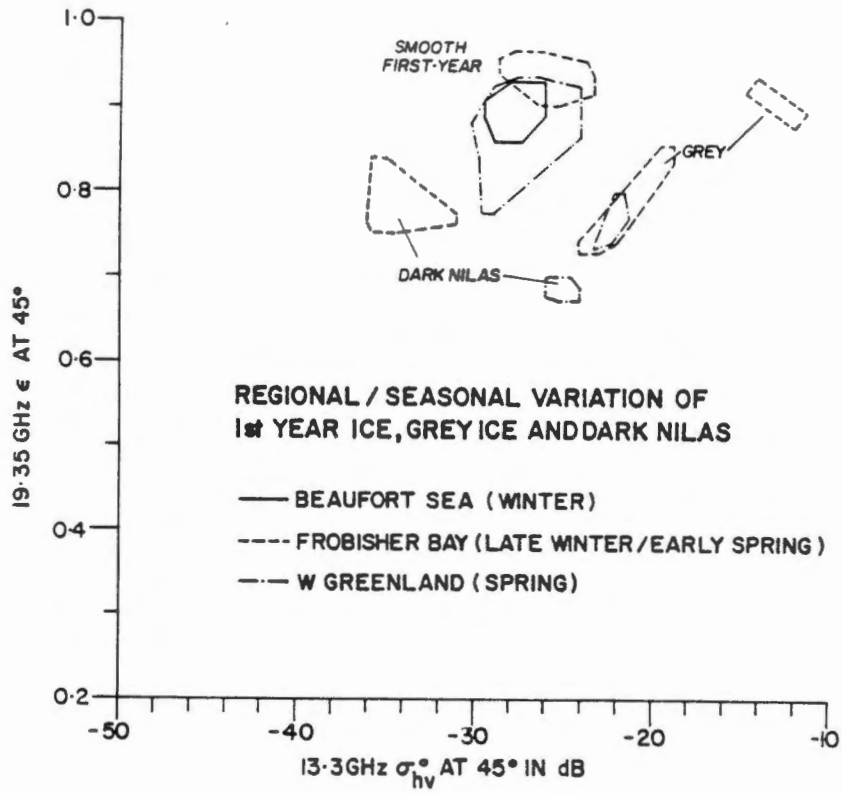

Figure 36. Cluster Envelopes of $\sigma^{\circ}_{hv}(\theta \simeq 45^{\circ})$ and ε Showing the Effect of Temperature and Season on First-year, Grey and Nilas Ice.

This figure brings together common classes from Figures 32 and 34. No common systematic change is present for all classes. They do however remain separated from one another under all conditions.

Table 16. The Variation of Measured Emissivity with Region and Temperature

Ice Class	Ambient Temperatures (^{o}C)	Region	Emissivity (ε)
FY* - rough	-30	Beaufort Sea	0.91 ± 0.02
- smooth	-30	Beaufort Sea	0.90 ± 0.02
- smooth	-5	Frobisher Bay	0.94 ± 0.02
- smooth	-2	Davis Strait	0.90 ± 0.03
- wave-broken	-5	Davis Strait	0.85 ± 0.04
Gray-white	-30	Beaufort Sea	0.90 ± 0.02
	-5	Frobisher Bay	0.93 ± 0.02
	-2	Davis Strait	0.74 ± 0.03
Grey	-30	Beaufort Sea	0.09 ± 0.02
	-5	Frobisher Bay	0.77 ± 0.05
	-2	Davis Strait	0.78 ± 0.03
Nilas - light	-5	Frobisher Bay	0.78 ± 0.03
- light	-2	Davis Strait	0.69 ± 0.02
- dark	-5	Frobisher Bay	0.78 ± 0.03

* First-year

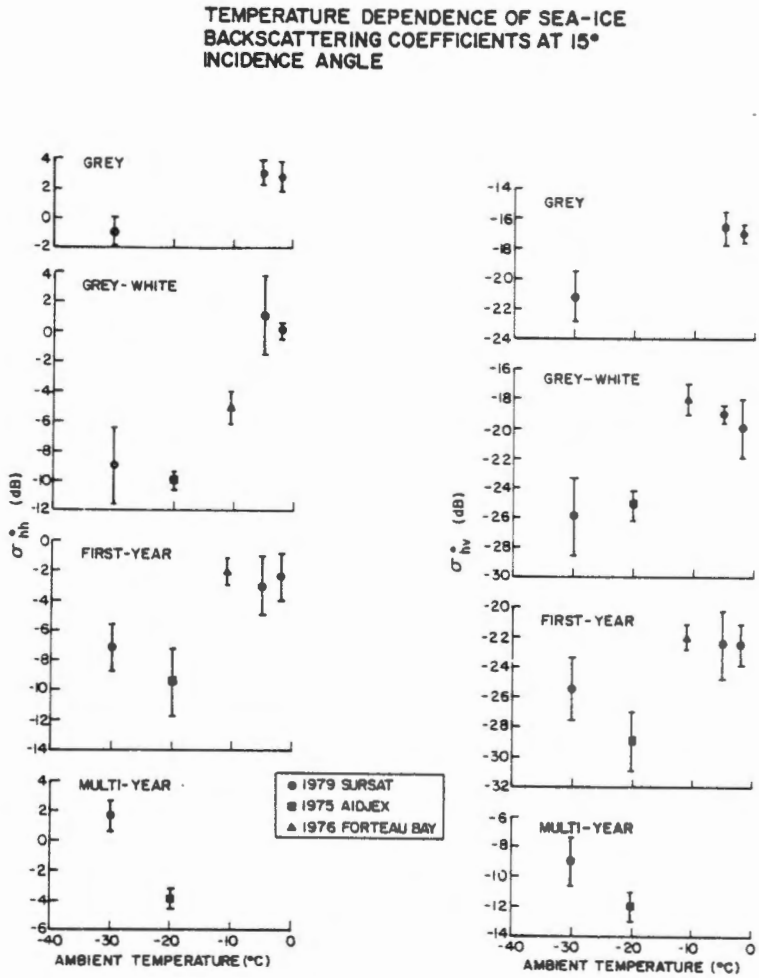

Figure 37. Temperature Dependence of $\sigma^{o}_{hh}(\theta \simeq 15^{o})$ and $\sigma^{o}_{hv}(\theta \simeq 15^{o})$ for Grey, Grey-white, First-year and Multi-year Ice.

Data shown are taken from three different experiments. Except for multi-year ice, there is a general increase in backscattering coefficient with increase in temperature. A minimum in the data, near $-20^{o}C$ is indicated by the AIDJEX result. Whether this is a real effect or due to some systematic difference in the instruments needs verification. This may also account for the variation of multi-year ice with temperature.

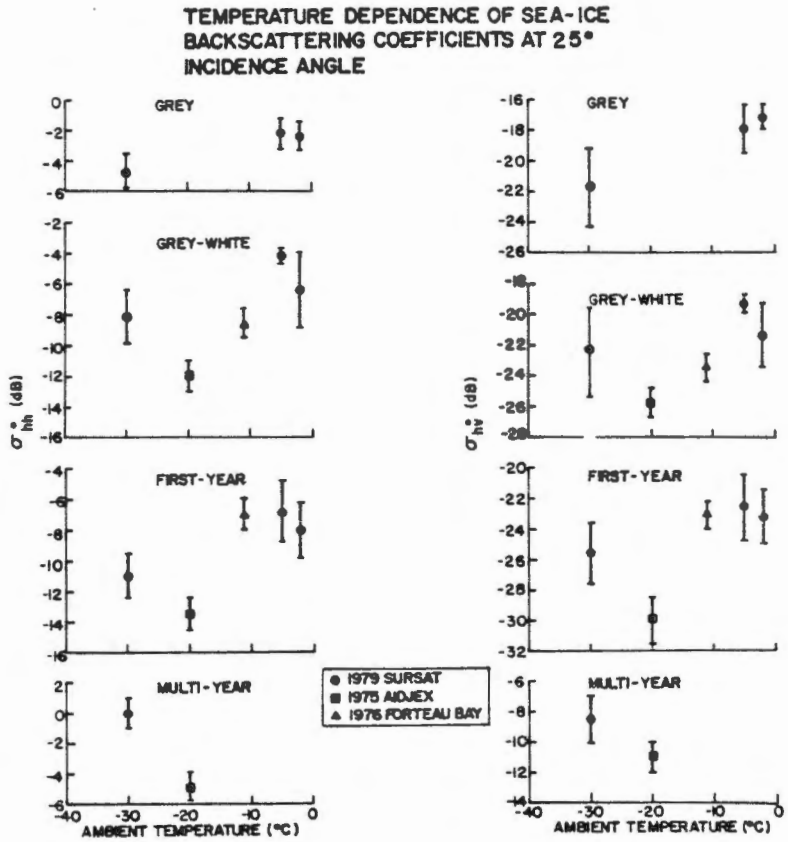

Figure 38. Temperature Dependence of $\sigma^{o}_{hh}(\theta \simeq 25^{o})$ and $\sigma^{o}_{hv}(\theta \simeq 25^{o})$ for Grey, Grey-white, First-year and Multi-year Ice.

Similar effects may be seen in this diagram to Figures 37 and 36.

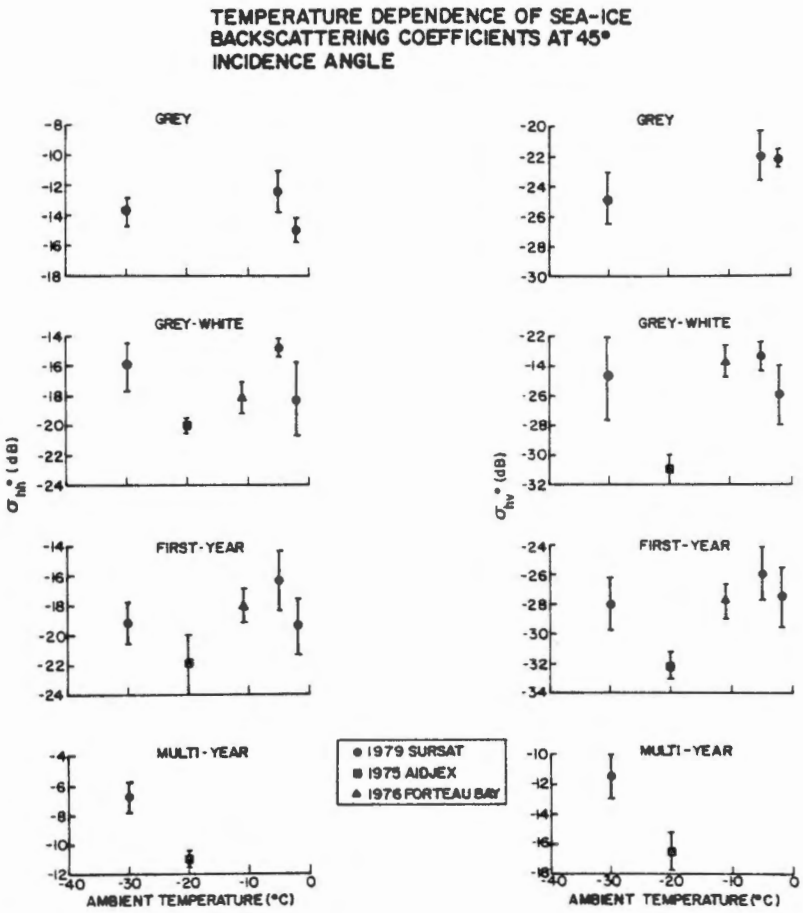

Figure 39. Temperature Dependence of $\sigma^{o}_{hh}(\theta \simeq 45^{o})$ and $\sigma^{o}_{hv}(\theta \simeq 45^{o})$ for Grey, Grey-white, First-year and Multi-year Ice.

The general comments of the caption of Figures 37 and 38 apply to this figure also.

make this comparison somewhat tenuous. The use of ambient temperature instead of ice surface temperature in Figures 37, 38, and 39 was limited by the availability of data and introduces unknown uncertainties along the temperature axis. Each of the data sets was collected under relatively stable (over several days) thermal conditions and thus the ambient temperature is felt to be a usable, if indirect, variable for demonstrating thermal effects.

Figures 37, 38 and 39 show steeper slopes in the σ^o vs. θ plane as the temperature increases from -30°C to -2°C, as expected from the observations in Section 3.3. The plotted results, however, do not show monotonic behaviour with temperature for any of the ice types. As the temperature of first-year ice increases from -30°C to -10°C, a local minimum is observed in both σ^o_{hh} and σ^o_{hv} near -20°C; as the temperature increases from -20°C to -2°C a local maximum is observed in both σ^o_{hh} and σ^o_{hv} between -10°C and -5°C. The minimum near -20°C may be fallacious because all the AIDJEX data is systematically lower than the SURSAT data and this probably arises from the bias introduced by the software changes.

The local maximum of σ^o_{hh}, found in Figures 37, 38 and 39 in the vicinity of -5°C, may be related to the onset of significant surface moisture. The increase in both slope and nadir return with increasing temperature (seen in Figures 23 and 24 for $\sigma^o_{hh}(\theta)$ is compatible with decreasing skin depth, increasing near-surface brine volume and decreasing brine concentration. This effect is largest from -5°C (Frobisher Bay data set) to -2°C (Danish W/E data set), as expected from the increase in surface moisture visible on the Danish W/E line, where in many cases the ice surface was quite wet.

As the ice ages further to form first-year ice on the Frobisher Bay line, a large change occurs in both the angular dependence of σ^o and the nadir intercept. It is noted that the change in both specularity and nadir intercept from grey-white ice to first-year ice is larger at -5°C than it is at -2°C, as expected from the degree of ice surface saturation visible in the two data sets (Frobisher Bay and the Danish W/E line).

3.6 Discussion of Ice Features Study Results

Two classes of floating ice features were selected for study in the Active-Passive Experiment: sea-ice ridges in the Beaufort Sea and icebergs in off West Greenland. The results in this section are biased by the event selection procedures, to concentrate on the widest ridges (with the greatest radar brightness in a background of well defined ice type, and the largest available icebergs (those with 'in beam' dimensions substantially greater than one scatterometer footprint).

3.6.1 Sea-ice ridges in the Beaufort Sea in winter

Detailed examination of the Beaufort Sea photography revealed that there were 173 sea-ice ridges (of all sizes and types) on the Beaufort Sea 030603 Cross line and 513 sea-ice ridges (of all sizes and types) on the Beaufort Sea 030803 N/S line. Of these totals, 16 ridges from the 030603 line and 22 ridges from the 030803 line were suitable for detailed study (5.5% of all ridges). Table 17 summarizes the characteristics of the selected ridges.

Table 17. Characteristics of the Beaufort Sea Ice Ridges Used in the Ice Features Study.

Event Number	Ridge Height (m)	Ridge Width (m)	Orientation to Track (°)	Ridge Type	Ridge Width on SAR Image (mm)	Comments
NS line						
30803.R01	4.8	17.9	100	Multi-year	0.2	High ridges in multi-year event 59
.R02	0.5	4.5	110	First-year	0.1	Small smooth ridge in first-year event 71
.R03	0.7	13.0	110	Multi-year	0.1	Ridge within multi-year floe event 72
.R04	2.9	17.9	40	First-year	0.15	Rough first-year ice event 88
.R05	2.4	9.9	115	Multi-year	0.2	In event 94
.R06	1.0	5.4	255	Second-year	0.1	In event 173
.R07	1.5	13.5	250	First-year	0.05	Old first-year ice event 186
.R08	1.3	7.3	90	Second-year	0.1	In event 202
.R09	2.2	9.11	90	First-year	0.1	In event 210
.R10	0.7	13.7	90	Multi-year	0.1	In event 228
.R11	0.7	13.7		First-year	0.05	In event 233
.R40	1.0	10.2	0	First-year	0.15	Crosses event 189
.R51	1.2	13.7	0	First-year		Ridge and large blocks, crosses an old first-year ridge
.R42	2.6	17.9	120	First-year	0.2	Knob in event 205
.R43	1.6	9.0	0	First-year	0.05	Crosses event 210
.R44	2.9	15.0	0	First-year	0.2	Rough first-year bordering multi-year floe
.R45	1.9	20.0	90	First-year	0.1	Very rough event 91
.R46	0.8	22.5	20	First-year	0.2	
.R55	1.9	22.5	0	First-year	0.05	Ridge in smooth first-year event 172
.R56	0.2	9.0	20	First-year	0.05	Ridge in smooth first-year ice
.R62	3.4	20.3	135	Multi-year		In event 94
.R63	2.6 2.6	15.7 11.2	95	Multi-year		In event 98, double ridge 22.5 m separation
Cross Line						
30603.R1	1.0	9.6	90	Multi-year	N/A*	In event 02
.R2	0.6	1.9	62	First-year		Very small ridge in event 03
.R3	N/A	7.2	85	Multi-year		Floe edge ridge on multi-year event bordering 03
.R4	2.3	24.0	90	First-year		New first-year ridge on edge of multi-year floe event 18 large blocks visible
.R5	2.5	14.4	0	Multi-year		In event 18
.R6	1.3	4.8	120	Multi-year		In event 44
.R7	1.3	8.0	135	Multi-year		In event 48, very rough multi-year
.R8	1.6	12.0	100	Multi-year		In event 53, rough multi-year
.R9	1.6	57.5	90	Multi-year		Old multi-year ridge on T3 edge
.R10	1.1	9.6	125	Ice island		T3 structure
.R11	1.0	11.0	90	Multi-year		Old multi-year on T3 edge in event 67
.R16	0.6	20.3	120	First-year		Edge on event 78
.R17	0.5	2.4	120	Grey-white		Event 79
.R04	1.2	7.2	85	First-year		First-year ice multi-year floe boundary
.R05	2.7	14.3	0.9	First-year		Large knob on first-year/multi-year broken boundary, event 45
.R06	1.0	4.6	150	Multi-year		In event 53, rough multi-year near R8

N/A Not available

First-year ridge widths in this group varied from 1.9m to 24m, with an average of 16m and multi-year ridges give widths ranging from 4.6m to 57m, with an average of 15m. Ridge heights were estimated from shadow lengths and range from 0.5m to 2.9m, averaging 1.5m for first-year and range from 0.7m to 4.8m, averaging 1.5m, for multi-year.

3.6.1.1 Scatterometer measurements of ridge contrasts

The ridge events were divided into categories by ridge and background ice class. Scatterometer data were used to estimate the backscattering coefficient of the ridge and average background ice and to calculate ridge contrast or signal-to-clutter ratio. Typical ridge contrasts are shown for σ^o_{hh} and σ^o_{hv} in Figure 40a, b for first-year ridges in a first-year background and in Figure 41 for multi-year ridges in a multi-year background.

In Figure 40a, b it is seen that the ridge contrasts for first-year ridges in first-year ice span a large range (σ^o_{hh} ~12 dB, σ^o_{hv} ~18 dB) and that the largest contrasts are found at incidence angles greater than 25° for σ^o_{hh} and greater than 15° for σ^o_{hv}. At incidence angles between 35° and 60° the ridge backscatter falls with angle at the same rate as that of the background ice. Some ridge contrast enhancement is seen between 8° incidence angle and 25° incidence angle but the very large ridge enhancements characteristic of side-looking airborne radar (SLAR) imagery are not found in this data until the incidence angle exceeds 80°. This was confirmed by a comparison of shallow depression angle SAR imagery, $\theta <$ 80°, with some super-shallow depression angle SAR imagery, < 88°, obtained over the Beaufort Sea cross line (line G marked on Figure 1).

A comparison of the like- and cross-polarized ridge contrasts from Figure 40a, b shows that cross-polarized radars are generally better suited for ridge detection than like-polarized radars at incidence angles less than 60°. At best, the cross-polarized ridge contrasts are 7 dB larger than the like-polarized ridge contrasts and, at worst, they are equal to the like-polarized contrasts.

In Figure 41a, b, it is seen that the ridge contrasts for multi-year ridges in multi-year ice span a much smaller range than first-year ridges in first-year ice. Over the incidence angle range 8° to 60° there is no clearly preferred incidence angle for multi-year ridge measurements. Cross-polarized ridge contrasts are larger by 2 to 3 dB than corresponding like-polarized results.

As well as examining ridge signal-to-clutter ratios for ridges wide enough to fill a scatterometer footprint completely, part of this study addressed the problem of the measurement of ridges which were narrower than one scatterometer resolution cell. To provide a quantitative measure of the effects of nonbeam-filling conditions, the following mixing formula was used:

$$\sigma_{\text{ridge}} \simeq \left(\frac{L_s}{L_R}\right) \sigma_R - \left(\frac{L_s - L_R}{L_R}\right) \bar{\sigma}_I$$

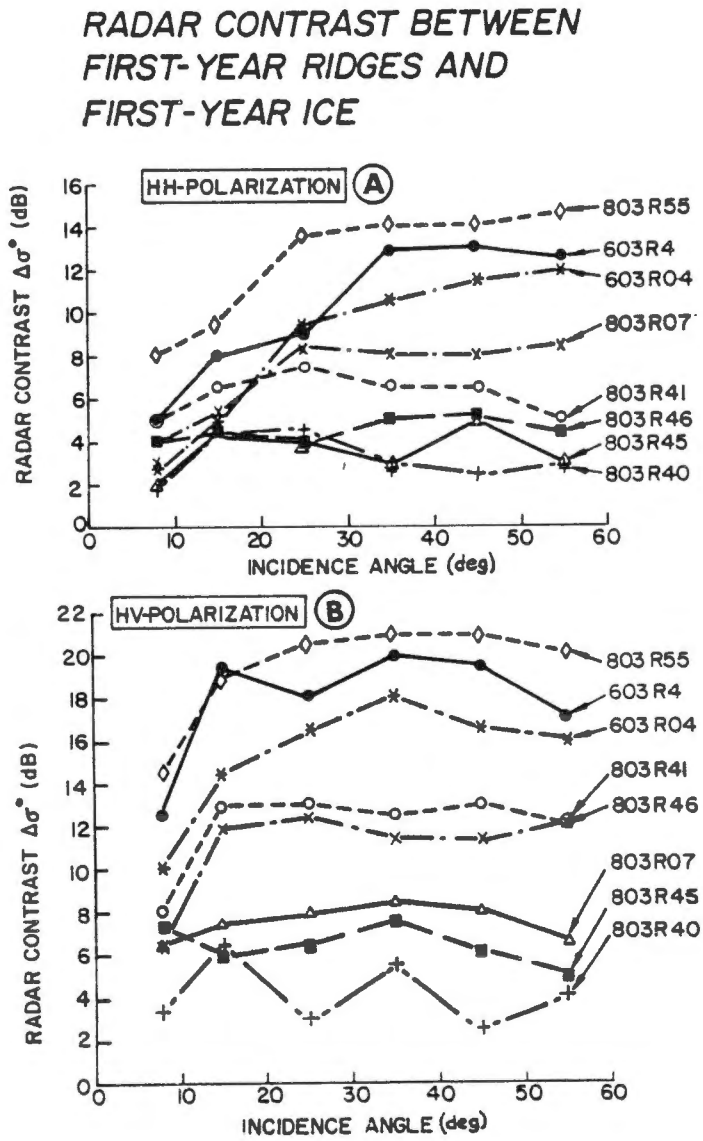

Figure 40. Radar Contrast between First-year Pressure Ridges and Surrounding First-year Ice.

Ridge contrasts are shown for selected ridges crossed by the scatterometer track and are indexed by their 'event' number. Increasing ridge contrast may be seen in both HH- and HV-polarizations up to incidence angles of 20°. For incidence angles in the range 20-60°, no significant change in radar contrast occurs. Generally HV-polarization yields greater contrast than HH-polarization by 2-6 dB.

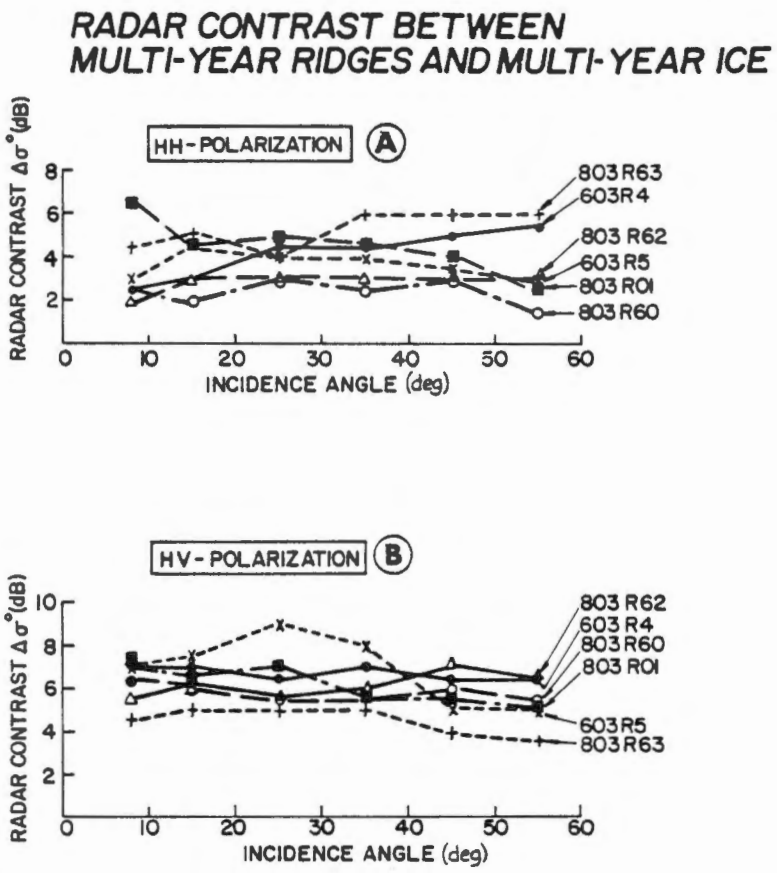

Figure 41. Radar Contrast between Multi-year Pressure Ridges and Surrounding Multi-year Ice.

Unlike the first-year results displayed in Figure 40, multi-year ridges show no incidence dependence in their radar contrast with surrounding multi-year ice in the range 0-20°. Approximately 2dB contrast advantage may be seen with HV-polarization over HH-polarization.

where: L_s is the length of the scatterometer footprint along track,

L_R is the ridge width along track,

σ_R is the average backscattering coefficient for the footprint containing the ridge,

$\bar{\sigma}_i$ is the mean value of the background ice backscattering coefficient.

The scaled ridge backscattering cross sections were compared with those from beam-filling ridges in ice having similar scattering characteristics to the ice containing the narrower ridge. The mixing formula gave reasonable results for ridges whose widths were greater than, or equal to, one half of the scatterometer footprint length (ridge widths $\geq$ 9m) and gave erratic results for ridges narrower than one third of the scatterometer footprint (ridge widths $\leq$ 6m). The scaling also fails utterly for small ridges when the magnitude of the ridge portion of the composite backscattering cross section approaches the radar texture of the background ice (Section 3). Some successfully scaled ridge contrasts are included in Figures 40a, b and 41a, b.

In Figure 42 radar contrasts are shown as a function of incidence angle between first-year ridges formed on the border of multi-year floes. The background used in this case is multi-year, while the ridges themselves are first-year. It can be seen that, on average, first-year ridges have radar cross sections 1-2 dB below the adjacent multi-year ice for these incidence angles, for both HV and HH polarizations.

The brightest observed first-year ridge (3.5 standard deviations above the first-year ridge mean return) has a backscattering cross section comparable to a bright multi-year ridge at all incidence angles.

3.6.1.2 SAR measurements of sea-ice ridges

A limited amount of SAR data has been analysed digitally to obtain SAR measurements of sea-ice ridge parameters. Specifically, this consisted of a 750m wide by 20km long strip of one SAR scene, near the polar pack edge (profiling sensor line events 135 to 190) in the March 18, 1979 HH-polarized SAR imagery of the Beaufort N/S line. The original photographic SAR imagery provided to the SURSAT office was digitized to 15m resolution using the CCRS scanning microdensitometer*. The resulting data could be used for relative measurements of ice type and ice feature brightness, at constant incidence angle, but was not corrected for antenna pattern or range losses and was not calibrated in absolute intensity.

Figure 43 displays the digitized scene as reconstructed on the CCRS CIAS and photographed from the display. The strip shown in Figure 43 is in four segments arranged sequentially from south to north, starting at the top left hand corner of the figure. The lower edge of each strip is at 71.7° incidence angle and the upper edge is at 74.9° incidence angle;

---

* We are grateful to Dr. R.T. Lowry of Intera for initiating this work and his guidance in the analysis.

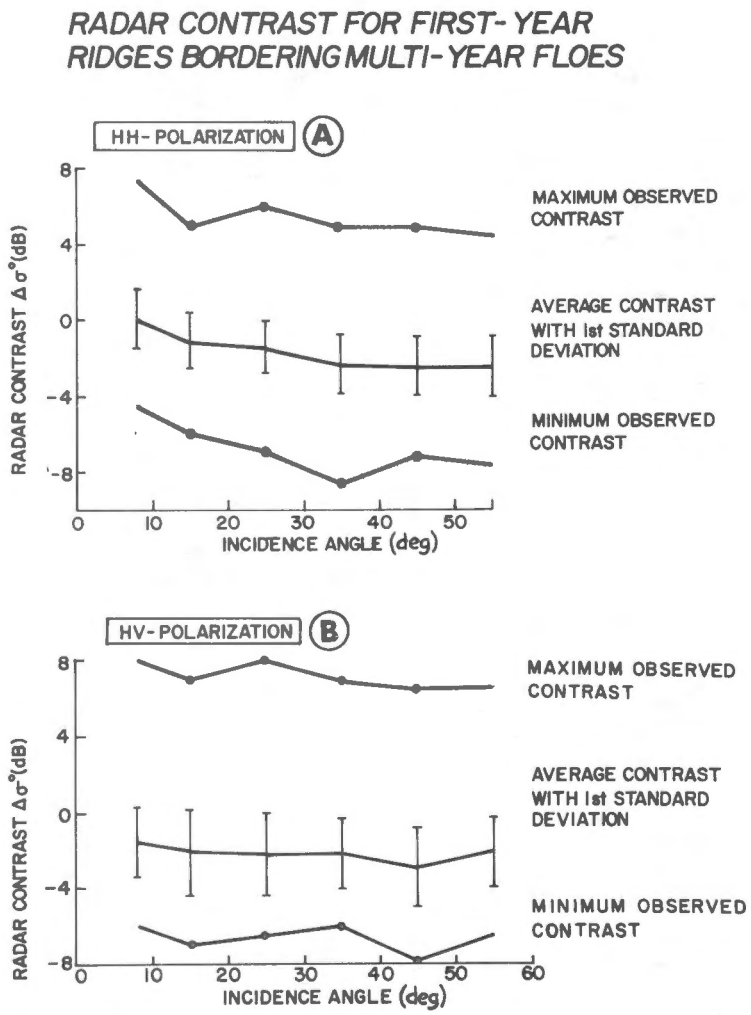

Figure 42. Radar Contrast between First-year Pressure Ridges Bordering Multi-year Floes.

In this case, unlike Figures 40 and 41, radar contrast is shown between ridged ice of one class (first-year) and a surrounding ice of another class. Although in some cases ridges showed positive contrasts of 6 dB seen in the the results, equally great negative contrasts were also seen and the average contrast was ~-2 dB with either polarization. Detection of these ridges is therefore difficult.

INCIDENCE ANGLE

74.9°

1

71.7°

74.9°

2

71.7°

74.9°

3

71.9°

74.9°

4

71.7°

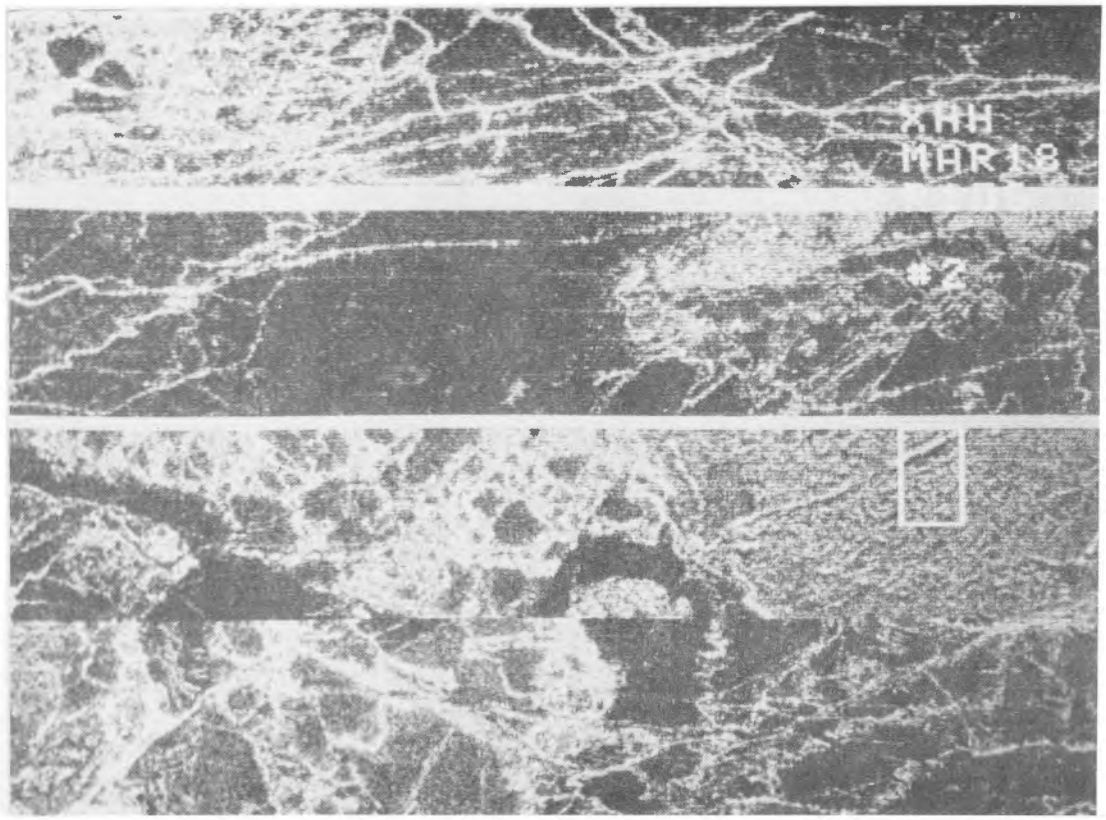

Figure 43. Photograph of Digitized X-band SAR Imagery.

The segment is taken from the March 18, steep depression, HH-polarization results. The highlighted area, depicted digitally in Figure 44, shows a ridge in a multi-year floe. The data runs sequentially from south to north (left to right and top to bottom along the flight line) and contains frames 105 to 106 of the SAR processor output.

thus none of the data can be calibrated directly by the scatterometer (incidence angle range 0° to 60°).

The white rectangle within the large multi-year floe in Figure 43 designates the area displayed as numeric maps in Figure 44 and 45. On these figures, the numbers are the relative SAR image intensity on a scale of 1 to 256 intensity units (the smallest numbers are the brightest pixels) as normalized to the dynamic range of the digitized strip. Horizontal (along track) scales have been increased by a factor of 2.75 in the tabular format.

Figure 44 emphasizes the bright multi-year ridge visible in Figure 43, with brightness contours at the 80, 40, 20 and 10 brightness index intervals. The overall scene has an average brightness of 119 brightness units, a maximum brightness of 4 units and a minimum brightness of 188 units. The ridge has an average brightness of 43.0 units, a maximum brightness of 4 units and a minimum brightness of 80 units. An estimate may be made of the variability of multi-year ridge average ice backscattering cross-section ratios, as observed by profiling sensors, by choosing various sections through the ridge. For the data of Figure 44, the largest observable ridge-to-ice contrast is 14.7 dB, the smallest observable ridge-to-ice contrast ratio is 1.91 dB and the average ridge-to-background ice contrast is 4.4 dB. Local contrasts are, of course, larger than this since the average background ice, backscattering cross-section combines all radar textural features of the ice as illustrated in Figure 45 by the same set of brightness unit contrast contours.

The effect of increasing the size of the radar resolution cell can be estimated from Figure 45, by averaging over an appropriate number of adjacent 15m x 15m pixels. A decrease in resolution to 30m x 30m results in a significant decrease in ridge contrast and a decrease in resolution to 90m x 90m eliminates almost all the textural information from the scene, with the exception of the ridge which is still visible locally.

Figure 46 shows the same radar scene as Figure 43 with a different portion of the same multi-year floe designated for detailed examination (Figures 47 and 48). Two ridges are visible in Figure 47, neither of which is as bright as that seen in Figure 44. In Figures 47 and 48, a different contour interval has been selected (100, 50, 25 brightness units) to emphasize the ridge structure. In this case, the 100 brightness unit contour was chosen, being the midpoint of the scene dynamic range (192 to 8 units). Although portions of the two ridges seen in Figure 47 are brighter than any other textural elements in the scene, the ridges are primarily recognizable by the geometric persistence of their local contrasts.

In Figure 49a, the scene designated by the white rectangle contains a ridge in relatively smooth first-year ice. Figures 49b and 49c are four times enlargements of the same region, designating subsections of the first scene for detailed examination. Figures 50 to 52 are the corresponding numerical maps (again in brightness units) contoured at intervals of 160, 80, 40, 20 brightness units. When Figure 51 is compared with Figures 45 and 48 it is evident that:

122	131	144	81	92	134	105	139	96	111	92	86	65	38	69	114	132	94	102	108	141	108	110	130	52	62	38	12	21	14
122	131	144	81	92	134	105	139	96	111	92	86	65	38	69	114	132	94	102	108	141	108	110	130	52	62	38	12	21	14
131	79	152	137	135	136	102	101	87	68	81	89	95	113	89	149	179	120	71	60	134	124	93	75	24	32	65	51	49	70
54	69	70	72	133	132	86	73	96	45	83	69	108	80	116	155	158	88	82	126	154	131	46	28	27	34	55	132	106	146
10	24	36	41	75	152	124	80	120	58	88	152	153	153	151	113	86	73	87	79	51	77	51	33	72	109	145	158	152	158
59	44	55	128	148	144	124	85	112	75	87	95	174	134	145	101	87	46	16	23	22	115	121	111	139	162	158	138	140	171
153	147	168	119	102	138	93	79	131	127	162	160	121	111	72	23	39	7	13	51	89	153	176	166	147	111	102	125	164	151
166	141	136	104	68	103	156	140	153	155	116	111	65	28	41	8	4	20	72	103	137	158	146	140	167	144	117	138	148	111
53	89	88	148	115	152	177	150	149	137	99	95	45	20	16	23	41	94	167	180	171	107	89	91	132	139	138	131	106	68
95	101	109	117	125	155	134	114	85	64	56	31	13	15	31	105	145	165	174	176	159	114	105	104	111	115	86	145	143	114
148	128	146	142	71	110	124	41	27	20	16	9	13	78	133	158	170	166	179	178	141	125	150	171	93	29	74	100	90	87
153	137	77	84	47	61	58	37	46	26	26	65	98	147	187	161	186	177	149	145	128	151	144	142	85	63	98	82	43	37
103	98	37	40	15	16	50	59	122	55	96	149	170	155	179	185	172	157	146	119	146	141	121	69	53	74	67	92	105	52
88	35	16	6	15	52	93	125	176	138	158	171	171	172	184	175	176	165	148	124	152	154	108	46	73	49	88	172	164	130
37	26	41	33	98	135	156	170	177	178	172	187	171	156	104	143	172	138	91	69	117	89	55	112	98	121	166	151	147	139
19	32	65	69	148	158	151	152	140	129	136	132	126	83	48	70	90	67	34	25	41	81	55	104	99	77	84	69	98	120
61	80	144	137	158	144	159	142	127	140	133	143	137	107	91	42	76	82	56	72	100	117	103	168	131	120	50	79	91	74
145	149	181	168	158	173	150	134	140	136	184	146	112	106	112	125	77	98	135	141	143	179	150	128	75	110	95	94	108	73
147	183	172	174	145	91	125	148	168	145	151	119	93	98	144	80	74	75	117	98	123	128	122	76	62	126	89	71	114	99
188	162	134	114	30	39	80	162	97	97	72	36	57	65	121	123	143	142	135	140	125	134	102	52	76	79	82	66	57	73
136	107	122	111	92	41	70	45	63	30	33	43	109	102	93	71	84	63	127	101	57	112	134	70	43	59	88	120	94	46
106	108	128	110	105	73	71	58	54	133	140	153	160	153	139	136	72	32	50	49	106	101	95	124	59	42	71	157	99	108
115	153	82	46	54	86	100	118	140	169	145	140	132	151	156	138	87	34	39	104	65	106	121	137	106	82	146	121	168	145
182	148	107	101	108	132	121	158	110	87	75	63	27	59	74	114	87	94	85	113	144	130	90	146	118	86	82	63	123	156
157	105	118	155	146	128	85	87	47	78	58	64	73	54	85	40	95	118	163	155	129	61	54	92	67	69	32	25	108	165
96	49	125	136	126	81	129	135	146	127	135	86	103	116	122	90	118	99	104	89	97	83	138	68	103	159	80	103	46	98
85	87	89	63	105	103	150	158	142	92	72	25	90	152	121	94	151	152	111	71	72	94	125	90	88	93	71	138	129	74
64	97	111	88	91	43	91	97	47	49	109	141	132	148	151	131	144	116	152	109	116	125	69	92	104	117	161	156	136	72
153	134	117	113	150	63	133	112	63	109	83	133	81	83	154	37	84	90	138	92	105	141	123	126	53	139	168	163	107	86
122	139	101	107	83	151	159	143	139	62	31	33	40	57	168	111	139	111	79	81	66	66	61	78	124	177	141	101	134	108
90	109	92	161	110	122	119	164	156	105	68	55	73	100	132	83	132	105	73	80	58	27	97	79	90	150	81	86	117	120
135	148	153	154	134	113	75	125	124	112	130	141	150	132	128	54	93	116	91	71	19	46	103	101	137	117	124	96	94	89
129	95	127	86	52	73	119	79	112	115	145	132	107	119	61	49	105	164	172	159	86	152	162	132	148	41	79	113	118	116
116	106	103	60	67	77	95	77	104	76	50	56	106	94	59	79	165	176	139	108	121	125	162	90	99	92	104	114	87	70
133	27	72	69	72	77	120	166	165	132	112	57	104	137	105	94	118	122	169	122	159	113	160	126	107	83	117	128	83	111
138	150	165	145	130	58	108	157	176	152	165	94	122	140	71	44	80	117	100	87	98	136	162	127	81	128	155	141	88	95
88	104	160	159	139	68	114	74	142	111	139	162	92	105	81	90	153	130	107	75	153	144	132	152	114	119	134	107	102	65
112	126	129	155	130	116	92	74	40	86	105	106	87	90	147	94	128	126	136	128	123	97	104	141	109	113	159	110	117	99
109	103	120	124	90	120	136	74	57	52	119	115	102	89	78	68	142	143	110	46	38	79	96	100	106	60	65	125	100	134
142	97	83	102	126	44	99	24	38	100	127	95	100	112	152	137	138	104	65	43	84	58	99	101	117	73	88	108	126	159
130	120	105	125	159	166	174	127	128	133	118	77	115	108	157	76	87	62	68	85	100	89	113	94	66	56	95	100	137	122
145	165	117	134	142	184	165	158	93	87	48	44	108	122	96	58	52	85	50	99	52	50	89	116	119	118	129	118	59	45
174	145	149	83	107	143	138	123	144	167	128	141	117	102	157	120	152	154	141	141	65	68	66	136	143	64	97	110	136	69
168	123	142	60	82	133	79	66	114	162	170	68	104	67	113	113	157	174	170	149	110	137	126	136	178	126	125	165	171	152
94	113	123	142	173	162	158	113	86	149	170	137	110	99	145	72	109	158	166	104	142	174	176	104	108	94	89	134	138	63
103	142	139	178	156	154	109	63	43	86	103	153	157	131	149	58	115	132	131	131	164	163	184	161	137	98	87	148	110	131
61	104	100	140	96	78	86	122	139	53	120	161	116	30	59	52	156	119	144	131	138	146	133	177	135	119	131	145	139	117
79	85	73	169	145	111	136	146	165	131	120	100	66	53	87	91	94	102	115	123	131	99	129	168	119	96	73	117	95	117
70	49	49	123	119	108	136	175	137	180	133	123	118	106	101	105	107	127	77	68	39	48	83	63	100	78	65	129	134	143

Figure 44. Digital Map of a Multi-year Ridge in a Multi-year Ice Background.

Contour intervals of 80, 40, 20, and 10 digital intensity units have been used to highlight the region of the multi-year ridge.

122	131	144	81	92	134	105	139	96	111	92	86	65	38	69	114	132	94	102	108	141	108	110	130	52	62	38	12	21	14
122	131	144	81	92	134	105	139	96	111	92	86	65	38	69	114	132	94	102	108	141	108	110	130	52	62	38	12	21	14
131	79	152	137	135	136	102	101	87	68	81	89	95	113	89	149	179	120	71	60	134	124	93	75	24	32	65	51	49	70
54	69	70	72	133	132	86	73	96	45	83	69	108	80	116	155	158	88	82	126	154	131	46	28	27	34	55	132	106	146
10	24	36	41	75	152	124	80	120	58	88	152	153	153	151	113	86	73	87	79	51	77	51	33	72	109	145	158	152	158
59	44	55	128	148	144	124	85	112	75	87	95	174	134	145	101	87	46	16	23	22	115	121	111	139	162	158	138	140	171
153	147	168	119	102	138	93	79	131	127	162	160	121	111	72	23	39	7	13	51	89	153	176	166	147	111	102	125	164	151
166	141	136	104	68	103	156	140	153	155	116	111	65	28	41	8	4	20	72	103	137	158	146	140	167	144	117	138	148	111
53	89	88	148	115	152	177	150	149	137	99	95	45	20	16	23	41	94	167	180	171	107	89	91	132	139	138	131	106	68
95	101	109	117	125	155	134	114	85	64	56	31	13	15	31	105	145	165	174	176	159	114	105	104	111	115	86	145	143	114
148	128	146	142	71	110	124	41	27	20	16	9	13	78	133	158	170	166	179	178	141	125	150	171	93	29	74	100	90	87
153	137	77	84	47	61	58	37	46	26	26	65	98	147	187	161	186	177	149	145	128	151	144	142	85	63	98	82	43	37
103	98	37	40	15	16	50	59	122	55	96	149	170	155	179	185	172	157	146	119	146	141	121	69	53	74	67	92	105	52
88	35	16	6	15	52	93	125	176	138	158	171	171	172	184	175	176	165	148	124	152	154	108	46	73	49	88	172	164	130
37	26	41	33	98	135	156	170	177	178	172	187	171	156	104	143	172	138	91	69	117	89	55	112	98	121	166	151	147	139
19	32	65	69	148	158	151	152	140	129	136	132	126	83	48	70	90	67	34	25	41	81	55	104	99	77	84	69	98	120
61	80	144	137	158	144	159	142	127	140	133	143	137	107	91	42	76	82	56	72	100	117	103	168	131	120	50	79	91	74
145	149	181	168	158	173	150	134	140	136	184	146	112	106	112	125	77	98	135	141	143	179	150	128	75	110	95	94	108	73
147	183	172	174	145	91	125	148	168	145	151	119	93	98	144	80	74	75	117	98	123	128	122	76	62	126	89	71	114	99
188	162	134	114	30	39	80	162	97	97	72	36	57	65	121	123	143	142	135	140	125	134	102	52	76	79	82	66	57	73
136	107	122	111	92	41	70	45	63	30	33	43	109	102	93	71	84	63	127	101	57	112	134	70	43	59	88	120	94	46
106	108	128	110	105	73	71	58	54	133	140	153	160	153	139	136	72	32	50	49	106	101	95	124	59	42	71	157	99	108
115	153	82	46	54	86	100	118	140	169	145	140	132	151	156	138	87	34	39	104	65	106	121	137	106	82	146	121	168	145
182	148	107	101	108	132	121	158	110	87	75	63	27	59	74	114	87	94	85	113	144	130	90	146	118	86	82	63	123	156
157	105	118	155	146	128	85	87	47	78	58	64	73	54	85	40	95	118	163	155	129	61	54	92	67	69	32	25	108	165
96	49	125	136	126	81	129	135	146	127	135	86	103	116	122	90	118	99	104	89	97	83	138	68	103	159	80	103	46	98
85	87	89	63	105	103	150	158	142	92	72	25	90	152	121	94	151	152	111	71	72	94	125	90	88	93	71	138	129	74
64	97	111	88	91	43	91	97	47	49	109	141	132	148	151	131	144	116	152	109	116	125	69	92	104	117	161	156	136	72
153	134	117	113	150	63	133	112	63	109	83	133	81	83	154	37	84	90	138	92	105	141	123	126	53	139	168	163	107	86
122	139	101	107	83	151	159	143	139	62	31	33	40	57	168	111	139	111	79	81	66	66	61	78	124	177	141	101	134	108
90	109	92	161	110	122	119	164	156	105	68	55	73	100	132	83	132	105	73	80	58	27	97	79	90	150	81	86	117	120
135	148	153	154	134	113	75	125	124	112	130	141	150	132	128	54	93	116	91	71	19	46	103	101	137	117	124	96	94	89
129	95	127	86	52	73	119	79	112	115	145	132	107	119	61	49	105	164	172	159	86	152	162	132	148	41	79	113	118	116
116	106	103	60	67	77	95	77	104	76	50	56	106	94	59	79	165	176	139	108	121	125	162	90	99	92	104	114	87	70
133	27	72	69	72	77	120	166	165	132	112	57	104	137	105	94	118	122	169	122	159	113	160	126	107	83	117	128	83	111
138	150	165	145	130	58	108	157	176	152	165	94	122	140	71	44	80	117	100	87	98	136	162	127	81	128	155	141	88	95
88	104	160	159	139	68	114	74	142	111	139	162	92	105	81	90	153	130	107	75	153	144	132	152	114	119	134	107	102	65
112	126	129	155	130	116	92	74	40	86	105	106	87	90	147	94	128	126	136	128	123	97	104	141	109	113	159	110	117	99
109	103	120	124	90	120	136	74	57	52	119	115	102	89	78	68	142	143	110	46	38	79	96	100	106	60	65	125	100	134
142	97	83	102	126	44	99	24	38	100	127	95	100	112	152	137	138	104	65	43	84	58	99	101	117	73	88	108	126	159
130	120	105	125	159	166	174	127	128	133	118	77	115	108	157	76	87	62	68	85	100	89	113	94	66	56	95	100	137	122
145	165	117	134	142	184	165	158	93	87	48	44	108	122	96	58	52	85	50	99	52	50	89	116	119	118	129	118	59	45
174	145	149	83	107	143	138	123	144	167	128	141	117	102	157	120	152	154	141	141	65	68	66	136	143	64	97	110	136	69
168	123	142	60	82	133	79	66	114	162	170	68	104	67	113	113	157	174	170	149	110	137	126	136	178	126	125	165	171	152
94	113	123	142	173	162	158	113	86	149	170	137	110	99	145	72	109	158	166	104	142	174	176	104	108	94	89	134	138	63
103	142	139	178	156	154	109	63	43	86	103	153	157	131	149	58	115	132	131	131	164	163	184	161	137	98	87	148	110	131
61	104	100	140	96	78	86	122	139	53	120	161	116	30	59	52	156	119	144	131	138	146	133	177	135	119	131	145	139	117
79	85	73	169	145	111	136	146	165	131	120	100	66	53	87	91	94	102	115	123	131	99	129	168	119	96	73	117	95	117
70	49	49	123	119	108	136	175	137	180	133	123	118	106	101	105	107	127	77	68	39	48	83	63	100	78	65	129	134	143

Figure 45. Digital Map of a Scene Showing a Multi-year Ridge Within a Multi-year Floe.

This map shows relative image density for the highlighted area indicated in Figure 43. Small numbers depict large radar backscatter at X-band using HH-polarization. Contour intervals of 80, 40 and 20 are marked. The ridge shown separated in Figure 44, is almost lost in the image texture accented by the contours.

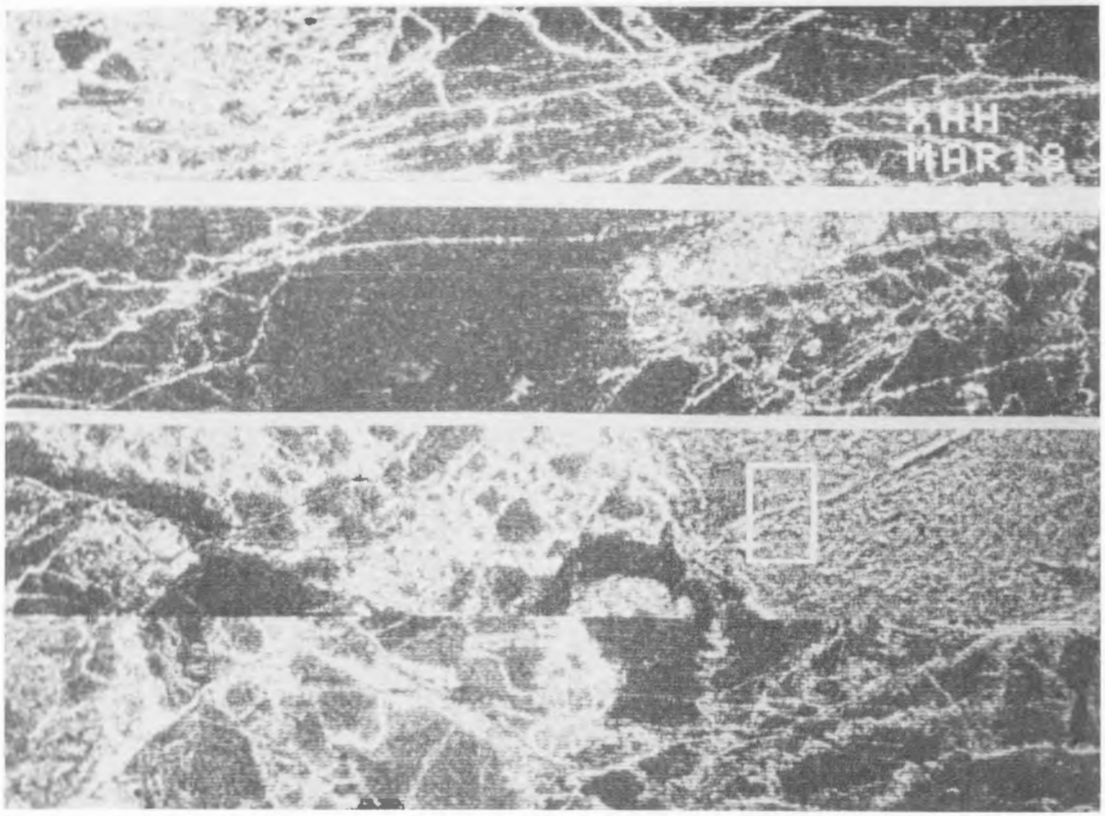

Figure 46. Photograph of Digitized X-Band SAR Imagery

This segment of the data is identical to that shown in Figure 43, but highlights a different segment of the multi-year ridge in the third strip. A digital map of the highlighted segment is given in Figures 47 and 48.

156	149	140	154	172	162	135	147	71	106	71	144	134	142	151	118	150	135	106	112	82	135	154	151	171	109	138	132	102	85
118	96	116	63	133	77	96	74	32	97	93	62	111	98	84	125	115	101	67	69	72	137	118	100	88	113	156	75	126	111
100	108	111	61	89	47	45	93	70	130	129	69	68	63	54	164	92	81	63	97	119	68	87	58	99	133	158	128	105	158
127	106	107	133	156	106	110	73	127	148	151	135	144	144	98	131	125	136	137	114	140	125	119	145	151	106	162	123	137	148
128	81	108	138	161	120	91	130	144	114	98	129	162	118	162	160	136	164	107	109	89	94	132	108	118	52	133	144	149	102
157	126	119	148	120	116	80	114	106	100	126	114	136	132	158	119	148	136	117	119	133	93	132	173	154	121	95	71	96	101
113	105	88	98	131	134	94	128	127	111	137	107	146	134	134	116	137	105	120	146	100	89	112	152	141	48	98	141	55	86
163	135	154	85	146	94	60	130	139	141	134	113	94	149	120	147	125	154	144	125	148	135	162	117	145	75	136	105	30	44
187	154	148	102	153	149	129	159	162	118	122	132	120	145	112	128	124	103	88	124	130	123	139	160	112	111	138	116	85	55
175	183	177	170	192	175	131	134	85	67	83	117	103	132	128	154	157	85	82	85	110	121	106	144	78	94	111	161	91	97
141	117	169	114	163	152	159	127	125	64	56	66	81	85	92	104	104	97	138	117	115	145	110	126	94	140	106	119	81	153
79	132	156	78	89	112	144	170	100	68	100	105	111	107	102	115	116	99	150	136	112	53	42	112	140	138	150	154	147	167
98	96	86	50	60	111	130	149	112	92	96	109	63	106	107	93	121	78	116	106	93	65	63	94	38	51	130	152	153	165
134	167	138	72	74	123	67	50	123	134	102	112	73	102	59	44	69	108	107	100	121	123	123	127	145	144	149	99	124	172
169	110	106	113	111	154	129	70	100	74	95	106	60	75	66	76	80	167	134	115	142	100	68	120	160	124	138	99	106	158
177	186	165	147	106	126	90	61	65	72	111	89	109	120	143	170	124	124	122	81	104	102	111	100	148	91	102	61	113	150
183	165	175	122	87	109	90	112	87	85	148	147	139	124	103	137	134	87	111	76	74	67	103	68	131	155	108	86	69	78
157	192	185	147	59	53	140	181	103	93	147	146	133	125	96	124	139	110	142	159	95	121	152	154	101	115	117	105	41	23
151	192	161	147	94	81	143	172	142	94	131	120	131	159	145	138	181	169	182	118	75	120	169	136	74	102	108	98	52	89
163	191	161	133	111	179	167	152	128	156	116	123	144	104	114	132	124	121	94	97	66	106	88	62	49	78	113	54	122	177
179	177	164	116	131	142	173	168	126	167	115	101	152	129	99	114	104	118	31	33	39	61	71	50	49	58	134	146	169	154
175	176	180	166	139	109	163	142	109	117	128	96	133	124	118	56	47	28	39	35	58	91	163	167	136	137	167	146	151	141
158	183	174	173	98	106	173	138	56	100	100	60	112	59	100	77	53	55	96	100	152	162	177	181	128	130	139	164	153	120
148	181	184	130	159	134	143	75	40	33	67	79	109	138	139	98	124	118	161	158	147	120	122	135	82	91	133	119	101	103
176	162	152	87	86	63	91	60	63	98	128	159	148	176	153	80	70	90	173	163	157	98	111	99	103	92	76	137	87	102
135	152	99	51	26	84	113	143	145	144	166	147	130	131	90	102	128	186	171	80	158	173	165	139	75	91	106	140	134	50
127	95	50	27	70	126	156	149	167	186	119	104	125	167	150	158	127	161	156	134	141	120	126	112	97	146	143	159	105	89
25	25	52	114	128	144	135	135	133	116	119	75	113	167	148	59	49	73	149	158	142	99	69	108	113	103	151	157	75	108
19	35	82	127	119	154	120	66	80	97	88	124	147	142	104	60	95	132	104	92	102	90	73	96	120	93	150	160	102	100
98	85	146	119	97	111	25	18	21	68	51	102	120	70	82	140	126	108	52	55	130	169	125	156	167	153	155	151	152	121
160	146	156	119	88	58	69	43	70	104	113	84	89	137	104	140	174	155	162	122	100	129	74	84	126	154	169	173	145	131
153	135	108	51	68	116	117	90	122	174	134	40	40	59	101	111	96	84	87	114	40	80	94	55	41	67	140	166	119	85
66	64	105	92	98	109	99	70	117	113	79	77	45	47	88	133	88	105	103	39	70	111	146	115	67	58	59	84	63	74
64	101	90	39	14	40	123	148	132	103	109	121	119	155	150	167	149	143	132	87	103	58	118	91	86	110	92	61	37	85
69	138	103	89	49	100	140	185	179	151	121	167	166	172	184	152	98	158	158	174	162	64	101	137	66	112	106	120	95	144
80	46	52	94	128	156	154	155	156	172	129	158	153	169	127	125	99	157	160	180	193	160	144	135	110	134	125	89	89	135
159	100	72	92	101	150	161	147	93	133	120	120	115	162	99	132	150	116	144	117	176	178	152	87	62	82	116	112	123	83
134	146	146	135	124	110	129	134	52	74	124	117	98	156	132	160	150	96	110	123	144	133	120	127	64	81	92	72	97	82
151	156	161	156	106	105	113	127	123	131	124	65	103	108	143	119	133	76	74	81	73	135	90	115	99	113	127	106	102	117
99	92	103	64	52	80	126	103	109	91	105	118	102	123	59	59	109	68	98	50	82	102	111	120	129	105	35	117	150	114
30	8	24	12	6	45	75	55	69	79	102	131	154	124	62	87	145	76	123	136	144	94	118	155	137	174	100	120	71	39
11	23	32	14	8	67	95	100	98	91	91	172	145	119	137	72	125	92	103	88	148	153	131	137	164	129	117	60	73	94
64	124	113	99	79	169	143	149	122	101	94	145	137	97	82	99	122	144	131	121	118	104	128	122	128	111	83	86	101	105
138	171	145	147	140	160	146	142	114	124	76	130	89	99	74	149	134	124	108	67	90	98	111	117	115	50	12	29	145	147
177	179	177	164	141	137	145	110	146	151	121	66	59	60	51	131	144	103	130	62	65	72	107	132	78	96	72	87	109	102
174	167	178	117	118	102	126	97	117	124	110	56	123	145	76	108	154	133	123	159	163	135	105	121	85	74	84	140	94	90
165	145	110	126	133	104	89	132	140	147	108	137	141	143	103	114	120	82	109	91	71	154	142	82	133	109	79	49	53	102
183	167	119	138	112	143	139	179	183	171	146	155	132	82	122	119	146	146	146	136	61	51	129	149	165	154	177	157	179	139
122	139	180	142	98	160	161	153	169	140	127	117	74	121	111	142	139	144	141	158	87	23	99	107	160	166	126	155	160	127
127	152	126	148	149	183	133	144	141	140	164	66	105	143	177	167	136	134	105	179	139	162	153	143	155	134	97	118	149	163

Figure 47. Digital Map of a Scene Showing Two Multi-year Ridges Within a Multi-year Floe.

This map shows relative image density for the highlighted area indicated in Figure 46. The contour interval and density scale are identical to that used in Figure 46.

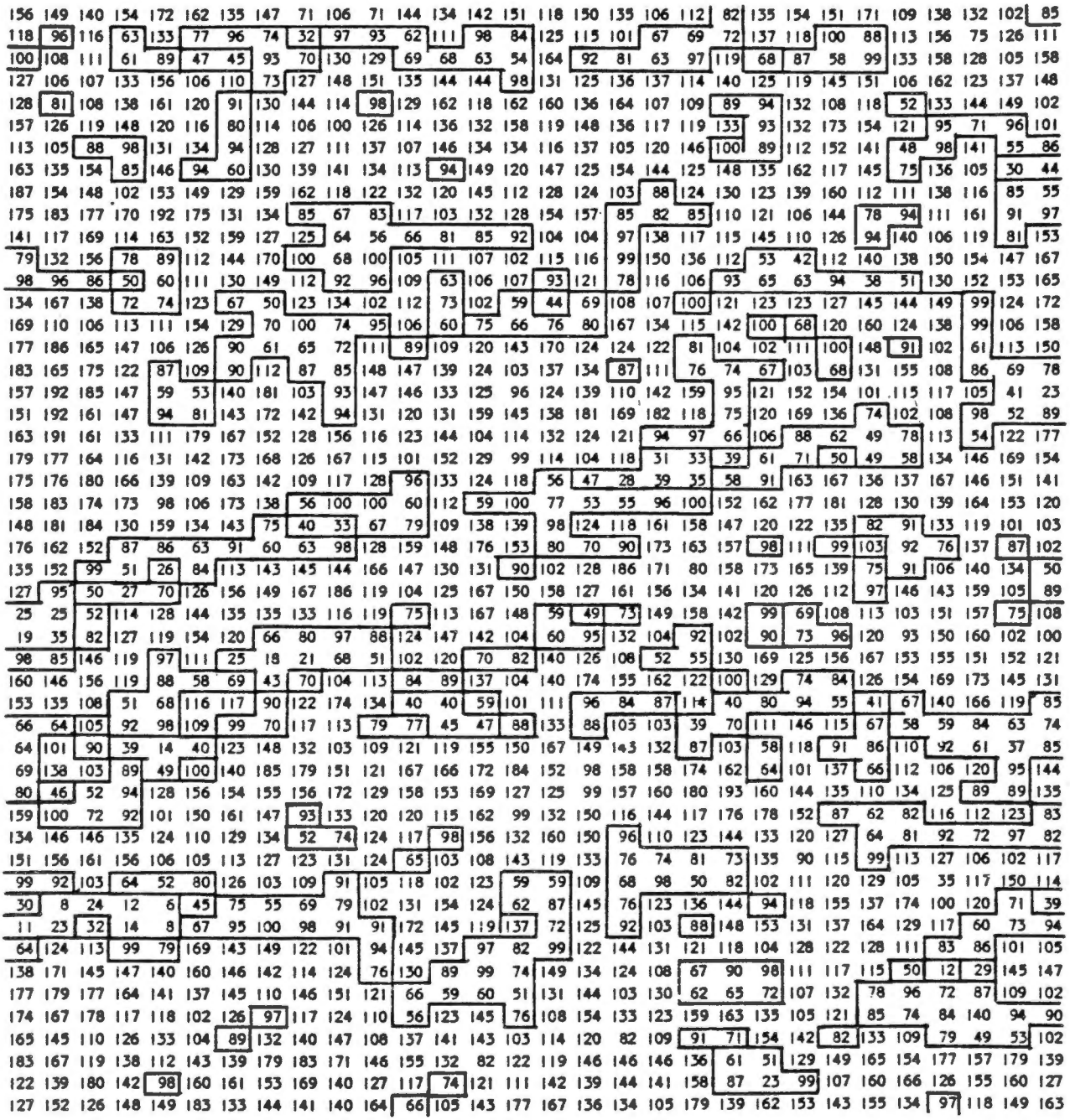

Figure 48. Digital Map of a Scene Showing Two Multi-year Ridges Within a Multi-year Floe.

Contour intervals of 100, 50 and 25 have been used.

Figure 49. Photographs of Digitized SAR Imagery

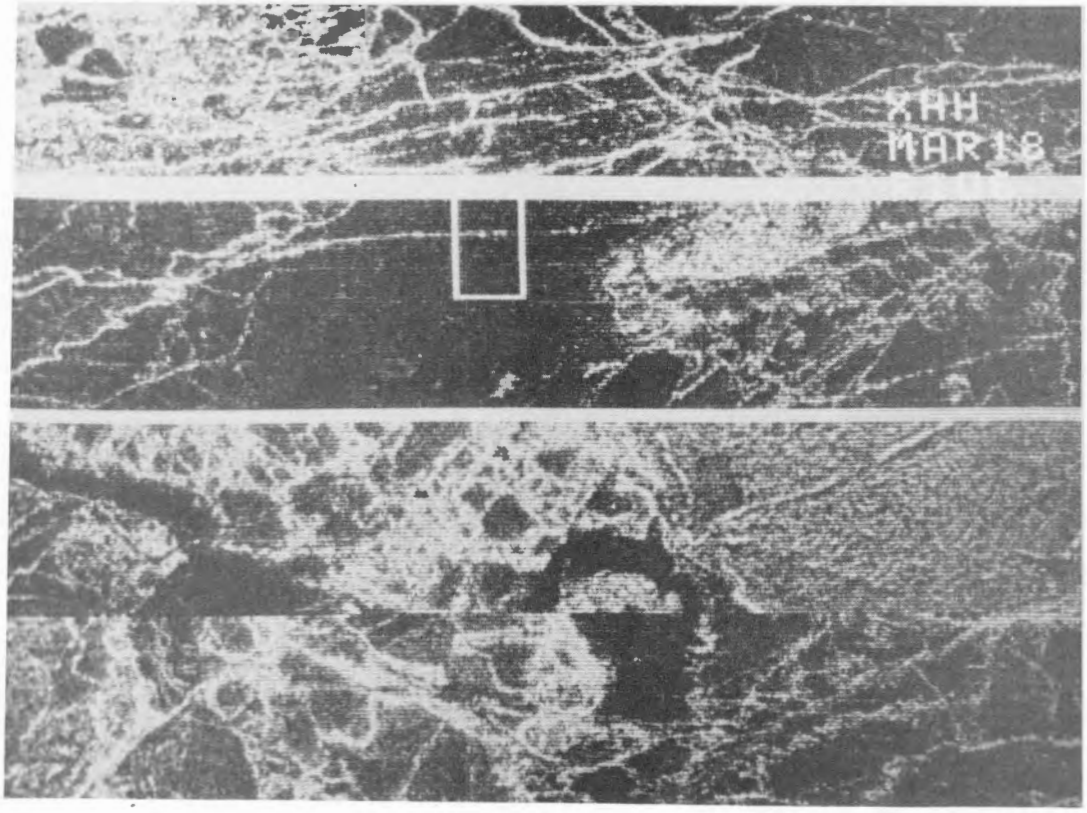

Figure 49a. The highlighted region shows a section of first-year ice crossed by a first-year ridge. The highlighted region is further illustrated in parts (b) and (c) below. The overall image is the same as indicated in Figure 43.

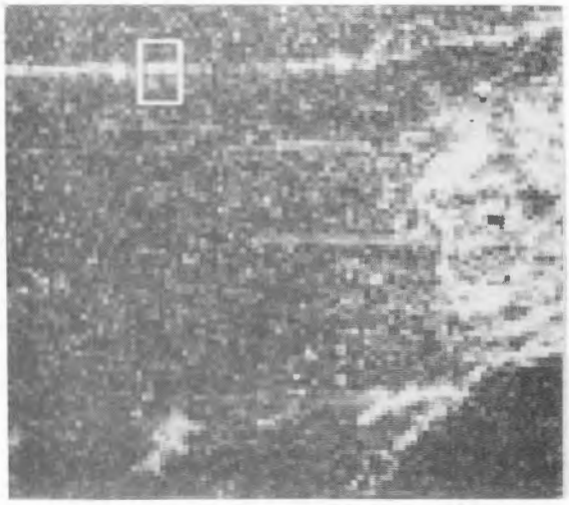

Figure 49b. A four-times blow-up of the section highlighted in (a), above. The highlighted area is discussed in the text. The bright area to the right of the image is a region of multi-year bits in a first-year matrix.

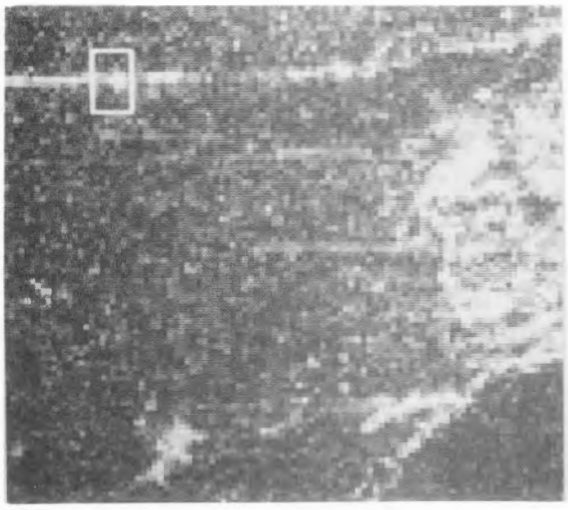

Figure 49c. A four-time blow-up of the same section. Again the highlighted section is discussed in the text.

191	205	206	193	197	185	186	188	187	199	197	190	189	188	180	200	190	175	155	177	200	191	200	201	190	204	191	177	184	178
191	205	206	193	197	185	186	188	187	199	197	190	189	188	180	200	190	175	155	177	200	191	200	201	190	204	191	177	184	178
194	204	204	200	202	199	194	189	189	207	206	199	196	187	191	205	207	203	186	194	195	190	200	187	161	187	181	203	201	180
193	193	174	186	193	188	205	206	187	200	188	202	196	171	199	198	156	189	195	183	174	190	196	197	166	182	179	187	179	180
192	181	180	198	185	189	180	198	182	179	184	198	206	185	207	196	198	183	162	178	190	201	193	204	196	175	175	178	185	202
192	179	167	192	173	190	189	193	196	200	189	193	192	196	200	205	187	198	202	180	193	182	174	179	200	194	193	195	205	189
188	196	191	183	188	190	200	195	203	182	194	200	195	191	198	200	191	194	203	185	187	166	190	166	197	199	199	188	192	186
184	161	189	188	190	174	199	196	170	188	195	190	158	185	194	186	179	197	186	187	171	174	163	192	177	205	189	194	192	198
201	184	176	180	161	197	173	187	167	195	179	170	175	140	165	174	184	171	169	190	154	189	199	192	188	191	189	165	175	188
177	177	164	162	183	196	159	198	198	198	171	184	195	193	188	181	171	183	201	188	201	193	195	171	187	164	193	184	179	153
190	206	154	174	180	180	177	196	203	201	179	191	177	204	197	200	170	198	201	192	161	173	196	193	193	194	195	199	171	188
158	193	193	179	200	196	197	198	187	187	190	196	199	185	195	199	189	196	204	194	192	185	188	187	187	196	198	201	180	169
187	193	167	184	180	197	190	203	178	199	182	197	174	186	188	192	186	185	192	181	170	189	181	172	179	200	191	197	186	193
187	176	177	200	195	199	182	201	188	199	195	166	196	191	188	175	173	197	204	199	187	191	176	192	182	187	191	183	160	176
196	168	170	191	196	183	173	185	187	196	169	155	176	190	178	168	192	198	187	188	168	168	159	193	184	205	168	200	179	185
173	176	174	172	173	140	120	98	135	144	156	103	93	152	177	166	149	66	80	76	55	67	111	163	149	156	179	164	203	186
105	93	106	46	105	96	114	133	129	128	69	9	22	137	147	166	155	68	105	136	71	91	157	170	152	154	180	139	191	184
136	174	155	141	169	198	168	145	177	177	167	57	71	164	142	191	185	158	173	185	175	170	186	191	184	179	197	188	202	178
168	185	193	166	180	176	188	163	175	199	197	141	168	188	169	191	168	148	169	195	171	164	176	171	192	190	185	180	207	183
187	194	176	186	187	190	193	177	194	182	187	184	184	192	184	184	176	143	152	193	189	183	176	191	188	177	196	187	198	192
182	198	200	189	191	189	201	198	198	186	177	193	179	187	206	183	178	188	184	188	198	197	201	166	172	191	198	195	197	194
177	194	184	195	202	184	200	204	199	188	200	195	192	201	201	193	201	192	196	188	201	195	180	198	200	197	196	208	192	191
191	203	190	206	207	180	189	191	204	194	197	191	189	186	206	189	196	194	197	195	190	204	199	199	193	182	174	190	202	185
179	198	159	174	194	194	202	201	196	179	178	172	166	187	191	201	191	186	209	196	192	191	206	201	187	198	192	174	194	194
174	191	155	176	199	200	196	189	184	158	167	188	184	151	188	150	167	193	197	176	202	170	198	202	194	169	190	168	189	202
195	192	196	194	186	183	199	164	188	184	203	194	179	191	178	185	175	192	199	188	185	179	179	191	193	198	193	186	186	197
192	180	202	190	190	172	197	172	167	151	157	174	192	200	186	204	168	168	181	193	199	204	197	199	179	175	191	170	196	200
182	162	188	195	184	203	183	184	153	153	158	168	182	177	183	190	159	161	171	176	176	184	185	177	171	176	156	160	169	171
195	180	205	201	193	188	182	192	173	190	202	167	194	197	206	208	191	197	189	182	199	205	187	200	190	184	169	189	183	181
202	185	179	191	179	185	170	184	182	177	207	180	196	207	205	203	201	202	197	179	189	204	188	190	173	188	163	193	188	201
197	172	176	177	192	178	189	190	175	195	180	196	194	193	194	205	186	187	198	192	187	179	187	172	156	201	193	202	188	191
194	195	206	204	201	177	179	180	188	190	176	194	189	191	202	192	181	185	169	171	168	154	186	177	189	195	186	189	187	180
187	171	182	188	179	174	186	189	189	179	172	174	186	180	185	181	187	186	188	167	186	187	191	183	189	184	195	192	168	197
189	188	181	179	205	192	199	194	199	204	193	190	198	193	188	161	191	186	199	184	195	196	191	194	204	196	184	191	183	187
190	185	170	198	175	184	199	193	188	197	202	204	186	183	194	174	204	203	190	173	183	192	203	204	198	199	186	165	180	183
197	190	193	186	196	181	198	185	199	181	196	194	185	198	195	199	178	182	201	194	185	192	199	197	195	183	194	183	204	178
183	184	177	169	159	192	206	195	198	170	206	188	193	191	191	190	190	192	200	201	197	198	196	176	185	198	196	191	206	191
190	185	193	186	189	184	188	175	186	185	199	195	191	192	181	181	197	193	195	205	205	192	188	184	188	198	191	203	196	172
187	196	180	192	193	192	176	191	202	197	183	190	196	199	193	194	196	192	165	177	180	187	190	184	182	202	193	201	194	192
182	190	148	185	180	193	187	187	189	190	194	199	200	196	181	159	188	178	190	176	190	190	200	170	177	191	201	205	185	148
207	196	176	198	191	177	184	176	192	196	179	200	199	178	193	200	187	187	170	177	186	169	198	190	168	176	180	181	200	191
186	204	195	193	187	192	198	191	207	191	195	204	199	185	199	200	193	188	171	176	197	203	197	197	201	193	170	194	184	201
188	205	194	200	195	174	188	191	194	181	200	196	209	187	198	202	195	171	184	208	206	188	183	189	197	202	199	200	195	189
185	194	199	199	197	201	198	192	164	175	200	192	187	199	205	209	198	200	200	185	206	206	197	188	190	198	200	187	198	140
195	171	201	181	190	193	175	198	184	198	193	188	180	192	200	207	192	205	199	203	199	206	185	187	190	207	196	198	199	188
181	152	196	196	198	198	191	205	195	183	190	183	197	187	190	199	190	207	197	200	199	188	187	189	179	181	195	174	187	198
199	185	198	170	201	182	187	200	203	196	185	187	197	191	175	167	193	201	203	179	198	197	184	190	192	180	202	186	190	186
201	194	191	193	185	193	200	182	186	197	187	192	172	192	195	199	202	203	196	197	202	193	181	187	199	192	181	184	208	185

Figure 50. Digital Map of a Scene Showing Two First-year Ridges in a First-year Background.

Contour intervals of 100, 80, 40, and 20 have been used.

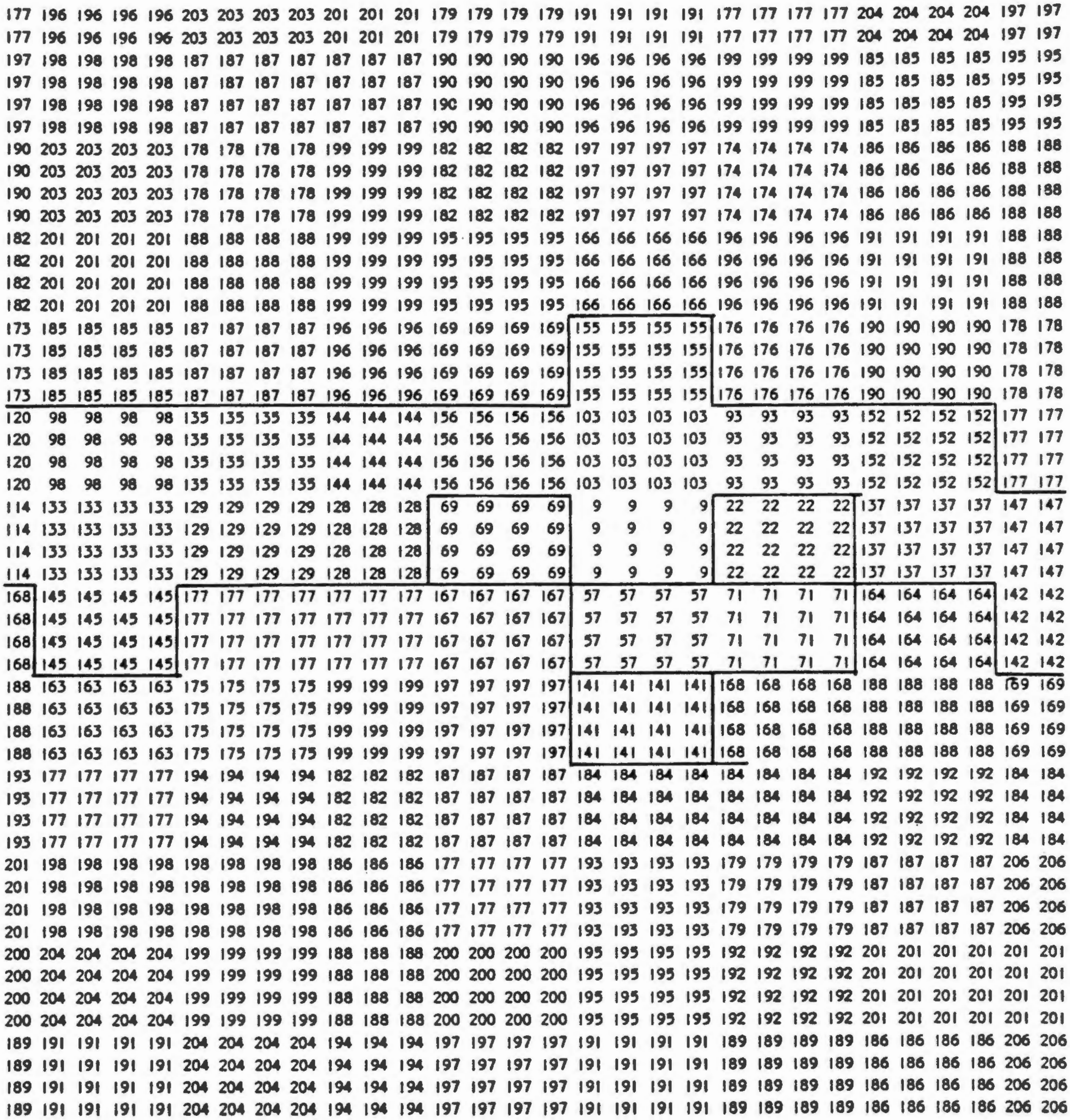

177	196	196	196	196	203	203	203	203	201	201	201	179	179	179	179	191	191	191	191	177	177	177	177	204	204	204	204	197	197
177	196	196	196	196	203	203	203	203	201	201	201	179	179	179	179	191	191	191	191	177	177	177	177	204	204	204	204	197	197
197	198	198	198	198	187	187	187	187	187	187	187	190	190	190	190	196	196	196	196	199	199	199	199	185	185	185	185	195	195
197	198	198	198	198	187	187	187	187	187	187	187	190	190	190	190	196	196	196	196	199	199	199	199	185	185	185	185	195	195
197	198	198	198	198	187	187	187	187	187	187	187	190	190	190	190	196	196	196	196	199	199	199	199	185	185	185	185	195	195
197	198	198	198	198	187	187	187	187	187	187	187	190	190	190	190	196	196	196	196	199	199	199	199	185	185	185	185	195	195
190	203	203	203	203	178	178	178	178	199	199	199	182	182	182	182	197	197	197	197	174	174	174	174	186	186	186	186	188	188
190	203	203	203	203	178	178	178	178	199	199	199	182	182	182	182	197	197	197	197	174	174	174	174	186	186	186	186	188	188
190	203	203	203	203	178	178	178	178	199	199	199	182	182	182	182	197	197	197	197	174	174	174	174	186	186	186	186	188	188
190	203	203	203	203	178	178	178	178	199	199	199	182	182	182	182	197	197	197	197	174	174	174	174	186	186	186	186	188	188
182	201	201	201	201	188	188	188	188	199	199	199	195	195	195	195	166	166	166	166	196	196	196	196	191	191	191	191	188	188
182	201	201	201	201	188	188	188	188	199	199	199	195	195	195	195	166	166	166	166	196	196	196	196	191	191	191	191	188	188
182	201	201	201	201	188	188	188	188	199	199	199	195	195	195	195	166	166	166	166	196	196	196	196	191	191	191	191	188	188
182	201	201	201	201	188	188	188	188	199	199	199	195	195	195	195	166	166	166	166	196	196	196	196	191	191	191	191	188	188
173	185	185	185	185	187	187	187	187	196	196	196	169	169	169	169	155	155	155	155	176	176	176	176	190	190	190	190	178	178
173	185	185	185	185	187	187	187	187	196	196	196	169	169	169	169	155	155	155	155	176	176	176	176	190	190	190	190	178	178
173	185	185	185	185	187	187	187	187	196	196	196	169	169	169	169	155	155	155	155	176	176	176	176	190	190	190	190	178	178
173	185	185	185	185	187	187	187	187	196	196	196	169	169	169	169	155	155	155	155	176	176	176	176	190	190	190	190	178	178
120	98	98	98	98	135	135	135	135	144	144	144	156	156	156	156	103	103	103	103	93	93	93	93	152	152	152	152	177	177
120	98	98	98	98	135	135	135	135	144	144	144	156	156	156	156	103	103	103	103	93	93	93	93	152	152	152	152	177	177
120	98	98	98	98	135	135	135	135	144	144	144	156	156	156	156	103	103	103	103	93	93	93	93	152	152	152	152	177	177
120	98	98	98	98	135	135	135	135	144	144	144	156	156	156	156	103	103	103	103	93	93	93	93	152	152	152	152	177	177
114	133	133	133	133	129	129	129	129	128	128	128	69	69	69	69	9	9	9	9	22	22	22	22	137	137	137	137	147	147
114	133	133	133	133	129	129	129	129	128	128	128	69	69	69	69	9	9	9	9	22	22	22	22	137	137	137	137	147	147
114	133	133	133	133	129	129	129	129	128	128	128	69	69	69	69	9	9	9	9	22	22	22	22	137	137	137	137	147	147
114	133	133	133	133	129	129	129	129	128	128	128	69	69	69	69	9	9	9	9	22	22	22	22	137	137	137	137	147	147
168	145	145	145	145	177	177	177	177	177	177	177	167	167	167	167	57	57	57	57	71	71	71	71	164	164	164	164	142	142
168	145	145	145	145	177	177	177	177	177	177	177	167	167	167	167	57	57	57	57	71	71	71	71	164	164	164	164	142	142
168	145	145	145	145	177	177	177	177	177	177	177	167	167	167	167	57	57	57	57	71	71	71	71	164	164	164	164	142	142
168	145	145	145	145	177	177	177	177	177	177	177	167	167	167	167	57	57	57	57	71	71	71	71	164	164	164	164	142	142
188	163	163	163	163	175	175	175	175	199	199	199	197	197	197	197	141	141	141	141	168	168	168	168	188	188	188	188	169	169
188	163	163	163	163	175	175	175	175	199	199	199	197	197	197	197	141	141	141	141	168	168	168	168	188	188	188	188	169	169
188	163	163	163	163	175	175	175	175	199	199	199	197	197	197	197	141	141	141	141	168	168	168	168	188	188	188	188	169	169
188	163	163	163	163	175	175	175	175	199	199	199	197	197	197	197	141	141	141	141	168	168	168	168	188	188	188	188	169	169
193	177	177	177	177	194	194	194	194	182	182	182	187	187	187	187	184	184	184	184	184	184	184	184	192	192	192	192	184	184
193	177	177	177	177	194	194	194	194	182	182	182	187	187	187	187	184	184	184	184	184	184	184	184	192	192	192	192	184	184
193	177	177	177	177	194	194	194	194	182	182	182	187	187	187	187	184	184	184	184	184	184	184	184	192	192	192	192	184	184
193	177	177	177	177	194	194	194	194	182	182	182	187	187	187	187	184	184	184	184	184	184	184	184	192	192	192	192	184	184
201	198	198	198	198	198	198	198	198	186	186	186	177	177	177	177	193	193	193	193	179	179	179	179	187	187	187	187	206	206
201	198	198	198	198	198	198	198	198	186	186	186	177	177	177	177	193	193	193	193	179	179	179	179	187	187	187	187	206	206
201	198	198	198	198	198	198	198	198	186	186	186	177	177	177	177	193	193	193	193	179	179	179	179	187	187	187	187	206	206
201	198	198	198	198	198	198	198	198	186	186	186	177	177	177	177	193	193	193	193	179	179	179	179	187	187	187	187	206	206
200	204	204	204	204	199	199	199	199	188	188	188	200	200	200	200	195	195	195	195	192	192	192	192	201	201	201	201	201	201
200	204	204	204	204	199	199	199	199	188	188	188	200	200	200	200	195	195	195	195	192	192	192	192	201	201	201	201	201	201
200	204	204	204	204	199	199	199	199	188	188	188	200	200	200	200	195	195	195	195	192	192	192	192	201	201	201	201	201	201
200	204	204	204	204	199	199	199	199	188	188	188	200	200	200	200	195	195	195	195	192	192	192	192	201	201	201	201	201	201
189	191	191	191	191	204	204	204	204	194	194	194	197	197	197	197	191	191	191	191	189	189	189	189	186	186	186	186	206	206
189	191	191	191	191	204	204	204	204	194	194	194	197	197	197	197	191	191	191	191	189	189	189	189	186	186	186	186	206	206
189	191	191	191	191	204	204	204	204	194	194	194	197	197	197	197	191	191	191	191	189	189	189	189	186	186	186	186	206	206
189	191	191	191	191	204	204	204	204	194	194	194	197	197	197	197	191	191	191	191	189	189	189	189	186	186	186	186	206	206

Figure 51. Digital Map of a Scene Showing a Bright First-year Ridge in a First-year Background.

Contour intervals of 160, 80, 40 and 20 have been used.

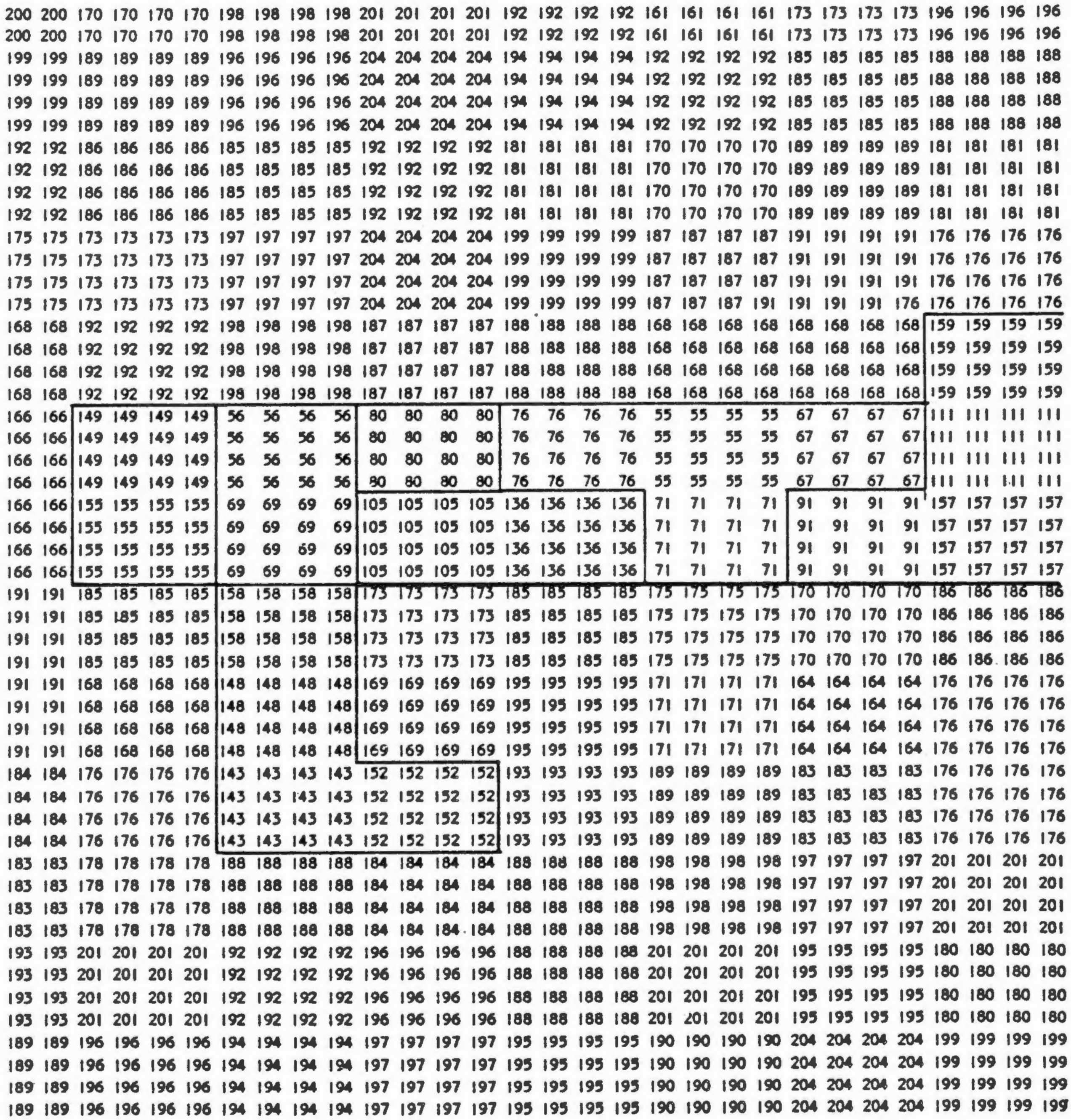

200	200	170	170	170	170	198	198	198	198	201	201	201	201	192	192	192	192	161	161	161	161	173	173	173	173	196	196	196	196
200	200	170	170	170	170	198	198	198	198	201	201	201	201	192	192	192	192	161	161	161	161	173	173	173	173	196	196	196	196
199	199	189	189	189	189	196	196	196	196	204	204	204	204	194	194	194	194	192	192	192	192	185	185	185	185	188	188	188	188
199	199	189	189	189	189	196	196	196	196	204	204	204	204	194	194	194	194	192	192	192	192	185	185	185	185	188	188	188	188
199	199	189	189	189	189	196	196	196	196	204	204	204	204	194	194	194	194	192	192	192	192	185	185	185	185	188	188	188	188
199	199	189	189	189	189	196	196	196	196	204	204	204	204	194	194	194	194	192	192	192	192	185	185	185	185	188	188	188	188
192	192	186	186	186	186	185	185	185	185	192	192	192	192	181	181	181	181	170	170	170	170	189	189	189	189	181	181	181	181
192	192	186	186	186	186	185	185	185	185	192	192	192	192	181	181	181	181	170	170	170	170	189	189	189	189	181	181	181	181
192	192	186	186	186	186	185	185	185	185	192	192	192	192	181	181	181	181	170	170	170	170	189	189	189	189	181	181	181	181
192	192	186	186	186	186	185	185	185	185	192	192	192	192	181	181	181	181	170	170	170	170	189	189	189	189	181	181	181	181
175	175	173	173	173	173	197	197	197	197	204	204	204	204	199	199	199	199	187	187	187	187	191	191	191	191	176	176	176	176
175	175	173	173	173	173	197	197	197	197	204	204	204	204	199	199	199	199	187	187	187	187	191	191	191	191	176	176	176	176
175	175	173	173	173	173	197	197	197	197	204	204	204	204	199	199	199	199	187	187	187	187	191	191	191	191	176	176	176	176
175	175	173	173	173	173	197	197	197	197	204	204	204	204	199	199	199	199	187	187	187	191	191	191	191	176	176	176	176	176
168	168	192	192	192	192	198	198	198	198	187	187	187	187	188	188	188	188	168	168	168	168	168	168	168	168	159	159	159	159
168	168	192	192	192	192	198	198	198	198	187	187	187	187	188	188	188	188	168	168	168	168	168	168	168	168	159	159	159	159
168	168	192	192	192	192	198	198	198	198	187	187	187	187	188	188	188	188	168	168	168	168	168	168	168	168	159	159	159	159
168	168	192	192	192	192	198	198	198	198	187	187	187	187	188	188	188	188	168	168	168	168	168	168	168	168	159	159	159	159
166	166	149	149	149	149	56	56	56	56	80	80	80	80	76	76	76	76	55	55	55	55	67	67	67	67	111	111	111	111
166	166	149	149	149	149	56	56	56	56	80	80	80	80	76	76	76	76	55	55	55	55	67	67	67	67	111	111	111	111
166	166	149	149	149	149	56	56	56	56	80	80	80	80	76	76	76	76	55	55	55	55	67	67	67	67	111	111	111	111
166	166	149	149	149	149	56	56	56	56	80	80	80	80	76	76	76	76	55	55	55	55	67	67	67	67	111	111	111	111
166	166	155	155	155	155	69	69	69	69	105	105	105	105	136	136	136	136	71	71	71	71	91	91	91	91	157	157	157	157
166	166	155	155	155	155	69	69	69	69	105	105	105	105	136	136	136	136	71	71	71	71	91	91	91	91	157	157	157	157
166	166	155	155	155	155	69	69	69	69	105	105	105	105	136	136	136	136	71	71	71	71	91	91	91	91	157	157	157	157
166	166	155	155	155	155	69	69	69	69	105	105	105	105	136	136	136	136	71	71	71	71	91	91	91	91	157	157	157	157
191	191	185	185	185	185	158	158	158	158	173	173	173	173	185	185	185	185	175	175	175	175	170	170	170	170	186	186	186	186
191	191	185	185	185	185	158	158	158	158	173	173	173	173	185	185	185	185	175	175	175	175	170	170	170	170	186	186	186	186
191	191	185	185	185	185	158	158	158	158	173	173	173	173	185	185	185	185	175	175	175	175	170	170	170	170	186	186	186	186
191	191	185	185	185	185	158	158	158	158	173	173	173	173	185	185	185	185	175	175	175	175	170	170	170	170	186	186	186	186
191	191	168	168	168	168	148	148	148	148	169	169	169	169	195	195	195	195	171	171	171	171	164	164	164	164	176	176	176	176
191	191	168	168	168	168	148	148	148	148	169	169	169	169	195	195	195	195	171	171	171	171	164	164	164	164	176	176	176	176
191	191	168	168	168	168	148	148	148	148	169	169	169	169	195	195	195	195	171	171	171	171	164	164	164	164	176	176	176	176
191	191	168	168	168	168	148	148	148	148	169	169	169	169	195	195	195	195	171	171	171	171	164	164	164	164	176	176	176	176
184	184	176	176	176	176	143	143	143	143	152	152	152	152	193	193	193	193	189	189	189	189	183	183	183	183	176	176	176	176
184	184	176	176	176	176	143	143	143	143	152	152	152	152	193	193	193	193	189	189	189	189	183	183	183	183	176	176	176	176
184	184	176	176	176	176	143	143	143	143	152	152	152	152	193	193	193	193	189	189	189	189	183	183	183	183	176	176	176	176
184	184	176	176	176	176	143	143	143	143	152	152	152	152	193	193	193	193	189	189	189	189	183	183	183	183	176	176	176	176
183	183	178	178	178	178	188	188	188	188	184	184	184	184	188	188	188	188	198	198	198	198	197	197	197	197	201	201	201	201
183	183	178	178	178	178	188	188	188	188	184	184	184	184	188	188	188	188	198	198	198	198	197	197	197	197	201	201	201	201
183	183	178	178	178	178	188	188	188	188	184	184	184	184	188	188	188	188	198	198	198	198	197	197	197	197	201	201	201	201
183	183	178	178	178	178	188	188	188	188	184	184	184	184	188	188	188	188	198	198	198	198	197	197	197	197	201	201	201	201
193	193	201	201	201	201	192	192	192	192	196	196	196	196	188	188	188	188	201	201	201	201	195	195	195	195	180	180	180	180
193	193	201	201	201	201	192	192	192	192	196	196	196	196	188	188	188	188	201	201	201	201	195	195	195	195	180	180	180	180
193	193	201	201	201	201	192	192	192	192	196	196	196	196	188	188	188	188	201	201	201	201	195	195	195	195	180	180	180	180
193	193	201	201	201	201	192	192	192	192	196	196	196	196	188	188	188	188	201	201	201	201	195	195	195	195	180	180	180	180
189	189	196	196	196	196	194	194	194	194	197	197	197	197	195	195	195	195	190	190	190	190	204	204	204	204	199	199	199	199
189	189	196	196	196	196	194	194	194	194	197	197	197	197	195	195	195	195	190	190	190	190	204	204	204	204	199	199	199	199
189	189	196	196	196	196	194	194	194	194	197	197	197	197	195	195	195	195	190	190	190	190	204	204	204	204	199	199	199	199
189	189	196	196	196	196	194	194	194	194	197	197	197	197	195	195	195	195	190	190	190	190	204	204	204	204	199	199	199	199

Figure 52. Digital Map of a Scene Showing a Bright First-year Ridge in a First-year Background.

Contour intervals of 160, 80, 40 and 20 intensity units have been used.

(1) radar texture of smooth first-year ice is much less pronounced than that of multi-year ice,

(2) very few of the ridge resolution cells in Figure 49a are as bright as the average multi-year ridge resolution cells seen in Figures 45 and 48.

No correlation was found between ridge backscattering cross-section (SAR image intensity) and ridge height, or between ridge-to-background contrast and ridge height at the radar incidence angles spanned by the digitized strip and scatterometer line photography.

3.6.1.3 Icebergs in a sea-ice background

In the data sets from the Eastern Arctic, nine icebergs were found to be suitable for study using the profiling sensor data and five icebergs were found in an area where the same ice was imaged by both the SAR and the mapping camera. The Danish N/S line data set was the only Eastern Arctic deployment data set that contained icebergs within the area sensed both by the SAR and the profiling sensors.

Of the five bergs visible in the profiling sensor line photography, only two were both clearly visible in the SAR imagery and completely filled the scatterometer beam. The data is summarized in Table 18. Both bergs clearly seen in the SAR imgery had along track dimensions greater than 200m and were imaged at incidence angles near 50°. The backscattering coefficients on one of these bergs were also measured by the scatterometer and yielded an iceberg-to-background ice cross-polarized contrast of 10.2 dB and a like-polarized contrast of 9.5 dB, at 55° incidence angle.

One of the bergs marginally detectable in the SAR was profiled by the scatterometer. This berg had along track dimensions greater than 100m and was viewed by the SAR at 50° incidence angle. The minimum cross-polarized iceberg-to-background ice contrast was 2 dB at 45° incidence angle. The HH-polarized data is not available for the berg due to data processing problems.

Marginally detectable and undetectable icebergs were found in the same incidence angle range (50° to 60°) and varied in size from 100m to 25m.

In the Melville Bay line, seven icebergs lay within the profiling sensor swath with beam-filling conditions for the scatterometer during a period when all instrumentation was operating at constant gain. The background ice was visually uniform, shore-fast first-year ice and some radar texture was found in the scatterometer trace indicating the presence of cracks and cemented floes. Figure 53a, b summarizes the iceberg-to-background ice contrasts for these bergs.

In general the cross-polarized backscattering coefficient contrasts are 2 to 4 dB larger than the like-polarized contrasts, there is no incidence angle dependent contrast enhancement in the range 15° to 60°; and the iceberg backscattering cross-sections vary with angle in the same manner as smooth first-year ice over this incidence angle range. Those icebergs with the lowest backscattering coefficients were weathered, domed

Table 18. Iceberg Detectability from the Danish N/S line, 032401.

RC-10 Photography Roll 1087			Ku-band Scatterometer			Detectability of Berg in the SAR Image				
Berg size (type) (m)	Frame	GMT (HH:MM:SS)	Incidence angle (°)	Contrast with FY Ice		Incidence angle (°)	X-Band		L-Band	
				HV(dB)	HH(db)		HV	HH	HV	HH
12 x 102 (drydock)	6687	15:38:14	45	2	N/A*	60	marginal	marginal	undetected	undetected
222 x 216 (tabular)	6773	15:53:43	off	scat	track	60	good	good	undetected	undetected
480 x 252 (tubular)	6781	15:55:04	55	10.2	9.5	51	excellent	very good	undetected	undetected
57 x 25 (pinnacular)	6781	15:55:04	off	scat	track	60	undetected	marginal	undetected	undetected
30 x 25 (pinnacular)	6781	15:55:04	off	scat	track	51	undetected	undetected	undetected	undetected

* N/A not available

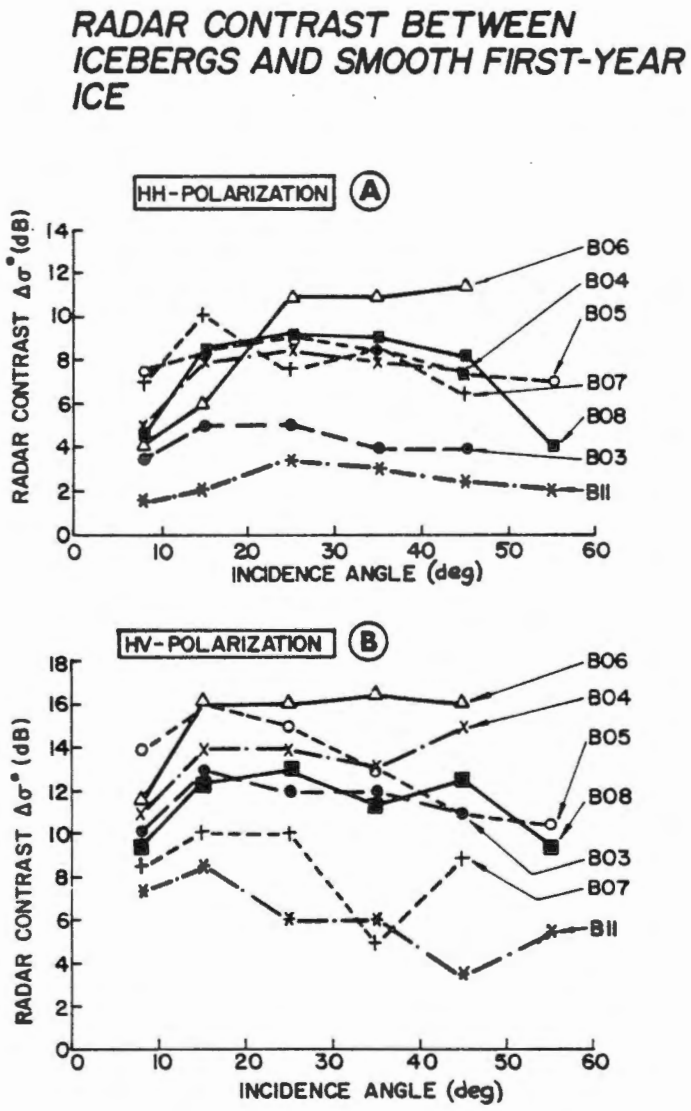

Figure 53. Radar Contrast Between Icebergs and Surrounding First-year Ice for 13.3 GHz and Incidence Angles between 0 and 60°.

Considerable variation may be seen in the data from each iceberg with no clear advantage for any incidence angle in this range. Results for HV-polarization are generally superior to HH-polarization by 4-6 dB.

bergs or tilted, tabular bergs observed from the side with the smallest slope.

An examination of the scatterometer time histories for many of the bergs in the Melville Bay line revealed an assymetry in the background ice in the immediate vicinity of the bergs, with the scattering coefficient on one side being depressed as much as 10 dB from that of the surrounding ice. These features, in combination with pressure cracks occasionally visible in the ice near the bergs, are interpreted to be evidence of recent motion of the pack ice around the bergs. The regions of depressed backscatter are tentatively interpreted to be regions of younger, wet or heavily snow-drifted ice.

The 19.35 GHz brightness temperatures of the icebergs measured on the Melville Bay line cluster in the vicinity of 216 K, or about 25 K colder than the surrounding ice.

4.0 SUMMARY DISCUSSION AND CONCLUSIONS

4.1 Sea-ice Classification Study

Of the sixteen WMO sea-ice classes and subclasses identified in the Active-Passive Experiment, our preliminary classification study has shown that eleven have microwave signatures defined by the combination of their HH- and HV-polarized backscattering coefficients (at 13.3 GHz and incidence angles between 8 and 60°), and H-polarized emissivity (at 45° incidence and 19.4 GHz) which lead to good separability of the classes. These are:

1. Ice island and iceberg
2. Multi-year
3. Second-year
4. Rough first-year
5. Smooth first-year
6. Grey-white
7. Grey
8. Light nilas
9. Dark nilas
10. Grease
11. Calm water

Rough multi-year ice and smooth multi-year ice are not separable and rough second-year and smooth second-year ice are marginally separable. It should be remembered that the rough and smooth subcategories were assigned on the basis of interpretation of low altitude RC-10 photography and are, consequently, somewhat arbitrary. Frazil and grease ice existed in some of the Eastern Arctic data, but in insufficient quantities to characterize these classes with certainty. Wave-broken first-year ice had similar characteristics to rough first-year ice and was not treated as a separate subclass in this study.

4.1.1 Classification spaces from the Active-Passive Experiment

Two different three-dimensional feature spaces were verified to be suitable for classifying ice under constant ambient temperature conditions. The first space is defined by: σ^{o}_{hh}, σ^{o}_{hv} (at 13.3 GHz) and θ, where θ is the incidence angle between 8 and 60°. This classification space has been identified previously and tested by Parashar et al. (1974) and was further investigated in the Active-Passive Experiment by the development of a set of parametric relationships between σ^{o}_{hh}, σ^{o}_{hv} and θ. The Active-Passive data confirm and extend the experimental results of Gray et al. (1977a) for this space.

This approach to sea-ice classification is constrained by the requirement that simultaneous backscattering measurements are available over a large incidence angle range with the attendant complex processing problems and requirement for accurate altitude and ground speed data.

The resulting airborne sensor package is:

1. a dual-polarization fanbeam scatterometer,
2. a LTN-51 inertial navigation system (or equivalent),
3. a precision radar altimeter.

The data processing requirements demand either a very efficient FFT device (or a parallel analogue filtering system) in combination with a minicomputer or a large, ground based computer. For these reasons, the σ^{o}_{hh}, σ^{o}_{hv}, θ space is primarily of research interest and is capable of providing information on the behaviour of imaging radars which have corresponding incidence angle ranges.

The second space* is defined by: σ^{o}_{hh}, σ^{o}_{hv} (at 13.3 GHz) and ε (at 19.4 GHz), each parameter measured at the same fixed incidence angle. From the results presented and discussed in Sections 3.1.1, 3.1.2, 3.1.3 and 3.5, it is evident there is no clearly defined incidence angle that maximizes the accuracy of the sea-ice classification in this feature space at all temperatures. The statistical data obtained suggest that greatest class separation may be found for incidence angles between 35 and 60° and thus some form of incidence angle selection is probably required for future ice classification systems using this feature space (pending further research results).

This approach to sea-ice classification along a narrow flight track has several advantages over the feature space involving the incidence angle dependence of the backscattering coefficients:

1. both the active and passive sensor data are required only at a single incidence angle,
2. the sensors can be side-looking,
3. precise estimates of aircraft ground speed are not required,
4. computational requirements are modest, being compatible with a microcomputer and are feasible as a 'real time' system at modest cost.

For ice at a uniform temperature, the required sensor package is:

1. a dual-polarized pencil-beam scatterometer,
2. a single-polarized pencil beam radiometer, bore-sighted with the scatterometer,
3. a radar altimeter.

This second feature space has thus a potential as an operational sea-ice classification tool. It is directly compatible with the support requirements of current and new generation ice thickness radars and may be useful for providing real-time ice identification along the near range portions of SAR and SLAR imagery.

The hyperspace boundaries for each ice class are dependent on large scale, (event-sized) systematic variations, as well as textural variations at the footprint scale. Younger ice classes show more variation between ice events than textural variation within ice events, but for first-year

---

* Equivalent spaces may be generated using other polarization combinations (e.g. VV, VH) and brightness temperature instead of emissivity; however, not all permutations have been verified to be equally advantageous.

and older classes, event texture is sufficiently large to mask event-to-event variations. For these older ice classes, cross-polarized radars (at Ku-band, X-band and L-band) show more textural variation than do like-polarized radars. Texture is correlated to surface roughness features including broken ice, snow cover irregularities, and melt ponding. In the case of water, radar texture is related to the sea state; particularly, wave size and roughness.

4.1.2 Temperature dependence of the microwave signatures of sea ice

Active-Passive Experiment results were combined with data published by Gray et al. (1977a) and Vant et al. (1974) for which ambient temperature was known, in order to try to estimate the effect of temperature on sea-ice signatures. These estimates are preliminary due to the problem of deducing ice temperatures from ambient temperatures. However, it is clear that ice signatures are significantly affected by ambient temperature, particularly when the temperature approaches and exceeds the ice melting point. Under these conditions surface water appears, surface scattering and reflection dominates, both the backscattering and emissivity decrease and at some unknown temperature the ability to classify ice on the basis of signatures becomes impossible. With colder ambient temperatures the surface of the ice will decrease in temperature, the brine volume will decrease and, consequently, the skin depth will increase. It is hard to estimate these effects for new and young ice because of the strong thermal gradients through the ice and the lack of a dielectric constant model for the ice. However, at wavelengths of order 1 cm it is probable that surface and near-surface effects dominate for both near-freezing and for ambient temperatures down to $\sim -30^{o}C$. Even at these temperatures it is possible for the surface of new or young ice to have a brine or saline frost flower layer on top of the ice. For very cold temperatures ($< -20^{o}C$) the top layers of multi-year ice will not contain any liquid phase and volume effects undoubtedly contribute to the signatures.

For general classification of sea ice under arbitrary conditions, the temperature of the visible surface (ice or snow) is required. Thus, both the first- and second-feature spaces, defined above, become four-dimensional by the addition of temperature*. The second space defined by σ^{o}_{hh}, σ^{o}_{hv} and ε at constant incidence angle, could still be the basis of a viable operational instrument package with the addition of a surface temperature monitor (such as a precision radiation temperature radiometer) bore-sighted with the scatterometer and microwave radiometer.

---

* Temperature is only a secondary variable, in that it does not uniquely control the physics of sea ice. Each of salinity, brine volume and salt content have hysteresis behaviour with temperature, making temperature an unsatisfactory classification parameter. Nevertheless, temperature has an overriding control of these more basic quantities and is easily accessible experimentally. Temperature should therefore be considered as a possible fourth variable in a classification scheme.

4.1.3 Automated sea-ice classification

From simulation studies using computer classification algorithms applied to unselected experimental data, it has been shown that simple, Euclidian classifiers without memory, working with the average class feature vectors, are capable of producing accuracies of 80% and err in the conservative direction. The separation of grey-white from first-year smooth ice had the lowest success rate (70%). Classifiers which are based on the associated class hyperspace ellipsoids are generally more successful and have produced accuracies > 95% for sea ice under cold temperature conditions. These results have been obtained with a limited, selected data set and future work will examine a larger data set. All work to date on automatic classifiers has been based on intermediate (Frobisher Bay) and cold (Beaufort Sea) temperature data, and has not been extended to other temperatures.

4.2 The Ice Feature Study

The results of the Active-Passive Experiment show that radars with incidence angles in the range 0 to 60° are not well suited for the detection and measurement of icebergs in a sea-ice background or for the detection and measurement of multi-year ridges in multi-year ice.

4.2.1 Pressure ridge detection

Scatterometer results show that first-year ridges in a first-year ice background are generally detectable by radars with incidence angles in the range 8 to 60° provided that the ridge width exceeds one radar resolution cell length. For smaller ridges, ridge-to-ice contrast (in dB) degrades approximately linearly with the ratio of ridge width to resolution cell length down to the point at which the ridge-to-ice contrast is equal to the general radar texture of the ice, implying that ridge cross sections in this angle range are independent of their overall dimensions. Ridge height showed no correlation with radar brightness in the 0 to 60° incidence angle range.

HV-polarized radar provided a 2 to 4 dB improvement in ridge-to-background contrast over HH-polarized radar for all ridges measured.

For imaging radars, the ridge detection limit is dependent on the ridge geometry, using spatial persistence of small contrasts to form recognizable patterns. For long ridges, the limit of detectability thus occurs when the ridge-to-ice contrast approximates the root mean square (RMS) ice texture ($\sim$ 2 dB at 13.3 GHz and incidence angles less than 60°). Inspection of Figures 40 and 41 shows that using HV-polarized, Ku-band radars of sufficiently high resolution, this condition is always satisfied for incidence angles in the range 8 to 60°.

These conclusions were confirmed in the X-band SAR imagery. Digitized SAR scenes were used to demonstrate how even the largest and most prominant multi-year ridges become lost in the clutter when the resolution cell dimensions exceed 90 x 90 m. First-year ridges required even larger resolution cells before they became washed out in the background ice returns. Optimum radar resolution, cell scale length for the detection of

ice ridges encountered in the region of the Beaufort Sea covered in this experiment appears to be in the 3 to 10 m range.

4.2.2 Iceberg detection

The detection of icebergs in a sea-ice background from radar imagery requires more radar contrast since the berg geometries are more complex than the linear geometry of pressure ridges. In addition, the local incidence angle at the berg surface is strongly dependent on the berg type, orientation and weathering, making radar contrast dependent on particular berg shape.

For successful detection by radars operating with 0 to 60° incidence angles at Ku-band, icebergs in a first-year background must, in general, have linear dimensions greater than 4 to 6 footprint lengths. The dependence of backscattering coefficient of icebergs with incidence angle, is sufficiently parallel to that of first-year ice that no significant increase in detectability was found for any incidence angle in the range of 0 to 60°. Radar contrasts of icebergs within a first-year ice background are ~ 4 dB greater using HV-polarization than HH-polarization, but again no preferred incidence angle was found.

Large icebergs fall near the 'ice island' classification when both radiometer and scatterometer data are combined.

4.3 Recommendations for Future Study

The SURSAT Active-Passive Experiment has demonstrated the complementarity of active and passive microwave sensors and has suggested that unique microwave signatures may exist that would allow a simple, operational, automated classification scheme. This suggestion is based on a limited data set under a few typical, but by no means comprehensive, ice conditions. Future experiments should be directed to bridging the data gaps and verifying the current data base under different temperature conditions. In addition we make the following particular recommendations:

(1) More attention be directed toward ground truth information in the overflight region including the following data:
   a. Surface temperature, and snow temperature gradient,
   b. Snow depth,
   c. Ice density,
   d. Ice thickness,
   e. Ice salinity,
   f. Ice brine volume fraction,
   g. Complex dielectric constant measurements.

(2) Continued study with particular emphasis on profiling sensor data since this data is most easily quantified and cross-compared. In such reconnaissance, the following sensor complement is recommended as a minimum requirement:

   a. Wide-angle aerial camera,
   b. Infrared profiling thermometer,
   c. Microwave scatterometer,

d. Microwave radiometer,
e. Inertial navigation system,
f. Radar altimeter.

In addition to these primary sensors, valuable complementary data could be obtained by simultaneous measurements with:

a. Impulse radar thickness profilometer,
b. Radar or lidar surface profilometer,
c. SAR imagery,
d. SMMR imagery.

(3) Missions using the sensors described in (2) should gather data for similar ice scenes over the complete seasonal cycle to assess the variation of microwave signatures with seasonal patterns.

(4) Continued analysis is required of current data sets to establish:

a. The effect of snow cover and conditions on sea-ice microwave signatures,
b. The uniqueness of the angular dependence of the backscattering in classifying sea ice,
c. The form and uniqueness of the probability distribution functions for microwave emissivity and backscattering cross section,
d. The cross-comparison of profiling sensor and imaging sensor data for (c),
e. The validity of current data for less frequently observed ice forms viz. nilas, frazil, grease, grey, grey-white. Much of the optimal data set has now been analysed but useful data may be retrieved from secondary results still largely untouched,
f. The study of roughness features: ridging, rafting, cracking and edges, to determine their utility in determining floe boundaries and ridge patterns,
g. Theoretical work on the prediction and modelling of microwave scattering coefficient and emissivity, comparing results with empirical data.

BIBLIOGRAPHY

----------, 1978, MANICE, (Manual of Standard Procedures and Practices for Ice Reconnaissance), Atmospheric Environment Service, Environment Canada, Ottawa, 60 p.

----------, N.D., Operations and Maintenance Manual, K-band Microwave Radiometer, Aeroject-General Corporation, Microwave Division, El Monte, Calif., 27 p.

----------, 1970, RC-10 Universal Film Camera Manual, Parts I and II, Wild-Heerbrugg Inc., 72 p.

----------, 1972, Technical Description, Litton LTN-51 Inertial Navigation System for Commercial Aviation, Aero Products Division, Litton Systems Inc., Woodland Hills, Calif., 265 p.

----------, 1975, Honeywell Component Maintenance Manual Part No. YG7500 and YG7600 Radar Altimeter Systems, Honeywell Government and Aeronautical Products Divisions, Minneapolis, Minn., 1122 p.

----------, 1978, "The SAR-580 production system". Intera Environmental Consultants Ltd., Intera Report ASP-78-8, 8 p.

Assur, A., 1958, "Composition of sea ice and its tensile strength". Arctic Sea, National Academy of Science, NRC, Washington, D.C. Publication 508, pp. 106-138.

Bogorodsky, V.V., G.P. Khokhlov, 1975, "Electrical properties of ice in the ice edge zone of the Bering Sea at 10 GHz frequency". USSR/USA Bering Sea Experiment. Proceedings of the Final Symposium on the Results of the Joint Soviet - American Expedition, May, 1974, Gidrometeoizdat, Leningrad, pp. 219-232.

Bridgeman, J.J., 1978, "DPD processing of airborne MUX data". CCRS Technical Memorandum No. DPD-TM-78-023.

Bridgeman, J.J., M.J. Gough, 1979, "ADAS sensor descriptions and NIM prototype headers". CCRS Technical Memorandum No. DPD-TM-79-051.

Chan, K.K., A.L. Gray, 1979, "A system study of the CCRS 13.3 GHz scatterometer and the design of a simple, optimized digital data processing scheme." CCRS internal report under review, 64 p.

Copeland, W.O., R.J. Wangler, J.C. Wiltse, 1966, "Radiometer sensor". Report OR8016 Martin Co., Orlando, Fla.

Dunbar, M., 1969, "A glossary of ice terms (WMO Terminology)" Ice Seminar, Special Volume 10, The Canadian Institute of Mining and Metallurgy, pp. 105-110.

Edel, H., 1979, "MUX processing on AIR computer". CCRS Technical Memorandum No. DPD-TM-79-052, 10 p.

Edel, H., M. Gough, 1979, "Non-imagery disk file specification". CCRS Technical Memorandum No. DPD-TM-79-055, 20 p.

Frankenstein, G., R. Garner, 1967, "Equations for determining the brine volume of sea ice from -.5 to -22.9°C". J. Glaciology 6, p. 943.

Fraser, R.S., N.E. Gaut, E.C. Reifenstein III H. Sievering, 1975, "Interaction mechanism - within the atmosphere". in Manual of Remote Sensing, R.G. Reeves ed., American Society of Photogrammetry, Falls Church, Va., pp. 181-233.

Gloersen, P., W. Nordberg, T.J. Schmugge, T.T. Wilheit, 1973, "Microwave signatures of first-year and multi-year sea ice". J. Geophysical Research 78, pp. 3564-3572.

Gray, A.L., J. Cihlar, S. Parashar, R. Worsfold, 1977a, "Scatterometer results from shorefast and floating sea ice". Proc. 11th Int. Symp. Remote Sensing Environment, Ann Arbor, Mich., pp. 645-657.

----------, R.O. Ramseier, W.J. Campbell, 1977b, "Scatterometer and SLAR results obtained over Arctic sea-ice and their relevance to the problem of Arctic ice reconnaissance". Proc. 4th Can. Symp. Remote Sensing, pp. 424-443.

----------, P. Gudmansen, S. Overgaard, N. Skou, F. Søndergaard Pedersen, 1979, "West Greenland sea ice experiment." SURSAT report no. 1, 29 p.

Hall, D.K., J.L. Foster, A.T.C. Chang, A. Rango, 1979, "Passive microwave applications to snowpack monitoring using satellite data." NASA (Goddard) Technical Memorandum No. 80310, 14 p.

Hawkins, R.K., C.E. Livingstone, L.D. Arsenault, 1980, "Event File Index of the SURSAT Active-Passive Experiment - March/April, 1979." CCRS DAD Internal Memorandum.

Helk, J.V., M. Dunbar, 1953, "Ice islands: evidence from north Greenland." Arctic 6, pp. 263-271.

Jackson, B.L., W.L. Jones, W.D. Stanley, 1979, "Measure of Arctic sea-ice characteristics using microwave scatterometry." IEEE 0000 (to be published).

Jernigan, M.E., 1979, "Pattern recognition course notes." Department of System Designs, Faculty of Engineering, University of Waterloo, 161 p.

Jones, W.L., L.C. Schroeder, J.L. Mitchel, 1977, "Aircraft measurements of microwave scattering signatures of the ocean." IEEE AP-25, pp. 52-61.

Ketchum, R.D., Jr., L.D. Farmer, 1980, "Eastern Arctic SURSAT SAR Ice Experiment: Radar signatures of sea ice features." NORDA Technical Note 68.

King, D.D., 1970, "Passive detection." in Radar Handbook, M.I. Skolnik ed. McGraw-Hill, Toronto, pp. 39-1 - 39-36.

Koenig, L.S., K.R. Greenaway, M. Dunbar, G. Hattersley-Smith, 1952, "Arctic ice islands." Arctic 5, pp. 66-103.

Kraus, J.D., 1950, "Antennas", McGraw-Hill, Toronto, pp. 371-381.
Meeks, D.C., G.A. Poe, R.O. Ramseier (1974) "A study of microwave emissivity properties of sea ice - AIDJEX 1972." Final Report 1786FR-1, 140 p., Aerojet Electrosystems Co., Azusa, California.

Montgomery, M.R., 1952, "Further notes on ice islands in the Canadian Arctic." Arctic 5, pp. 183-187.

Moore, R.K., L.J. Chastant, L.J. Porcello, J. Stevenson, F.T. Ulaby, 1975, "Microwave remote sensors." in Manual of Remote Sensing, R.G. Reeves ed., American Society of Photogrammetry, Falls Church, Va., pp. 399-537.

Onstott, R.G., R.K. Moore, W.F. Weeks, 1979, "Surface-based scatterometer results of Arctic sea ice." IEEE Trans. GE-17, pp. 78-85.

Parashar, S.K., A.W. Biggs, A.K. Fung, R.K. Moore, 1974, "Investigation of radar discrimination of sea ice. Proc. 11th Int. Symp. Remote Sensing Environment, Ann Arbor, Mich., pp. 323-332.

Peake, W.H., 1959, "Interaction of electromagnetic waves with some natural surfaces." IRE Transactions on Antenna and Propagation, pp. S324-S329.

Rawson, R., F. Smith, R. Larson, 1975, "The ERIM simultaneous X- and L-band dual polarization radar." IEEE International Radar Conference, pp. 505-510.

Rossiter, J.R., K.A. Butt, 1979, "Remote estimation of the properties of sea ice, Beaufort Sea field report - March 1979." C-CORE publication no. 79-9, 40 p.

Rouse, J.W., Jr., 1969, "Arctic ice type identification by radar." Proc. IEEE 57, pp. 605-611.

Snellen, J.B., J.R. Rossiter, 1980, "Remote estimation of the properties of sea ice. Surface truth measurements, Beaufort Sea, March 1979." Technical Report, C-CORE Publication No. 00 (under review) 111 p.

Vant, M.R., R.B. Gray, R.O. Ramseier, V. Makios, 1974, "Dielectric properties of fresh and sea ice at 10 and 35 GHz." J. Appl. Phys. 45, pp. 4712-4717.

----------, R.B. Gray, R.O. Ramseier, V. Makios, 1975, "Erratum: Dielectric properties of fresh and sea ice at 10 and 35 GHz." J. Appl. Phys. 46, p. 2339.

----------, 1976, "A combined empirical and theoretical study of the dielectric properties of sea ice over the frequency range 100 MHz to 40 GHz", Ph.D. Thesis, Carleton University, 462 p.

Wilheit, T., W. Nordberg, J. Blinn, W. Campbell, A. Edgerton, 1972, "Aircraft measurments of microwave emission from Arctic sea ice." Remote Sensing Env. 2, pp. 129-139.

Wilkinson, T.L., 1979, "Automatic ice classification." Term report for Dr. K. Huseyin, Dept. of Systems Design, Faculty of Engineering, University of Waterloo, 82 p.

Young, S., T.L. Wilkinson, 1980, "Automatic ice classification and ridge detection." Course report for M.E. Jernigan, Dept. of Systems Design, Faculty of Engineering, University of Waterloo, 69 p.

APPENDIX 1

OVERLAPPING DATA FROM THE BEAUFORT SEA DEPLOYMENT

A1.1 Ground Truth Information from the Beaufort Sea Deployment

The ground truth data has been collected into two main reports in addition to information in other individual SURSAT Ice Experiment reports. These are:

(1) Remote Estimation of the Properties of Sea Ice, Surface Truth Measurements, Beaufort Sea, March, 1980, J.B. Snellen, J.R. Rossiter, C-CORE Technical Report, No. 80-0, (under review) June 1980.

(2) Remote Estimation of the Properties of Sea Ice, Beaufort Sea Field Trip Report - March 1979, J.R. Rossiter and D.A. Butt, C-CORE Data Report, No. 79-9, June 1979.

A1.2 Ground Truth Sites from the Beaufort Sea Deployment

Figure A1.1 shows the main ground truth areas during the Beaufort Sea mission. In addition to the sites shown in Figure A1.1, five other sites were examined in the vicinity of Tuktoyaktuk harbour. The following measurements were obtained at most of these sites:

(1) Qualitative description of site,
(2) Ground photography, 35 mm colour,
(3) Low level photography (Twin Otter or helicopter),
(4) Surface feature size measurements, surface roughness,
(5) Snow sampling - depth, temperature, salinity,
(6) Ice sampling - surface cores - total cores: temperature and salinity and crystal structure with depth,
(7) Ambient temperature - air and sea temperature, if applicable,
(8) Threshold water current measurement at some locations,
(9) Surface radiometry and electrical properties at most locations.

A1.3 Flights by Other Participating Aircraft

Table A1.1* lists a series of flight lines describing the work done by NASA Lewis Research Centre in their Sea Ice Radar Experiment (SIRE) using a C-131 SLAR (side looking airborne radar) in the same period as the Active-Passive Experiment. This work was performed on three separate days. The area of the SLAR coverage for their runs is presented in Figures A1.2, A1.3, and A1.4*.

The impulse radar flights of C-CORE and NRC are described in the C-CORE Field Trip Report.

---

* Table A1.1 and Figures A1.2, A1.3, and A1.4 are taken from the Sursat Ice Experiment Workshop, Summary of Activities and Research Projects, May 30-31, 1979, Toronto.

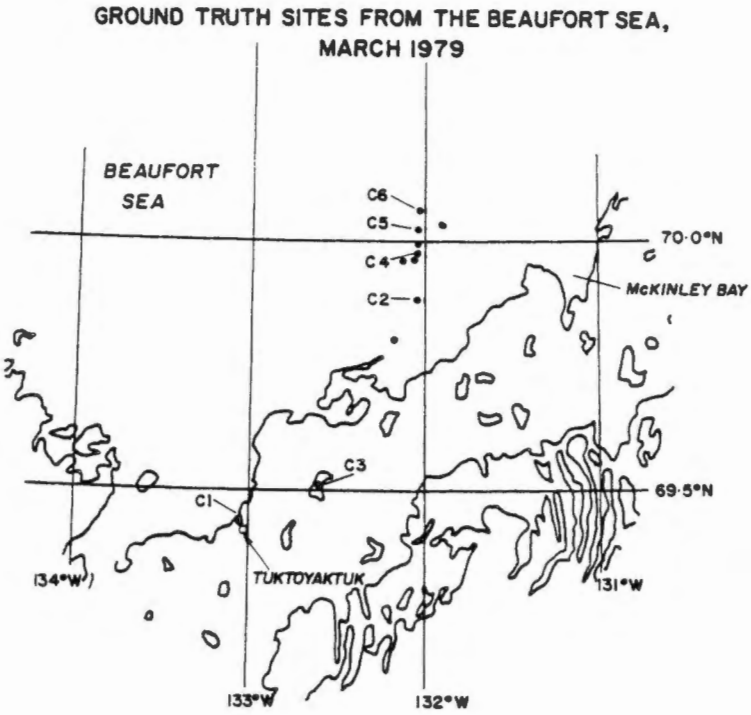

Figure A1.1. Ground Truth Sites from the Beaufort Sea, March, 1979.

Table A1.1 1979 Sea Ice Radar Experiment (SIRE)

LOCATION: Mackenzie Delta/Beaufort Sea AIRCRAFT: NASA LeRC C-131/SLAR

DATE	RUN	ALTITUDE, FT	HDG	ANTENNA	SAMPLING	TIME (Alaska Time)	LATITUDE/LONGITUDE	PHOTOGRAPHY
7 March 1979	01	10,500	000°	D-Both (100 KM Swath)	x3	10:43 11:50	N69°00' W132°30' N72°30' W132°35'	9" Mapping, Vertical 70 mm, Right Side
	02	10,500	090°	D-Both	x3	11:58 12:15	N72°30' W132°35' N72°30' W130°15'	9" Mapping, Vertical 70 mm, Right Side
	03	10,500	180°	D-Both	x3	12:22 13:23	N72°30' W130°15' N69°30' W130°25'	70 mm, Right Side
	04	10,500	289°	D-Both	x3	13:27 14:04	N69°23' W130°45' N69°58' W135°50'	——
	05	10,500	150°	D-Both	x3	14:16 14:45	N69°58' W135°50' N68°32' W133°30'	——
12 March 1979	D1	5,000	000°	C-Right (50 KM Swath)	x8	11:22 12:38	N69°26.5' W132°17.5' N72°54' W131°37'	70 mm, Right Side
	C2	5,000	180°	D-Both	x8	12:48 14:03	N72°40' W131°40' N69°10' W131°45'	——
18 March 1979	01	10,500	000°	D-Both	x8	10:59 12:02	N69°46' W131°50' N73° W131°40'	9" Mapping (1)
	02	5,000	180°	D-Left (50 KM Swath)	x8	12:16 13:31	N73°03' W131°46' N69°30' W131°48'	9" Mapping (1)

(1) Photography along 132°W longitude available from NASA JSC C-130 flight on 18 March 1979

SIRE 1979

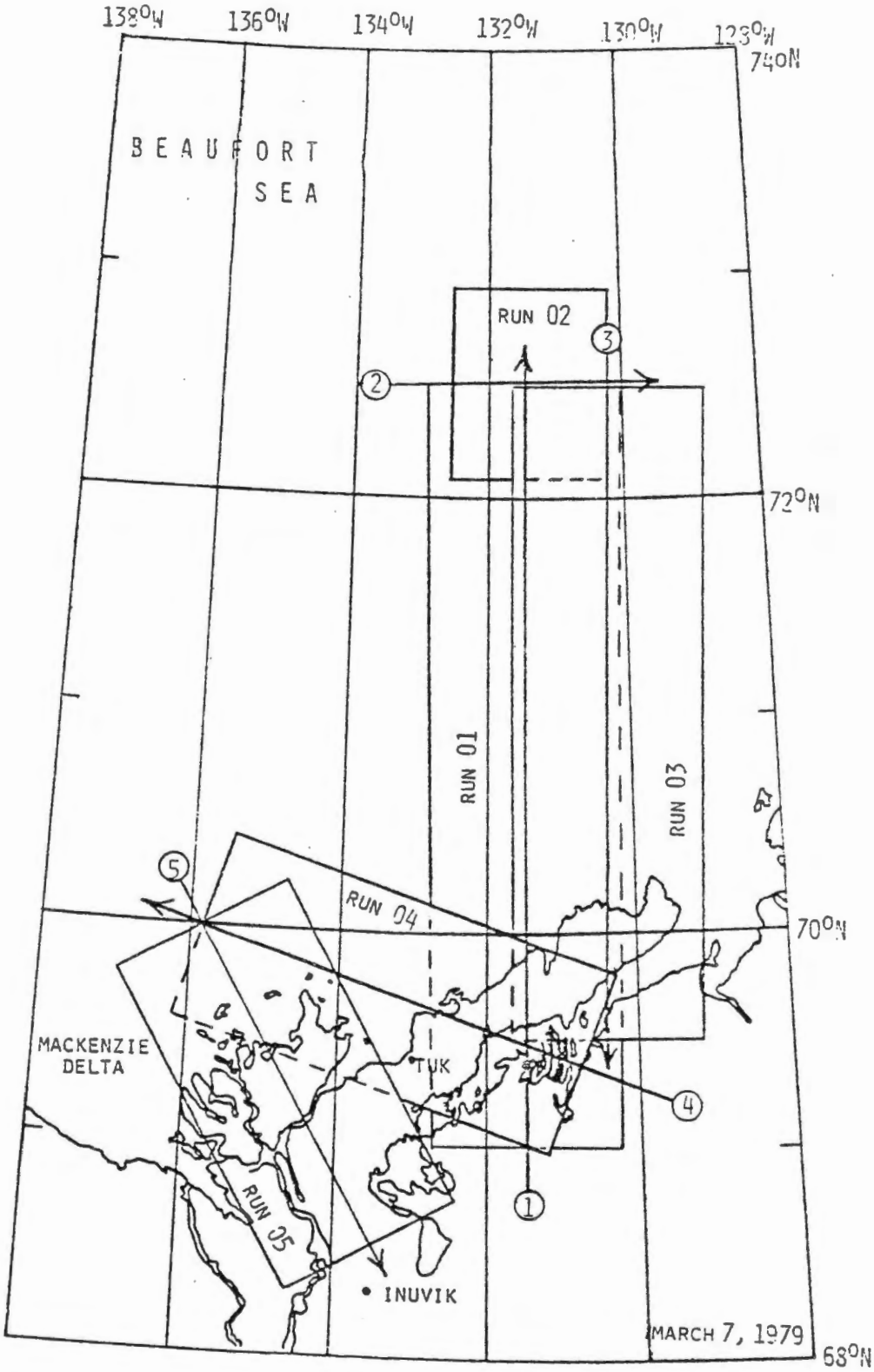

Figure A1.2. NASA Lewis Research Centre C-131/SLAR coverage in Beaufort Sea on March 7, 1979 for Sea Ice Radar Experiment (SIRE).

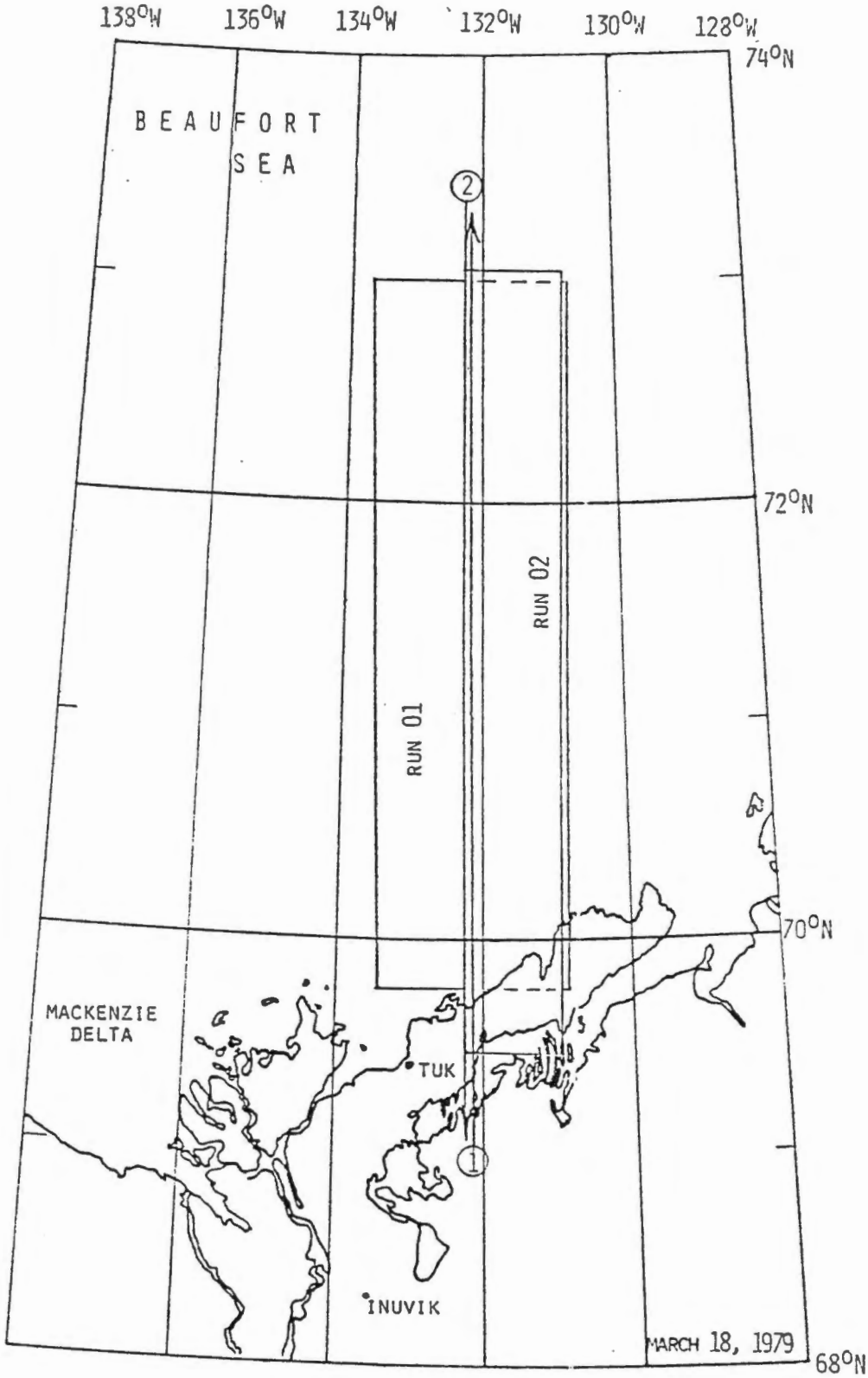

Figure A1.3. NASA Lewis Reserach Centre C-131/SLAR Coverage in Beaufort Sea on March 18, 1979 for Sea Ice Radar Experiment (SIRE).

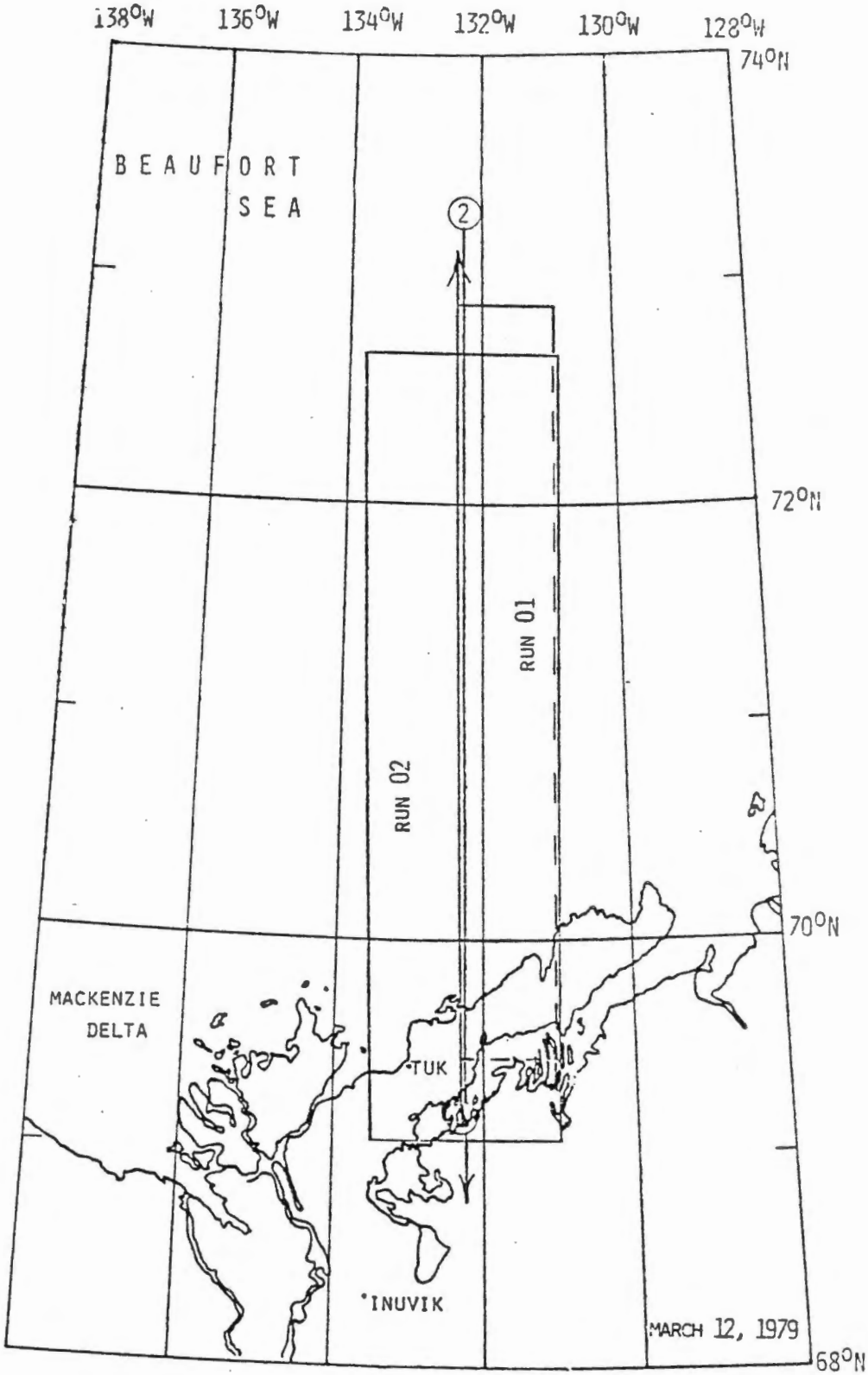

Figure A1.4. NASA Lewis Research Centre C-131/SLAR Coverage in Beaufort Sea on March 12, 1979 for Sea Ice Radar Experimetn (SIRE).

APPENDIX 2

OVERLAPPING DATA FROM THE EASTERN ARCTIC DEPLOYMENT

A2.1 Ground Truth Information from the Eastern Arctic Deployment

Two main ground truthing areas were used in the deployment: one off the west coast of Greenland in the Danish Experiment area and the other near Pond Inlet.

Ground truth data in the Danish Experiment area are reported in "West Greenland Sea Ice Experiment", Gray et al., 1979.

Ground truth data were collected in the Pond Inlet area and are reported in the April 1979 Monthly Report of Data Collected by the Arctic Research Establishment, Pond Inlet, N.W.T. and made available by the Department of Fisheries and Oceans. Data collected include meteorological data, snow and ice surface characteristics and ice core measurements (temperature and salinity). Measurements were made on the day of the SURSAT overflight, and on a routine basis throughout the entire ice season, including regional surveys of grounded floes and icebergs.

A2.2 Flights by Other Aircraft

(1) Eastcan Twin Otter
A photographic mission flown as part of a weekly survey of ice conditions off Labrador during the 1978-79 season.

(2) Atmospheric Environment Service (AES), Ice Reconnaissance Aircraft
A routine Ice Branch mission was flown in the eastern seaboard area approximately one/two days after the Convair-580 sorties. This covered the Labrador, Frobisher Bay and Baffin Bay areas; ice charts are available from Ice Central, AES, Ottawa.

(3) Danish Experiment Aircraft
The Danish scientific program and SURSAT area were overflown using a C-130 carrying three scanning microwave radiometers, SAR and photographic cameras; the Greenland Ice Patrol Twin Otter carried a SLAR and laser profilometer; the ground truth team was supported by a helicopter, (Gray et al., 1979).

(4) NASA Ames Convair-990
An overflight of the Pond Inlet ground truth site occurred on 8 November 1978, with scanning multifrequency microwave radiometer (SMMR), SAR and mapping camera on board.

(5) NASA Wallops P3
The P3 flew in tandem with the Convair-580 on several of the east coast sorties: Frobisher Bay line, Davis Strait line and Danish W/E Cross line. Refer to NORDA report for routes (Ketchum et al. 1980).

APPENDIX 3

TAPE RECORDER CHARACTERISTICS

The raw data from the Active-Passive Experiment profiling sensors were recorded in-flight on 9200 ft. rolls of one-inch tape, by a 14 channel 3M Mincom 110 instrumentation recorder, operated at 30 inch per second (ips) tape speed.

The analogue data channels were FM modulated by FM 1 recording modules (input band width at 30 ips DC to 20 kHz) and the digital data channels were recorded directly.

A3.1 Mincom Track Allocation

Each recorded analogue channel on the tape contains a short segment of one volts root mean square (VRMS) 1 kHz sinusoid at the beginning and end of the tape record for channel calibration purposes.

The tape track allocation is shown in Table A3.1.

A3.2 ADAS MUX Track

ADAS reads and monitors all of the low data rate sensors and formats the sensor data and status information into data frames. Each frame consists of 150 sixteen- bit words as shown in Table A3.2. A new data frame is recorded on tape every 10 ms.

In Table A3.2 the MUX track frame entries, marked GDI, are the Generalized Data Interface channel allocations and contain all data from the 'user sensors'.

The GDI are divided into two groups of 16 channels with each channel labelled by a hexadecimal number. Each of the 32 channels has one 'data' word and one 'status' word. The partitioning of the data between the data word and the status word is dependent on the sensor used but, in general, the data word contains data only and the status word contains the data overflow, sensor interface status and scaling information.

The GDI channel allocations used in the Active-Passive Experiment are shown in Table A3.3.

A3.3 Mincom Table Index and Retrieval Codes

The Active-Passive Experiment took place over a period of two months in two Arctic regions. During this period 10 mincom tapes were recorded.

During the experiment deployments, each tape was labelled with a four-digit field roll number. Upon mission completion, each tape was relabelled with an airborne roll (AR) number which became the tape reference number for storage and retrieval. Several data segments (or flight lines) may be contained on a single tape. Table A3.4 is the Active-Passive Experiment tape index which describes the tape contents and assigns an experiment flight-line number composed of a tape roll number with a flight-line sequence number suffix.

Table A3.1 Mincom Track Allocation and Recording Levels

Track	Recording Card	Signal Recorded	Input Form/Modulation	Signal Level
1	Direct record	Time code	BCD	1V RMS
2	FM 2	Not used		
3	FM 1	Scatterometer vertical combiner	Analogue - double side-band suppressed carrier	1V RMS max
4	FM 1	Radiometer output	Analogue 0-10Hz	1V max
5	FM 1	Scatterometer horizontal combiner suppressed carrier	Analogue - double side-band	1V RMS max
6	FM 2	Not used		
7	Direct record	Tape speed reference	AC sinusoid	1V RMS
8	FM 1	Scatterometer H SIN output	AC 0-8kHz	1V RMS max
9	FM 1	Radiometer thermistor T6	DC	2V max
10	FM 1	Scatterometer H COS output	AC 0-8kHz	1V RMS max
11	FM 1	Radiometer thermistor T7	DC	2V max
12	FM 1	Radiometer thermistor T8	DC	2V max
13	Direct record	ADAS MUX track	Biphase L	1V
14	FM 1	Not used		

Table A3.2 ADAS MUX Track Frame Format

Word	Function
0	Frame phase/frame format header
1	Mincom call number
2	T0 Least significant part of time
3	T1 Most significant part of time
4	Flight line sequence number/frame sequence number
5	Trace
6	Camera firing list
7	GDI error summary
8	1 Hz header
9-18	1 Hz data (very low rate data with 1 Hz repetition rate)
19	Navigation data header
20-31	Navigation data from the INS
32-63	GDI data words
34-95	GDI status words
96-148	Unused locations
149	Flight line sequence number/frame sequence number

Table A3.3 GDI Channel Allocations

GDI Channel	Sensor Interface	Sensor Data
00	Not used	
01	RC10 interface	RC10 camera setting, roll number, frame number
02-04	Not used	
0B	3AD8 (3, 8-bit ADC'S)	Radiometer thermistor voltages from T7, T8 and thermistor reference voltage
0C	3AD8 (3, 7-bit ADC'S)	Radiometer thermistor voltages T4, T5, T6
0D	3AD8 (3, 7-bit ADC'S)	Radiometer thermistor voltages T1,T2, T3
0E	2 AD12 (2, 12-bit ADC'S)	Radiometer output and narrow band filtered scatterometer output
0F	Radar altimeter interface	Radar altimeter output voltage

Table A3.4. Mincom Tape Index for the Active-Passive Sea-Ice Experiment

Mincom Tape	No. of Flight Line	Line Label	Line Location	Line Date	Mean Altitude (ft)	Line Description	Recording Times (GMT)	Line Designation
1063-AR0305	1	78-116-01	Beaufort Sea	13 Mar. 79 (day 0072)	20,000	High altitude wide swath SAR line S/N	00:39:48 - 00:57:47	030501
1066-AR0306	4	78-116-02	Beaufort Sea	13 Mar. 79	12,500	High altitude profiling line	00:14:37 - 01:22:45	030602
		78-116-03		(day 0072)	1500	Low altitude profiling line across T3	01:34:32 - 01:46:48	030603
		78-116-00				Radiometer calibration	01:48:16 - 01:48:48	030600
		78-116-04			1500	Low altitude profiling N/S line	01:59:35 - 02:12:50	030604
1067-AR0307	2	78-116-00	Beaufort Sea	16 Mar. 79		Analogue calibration line (1 VRMS on each channel)	17:19:46 - 17:21:32	030700
		78-116-01		(day 0075)	20,000	Steep depression SAR S/N line	21:40:30 - 22:21:15	030701
1070-AR0308	2	78-116-02	Beaufort Sea	16 Mar. 79	20,000	Steep depression SAR SSE line	22:31:46 - 22:39:25	030802
		78-116-03		(day 0075)	1500	Profiling N/S sensor line	23:09:33 - 23:42:26	030803
1085-AR0322	1	78-116-01	Frobisher Bay	8 Apr. 79 (day 098)	1300	Profiling sensor line	20:42:55 - 21:12:42	032201
1086-AR0323	2	78-116-01	Davis Strait	9 Apr. 79		Steep depression SAR line	17:40:29 - 17:56:31	032301
		78-116-02		(day 099)	2000	Profiling sensor line	18:07:59 - 18:35:42	032302
1088-AR0324	1	78-116-01	Davis Strait	10 Apr. 79	1375	Danish experiment profiling N/S line	15:30:40 - 16:3:14	032401
1090-AR0325	2	78-116-01	Davis Strait	10 Apr. 79	1400			
		78-116-02		(day 100)	1400	Danish experiment profiling W/E line	16:30:49 - 17:00:00	032501
1091-AR0318	1	78-116-02	Melville Bay	11 Apr. 79	1275	Profiling sensor line	15:04:46 - 15:13:46	031802
1093-AR0319	1	78-116-01	Pond Inlet	12 Apr. 79	1500	Profiling sensor line	20:35:33 - 20:53:52	031901

APPENDIX 4

RC-10 CAMERA DATA

All of the nadir-looking photography in the missions of the Active-Passive Experiment was taken with the Wilde RC-10 mapping camera using the configuration given in Section 2.2.3. The Kodak 2402 Aerographic film is in rolls of 250 ft. (76.2 m) and four such rolls were exposed in the Beaufort Sea deployment and six rolls in the Eastern Arctic. The quality of the imaging varies considerably over the data set due to atmospheric conditions.

When ADAS is running, each RC-10 is annotated with a data block giving the following parameters:

1. Latitude
2. Longitude
3. Time
4. Year
5. Flight line
6. Roll
7. ADAS RC-10 frame
8. Project
9. Heading

The location and heading are supplied from the INS; time, from the time code generator; and year, flight line and ADAS frame number are generated by the ADAS.

A mechanical camera frame index number is generated on each frame, regardless of the ADAS status and this frame number together with the roll number was used to reference the photography. Figure A4.1 shows the format of the RC-10 annotation. Table A4.1 is an index of RC-10 imagery information from the Beaufort Sea deployment and Table A4.2 is a similar tabulation for the Eastern Arctic deployment.

Figure A4.1 RC-10 Camera Annotation and Orientation

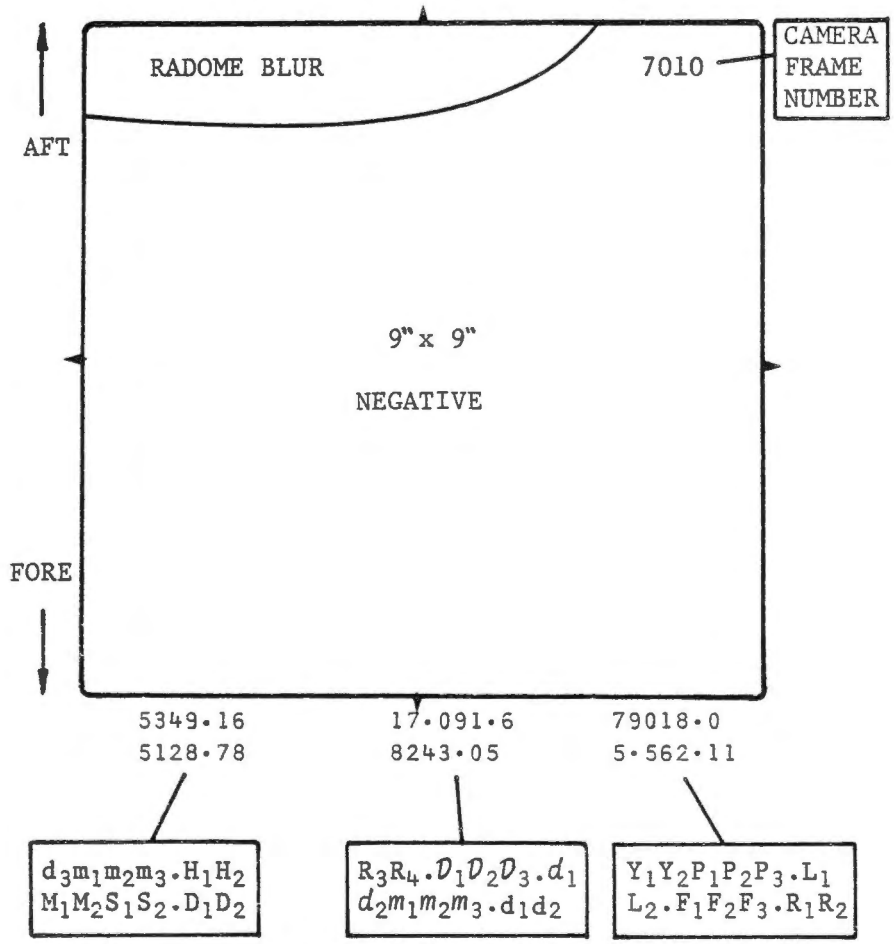

LATITUDE:	$d_1d_2{}^{\circ}\ m_1m_2.m_3'$	$68^{\circ}\ 24.3'$
LONGITUDE:	$d_1d_2d_3{}^{\circ}\ m_1m_2.m_3'$	$055^{\circ}\ 34.9'$
TIME:	$H_1H_2:M_1M_2:S_1S_2.D_1D_2$	16:51:28.78
YEAR:	Y_1Y_2	79
FLIGHT LINE:	L_1L_2	05
ROLL:	$R_1R_2R_3R_4$	1117
ADAS RC-10 FRAME:	$F_1F_2F_3$	562
PROJECT:	$P_1P_2P_3$	018
HEADING:	$\mathcal{D}_1\mathcal{D}_2\mathcal{D}_3$	091°

Table A4.1. Index of RC-10 Imagery From the CCRS Convair-580 Beaufort Sea Deployment, 1979

Date	Line	Roll No.	Altitude (ft)	Over-Lap (%)	Start of Flight Line				End of Flight Line				Annotation Block
					Time (HH:MM:SS.S)	Latitude (DD:MM.M)	Longitude (DDD:MM.M)	Frame No.	Time (HH:MM:SS.S)	Latitude (DD:MM.M)	Longitude (DDD:MM.M)	Frame No.	
March 13	1	1064	12500	20	00:14:31.09	69:43.2	132:18.2	4454	01:00:20	72:52.4	132:25.8	4522	ON
	2	1064	12500	20		1 frame only		4525					
	3	1064	1400	60	01:34:32	72:52:.7	131:02.7	4527	01:46:48	72:27.5	131:54:.1	4651	OFF
	(030603)												
	4	-	1400	-*	-	-	-	-	-	-	-	-	-
March 16	5	1064	20000	20	21:28:14.92	66:19.2	132:38.0	4654	21:31:35.33	69:28.2	133:09.9	4658	ON
	6	1064	20000	20	21:41:56.24	69:39.1	132:08.3	4659	22:20:35.7	72:46.7	132:11.9	4692	ON
	7	1064	20000	20	22:32:44.84	72:51.6	131:01.5	4694	22:38:41.71	72:28.5	131:44.6	4699	ON
	8	1071	1500	20	23:09:33.	73:05.2	131:52.6	4763	23:41:38.83	71:44.6	132:02.3	4947	ON
	(030803)												
March 18	11	1071	3000	20	21:32:36.16			4951	21:39:44.09			5010	ON
	12	1071	3000	20	22:10:17.80	69:26.9	132:10.7	5021	22:16:37.41	69:50.	132:11.	5045	ON
		1073		20	22:21:53.87	70:15.	132:11.	5069	23:12:54.	72:41.0	132:11.0	5257	OFF
	13	1073	1500	20	23:20:	72:35.6	132:00.	5260	23:32:	72:02.	131:59.4	5332	OFF
		1078	1500	20	23:35:26.	71:51.6	131:58.9	5337	00:24:	69:57.9	131:55.9	5621	OFF
		-	1500	-	00:24:	60:57.9	131:55.9	-	00:31:04	69:41.1	131:56.1	-	OFF

* Insufficient light.

Table A4.2. Index of RC-10 Imagery From the CCRS Convair-580 Eastern Arctic Deployment 1979

					Start of Flight Line				End of Flight Line				
Date	Line	Roll No.	Altitude (ft)	Overlap (%)	Time (HH:MM:SS.S)	Latitude (DD:MM.M)	Longitude (DDD:MM.M)	Frame No.	Time (HH:MM:SS.S)	Latitude (DD:MM.M)	Longitude (DDD:MM.M)	Frame No.	Annotation Block
April 7	1	1083	18000	20	20:10:	53:29.5	069:19.6	6308	20:11:	-	-	6311	ON
	1	1083	18000	20	20:27:	-	-	6314	21:09:	54:55.3	056:17.2	6338	ON
April 8	5	1983	1500	20	20:43:	62:30.8	066:06.2	6342	21:12:91	63:18.5	067:27.5	6514	ON
April 9	8	1083	2500	20	18:12:17	66:50.2	055:47.7	6518	18:26:13	66:47.0	057:28.9	6577	ON
		1087	1000	20	18:34:33	66:45.0	058:24.9	6608	18:34:46	66:44.9	058:26.5	6610	ON
April 10	9	1087	18000	20	14:12:47	66:42.7	051:48.3	6635	14:19:48	67:42.7	051:48.3	6641	ON
	11	1087	1500	20	15:30:55	69:07.4	055:54.2	6645	16:03:39	67:38.8	055:50.2	6832	ON
	12	1089	1500	20	16:30:50	68:24.7	058:06.8	6896	16:57:38	68:33.1	054:51.0	7043	ON
	13	1089	1500	20	17:03:44	68:20.1	054:08.0	7044	17:03:55	68:20.0	054:07.0	7048	ON
	14	1089	600	-	17:09:41	68:19.9	054:08.0	7051	1 frame only				
April 11	16	1089	18000	20	14:47:47	70:56.2	055:36.3	7063	15:13:06	72:42.2	056:40.3	7083	ON
	17	1089	18000	20	15:23:26	73:24.3	057:27.3	7086	15:48:54	75:12.2	059:18.1	7105	ON
	18	1089	18000	20	15:55:10	75:29.1	075:50.3	7111	16:02:21	75:50.3	062:	7118	ON
	20	1092	1500	60	17:04:06	76:03.4	063:26.2	7179	17:20:31	75:53.0	066:26.1	7382	ON
April 12	26	1094	1500	60	20:39:24	72:49.0	077:32.6	7471	20:53:23	72:40.6	079:35.3	7619	ON

APPENDIX 5

RADIOMETER ANALYSIS AND CALIBRATION

The 19.35 GHz radiometer on loan to CCRS for this experiment was designed and built by the microwave division of Aerojet-General for the NASA Langley Research Centre. The latter organization built the external waveguide assembly and the horn antenna. The instrument was calibrated by NASA*. Corrections for the antenna gain, the waveguide losses and the waveguide reflections were included in this calibration. This appendix gives equations used in the reduction of the radiometer readings to target brightness temperature, a smoothing algorithm used in removing system noise, and the procedure used to register the radiometer and scatterometer time histories.

A5.1 Reduction of Radiometer Readings to Brightness Temperature

The radiometer output consists of 10 voltage readings corresponding to:

V_1	warm load temperature	$t_{WL}(R_1)$
V_2	hot load temperature	$t_{HL}(R_2)$
V_3	L_2 waveguide temperature	$t_{L2}(R_3)$
V_4	switch temperature	$t_{SW}(R_4)$
V_5	enclosure temperature	$t_{ENC}(R_5)$
V_6	L_1 waveguide temperature	$t_{L1}(R_6)$
V_7	antenna aperture temperature	$t_{ANT}(V_7) = t_7$
V_8	antenna/waveguide junction temperature	$t_{ANT}(V_8) = t_8$
V_9	reference voltage	
V_{10}	radiometer output voltage	

The various temperatures were measured using thermistors as voltage divider elements with the voltage dividers supplied by a constant source. The thermistor resistances, R, are converted to physical temperatures using the calibration curves listed below:

$$t_{WL}(R) = 376.19 - 2.41906 \times 10^{-3} R + 2.65528 \times 10^{-8} R^2 \quad \text{(A1)}$$

$$t_{HL}(R) = 451.512 - 2.2776 \times 10^{-2} R + 1.6839 \times 10^{-6} R^2 \quad \text{(A2)}$$

$$\begin{aligned} t_{L2}(R) = t_{SW}(R) = t_{ENC}(R) &= t_{L1}(R) \\ &= 371.52 - 2.250 \times 10^{-3} R + 3.2942 \times 10^{-8} R^2 \\ &\quad - 2.71296 \times 10^{-13} R^3 + 1.1164 \times 10^{-18} R^4 \\ &\quad - 1.178739 \times 10^{-24} R^5 \end{aligned} \quad \text{(A3)}$$

$$t_{ANT}(V_i) \cdot 77.1565 \times 10^{-0.74922} V_i/G_i + 255.4 \quad \text{(A4)}$$

---

* We are indebted to Dr. W. Linwood Jones of NASA for this work and his cooperation in the project.

In these relations, the thermistor resistances are found from

$$R_i = \frac{200000}{\frac{V_9 \; G_i}{V_i}} - 1 \qquad \text{(A5)}$$

where V_i are the raw output voltages from the radiometer, which have amplifier gain factors G_i. These gain factors are:

G_1 = 10.83
G_2 = 104.5
G_3 = 10.49
G_4 = 11.07
G_5 = 10.26
G_6 = 5.629
G_7 = 4.776
G_8 = 4.414

Once the physical temperatures are found, they are used in the radiometer equation to yield a brightness temperature, T_B. Determined T_B values, however, proved to be offset from accepted results and it was necessary to correct the calculated values empirically. Figure A5.1 is a comparison of calculated T_B and expected results for five points on the calibration curve for the instrument. The two lower temperatures are well known, (Wilheit et al. 1972). The three higher temperatures were obtained by shrouding the radiometer antenna in microwave absorber, placing the instrument in a cold room and varying the ambient temperature. In the figure, it can be seen that a constant offset of ≃ 32 K adequately corrects the results on the full range of measurements, with an uncertainty of ±2 K.

When this correction is included, the brightness temperature is given by:

$$T_B = 2.0165\, t_{H1}\; 0.0601\, t_{SW} - 0.012\, t_{L1} - 0.0667\, t_{L2} - 27.44 + \left[\frac{(V_{OUT} - V_{BL})}{V_{CAL} - V_{BL}}\right] \left[1.9707\, t_{W1} + 0.0458\, t_{SW} - 2.0165\, t_{H1}\right] - 0.1642\, t_7 - 0.6735\, t_8 \qquad \text{(A6)}$$

During the experiment, the instrument was operated in a calibration mode during which V_{BL} and V_{CAL} were determined. Normally these measurements occurred before and after each flight line. During the analysis stages, the radiometer non-imagery disk file was searched for these baseline/calibrate readings in the output, V_9 . Program RADISP was required to display V_9 and extract the averages as indicated in Figure 9 of Section 2.4.2. Averages were taken and are reported for all flight lines in Table A5.1.

Table A5.1. Microwave Radiometer Calibration Data March-April, 1979

File	Baseline Voltage (V)		Calibration Voltage (V)		Ground Speed (knots)	Altitude (ft)	Sample Smoothed
	Average	Samples	Average	Samples			
030501	<.1626>	-	<.7108>	-	250	12500	45
030600	.1560 ±.01	(1-85)	.6912 ±.03	(95-165)	275	12500	41
030602	<.1560>	-	<.6912>	-	275	12500	41
030603	<.1560>	-	<.6912>	-	150	1400	7
030604	.1588 ±.02	(7710-7770)	.6850 ±.02	(7785-7870)	150	1500	9
030701	.1610 ±.01	(10465-10540)	.7090 ±.02	(10560-10645)	300	20000	61
030802	.1619 ±.02	(70-150)	.7121 ±.02	(160-250)	270	20000	67
	.1633 ±.03	(4440-4465)	.7094 ±.03	(4475-4530)			
	<.1626>		<.7108>				
030803	.1609 ±.01	(60-140)	.7085 ±.02	(160-240)	155	1300	7
	.1596 ±.01	(19440-19520)	.7250 ±.02	(19530-19630)			
	<.1603>		<.7168>				
031801	.1593 ±.014	(2460-2550)	.6901 ±.02	(2570-2650)	260	18000	63
031802	.160 ±.02	(1-50)	.6866 ±.02	(60-150)	170	1275	5
	.1582 ±.02	(3200-3280)	.6893 ±.02	(3300-3380)			
	.157 ±.01	(6430-6520)	.6870 ±.02	(6530-6620)			
	.156 ±.01	(9420-9500)	.6852 ±.02	(9510-9600)			
	<.1578>		<.6870>				
031901	.1604 ±.02	(40-120)	.7072 ±.02	(140-220)	160	1500	7
	.1611 ±.01	(3220-3310)	.7041 ±.02	(3320-3400)			
	.1600 ±.01	(6398-6480)	.7019 ±.02	(6490-6570)			
	.158 ±.02	(9570-9650)	.7016 ±.02	(9670-9750)			
	<.1599>		<.7037>				
032201	.1588 ±.01	(80-160)	.7054 ±.02	(180-270)	150	1300	7
032301	.1571 ±.01	(95-175)	.6923 ±.02	(200-275)	265	18000	61
	.1605 ±.01	(3320-3410)	.6958 ±.02	(3430-3500)			
	.1577 ±.01	(6550-6640)	.6913 ±.02	(6660-6740)			
	<.1584>		<.6931>				
032302	.1566 ±.01	(60-140)	.6924 ±.02	(150-230)	175	2000	9
032401	.1677 ±.02	(670-750)	.7276 ±.02	(770-860)	180	1375	7
	.1592 ±.01	(3895-3985)	.6891 ±.05	(3990-4010)			
	<.1635>		<.7084>				
032501	.1576 ±.02	(330-410)	.6965 ±.02	(430-510)	160	1400	7
	.1600 ±.02	(16280-16360)	.6971 ±.02	(16380-16460)			
	<.1588>		<.6968>				
032502	.1582 ±.01	(1480-1570)	.7157 ±.04	(1580-1605)	180	600	3

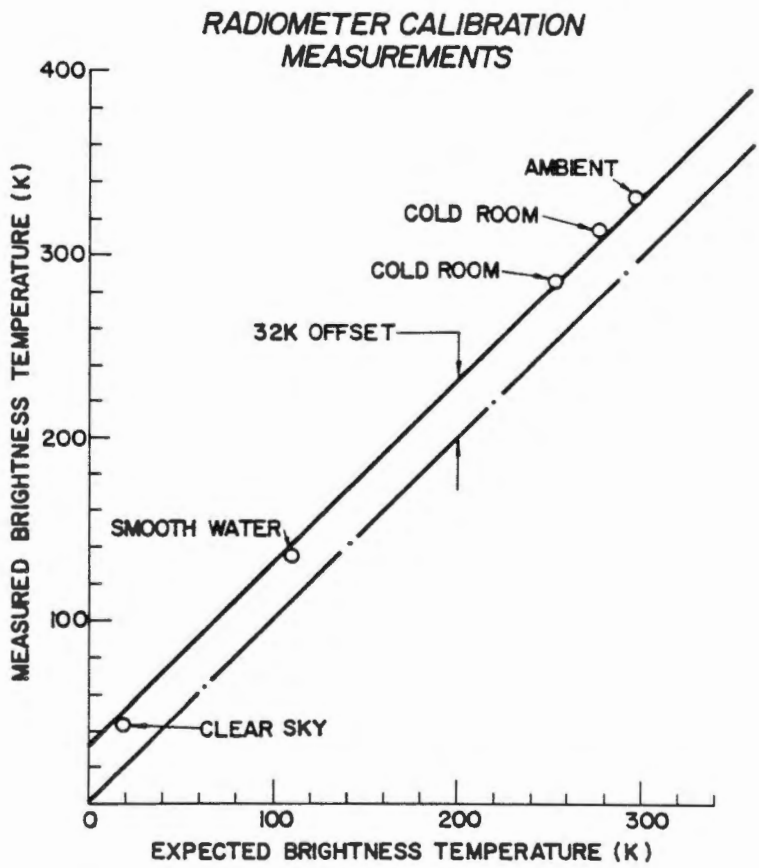

Figure A5.1 Radiometer Calibration Curve.

This figure shows a comparison of measured and expected radiometer brightness temperatures. An apparent offset of 32K is seen in the results which is constant within the range of measurements.

A5.2 Smoothing

The radiometer data was recorded at .01 s and subsequently stripped at 0.1 s intervals. By smoothing the data, this sampling rate could be matched with the radiometer footprint size and integration time. From Figure 6, the time required to cross the radiometer footprint including an instrumental integration time,
τ (0.1 sec), is given by:

$$\tau = \frac{\left[h\left(\tan\left(\theta_o + \frac{\Delta}{2}\right) - \tan\left(\theta_o - \frac{\Delta}{2}\right)\right)\right]}{V_g} \qquad \text{(A7)}$$

where h is the aircraft altitude, θ_o (~ 45°) is the nominal incidence angle of the radiometer, V_g is the ground speed and Δ (~5°) is antenna beam width. Using (A7) and the average flight parameters listed in Table A5.2 a smoothed brightness temperature, T_B', was determined by:

$$T_B'(i) = \sum_{j = i - \frac{N}{2}}^{i + \frac{N}{2}} T_B(j)/N \qquad \text{(A8)}$$

$$\text{and } N = \frac{t}{\Delta t}$$

where N is an odd integer equal to the number of samples in the footprint/integration step of duration t, Δt is the sampling rate and $T_B(j)$ is the brightness temperature for the jth sample. The smoothing operations are done by routine SMOOTH, as indicated in Figure 9.

A5.3 Radiometer - Scatterometer Footprint Alignment

Because the radiometer incidence angle was not known precisely, an estimation was made by comparison of several outstanding features in their respective time histories. (This comparison is aided considerably by inverting the radiometer data, since in general an anticorrelation exists between the H-polarized scattering coefficient and T_B.) The scatterometer and radiometer time histories for 12 events, dispersed in time over the whole mission, were plotted separately, overlaid and shifted until a maximum visual correlation was established.

The time difference so determined, Δt_d, may be related to the mounting or look angle, θ_o, using the relation:

$$\Delta t_d = \frac{h \tan(\theta_o + \theta_p)}{1.687\ V_g} \qquad \text{(A9)}$$

Table A5.2 Radiometer Incidence Angle Determination

Event	Ground Speed V_g (knots)	Altitude h (ft)	Pitch $\theta p(^o)$	Time Offset Δt_d (s)	Antenna Angle (^{o})
E30603.014 (Beaufort Sea)	150	1385	2.90	5.77	43.63
E30803.070	154	1294	2.36	5.38	44.86*
.083	155	1295	2.35	5.32	44.71
.091	154	1294	2.30	5.17	43.77
.101 (Beaufort Sea)	154	1302	2.31	5.38	44.71
E31802.B02	167	1269	3.00	4.97	44.81
.B04 (Melville Bay)	171	1279	2.56	4.63	44.03
E32201.138 (Frobisher Bay)	139	1309	2.95	5.83	43.29*
E32501.001	164	1388	2.73	5.47	44.74
.003	164	1386	2.70	5.24	44.60
.023	166	1401	2.50	5.37	44.54
.044 (Davis Strait)	166	1405	2.46	5.39	44.58
					$<44.3 \pm 0.50^o>$

* Highest and lowest values removed from statistics.

where V_g is the ground speed (knots), h is the altitude (ft.), θ_p is the aircraft pitch (^{o}) and θ_o is the antenna mounting angle (^{o}). Table A5.2 is a listing of the events and offsets used to determine that:

$$\theta_o = 44.3^o \pm 0.5^o$$

Routine EVRDM, indicated in Figure 10, uses θ_o and the aircraft flight parameters to select radiometer data, which corresponds to the scatterometer nadir footprint.

APPENDIX 6

THEORETICAL BACKGROUND OF MICROWAVE RADIOMETRY

In Section A6.1 of this Appendix, some theoretical aspects of the emission and detection of microwaves are considered. The radiometer antenna pattern is included explicitly in the treatment with contributions from both side and main lobes. Those assumptions used in the data reduction to target brightness temperature and emissivity are assessed in Section A6.2. Section A6.3 details the calculation of microwave emissivity, due to Fresnel, for a smooth homogeneous surface appropriate to very young ice forms. In Section A6.4 the relation between dielectric constant and skin depth is given.

A6.1 Microwave Emissivity Determination

If the antenna radiation efficiency is assumed to be unity, the antenna temperature T_m measured at the input of the antenna is given (Moore et al., 1975) by:

$$T_m = \frac{\int_{4\pi} T_A(\Omega)G(\Omega)d\Omega}{\int_{4\pi} G(\Omega)d\Omega} \tag{1}$$

where $G(\Omega)$ is the antenna pattern at the solid angle Ω and $T_A(\Omega)$ is the apparent radiation temperature seen by the antenna in the solid angle Ω.

The apparent temperature $T_A(\Omega)$ is given by:

$$T_A(\Omega) = \frac{1}{L_{atm}}\left\{T_B(\Omega) + T_R(\Omega)\right\} + T_U(\Omega) \tag{2}$$

where $T_B(\Omega)$ is the brightness temperature or the self emission of the surface being measured, $T_R(\Omega)$ is the component of the downward emission impinging on the surface from the upper hemisphere which is scattered into solid angle Ω by the surface, $T_U(\Omega)$ is the upward emission from the atmosphere between the surface and the antenna, and L_{atm} is the atmospheric loss factor between the surface and antenna. L_{atm} attenuates the contribution of $T_B(\Omega)$ and $T_R(\Omega)$.

The measured antenna temperature, T_m, is expressed by:

$$T_m = \alpha_m \langle T_A(\Omega)\rangle_m + (1-\alpha_m)T_{s\ell} \tag{3}$$

$$\langle T_A(\Omega)\rangle_m = \frac{\int_{\Omega_m} T_A(\Omega)G(\Omega)d\Omega}{\int_{\Omega_m} G(\Omega)d\Omega} \tag{4}$$

$$T_{s\ell} = \frac{\int_{4\pi-\Omega_m} T_A(\Omega)G(\Omega)d\Omega}{\int_{4\pi-\Omega_m} G(\Omega)d\Omega} \tag{5}$$

$$\alpha_m = \frac{\int_{\Omega_m} G(\Omega)\,d\Omega}{\int_{4\pi} G(\Omega)\,d\Omega} \tag{6}$$

where Ω_m is the solid angle subtended by the mainlobe of the antenna, α_m is the antenna main lobe efficiency, $< T_A(\Omega) >_m$ is the average of the apparent temperature in the main lobe of the antenna, and $T_{s\ell}$ is the average of the apparent temperature in the side lobe of the antenna.

The value that we would like to know is the average brightness temperature of the surface in the main lobe of the antenna. This is given by:

$$T_B^j(\Omega)>_m = \frac{L_{atm}}{\alpha_m} T_m^j - <T_R^j(\Omega)>_m - \frac{L_{atm}}{\alpha_m}(1-\alpha_m)T_{s\ell}^j - L_{atm} <T_U(\Omega)>_m \tag{7}$$

where the addition of the superscript j denotes horizontal or vertical polarizations.

If we assume that the antenna main lobe efficiency α_m is nearly equal to unity and neglect both the atmospheric loss ($L_{atm} = 1$) and the upward atmospheric emission between the surface and antenna ($< T_U(\Omega) >_m = 0$), the average brightness temperature from the surface in the main lobe of antenna is given by:

$$<T_B(\Omega)>_m = T_m^j - <T_R^j(\Omega)>_m \tag{8}$$

The total contribution of downward emission impinging on the surface from the upper hemisphere, $T_R(\Omega)$, is given by integrating the contribution of the downward emission impinging on the surface from the direction i and scattered to the direction s (into the antenna in solid angle Ω).

The generalized expression of $T_R(\Omega)$ developed by Peake (1959) is given by:

$$T_R^j(\Omega) = \frac{1}{4\pi}\int_{u.h.} d\Omega_i \left\{T_D^j(i)\gamma_{jj}(\vec{s}, \vec{i}) + T_D^k(\vec{i})\gamma_{jk}(\vec{s}, \vec{i})\right\} \tag{9}$$

and the microwave emissivity for polarization j, $\varepsilon^j(\Omega)$, is given by

$$\varepsilon^j(\Omega) = 1 - \frac{1}{4\pi}\int_{u.h.} d\Omega_i \left\{\gamma_{jj}(\vec{s}, \vec{i}) + \gamma_{jk}(\vec{s}, \vec{i})\right\} \tag{10}$$

where $\gamma_{jk}(\vec{s}, \vec{i})$ is the differential scattering coefficient of the radiation from the direction $\vec{s}$, with polarization j, to the direction $\vec{i}$ with polarization k; $T_D(\vec{i})$ is the downward emission of the atmosphere from the direction $\vec{i}$, which forms the upward-looking apparent temperature in that direction. As a first approximation the downward emission, $T_D(\vec{i})$, can be assumed as:

$$T_D^j(\vec{i}) = T_D^k(\vec{i}) = T_D(\theta_i)$$

That is, it is independent of polarization and it depends only on the incidence angle θ_i. A surface can be defined as smooth if its projected height variations are much smaller than the radiation wavelength, (Rayleigh roughness criterion). Under this condition, the differential scattering coefficient will only have a specular component which mathematically can be described by:

$$\gamma_{jk}(\vec{s}, \vec{i}) = \frac{4\pi|\rho_j(\theta_s)|^2}{\sin\theta_s} \delta(\theta_s - \theta_i)\delta(\phi_s + \phi_i)\delta_{jk} \tag{11}$$

where $|\rho_j(\theta_s)|^2$ is the Fresnel (Moore et al., 1975) power reflection coefficient for polarization j.

If (11) is substituted into (9), the result is:

$$T_R^j(\Omega) = T_D(\theta_s)|\rho_j(\theta_s)|^2 \tag{12}$$

Also, if (11) is substituted into (10),

$$\varepsilon^j(\Omega) = 1 - |\rho_j(\theta_s)|^2 \tag{13}$$

From (12) and (13)

$$T_R^j(\Omega) = T_D(\theta_s) \quad (1 - \varepsilon^j(\Omega)) \tag{14}$$

The brightness temperature of the surface can be expressed by:

$$T_B^j(\Omega) = \varepsilon^j(\Omega) \quad T_{surf} \tag{15}$$

where T_{surf} is the thermal temperature of the surface.*

Substituting equations (14) and (15) into (8) gives:

$$\langle\varepsilon^j(\Omega)\ T_{surf}\rangle_m = T_m^j - \langle T_D(\theta_s)\ (1 - \varepsilon^j(\Omega))\rangle_m \tag{16}$$

---

* An additional assumption required at this point is that the ice is in thermal equilibrium with surface temperature T_{surf}.

Assuming that T_{surf} and $T_D(\theta_s)$ vary slowly in the solid angle of antenna main lobe, Ω_m, the average value of microwave emissivity may be computed as:

$$<\varepsilon^j(\Omega)>_m = \frac{T_m^j - T_{sky}^m}{T_{surf} - T_{sky}^m} \tag{17}$$

where $T_D(\theta_s) = T_{sky}^m$ which means the upward looking sky temperature in the antenna pointing direction. For the case of perfectly rough surface model, according to Lambert's law:

$$\gamma_{jj}(\vec{s}, \vec{i}) + \gamma_{jk}(\vec{s}, \vec{i}) = \gamma(\vec{s})\cos\theta_i \tag{18}$$

Substituting (18) into (9), one obtains:

$$\begin{aligned} T_R^j(\Omega) &= \tfrac{1}{2}\ \gamma(s)\int_0^{\pi/2} d\theta_i \sin\theta_i \cos\theta_i T_D(\theta_i) \\ &= \tfrac{1}{2}\gamma(s)\ T_{sky} \end{aligned} \tag{19}$$

where the measured sky temperature is given by:

$$T_{sky} = 2\int_0^{\pi/2} d\theta_i \sin\theta_i \cos\theta_i T_D(\theta_i) \tag{20}$$

Also, if (18) is substituted into (10) the result is:

$$\varepsilon^j(\Omega) = 1 - \tfrac{1}{2}\gamma(\vec{s}) \tag{21}$$

From (20), (21),

$$T_R^j(\Omega) = (1 - \varepsilon^j(\Omega))T_{sky} \tag{22}$$

If equations (15) and (22) are substituted into (8),

$$<\varepsilon^j(\Omega)>_m = \frac{T_m^j - T_{sky}}{T_{surf} - T_{sky}} \tag{23}$$

which is similar to expression (17).

When operating in the microwave region below 20 GHz, and under relatively good weather conditions, T_{sky} is typically an order of magnitude smaller than T_B.

According to the calculation by Wilheit et al. (1972), at 19.35 GHz (1.55 cm), the T_{sky} defined by (20) is ~20 K and according to the Copeland et al. (1966), cited by King (1970), T_{sky} at 1.8 cm wavelength is about 13 K at 45° incidence angle.

In this report, the averaged microwave emissivity in the antenna main lobe is defined as the microwave emissivity, ε, using (23) with T_{sky} = 18 K ± 3 K.

A6.2 Adequacy of Assumptions in Data Reduction to Microwave Emissivity

A6.2.1 The effect of the atmosphere

In the calculation of microwave emissivity, the loss by atmosphere has been neglected ($L_{atm} = 1$) and the contribution of the upward emission from the atmosphere between the surface and antenna has been ignored in (8), ($\langle T_U(\Omega)\rangle_m = 0$). The adequacy of these assumptions will be assessed here. The attenuation by atmosphere L_{atm} between the surface and detector at elevation, H, and incidence angle, θ , is given by:

$$L_{atm} = \exp\left[-\int_0^H \Gamma(z)\sec\theta dz\right] \tag{24}$$

and the upward emission from the atmosphere between the ground and antenna is given by:

$$T_U = \int_0^H dz\Gamma(z)\sec\theta T(z)\exp\left[-\int_Z^H \Gamma(z)\sec\theta dz\right] \tag{25}$$

where T(z) is the temperature of the atmosphere at the height of z, and Γ (z) is the attenuation coefficient of the radiation of the atmosphere per unit path length. For low flying altitudes, the variation of the atmosphere with altitude may be neglected so that $T(z) \simeq T(0)$ and $\Gamma(z) \simeq \Gamma(0)$ in estimating the value of L_{atm} and T_U. Then,

$$L_{atm} = \exp\left[H\Gamma(0)\sec\theta\right] \tag{26}$$

$$T_U = T(0)\left(1 - \exp[-H\Gamma(0)\sec\theta]\right) \tag{27}$$

The absorption coefficient of atmospheric oxygen is about 0.013 (dB/km) and absorption coefficient of water vapour is about 0.020 (dB/km) at sea level (Fraser et al., 1975).

Using H = 1350 ft., (θ=45°) and T(0) = 300 K, L_{atm} and T_U take the values L_{atm} = 1.004 and T_U = 1.3 K. The contribution of L_{atm} and T_U are small and we can put L_{atm} = 1.0 and neglect the term $\langle T_U(\Omega)\rangle_m$.

A6.2.2 Antenna beam efficiency and side lobe contributions

In the calculation of microwave emissivity, the antenna main lobe efficiency, α_m, was assumed nearly equal to unity and the contribution from the antenna side lobe was neglected. Unfortunately, the radiation pattern of the pyramidal horn used in this experiment was not known and thus an assumed radiation pattern must be used to estimate the antenna main lobe efficiency.

Kraus (1950) showed that the H(E)-plane pattern of an H(E)-plane sectoral horn is the same as the H(E)-plane pattern of a pyramidal horn with the same H(E)-plane cross section. The beam widths, in degrees, between half-power points and between first nulls are empirically given as

$56\,\lambda/\ell_E$ and $115\lambda/\ell_E$ respectively for an E-plane rectangular horn, where ℓ_E is the aperture dimension in the E-plane and λ is the wavelength. For an H-plane rectangular horn, the beam widths in degrees, between half-power points and between first nulls are empirically given as $67\,\lambda/\ell_H$ and $172\,\lambda/\ell_H$ respectively, where ℓ_H is the aperture dimension in the H-plane.

The pyramidal horn used in the experiment has $\ell_H = \ell_E \simeq 12.1\lambda$ (λ = 1.55 cm), so the beam widths between half-power points and between first nulls are 4.63^o and 9.5^o respectively in the case of E-plane rectangular horn and are 5.54^o and 14.2^o respectively in the case of H-plane rectangular horn. The average value of beam widths between half-power points 2θ and between first nulls $2\theta_{max}$ are 5.09^o and 11.85^o respectively.

The antenna pattern may be approximated by an axially symetric pattern with the average values of θ_h and θ_{max} as:

$$G(\Omega) = G(\theta) = G_o \exp[-\ell n2\ (\theta/\theta_h)^2] \tag{28}$$

Assuming the antenna power pattern of (28), the antenna main lobe efficiency, α_m , can be calculated by inserting (28) into (6), which becomes:

$$\alpha_m = 1-\exp[-\ell n2\ (\theta_{max}/\theta_h\ )^2] = 0.977 \tag{29}$$

The contribution from the antenna side lobe is given by (5).

To estimate the size of the side lobe contribution, $T_{s\ell}$ may be estimated using the following assumptions:

(1) the incidence angle is 0° (normal incidence),
(2) antenna power pattern $G(\Omega)$ is to be a constant outside the main lobe,
(3) $T_A(\Omega)$ is the emission from a specular ice surface,
(4) horizontal polarization.

With these assumptions,

$T_A(\Omega) = \varepsilon_h\ T_{surf}$, where T_{surf} is the thermal temperature of the surface and ε_h is the emissivity from a specular surface and is given by using Fresnel reflection formula, as described in Section A6.3. For ice, the real part of the relative dielectric constant, ε_r', ($\varepsilon_r >> \varepsilon_r''$), so that the imaginary part of the complex dielectric constant may be neglected in (40) and (41), (see section A6.4).

The contribution of the side lobe, $T_{s\ell}$, is then given by:

$$T_{s\ell} = \frac{\displaystyle\int_{\theta_{max}}^{\pi/2} \sin\theta\ \varepsilon_h(\theta)\ T_{surf}\ d\theta}{\displaystyle\int_{\theta_{max}}^{\pi/2} \sin\theta\ d\theta} \tag{30}$$

Using, (38), (40), and (41) with $\varepsilon_r'' << \varepsilon_r'$.

$$T_{s\ell} \simeq 4 \frac{T_{surf}}{\cos\theta_{max}} \int_{\theta_{max}}^{\pi/2} \sin\theta \frac{(\varepsilon_r' - \sin^2\theta)\cos\theta}{\{\cos\theta + (\varepsilon_r' - \sin^2\theta)\}^2} d\theta \tag{31}$$

Using $\varepsilon_r' \simeq 3.2$, $\theta_{max} = 5.925^o$, $T_{s\ell} = 0.392\ T_{surf}$, and when $T_{surf} = 300$ K, $T_{s\ell} = 118$ K, the contribution of the side lobe level in (7) becomes:

$$\frac{L_{atm}}{\alpha_m} (1-\alpha_m)\ T_{s\ell} \simeq 3 \text{ K}$$

Although this antenna assumption used is used, it usually can be considered that the antenna side lobe contribution can be neglected.

A6.3 Formula to Calculate Microwave Emissivity by Fresnel

If a horizontally or vertically polarized plane wave is incident from the air on a medium which is homogenous and infinite in depth and with a perfectly smooth surface at an incidence angle θ, the horizontally or vertically polarized voltage reflection coefficients ρ_h, ρ_v at the surface which are defined as the ratio of the electric, or respectively the magnetic field amplitude of the reflected wave to that of the incident wave, are expressed by the Fresnel's reflection coefficients as:

(Moore et al., 1975)

$$\rho_h(\theta) = \frac{\cos\theta - \sqrt{\mu_r\varepsilon_r - \sin^2\theta}}{\cos\theta + \sqrt{\mu_r\varepsilon_r' - \sin^2\theta}} \text{, and} \tag{32}$$

$$\rho_v(\theta) = \frac{\mu_r\varepsilon_r \cos\theta - \sqrt{\mu_r\varepsilon_r - \sin^2\theta}}{\mu_r\varepsilon_r \cos\theta + \sqrt{\mu_r\varepsilon_r - \sin^2\theta}} \tag{33}$$

Here θ is the incidence angle, μ_r is the relative dimensionless permeability scaled by the permeability of free space, ε_r is the relative dimensionless dielectric constant scaled by the permittivity of free space. At microwave frequencies, most of the materials on the earth's surface, except ferro-magnetic materials, have a μ_r nearly equal to unity. The dielectric constant, on the other hand, may be a strong function of frequency or water content. In general, ε_r is a complex function composed of a real and imaginary part,

$$\varepsilon_r = \varepsilon_r' - j\varepsilon_r'' \tag{34}$$

where real part, ε_r' is the relative permittivity of the medium and ε_r'' can be expressed in terms of effective conductivity, σ , free space permittivity, ε_o, and frequency, f, as:

$$\varepsilon_r'' = \frac{\sigma}{2\pi f \varepsilon_o} \tag{35}$$

The microwave emissivity for horizontal and vertical polarization, $\varepsilon_h, \varepsilon_v$, from the perfectly smooth surface of the homogeneous medium (in terms of its dielectric properties and thermometric temperature) can be expressed by Fresnel voltage reflection coefficients, ρ_h, ρ_v, as:

$$\varepsilon_h = 1 - |\rho_h|^2 \tag{36}$$

$$\varepsilon_v = 1 - |\rho_v|^2 \tag{37}$$

Putting $\mu_r = 1$ and inserting (32) and (33) into (36), (37) respectively, the result is:

$$\varepsilon_h = \frac{4P\cos\theta}{(\cos\theta + P)^2 + Q^2} \tag{38}$$

$$\varepsilon_v = \frac{4(P\varepsilon_r' + Q\varepsilon_r'')\cos\theta}{(\varepsilon_r'\cos\theta + P)^2 + (\varepsilon_r''\cos\theta + Q)^2} \tag{39}$$

respectively, where:

$$P = \{\tfrac{1}{2}[(\varepsilon_r' - \sin^2\theta) + \sqrt{(\varepsilon_r' - \sin^2\theta)^2 + (\varepsilon_r'')^2}\,]\}^{\frac{1}{2}}, \text{ and} \tag{40}$$

$$Q = \{\tfrac{1}{2}[-(\varepsilon_r' - \sin^2\theta) + \sqrt{(\varepsilon_r' - \sin^2\theta)^2 + (\varepsilon_r'')^2}\,]\}^{\frac{1}{2}} \tag{41}$$

A6.4 Microwave Skin Depth Calculation for Sea Ice

The effective depth of the emitting surface layer, by which most of the emitted energy received at the surface is contributed, is called skin depth. The skin depth is defined as the depth at which the electric or magnetic field magnitude of the transmitted wave will have been reduced to 1/e (37%) of its surface value and the power (which is proportional to the square of the electric or magnetic field amplitude) will have been reduced to 1/e (13.5%) of the transmitted power at the surface. For a homogeneous medium, the skin depth, δ, is given by:

$$\delta = \frac{\lambda}{2\pi}\left\{\frac{\mu_r\varepsilon_r'}{2}\left(\sqrt{1 + (\varepsilon_r''/\varepsilon_r')^2} - 1\right)\right\}^{-\frac{1}{2}} \tag{42}$$

where λ is the wave length of the electromagnetic wave. If the skin depth is expressed in cm, the power attenuation coefficient α (dB/m) is expressed by:

$$\alpha = 868.6\left(\frac{1}{\delta}\right) \tag{43}$$

APPENDIX 7

EXAMPLES OF SEA-ICE CLASSES: RC-10 PHOTOGRAPHY AND MICROWAVE SIGNATURES

Complete examples showing data from all sensors are illustrated in this appendix. Segments from the linear mosaic of aerial photographs referred to in 2.4.1 are displayed with corresponding scatterometer and radiometer time histories to demonstrate features of each sea-ice class. The order of the examples given is generally that of increasing age and ice thickness.

At the top of each ice example, is a segment of the RC-10 mosaic with the aircraft track indicated as a line across the centre. Time histories for the 13.3 GHz scatterometer cross-polarization (HV), like-polarization (HH) and 19.4 GHz H-polarized brightness temperature are shown down the figure, on the same time scale as the photograph. The scatterometer data are indicated for six aft-looking incidence angles. An implicit time shifting, appropriate to the look angle of the sensor, has been made to all data to force alignment of the diagrams with the nadir-looking camera image.

Throughout this example series, vertical centre lines have been used to demark common features. 'Event' boundaries, described in Section 2.4.3 are indicated by dashed vertical lines and event numbers are shown as circled numerals. Detailed graphic summaries of each of the events indicated are further illustrated by accompanying figures.

The accompanying graphs describing the individual events consist of three time histories similar to those above, but for the time segment of the event alone; three scatter plots of the data showing the pairs of data from each of the data types: σ^o_{hh}, σ^o_{hv}, T_B; and a graph indicating the angular dependence of σ^o_{hh} and σ^o_{hv} on incidence angle θ. Tables (the ESF's mentioned in Section 2.4.3) showing the statistics of each of these events are also given.

A7.1 Calm Sea Water

Figure A7.1 illustrates relatively calm sea water from the Danish W/E line adjacent to the wave-broken sea ice shown in Figure A7.19. The sunglint pattern indicated at A shows that the surface waves have an approximate wavelength of 6 m.

The strong angular dependence of the radar backscattering coefficient of water is clearly shown in both polarizations. Water appears more specular than any sea-ice form and its brightness temperature is lower than any of the measured sea-ice classes. These two characteristics make water unambiguously classifiable. The effect of surface roughness due to wind and wave action strongly influences the microwave properties of water however, (Jones et al., 1977) complicating its classification.

Figure A7.1.

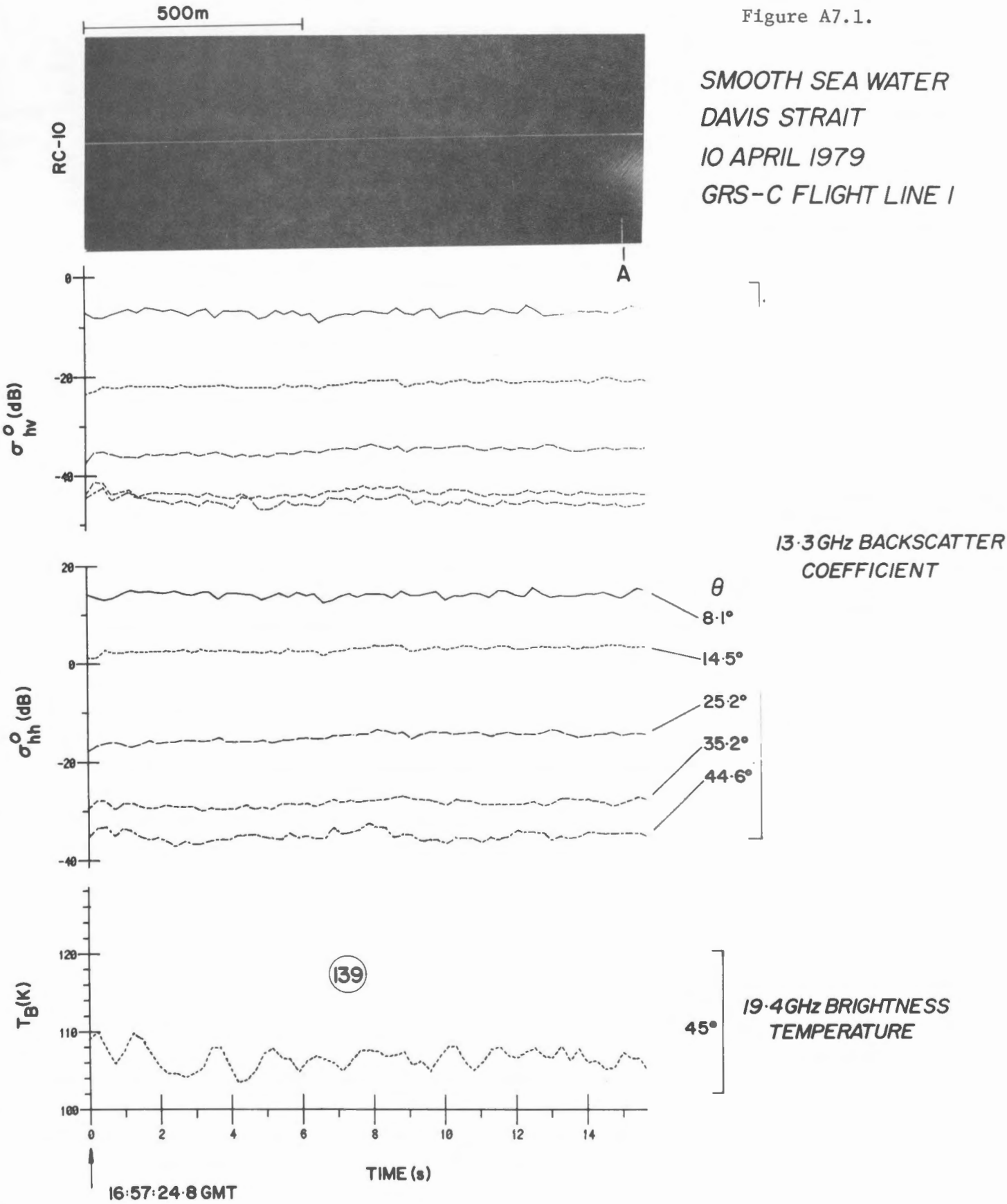
500m
RC-10
A
SMOOTH SEA WATER
DAVIS STRAIT
10 APRIL 1979
GRS-C FLIGHT LINE 1
σ^o_{hv} (dB)
0
-20
-40
13·3 GHz BACKSCATTER COEFFICIENT
σ^o_{hh} (dB)
20
0
-20
-40
θ
8·1°
14·5°
25·2°
35·2°
44·6°
T_B(K)
120
110
100
139
45°
19·4 GHz BRIGHTNESS TEMPERATURE
0
2
4
6
8
10
12
14
TIME (s)
16:57:24·8 GMT

The isotropic nature of the water surface makes it a candidate to estimate system noise. The entire water segment which forms event E32501.139 (further illustrated in Figure A7.2) shows a RMS deviation of less than 1 dB in σ^o for all look angles and 1.7 K in T_B, as indicated in Table A7.1.

A7.2 Frazil and Grease Ice

Large data segments of frazil and grease ice were rare in the flight lines of the Active-Passive Experiment but examples are given in Figures A7.3 and A7.5. The grease ice is distinguished in the RC-10 imagery as cloudy, nebulous grey matter on the surface of an open lead*. The frazil ice component of Figure A7.5 consists of floating plumes of ice spicules beside the newly formed nilas ice of the same figure. Frazil sparcely covers the area and much of this example consists of open water; therefore, this example constitutes a mixture.

The grease ice example shows a reduction in both brightness temperature and radar backscattering coefficient, at all incidence angles, compared with the adjacent first-year ice. It is also interesting to compare the behaviour of grease ice with the calm water example previously discussed. Grease ice shows a very subdued dependence on incidence angle from that of water at all angles which can be seen as a compressed dynamic range in Figure A7.3. The brightness temperature is higher than water by about 30 K but is not as great as might be anticipated from the scattering properties. This ice form must be very lossy and internally rough to account for these two effects. The peculiar microwave properties of grease ice are further illustrated in Figure A7.4 and Table A7.2. Grease ice is also seen as feature A in Figure A7.5. In that case, however, the brightness temperature expresses a mixing with the surrounding nilas.

A7.3 Nilas

All of the nilas identified was from the Eastern Arctic deployment. The class was subdivided into dark and light nilas as outlined in Section 2.4.1.

Examples of nilas ice may be seen in Figures A7.3 and A7.5. This consolidated transparent ice form is plastic, forming in the open area between larger ice floes. It is therefore subject to rafting due to the relative motion of these floes. Finger rafting is clearly seen in Figure A7.3. The degree of rafting and resulting roughness affects the microwave return, as seen in Figure A7.5 where rafting raises the backscattering level by ~ 4 dB.

---

* Unfortunately this effect is lost in the reproduction shown and may only be detected from analysis of the original RC-10 negative.

Figure A7.2.

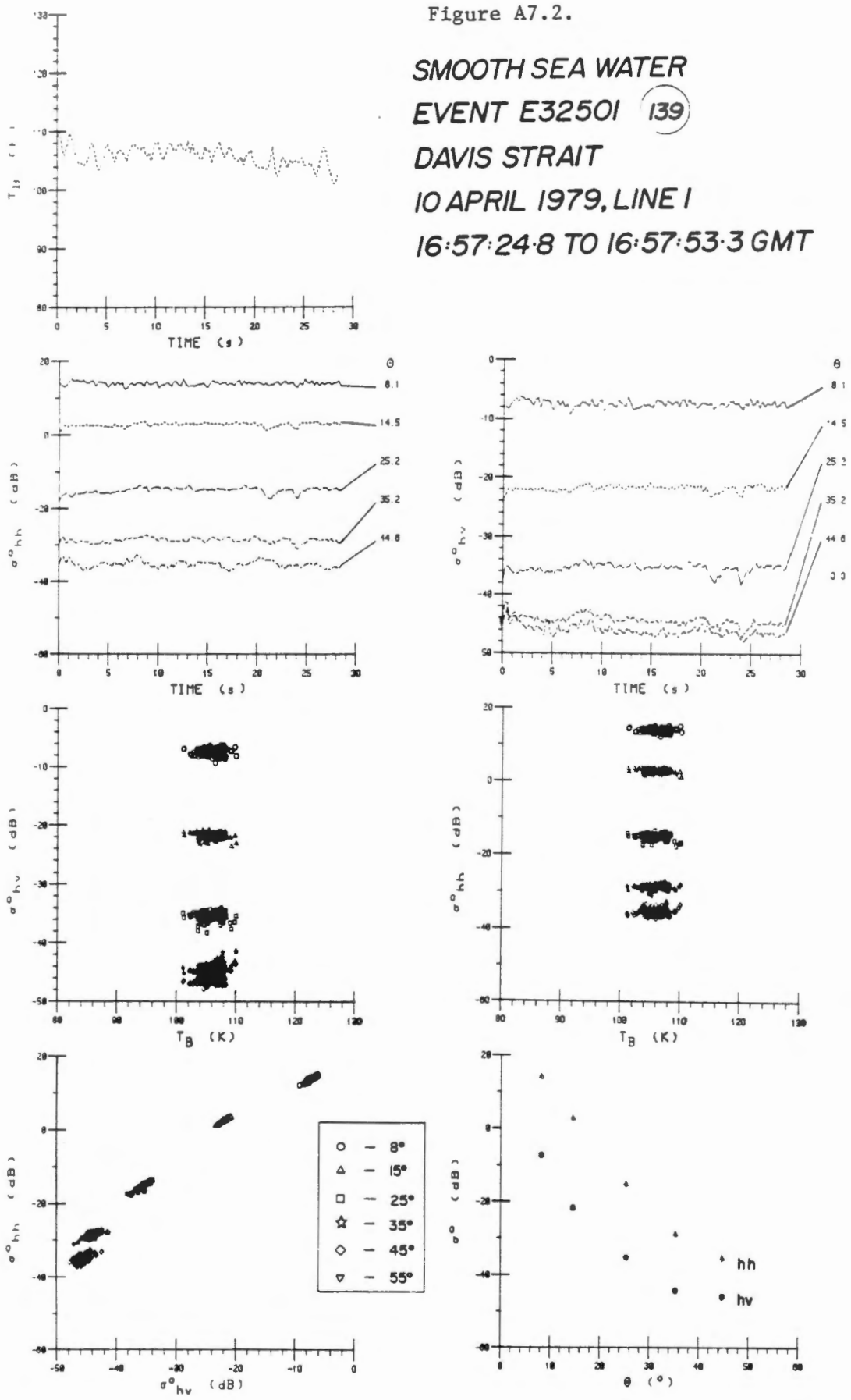
SMOOTH SEA WATER
EVENT E32501 139
DAVIS STRAIT
10 APRIL 1979, LINE I
16:57:24.8 TO 16:57:53.3 GMT
TIME (s)
θ
8.1
14.5
25.2
35.2
44.6
σ°hh (dB)
σ°hv (dB)
TB (K)
σ°hv (dB)
θ (°)
○ — 8°
△ — 15°
□ — 25°
☆ — 35°
◇ — 45°
▽ — 55°
hh
hv

Table A7.1 SUMMARY OF EVENT E32501.139: SMOOTH SEA WATER

EVENT DESCRIPTION:

DANISH E/W 032501 (W)

ASSOCIATED FILES

SCA2:EA2501.L32[64,400]
SCA2:EA2501.C32[64,400]
SCA3:032501.SMO[64,400]
SCA3:032501.INC[64,400]
SCA3:032501.RAD[64,400]
SCA3:D32501.139[64,400]

EVENT TIME

FROM: 100 16:57:24.8160
TO: 100 16:57:53.3280

NAV PARAMETERS	Alt (ft)	Vg (knots)	Lat.	Long.	Pitch	Roll	Drift
	1401.853	159.65	68.3842	-54.8486	2.45	-0.09	3.76
+/-	0.261	0.02	0.0013	0.0034	0.01	0.02	0.02

ANGLES †

	8.060	14.518	25.190	35.222	44.620	0.000

SCATTEROMETER STATISTICS

LMEAN	14.003	2.810	-15.092	-28.693	-35.375	0.000
XMEAN	-7.398	-21.755	-35.417	-44.278	-46.007	0.000
LSTD	0.564	0.559	0.830	0.692	0.906	0.000
XSTD	0.563	0.545	0.748	0.818	0.885	0.000
CORREL COEF	0.931	0.960	0.922	0.605	0.528	0.000

BRIGHTNESS TEMPERATURE STD 1.7 MEAN 105.8

CORRELATION COEFFICIENTS FOR RADIOMETER AND SCATTEROMETER

TB VS LPOL	-0.208	-0.127	-0.074	0.165	0.140	0.000
TB VS XPOL	-0.137	-0.114	0.022	0.430	0.360	0.000

† In this table, the columns of statistics below refer to the six scatterometer angles indicated here. LMEAN, XMEAN, XSTD, and LSTD are the averages and standard deviations of the like- and cross-polarized backscattering coefficients. TB refers to the microwave brightness temperature.

Figure A7.3.

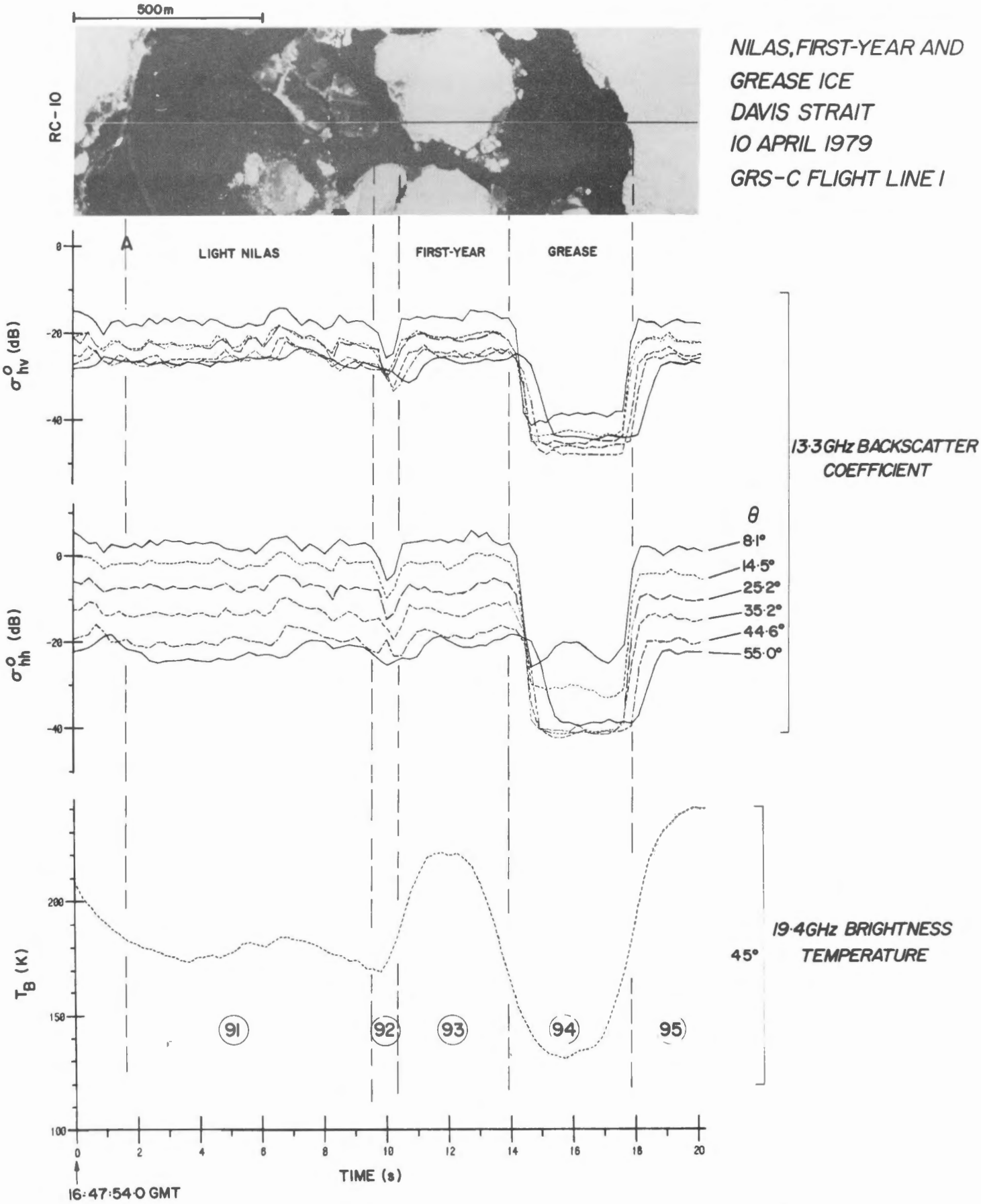
500m
RC-10
NILAS, FIRST-YEAR AND
GREASE ICE
DAVIS STRAIT
10 APRIL 1979
GRS-C FLIGHT LINE I
A
LIGHT NILAS
FIRST-YEAR
GREASE
σ^o_{hv} (dB)
σ^o_{hh} (dB)
0
-20
-40
13·3GHz BACKSCATTER
COEFFICIENT
θ
8·1°
14·5°
25·2°
35·2°
44·6°
55·0°
T_B (K)
200
150
100
45°
19·4GHz BRIGHTNESS
TEMPERATURE
91
92
93
94
95
0
2
4
6
8
10
12
14
16
18
20
TIME (s)
16:47:54·0 GMT

Figure A7.4.

GREASE ICE
EVENT E32501 (94)
DAVIS STRAIT
10 APRIL 1979, LINE 1
16:48:09.1 TO 16:48:11.1

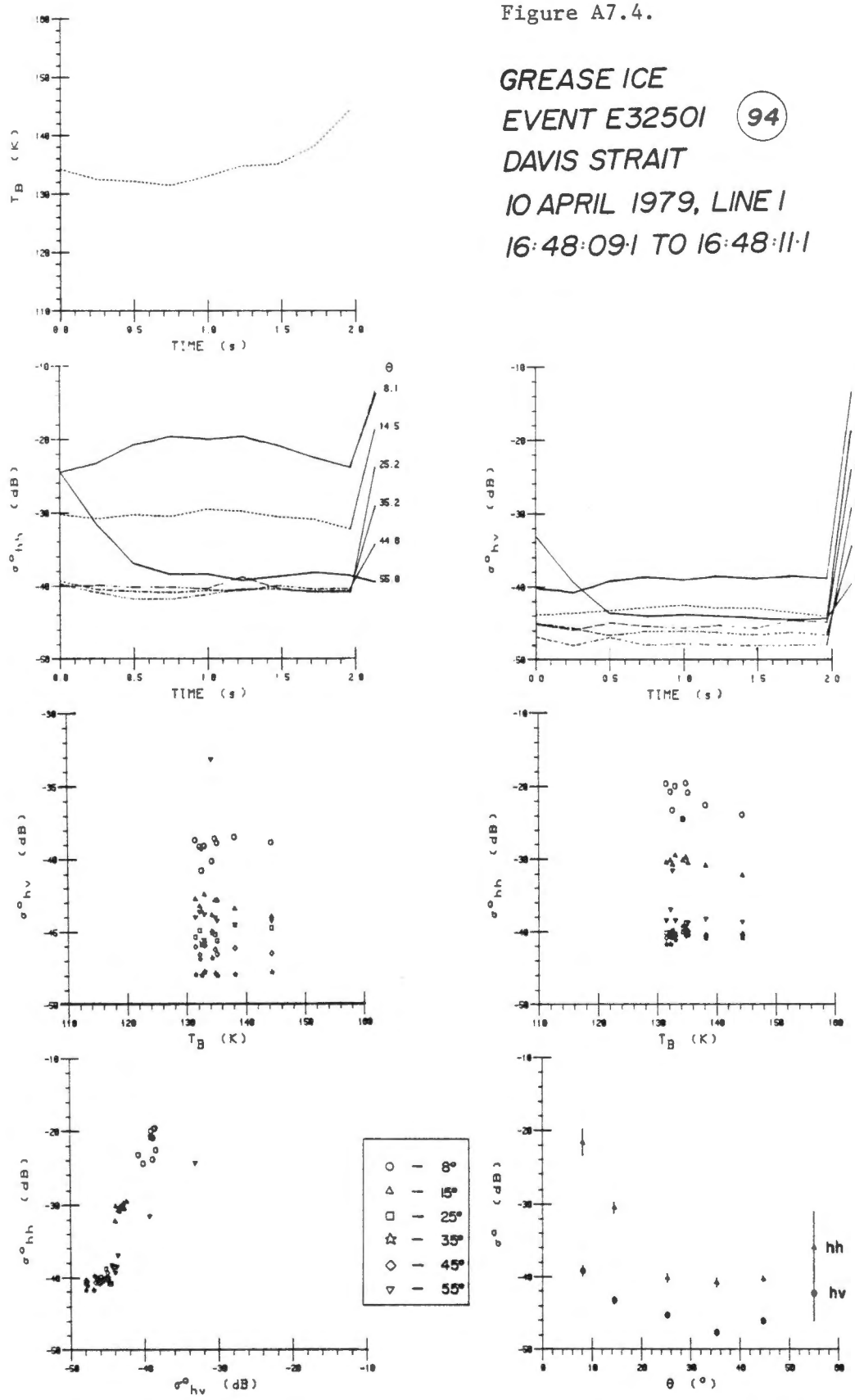

Table A7.2 SUMMARY OF EVENT E32501.094: GREASE ICE

EVENT DESCRIPTION:
DANISH E/W 032501 (R)

ASSOCIATED FILES
SCA2:EA2501.L20[64,400]
SCA2:EA2501.C20[64,400]
SCA3:032501.SMO[64,400]
SCA3:032501.INC[64,400]
SCA3:032501.RAD[64,400]
SCA3:D32501.094[64,400]

EVENT TIME
FROM: 100 16:48: 9.1000
TO: 100 16:48:11.3000

NAV PARAMETERS		Alt (ft)	Vg (knots)	Lat.	Long.	Pitch	Roll	Drift
		1409.000	160.55	68.4151	-55.9700	2.33	0.13	3.29
	+/-	0.000	0.01	0.0000	0.0000	0.00	0.01	0.00

ANGLES †						
	8.060	14.515	25.190	35.218	44.619	54.981

SCATTEROMETER STATISTICS

LMEAN	-21.700	-30.553	-40.191	-40.860	-40.384	-36.067
XMEAN	-39.211	-43.258	-45.267	-47.704	-46.117	-42.343
LSTD	1.789	0.737	0.577	0.620	0.431	4.681
XSTD	0.734	0.502	0.419	0.449	0.478	3.584
CORREL COEF	0.570	0.701	-0.346	0.083	0.537	0.993

BRIGHTNESS TEMPERATURE STD 3.8 MEAN 135.1

CORRELATION COEFFICIENTS FOR RADIOMETER AND SCATTEROMETER

TB VS LPOL	-0.436	-0.855	-0.787	0.365	0.160	-0.252
TB VS XPOL	0.434	-0.459	0.881	-0.388	-0.307	-0.268

† In this table, the columns of statistics below refer to the six scatterometer angles indicated here. LMEAN, XMEAN, XSTD, and LSTD are the averages and standard deviations of the like- and cross-polarized backscattering coefficients. TB refers to the microwave brightness temperature.

Figure A7.5.

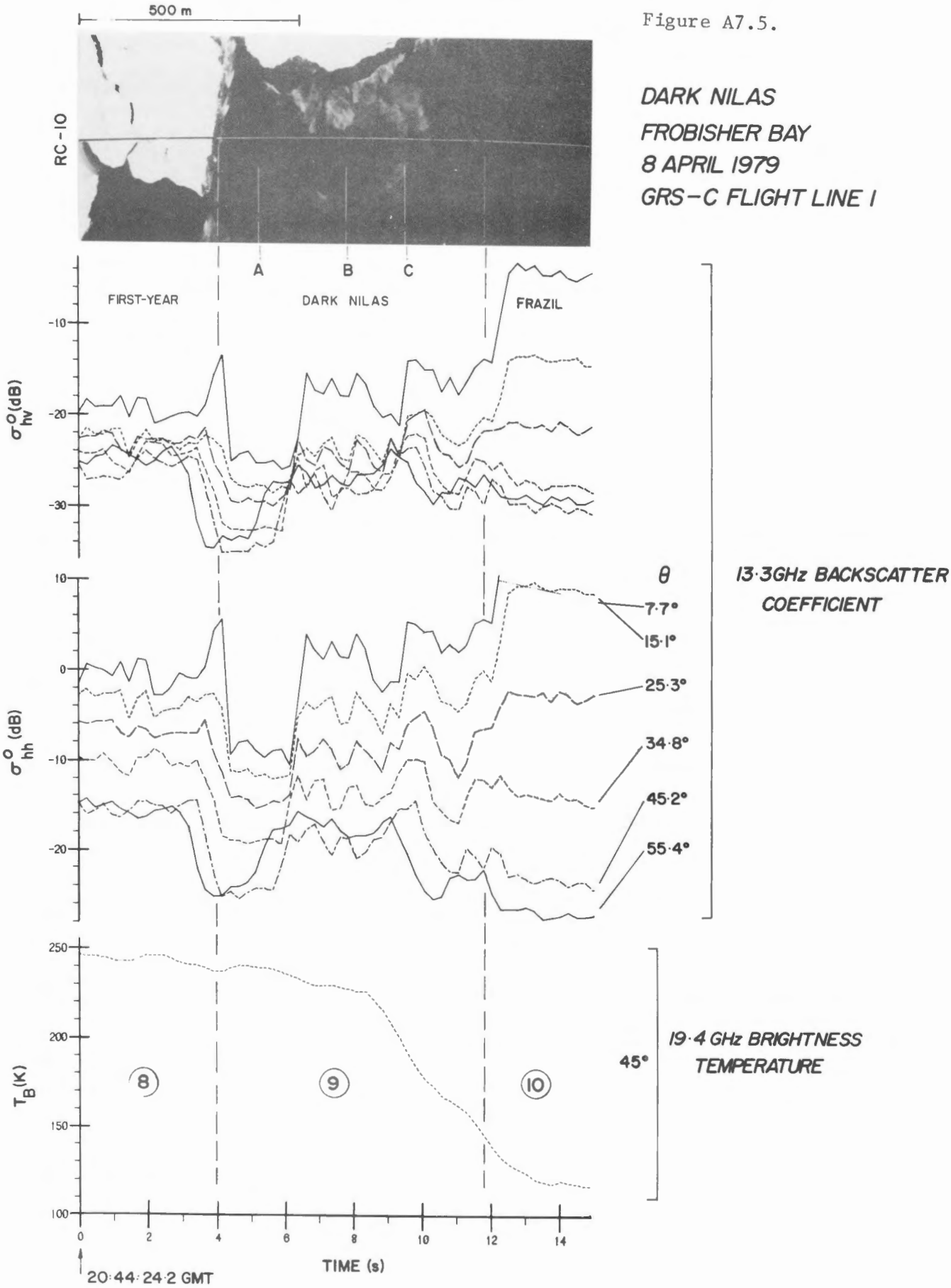
500 m
RC-10
A
B
C
FIRST-YEAR
DARK NILAS
FRAZIL
DARK NILAS
FROBISHER BAY
8 APRIL 1979
GRS-C FLIGHT LINE I
σ^o_{hv}(dB)
-10
-20
-30
σ^o_{hh} (dB)
10
0
-10
-20
θ
7·7°
15·1°
25·3°
34·8°
45·2°
55·4°
13·3GHz BACKSCATTER COEFFICIENT
T_B(K)
250
200
150
100
8
9
10
45°
19·4 GHz BRIGHTNESS TEMPERATURE
0
2
4
6
8
10
12
14
TIME (s)
20:44:24·2 GMT

Both Figure A7.3 and A7.5 show little or no contrast in the backscattering behaviour of nilas and adjacent first-year ice. There is, however, an unmistakable delineation shown in Figure A7.2 between the brightness temperature of first-year and nilas, which demonstrates the importance of radiometer measurements for discriminating younger ice forms. Figure A7.6 and Table A7.3 summarize the light nilas data from event E32501.091 while the dark nilas data of event E32201.009 are given in Figure A7.7 and Table A7.4.

A7.4 Grey and Grey-white Ice

Figure A7.8 shows a section of young ice between two regions of first-year ice from the March 13, 030603 line in the Beaufort Sea. That considerable ice motion has ensued, is inferred from numerous rafts, ridges and cracks seen in the RC-10 image. Ice roughness varies considerably across the figure, with the central section being extensively mottled. Little radar contrast may be seen in the scatterometer time histories between any of the ice forms shown. The ridges and rafts give the textural contrasts of ~ 4 dB in the cross-polarized data; however, in the like-polarized return, the ridging and rafting contrasts are largely lost. The radiometer time history indicates a high sensitivity to the rough ice region.

Grey ice shows a brightness temperature of ~ 7 K lower than the neighbouring, thicker grey-white ice, while the radar backscattering coefficient increases ~3 dB. The detailed comparison of the grey and grey-white forms may be seen in Figures A7.9 and A7.10 with accompanying Tables A7.5 and A7.6.

A7.5 First-year Ice

The most frequently occurring form of sea ice in the experiment was first-year, although several different forms were observed. Examples of smooth, rough, snow-drifted, rotten and wave-broken first-year ice are given in the subsections below.

A7.5.1 Smooth first-year ice

Figure A7.11 shows part of an extensive sample of smooth first-year ice represented by event E30803.172. The ice is cold (~-30° C) from the Beaufort 030803 N/S line. This smooth ice is adjacent to, and older than, the smooth grey-white ice seen in Figure A7.8.

The region is crossed by several low pressure ridges at A, B, C, D, E, F, but the dominant impression is of a smooth, uniform white surface. The short, whisker-like features extending predominantly from the east face (upper portion of the figure) of these ridges are drifted snow. Ridges are shown in slightly better contrast in the cross-polarized radar returns, with little dependence on incidence angle. The contrast disappears for ridges marked at E and F in the smaller incidence angles.

Figure A7.6.

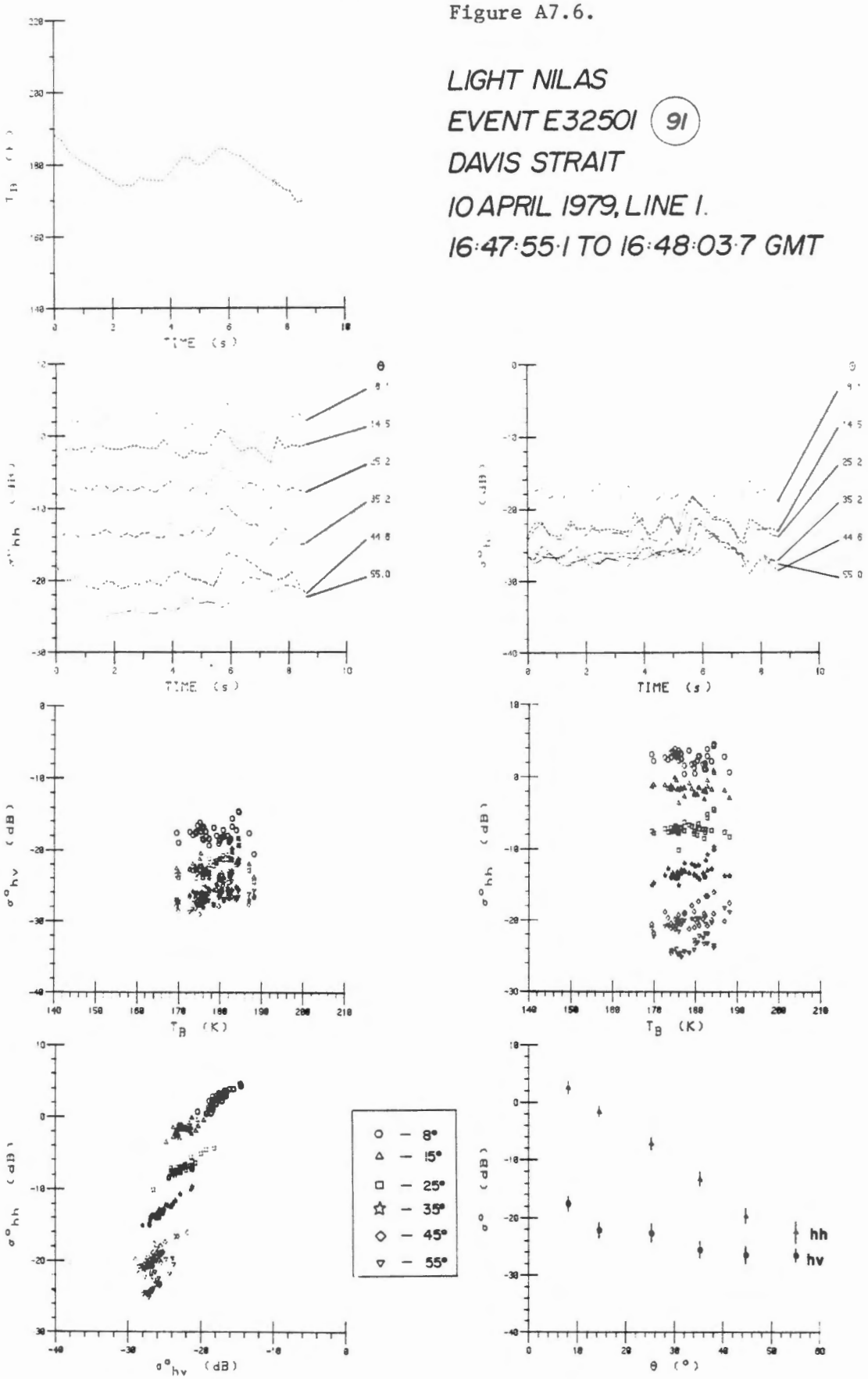
LIGHT NILAS
EVENT E32501 (91)
DAVIS STRAIT
10 APRIL 1979, LINE I.
16:47:55.1 TO 16:48:03.7 GMT
TIME (s)
θ
8°
14.5
25.2
35.2
44.8
55.0
σ°hh (dB)
σ°hv (dB)
T_B (K)
σ° (dB)
θ (°)
hh
hv
○ — 8°
△ — 15°
□ — 25°
☆ — 35°
◇ — 45°
▽ — 55°

Table A7.3 SUMMARY OF EVENT E32501.091: LIGHT NILAS

EVENT DESCRIPTION:

DANISH E/W 032501 (N)

ASSOCIATED FILES

SCA2:EA2501.L20[64,400]
SCA2:EA2501.C20[64,400]
SCA3:032501.SMO[64,400]
SCAT:032501.INC[64,400]
SCAT:032501.RAD[64,400]
SCA3:D32501.091[64,400]

EVENT TIME

FROM: 100 16:47:55.1000
TO: 100 16:48: 3.7000

NAV PARAMETERS	Alt (ft)	Vg (knots)	Lat.	Long.	Pitch	Roll	Drift
	1408.125	160.68	68.4155	-55.9921	2.41	0.08	3.32
+/-	0.350	0.03	0.0000	0.0018	0.02	0.03	0.01

ANGLES †

8.060	14.515	25.190	35.218	44.619	54.981

SCATTEROMETER STATISTICS

LMEAN	2.522	-1.630	-7.185	-13.241	-19.611	-22.478
XMEAN	-17.606	-22.205	-22.662	-25.583	-26.424	-26.526
LSTD	1.027	0.898	1.041	1.210	1.366	1.872
XSTD	1.211	1.361	1.597	1.481	1.430	1.096
CORREL COEF	0.876	0.756	0.911	0.962	0.848	0.421

BRIGHTNESS TEMPERATURE STD 4.4 MEAN 178.5

CORRELATION COEFFICIENTS FOR RADIOMETER AND SCATTEROMETER

TB VS LPOL	-0.290	-0.103	0.322	0.563	0.572	0.323
TB VS XPOL	-0.037	0.362	0.417	0.515	0.590	0.691

† In this table, the columns of statistics below refer to the six scatterometer angles indicated here. LMEAN, XMEAN, XSTD, and LSTD are the averages and standard deviations of the like- and cross-polarized backscattering coefficients. TB refers to the microwave brightness temperature.

Figure A7.7.

RAFTED DARK NILAS
EVENT E32201 9
FROBISHER BAY
8 APRIL 1979, LINE I
20:44:30.5 TO 20:44:32.7 GMT

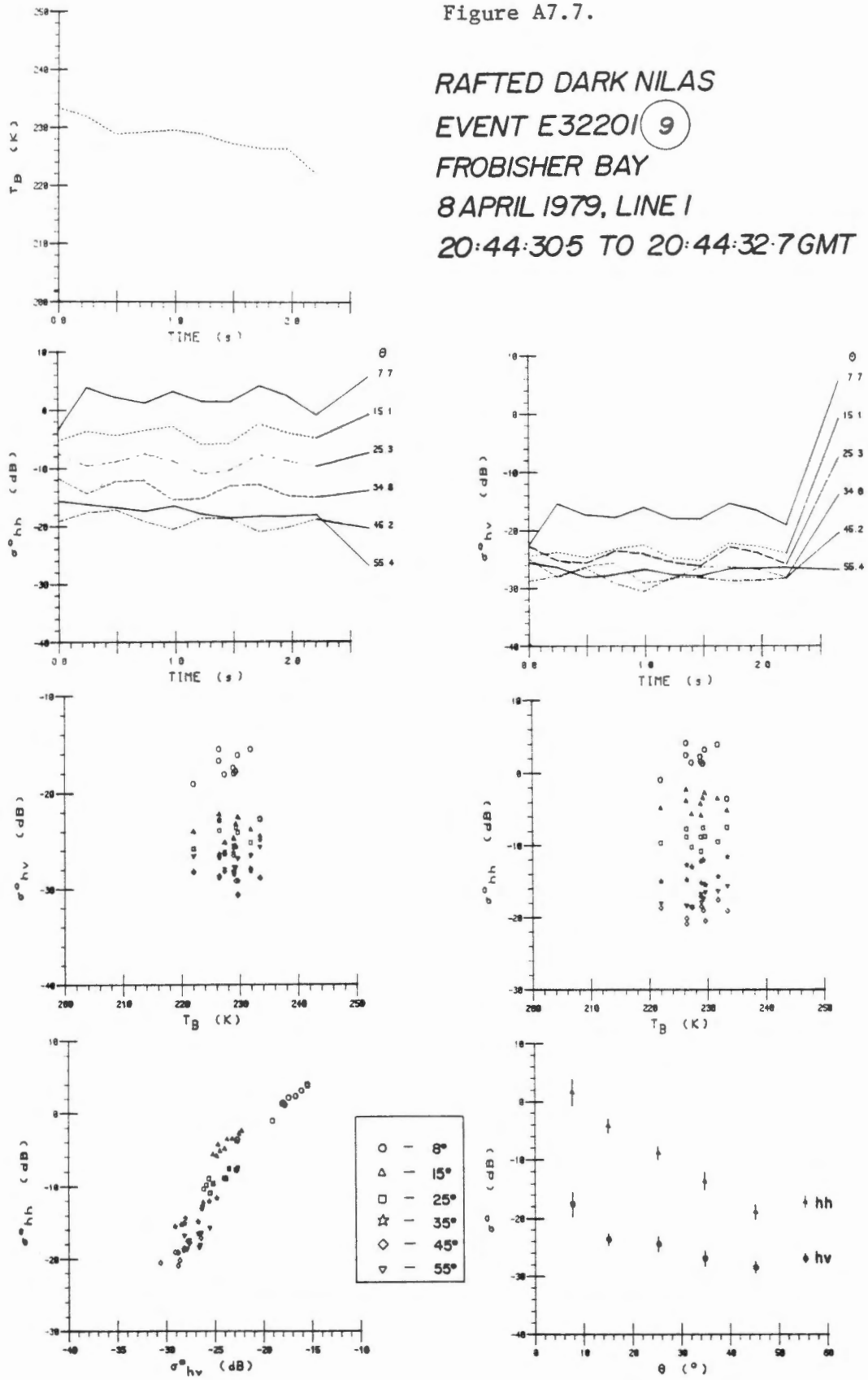

Table A7.4 SUMMARY OF EVENT E32201.009: RAFTED NILAS

EVENT DESCRIPTION:

FROBISHER BAY 032201 SE/NW (RAFTED NILAS)

ASSOCIATED FILES

SCA2:EA2201.L01[64,400]
SCA2:EA2201.C01[64,400]
SCA3:032201.SM0[64,400]
SCA3:032201.INC[64,400]
SCA3:032201.RAD[64,400]
SCA3:D32201.009[64,400]

EVENT TIME

FROM: 98 20:44:30.5000
TO: 98 20:44:32.9000

NAV PARAMETERS		Alt (ft)	Vs (knots)	Lat.	Long.	Pitch	Roll	Drift
		1271.000	152.10	62.4285	-65.8932	3.15	0.87	-4.49
	+/-	1.000	0.08	0.0000	0.0000	0.11	0.48	0.50

ANGLES †

7.690	15.066	25.260	34.810	45.226	55.450

SCATTEROMETER STATISTICS

LMEAN	1.530	-4.234	-8.990	-13.670	-19.064	-17.383
XMEAN	-17.690	-23.766	-24.543	-26.997	-28.498	-27.010
LSTD	2.215	1.145	1.113	1.396	1.163	0.953
XSTD	2.014	0.986	1.224	1.315	0.994	0.772
CORREL COEF	0.984	0.904	0.871	0.925	0.794	0.396

BRIGHTNESS TEMPERATURE STD 3.0 MEAN 228.4

CORRELATION COEFFICIENTS FOR RADIOMETER AND SCATTEROMETER

TB VS LPOL	-0.471	-0.319	0.549	0.776	0.513	0.858
TB VS XPOL	-0.573	-0.689	0.535	0.550	-0.015	0.220

† In this table, the columns of statistics below refer to the six scatterometer angles indicated here. LMEAN, XMEAN, XSTD, and LSTD are the averages and standard deviations of the like- and cross-polarized backscattering coefficients. TB refers to the microwave brightness temperature.

Figure A7.8.

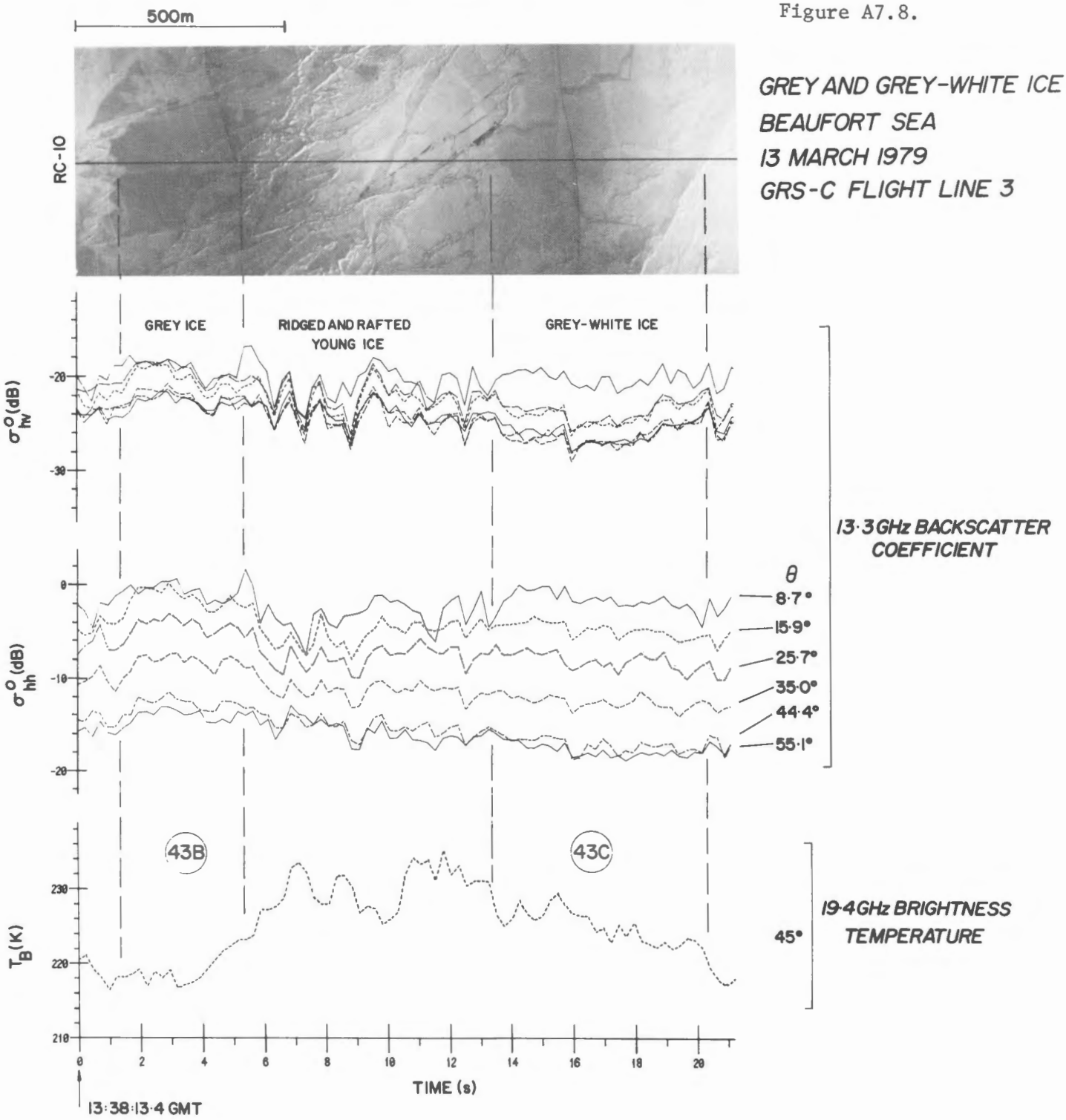
500m
RC-10
GREY AND GREY-WHITE ICE
BEAUFORT SEA
13 MARCH 1979
GRS-C FLIGHT LINE 3
GREY ICE
RIDGED AND RAFTED YOUNG ICE
GREY-WHITE ICE
σ^0_{hv}(dB)
-20
-30
13·3 GHz BACKSCATTER COEFFICIENT
θ
8·7°
15·9°
25·7°
35·0°
44·4°
55·1°
σ^0_{hh}(dB)
0
-10
-20
43B
43C
T_B(K)
230
220
210
45°
19·4 GHz BRIGHTNESS TEMPERATURE
0
2
4
6
8
10
12
14
16
18
20
TIME (s)
13:38:13·4 GMT

 Figure A7.9

GREY ICE
EVENT E30603 43B
BEAUFORT SEA
12 MARCH 1979, LINE 3
01:38:15.1 TO 01:38:16.6 GMT

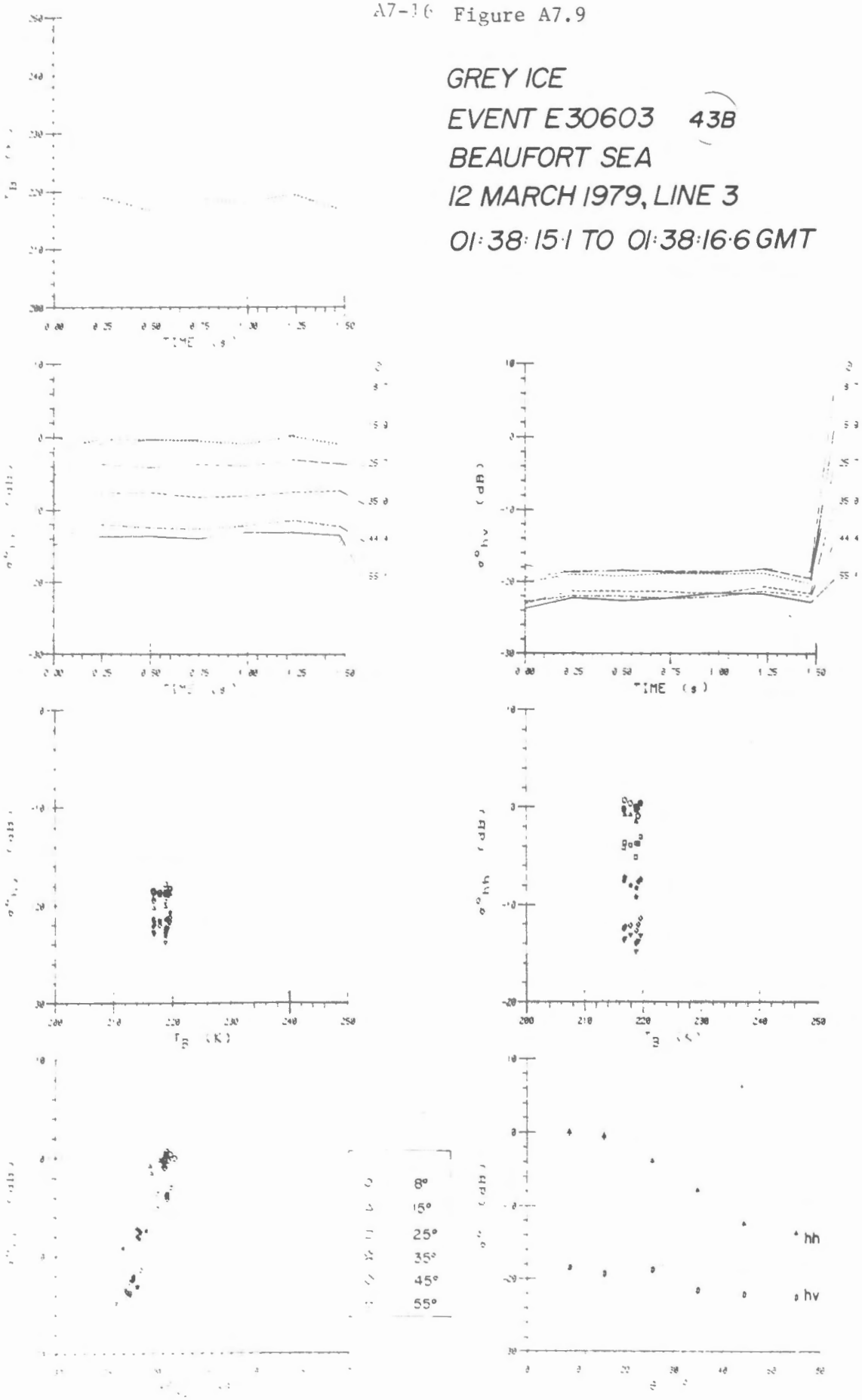

Table A7.5 SUMMARY OF EVENT E30603.43B: GREY ICE

EVENT DESCRIPTION:

BEAUFORT 030603 LINE (GREY)

ASSOCIATED FILES

SCAT:BA0603.L05[64,400]
SCAT:BA0603.C05[64,400]
SCA3:030603.SMO[64,400]
SCAT:030603.INC[64,400]
SCAT:030603.RAD[64,400]
SCA3:D30603.43B[64,400]

EVENT TIME

FROM: 71 1:38:15.1000
TO: 71 1:38:16.7000

NAV PARAMETERS	Alt (ft)	Vg (knots)	Lat.	Long.	Pitch	Roll	Drift
	1379.000	145.83	72.7720	-131.3049	3.40	-0.68	-0.75
+/-	0.000	0.03	0.0000	0.0000	0.01	0.02	0.01

ANGLES †						
	8.715	15.865	25.664	34.964	44.446	55.098

SCATTEROMETER STATISTICS

LMEAN	-0.050	-0.582	-3.929	-7.897	-12.454	-13.715
XMEAN	-18.493	-19.339	-18.811	-21.609	-22.107	-22.481
LSTD	0.507	0.532	0.607	0.610	0.734	0.537
XSTD	0.337	0.580	0.502	0.688	0.435	0.698
CORREL COEF	0.227	0.738	0.612	0.824	0.932	0.873

BRIGHTNESS TEMPERATURE STD 1.1 MEAN 218.3

CORRELATION COEFFICIENTS FOR RADIOMETER AND SCATTEROMETER

TB VS LPOL	0.055	-0.454	-0.373	-0.348	-0.319	-0.208
TB VS XPOL	0.302	-0.246	-0.296	-0.387	-0.297	-0.206

† In this table, the columns of statistics below refer to the six scatterometer angles indicated here. LMEAN, XMEAN, XSTD, and LSTD are the averages and standard deviations of the like- and cross-polarized backscattering coefficients. TB refers to the microwave brightness temperature.

Figure A7.10.

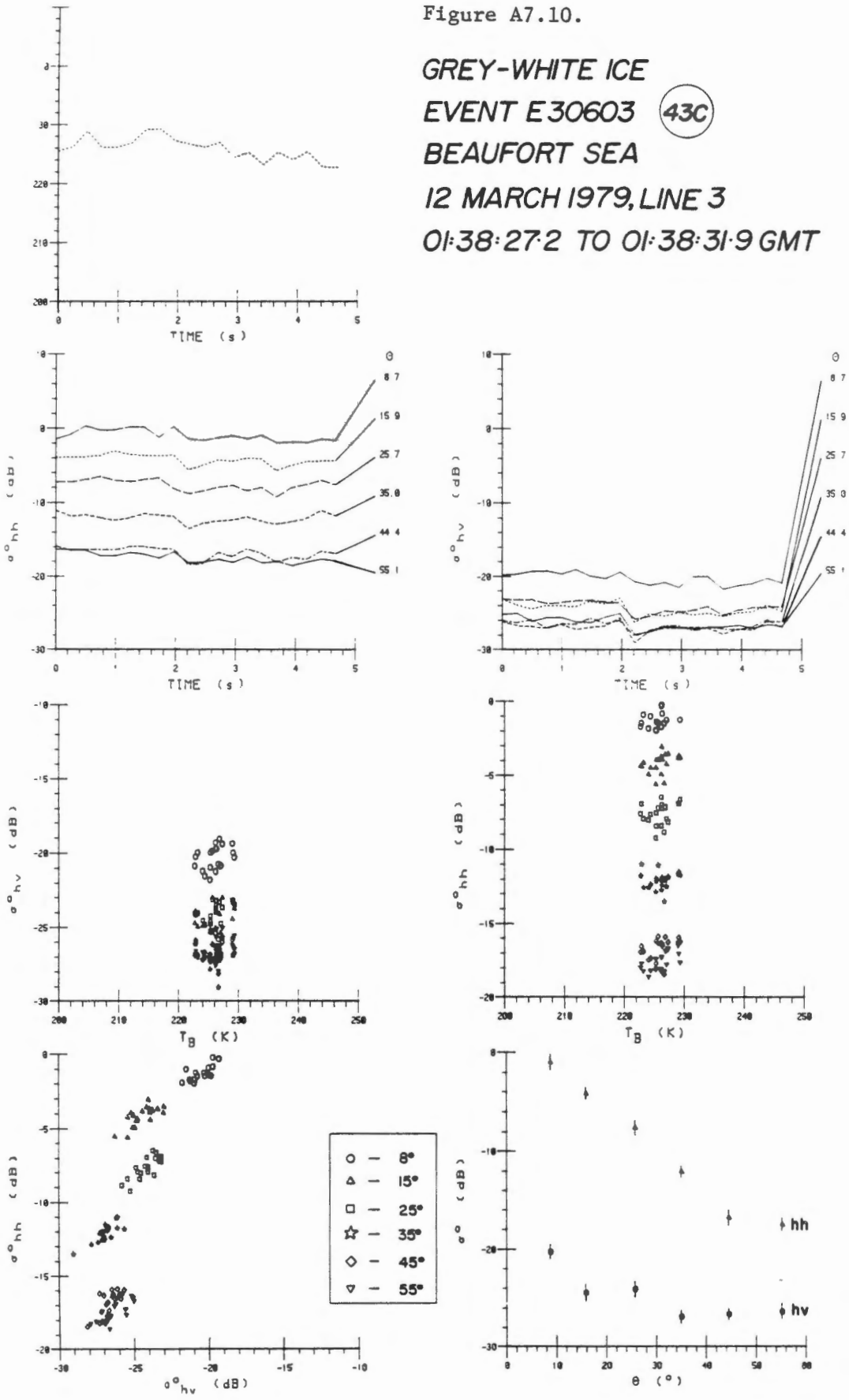
GREY-WHITE ICE
EVENT E30603
43C
BEAUFORT SEA
12 MARCH 1979, LINE 3
01:38:27.2 TO 01:38:31.9 GMT
TIME (s)
θ
8.7
15.9
25.7
35.0
44.4
55.1
σ°hh (dB)
σ°hv (dB)
TB (K)
σ° (dB)
θ (°)
hh
hv
8°
15°
25°
35°
45°
55°

Table A7.6 SUMMARY OF EVENT E30603.43C: GREY-WHITE ICE

EVENT DESCRIPTION:

BEAUFORT 030603 LINE (LIGHT)

ASSOCIATED FILES

SCAT:BA0603.L05[64,400]
SCAT:BA0603.C05[64,400]
SCA3:030603.SMO[64,400]
SCAT:030603.INC[64,400]
SCAT:030603.RAD[64,400]
SCA3:D30603.43C[64,400]

EVENT TIME

FROM: 71 1:38:27.2000
TO: 71 1:38:32. 0

NAV PARAMETERS	Alt (ft)	Vg (knots)	Lat.	Long.	Pitch	Roll	Drift
	1380.750	145.66	72.7642	-131.3202	3.35	-0.29	-0.67
+/-	0.250	0.02	0.0049	0.0070	0.01	0.03	0.03

ANGLES †

	8.715	15.865	25.664	34.964	44.446	55.098

SCATTEROMETER STATISTICS

LMEAN	-1.003	-4.215	-7.627	-12.103	-16.830	-17.520
XMEAN	-20.303	-24.455	-24.113	-26.945	-26.679	-26.418
LSTD	0.751	0.642	0.737	0.588	0.776	0.670
XSTD	0.775	0.834	0.782	0.697	0.596	0.813
CORREL COEF	0.792	0.735	0.807	0.800	0.735	0.763

BRIGHTNESS TEMPERATURE STD 1.9 MEAN 225.9

CORRELATION COEFFICIENTS FOR RADIOMETER AND SCATTEROMETER

TB VS LPOL	0.706	0.512	0.378	0.033	0.389	0.506
TB VS XPOL	0.531	0.451	0.396	-0.073	0.364	0.510

† In this table, the columns of statistics below refer to the six scatterometer angles indicated here. LMEAN, XMEAN, XSTD, and LSTD are the averages and standard deviations of the like- and cross-polarized backscattering coefficients. TB refers to the microwave brightness temperature.

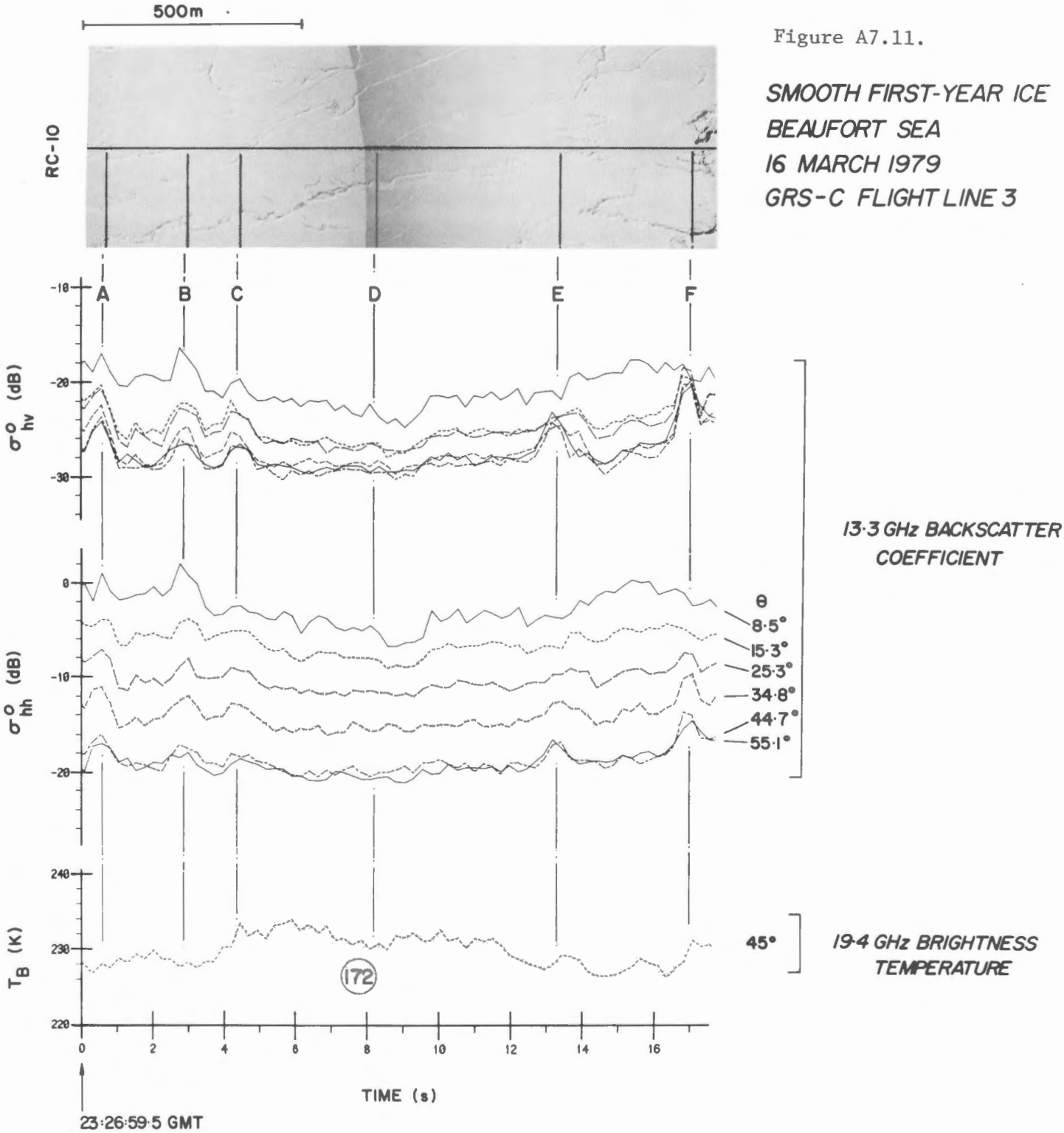

Figure A7.11.

SMOOTH FIRST-YEAR ICE
BEAUFORT SEA
16 MARCH 1979
GRS-C FLIGHT LINE 3

Figure A7.12

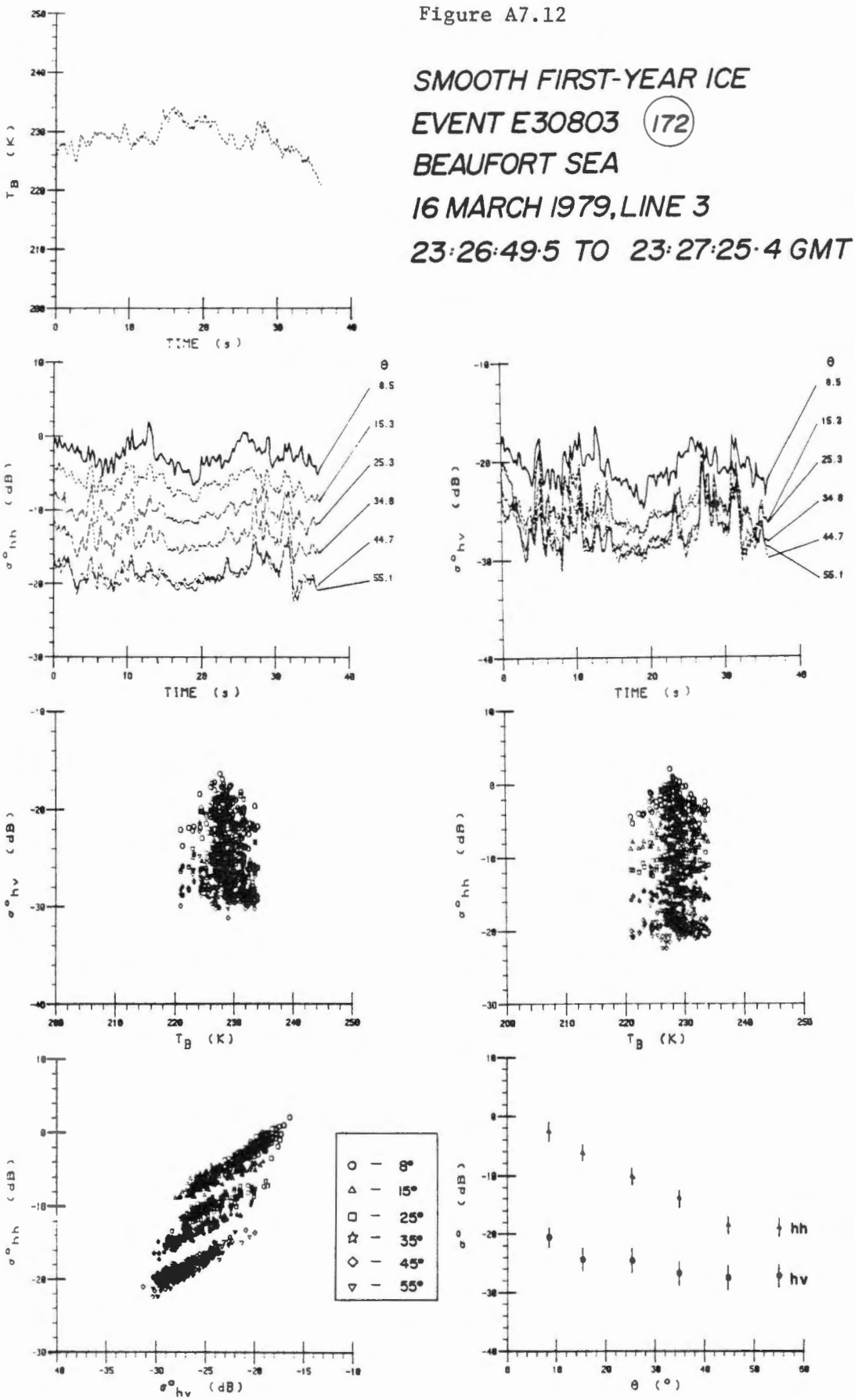
SMOOTH FIRST-YEAR ICE
EVENT E30803 (172)
BEAUFORT SEA
16 MARCH 1979, LINE 3
23:26:49.5 TO 23:27:25.4 GMT
TIME (s)
θ
8.5
15.3
25.3
34.8
44.7
55.1
σ°hh (dB)
σ°hv (dB)
TB (K)
8°
15°
25°
35°
45°
55°
hh
hv
θ (°)

Table A7.7 SUMMARY OF EVENT E30803.172: SMOOTH FIRST-YEAR ICE

EVENT DESCRIPTION:

BEAUFORT 030803 N/S (F)

ASSOCIATED FILES

SCA2:BA0803.L19[64,400]
SCA2:BA0803.C19[64,400]
SCA3:030803.SMO[64,400]
SCAT:030803.INC[64,400]
SCAT:030803.RAD[64,400]
SCA3:D30803.172[64,400]

EVENT TIME

FROM: 75 23:26:49.5000
TO: 75 23:27:25.6000

NAV PARAMETERS	Alt (ft)	Vg (knots)	Lat.	Long.	Pitch	Roll	Drift
	1303.444	155.88	72.3670	-131.9876	2.18	0.43	-0.74
+/-	0.234	0.01	0.0000	0.0025	0.01	0.03	0.01

ANGLES †

	8.490	15.268	25.250	34.778	44.727	55.069

SCATTEROMETER STATISTICS

LMEAN	-2.622	-6.259	-10.140	-13.922	-18.446	-18.859
XMEAN	-20.578	-24.310	-24.547	-26.701	-27.470	-27.150
LSTD	1.637	1.361	1.368	1.503	1.529	1.618
XSTD	1.692	1.991	2.093	2.066	2.055	1.942
CORREL COEF	0.915	0.813	0.902	0.929	0.926	0.915

BRIGHTNESS TEMPERATURE STD 2.5 MEAN 228.7

CORRELATION COEFFICIENTS FOR RADIOMETER AND SCATTEROMETER

TB VS LPOL	-0.254	-0.031	-0.010	-0.036	-0.071	-0.115
TB VS XPOL	-0.267	-0.129	-0.124	-0.145	-0.231	-0.216

† In this table, the columns of statistics below refer to the six scatterometer angles indicated here. LMEAN, XMEAN, XSTD, and LSTD are the averages and standard deviations of the like- and cross-polarized backscattering coefficients. TB refers to the microwave brightness temperature.

Figure A7.13.

ROUGH FIRST-YEAR ICE
BEAUFORT SEA
16 MARCH 1979
GRS-C FLIGHT LINE 3

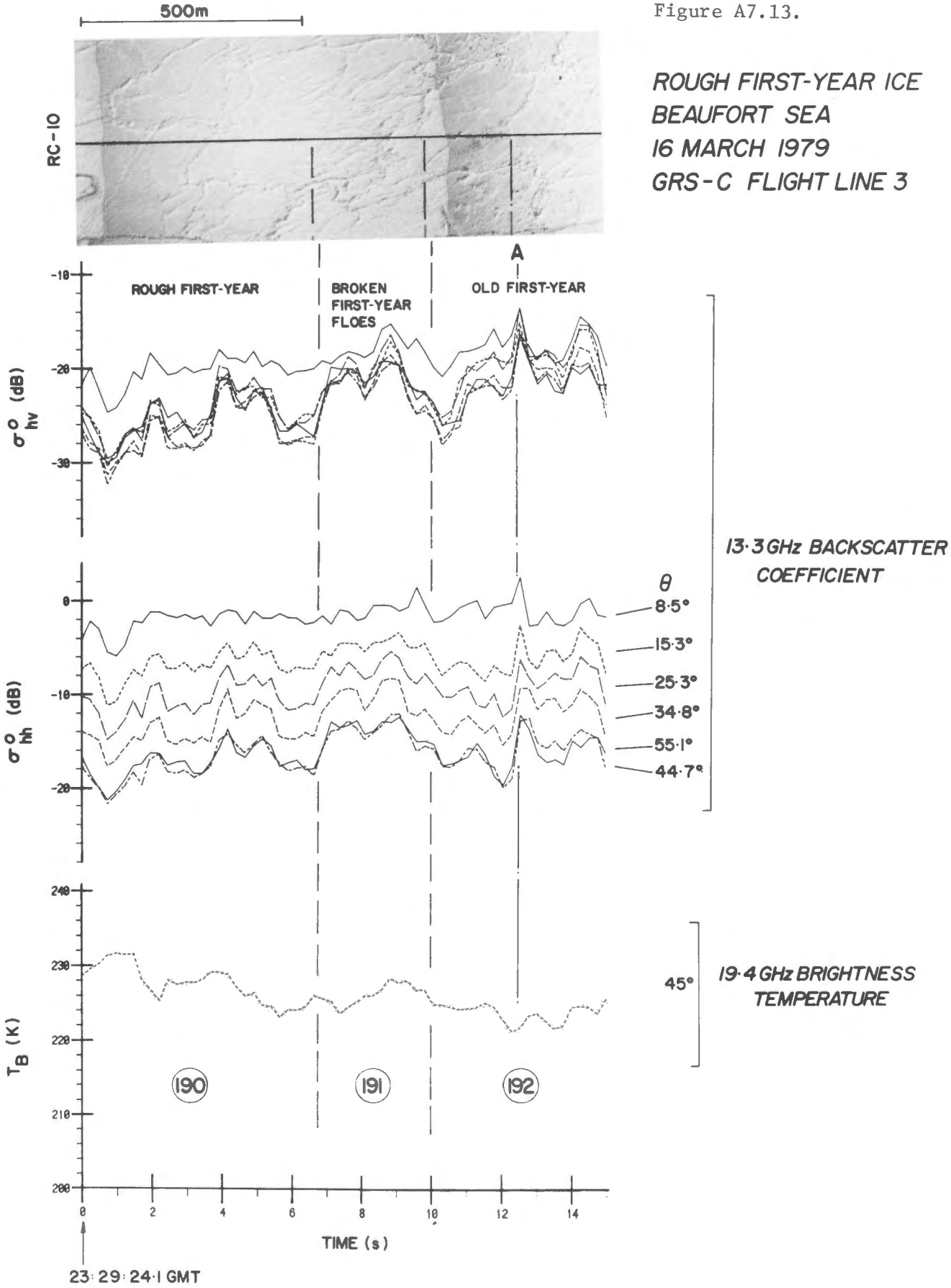

Figure A7.14.

ROUGH FIRST-YEAR ICE
EVENT E30803 (190)
BEAUFORT SEA
16 MARCH 1979, LINE 3
23:28:45.4 TO 23:29:19.1 GMT

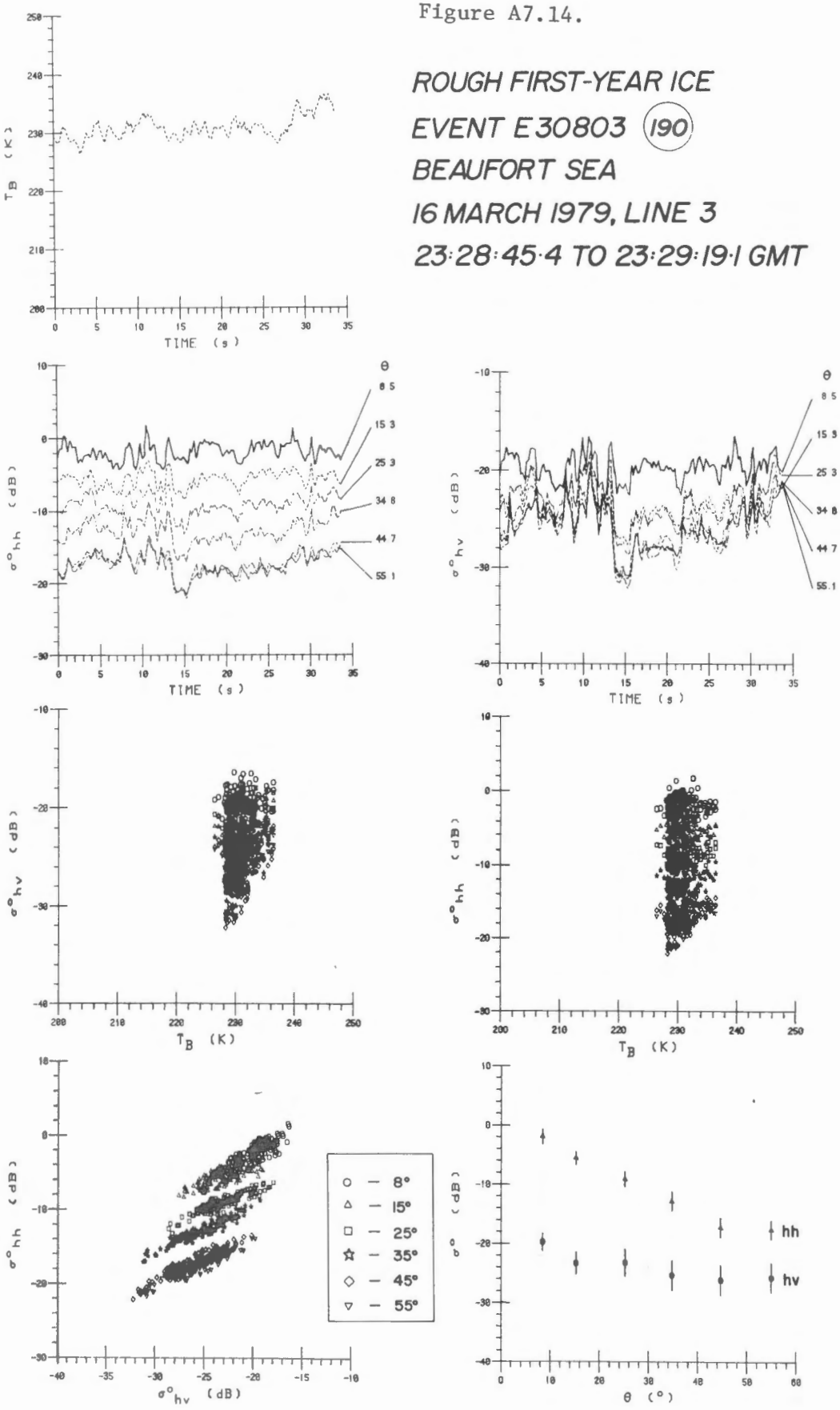

Table A7.8 SUMMARY OF EVENT E30803.190: ROUGH FIRST-YEAR ICE

EVENT DESCRIPTION:

BEAUFORT 030803 N/S (F)

ASSOCIATED FILES

SCA2:BA0803.L21[64,400]
SCA2:BA0803.C21[64,400]
SCAT:030803.SMO[64,400]
SCAT:030803.INC[64,400]
SCAT:030803.RAD[64,400]
SCA3:D30803.190[64,400]

EVENT TIME

FROM: 75 23:28:45.4000
TO: 75 23:29:19.2000

NAV PARAMETERS	Alt (ft)	Vg (knots)	Lat.	Long.	Pitch	Roll	Drift
	1310.735	155.88	72.2844	-131.9952	2.14	0.46	-0.92
+/-	0.221	0.02	0.0013	0.0026	0.01	0.07	0.01

ANGLES †

	8.490	15.268	25.250	34.778	44.727	55.069

SCATTEROMETER STATISTICS

LMEAN	-1.878	-5.645	-9.123	-12.830	-17.230	-17.546
XMEAN	-19.698	-23.270	-23.222	-25.277	-26.098	-25.648
LSTD	1.219	1.119	1.287	1.576	1.654	1.557
XSTD	1.389	1.878	2.251	2.499	2.490	2.405
CORREL COEF	0.776	0.735	0.920	0.953	0.944	0.925

BRIGHTNESS TEMPERATURE STD 2.0 MEAN 230.9

CORRELATION COEFFICIENTS FOR RADIOMETER AND SCATTEROMETER

TB VS LPOL	0.007	0.136	0.373	0.459	0.478	0.448
TB VS XPOL	0.182	0.346	0.388	0.390	0.401	0.393

† In this table, the columns of statistics below refer to the six scatterometer angles indicated here. LMEAN, XMEAN, XSTD, and LSTD are the averages and standard deviations of the like- and cross-polarized backscattering coefficients. TB refers to the microwave brightness temperature.

Figure A7.15

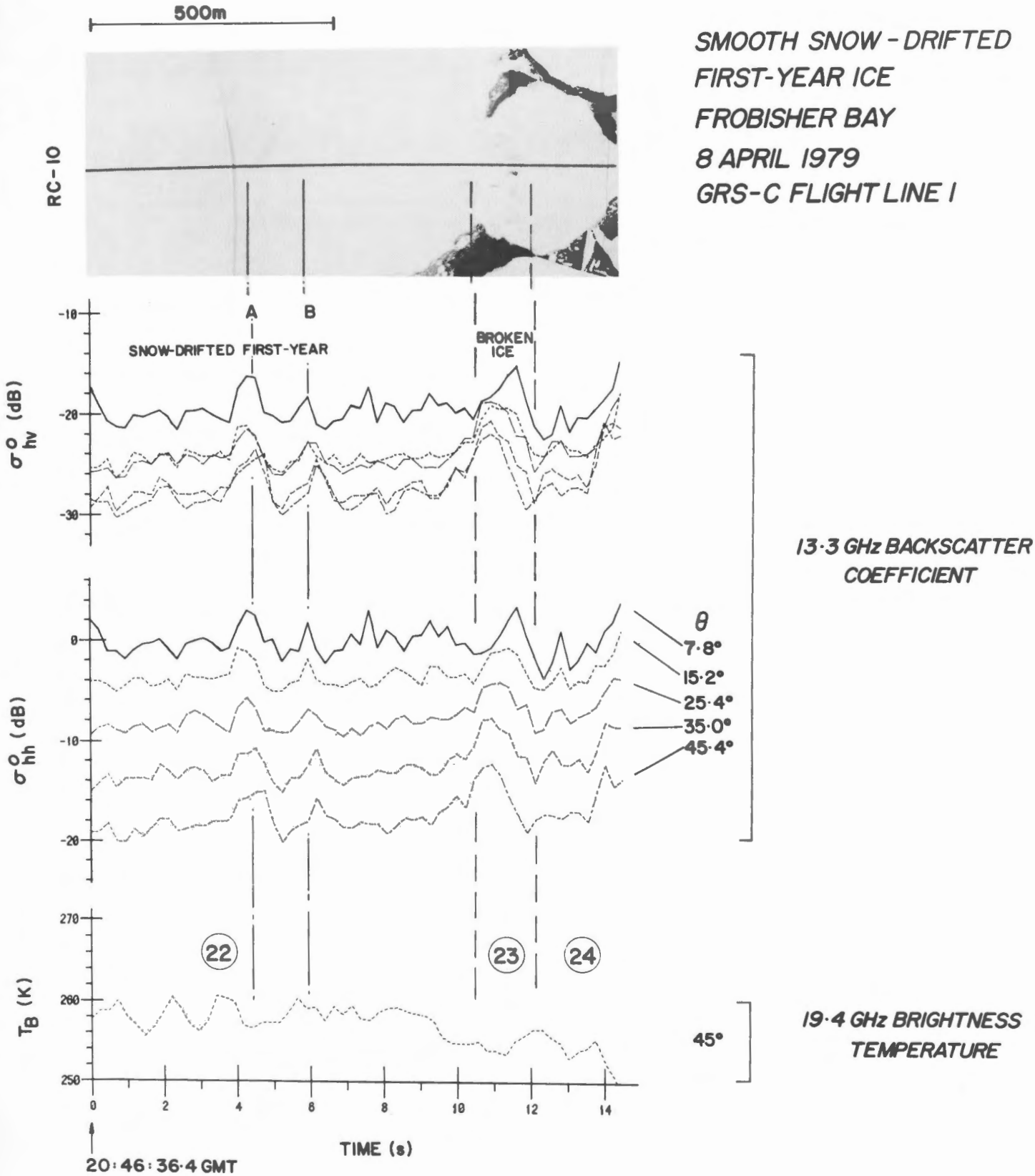
500m
RC-10
SMOOTH SNOW - DRIFTED
FIRST-YEAR ICE
FROBISHER BAY
8 APRIL 1979
GRS-C FLIGHT LINE I
A
B
SNOW-DRIFTED FIRST-YEAR
BROKEN ICE
σ^o_{hv} (dB)
-10
-20
-30
13·3 GHz BACKSCATTER COEFFICIENT
σ^o_{hh} (dB)
0
-10
-20
θ
7·8°
15·2°
25·4°
35·0°
45·4°
T_B (K)
270
260
250
22
23
24
45°
19·4 GHz BRIGHTNESS TEMPERATURE
0
2
4
6
8
10
12
14
TIME (s)
20:46:36·4 GMT

This may be explained by the narrow across-track beam width near nadir*, since the ridges at E and F run parallel to the aircraft track and slightly to the right. The very smooth central section of the figure between ridge C and E is represented in the microwave data by reduced backscatter (~ 2 dB) and elevated brightness temperature (~ 5 K). The details and statistics of these data are given in Figure A7.12 and Table A7.7.

A7.5.2 Rough first-year ice

Figure A7.13 shows a region of rough (heavily ridged) first-year ice again from the March 16, Beaufort Sea line, comprising events E30803.190, 191, and 192. The many ridges and rubble areas that cross the region give it a rough appearance which contrasts with the smooth ice shown in Figure A7.11. Comparison of these data and Figure A7.11 (event E30803.172) shows that the microwave signatures are similar, except for the undulations between the rougher and smoother ice sections. Cross-polarized radar returns accentuate the contrast between ridges and smoother ice, with a maximum of 10 dB seen in event 191 at 55° incidence, while the corresponding like-polarized data show a contrast of ~ 5 dB. The ridge contrast is enhanced with higher incidence angles in this broken first-year region.

The ridge marked as feature A, in the old first-year ice designated as event 192, is equally well discriminated by either σ^o_{hh} or σ^o_{hv}, with maximum contrast obtained at the largest incidence angle. The ridge height in this section** of the data is modest, with the tallest feature in the entire scene being less than 2 m; all ridges crossed by the sensor path were lower than this.

Figure A7.14 gives a detailed analysis of the features in event E30803.190 and its statistics are given in Table A7.8. The higher variances of these results are the primary differences between Table A7.8 and Table A7.7.

A7.5.3 Snow-drifted first-year ice

Figure A7.15 shows smooth, snow-drifted first-year ice from the Frobisher Bay line, event E32201.022. Two floes have pushed together forming a section of broken ice producing contrasts in the radar time history similar to a pressure ridge signature. The undulations at A and B are due to low ridging, partially obscured by the snow cover.

Ice of this class and degree of snow cover was prevalent on this line. A comparison of the results of Figure 7.15 with those of Figure 7.11, shows that neither the snow cover nor the large surface temperature

---

* See Figure 5.

** Ridge heights were estimated from shadow length measurements. The sun angle of elevation in this image was 12.11° above the horizon.

difference* has much effect on the backscattering coefficient**. There is, however, a large difference in the measured brightness temperature of these two examples, which is due partially to the difference in surface temperature (~30° C) and a change in emissivity, from 0.92 in event E30803.172 to 0.95 in event E32201.022. Table A7.9 and Figure A7.16 further characterize event E32201.022.

A7.5.4 Rotten, wet first-year ice

Much of the sea ice seen in the Davis Strait was rotten and decaying first-year, nearing break-up conditions. The ice showed melting cavities and in places was penetrated by the underlying sea (Gray et al., 1979).

Figure A7.17 shows an example of this rotting first-year ice. The surface is mottled from differential surface accumulations of water and saturated snow. This surface saturation may account for the higher backscatter coefficients and increased specularity. It also is qualitatively consistent with the 10 K lowering of brightness temperature, in going from normal (consolidated) to rotten conditions, as can be seen from reference to event E32201.023 in Figure A7.15.

The small feature at A is probably nilas or grease ice, although it is too narrow to confirm its type positively. Figure A7.18 gives more detail for event E32201.056 and its statistics are given in Table A7.10.

A wide variation in brightness temerature (~20 K) is seen between different first-year floes from the Davis Strait lines. No explanation is revealed from the aerial photography. Degree of puddling and/or percentage of snow cover may be relevant factors in controlling this effect on brightness temperature.

A7.5.5 Wave-broken first-year ice

Figure A7.19 shows an example of wave-broken first-year ice at the margin of the ice in the Davis Strait***. A distinct separation of ice cake sizes, between large bits of ~8 m and smaller ice fragments of > 2 m can be seen. These ice cakes give higher backscatter return than the unbroken ice, presumably because of the increased roughness at the cake boundaries.

---

* The ambient temperature during the data collection period recorded at the Frobisher Bay weather station, was ~ -5° C, whereas the Beaufort deployment was in temperatures of ~-30°C.

** From Figures 37, 38, and 39, it can be seen that these two examples fall on the edge of the distribution of scatttering coefficients with temperature and in general, an effect can be seen.

*** The dark shape at A on the RC-10 image is the aircraft radome.

Figure A7.16.

SNOW-DRIFTED FIRST-YEAR ICE
EVENT E32201.022
FROBISHER BAY
APRIL 8,1979
C-GRSC FLIGHT LINE I

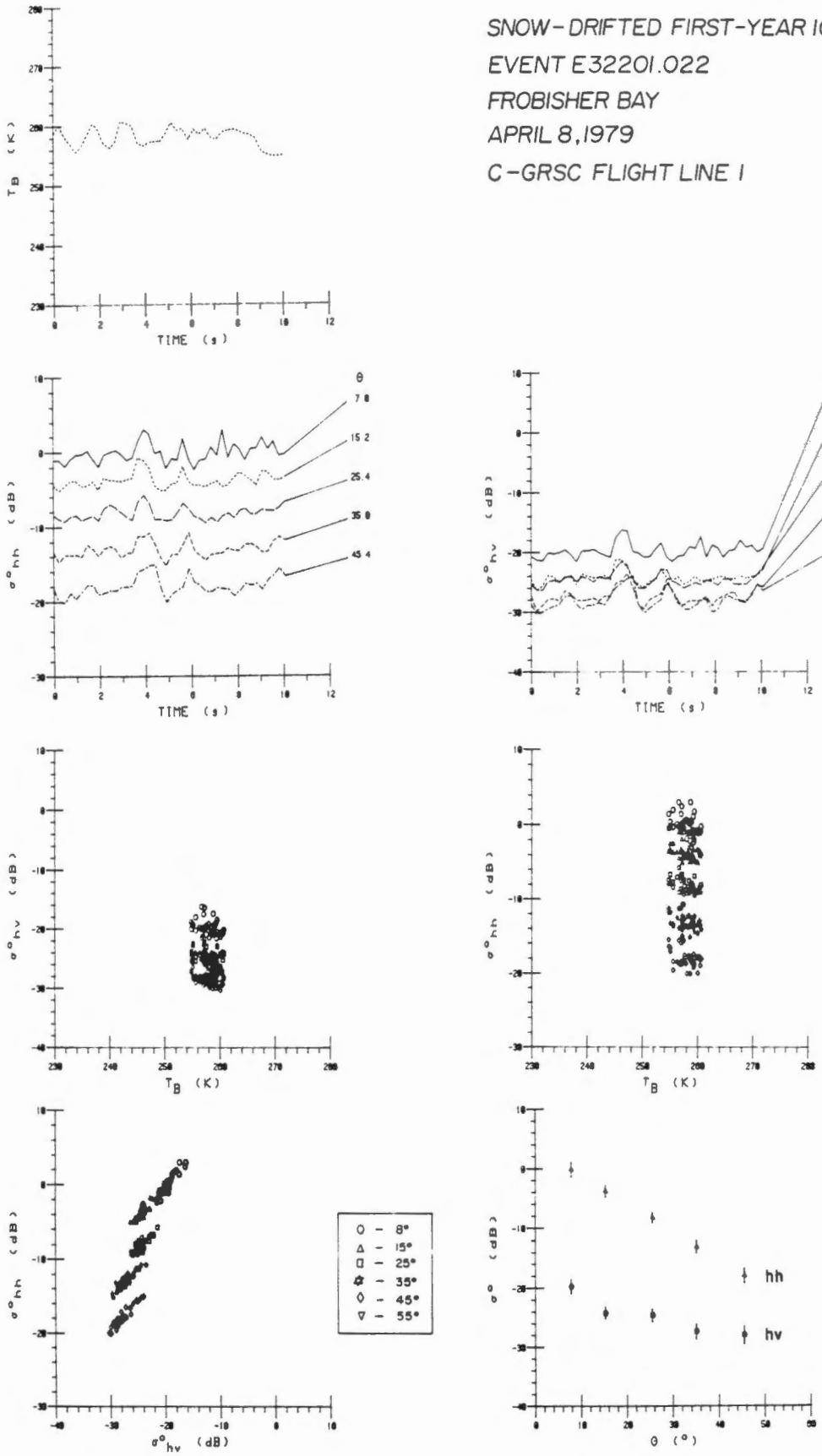

Table A7.9 SUMMARY OF EVENT E32201.022: SMOOTH SNOW-DRIFTED FIRST-YEAR ICE

EVENT DESCRIPTION:

FROBISHER BAY 032201 SE/NW (FIRST)

ASSOCIATED FILES

SCA2:EA2201.L04[64,400]
SCA2:EA2201.C04[64,400]
SCA3:032201.SMO[64,400]
SCAT:032201.INC[64,400]
SCAT:032201.RAD[64,400]
SCA3:D32201.022[64,400]

EVENT TIME

FROM: 98 20:46:36.8000
TO: 98 20:46:46.9000

NAV PARAMETERS	Alt (ft)	Vs (knots)	Lat.	Long.	Pitch	Roll	Drift
	1253.200	145.06	62.4967	-66.0062	3.86	0.12	-4.17
+/-	0.772	0.10	0.0000	0.0000	0.07	0.11	0.07

ANGLES †

	7.750	15.178	25.432	35.018	45.449	0.000

SCATTEROMETER STATISTICS

LMEAN	-0.148	-3.786	-8.243	-13.080	-17.968	0.000
XMEAN	-19.764	-24.236	-24.607	-27.410	-28.008	0.000
LSTD	1.272	0.995	0.863	1.011	1.265	0.000
XSTD	1.247	1.008	1.104	1.330	1.556	0.000
CORREL COEF	0.935	0.883	0.774	0.909	0.941	0.000

BRIGHTNESS TEMPERATURE STD 1.6 MEAN 258.0

CORRELATION COEFFICIENTS FOR RADIOMETER AND SCATTEROMETER

TB VS LPOL	-0.422	-0.292	-0.440	-0.433	-0.413	0.000
TB VS XPOL	-0.414	-0.333	-0.215	-0.288	-0.347	0.000

† In this table, the columns of statistics below refer to the six scatterometer angles indicated here. LMEAN, XMEAN, XSTD, and LSTD are the averages and standard deviations of the like- and cross-polarized backscattering coefficients. TB refers to the microwave brightness temperature.

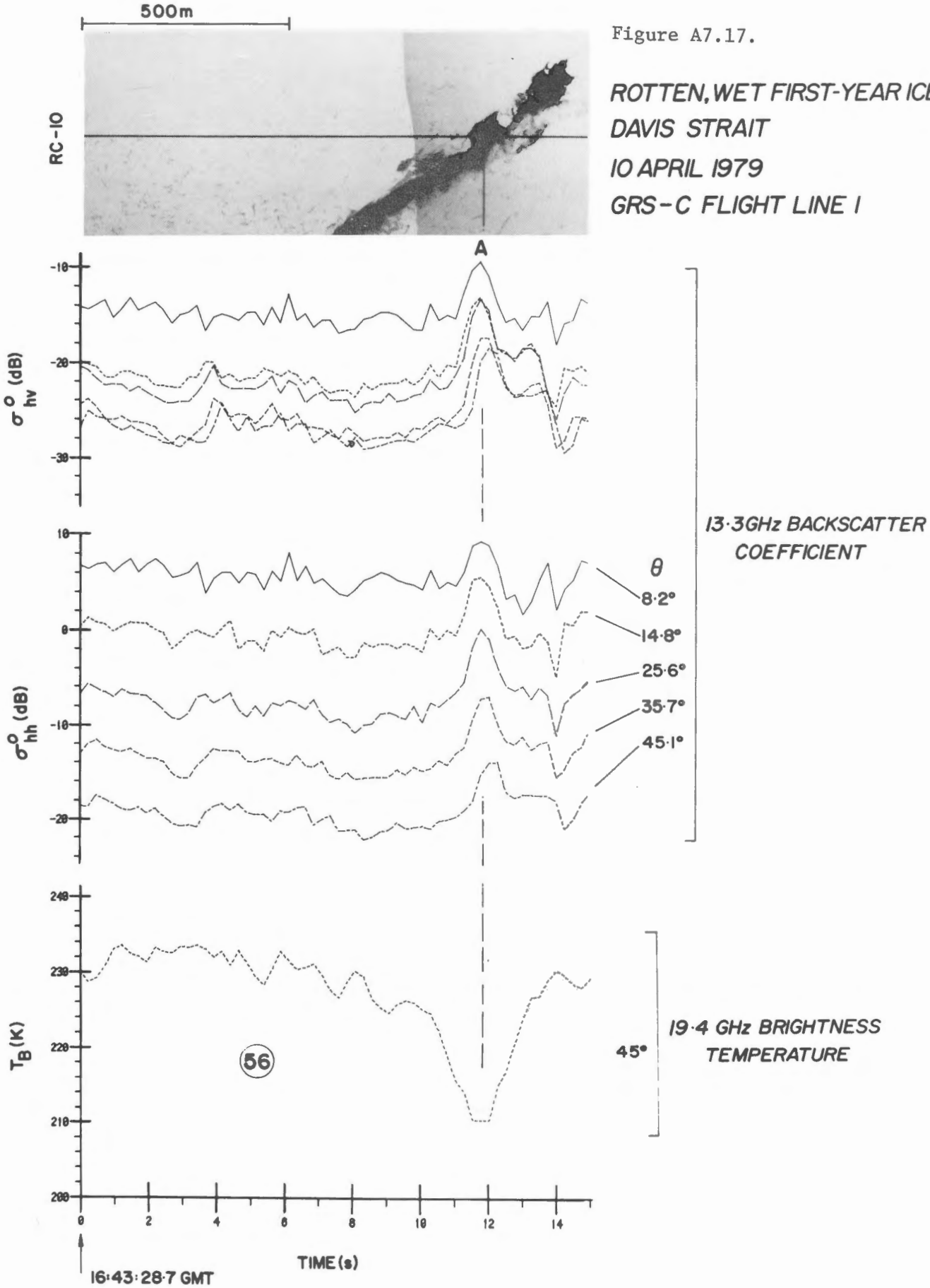
500m
RC-10
A
ROTTEN, WET FIRST-YEAR ICE
DAVIS STRAIT
10 APRIL 1979
GRS-C FLIGHT LINE I
σ^o_{hv} (dB)
-10
-20
-30
13·3GHz BACKSCATTER COEFFICIENT
σ^o_{hh} (dB)
10
0
-10
-20
θ
8·2°
14·8°
25·6°
35·7°
45·1°
T_B (K)
240
230
220
210
200
56
45°
19·4 GHz BRIGHTNESS TEMPERATURE
0
2
4
6
8
10
12
14
TIME (s)
16:43:28·7 GMT

Figure A7.17.

Figure A7.18.

ROTTEN, WET FIRST-YEAR ICE
EVENT E32501 56
DAVIS STRAIT
10 APRIL 1979, LINE I
16:43:28.7 TO 16:43:40.0 GMT

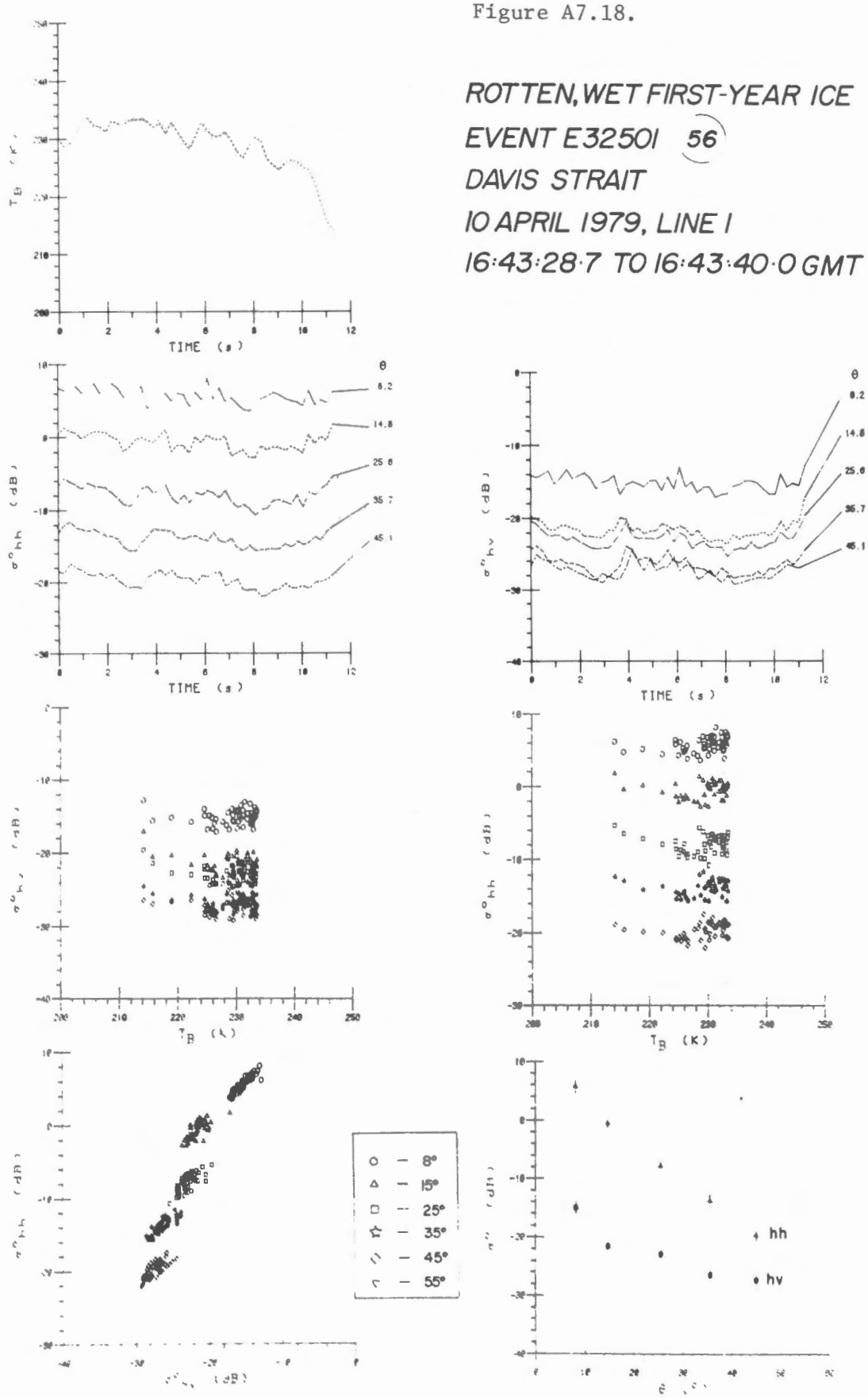

Table A7.10 SUMMARY OF EVENT E32501.056: ROTTEN, WET FIRST-YEAR ICE

EVENT DESCRIPTION:

DANISH E/W 032501 (F)

ASSOCIATED FILES

SCA2:EA2501.L15[64,400]
SCA2:EA2501.C15[64,400]
SCA3:032501.SMO[64,400]
SCAT:032501.INC[64,400]
SCAT:032501.RAD[64,400]
SCA3:D32501.056[64,400]

EVENT TIME

FROM: 100 16:43:28.7000
TO: 100 16:43:40. 0

NAV PARAMETERS	Alt (ft)	Vg (knots)	Lat.	Long.	Pitch	Roll	Drift
	1410.000	163.73	68.4234	-56.5293	2.31	0.16	1.49
+/-	0.701	0.02	0.0021	0.0021	0.03	0.03	0.02

ANGLES †

	8.200	14.765	25.582	35.698	45.127	0.000

SCATTEROMETER STATISTICS

LMEAN	5.694	-0.611	-7.953	-13.932	-19.723	0.000
XMEAN	-15.145	-21.610	-22.996	-26.499	-27.398	0.000
LSTD	1.030	1.138	1.229	1.121	1.057	0.000
XSTD	1.030	1.147	1.200	1.243	1.111	0.000
CORREL COEF	0.904	0.694	0.761	0.853	0.758	0.000

BRIGHTNESS TEMPERATURE STD 4.4 MEAN 229.1

CORRELATION COEFFICIENTS FOR RADIOMETER AND SCATTEROMETER

TB VS LPOL	0.425	0.073	-0.063	0.070	0.278	0.000
TB VS XPOL	0.092	-0.328	-0.226	-0.045	-0.008	0.000

† In this table, the columns of statistics below refer to the six scatterometer angles indicated here. LMEAN, XMEAN, XSTD, and LSTD are the averages and standard deviations of the like- and cross-polarized backscattering coefficients. TB refers to the microwave brightness temperature.

Figure A7.19.

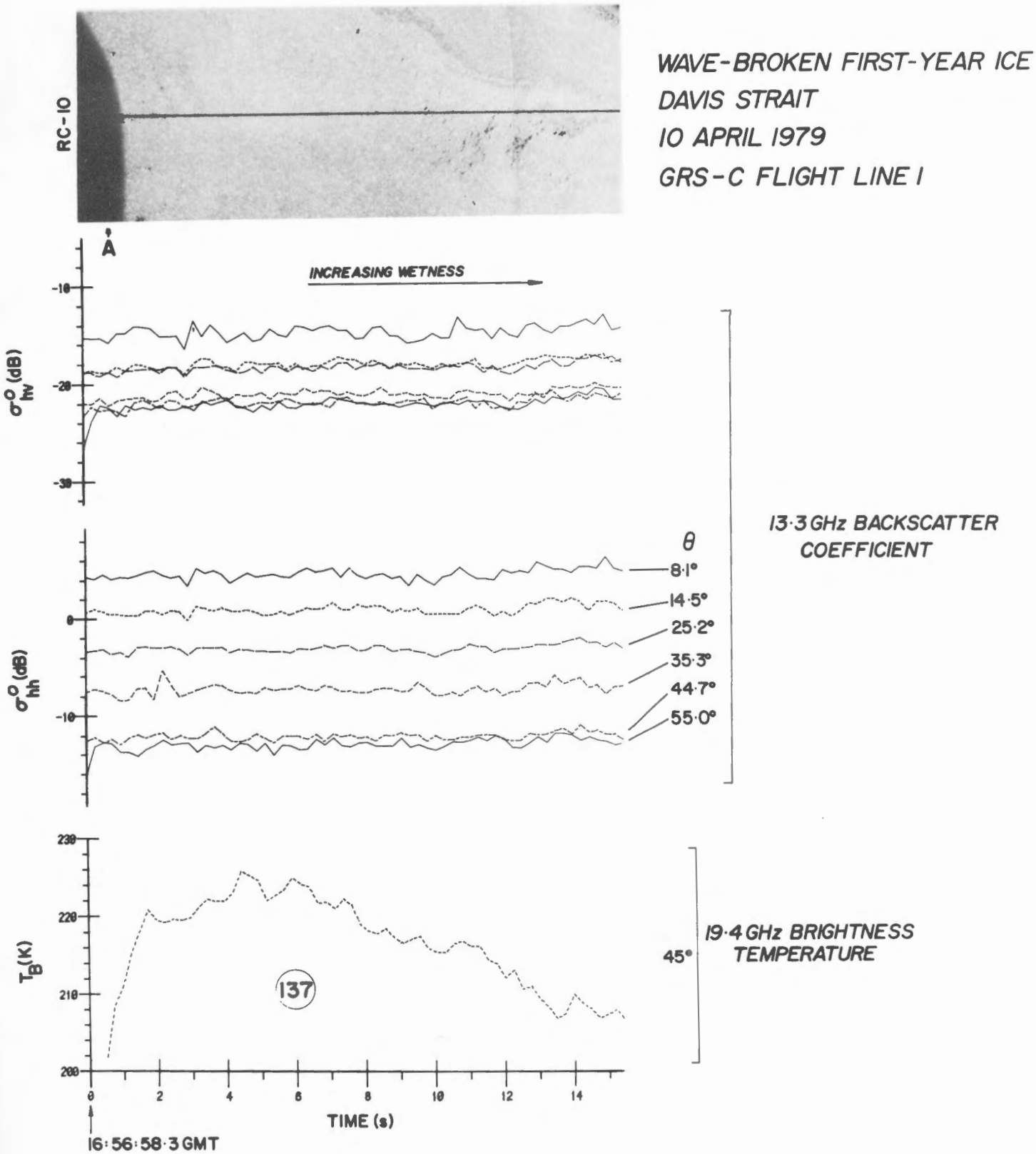
WAVE-BROKEN FIRST-YEAR ICE
DAVIS STRAIT
10 APRIL 1979
GRS-C FLIGHT LINE I
RC-10
A
INCREASING WETNESS
σ^o_{hv} (dB)
-10
-20
-30
σ^o_{hh} (dB)
0
-10
θ
8.1°
14.5°
25.2°
35.3°
44.7°
55.0°
13.3 GHz BACKSCATTER COEFFICIENT
T_B(K)
230
220
210
200
137
45°
19.4 GHz BRIGHTNESS TEMPERATURE
0
2
4
6
8
10
12
14
TIME (s)
16:56:58.3 GMT

The arrow indicates increasing water content with the radiometer footprint, especially to the right of the track, as the flight line approaches open water. It is interesting to note that radiometer brightness temperature is sensitive to this gradual change but the scatterometer backscatter coefficient shows only a slight change. In the radiometer time history, T_B rises from an area of open water preceding this event, levels off over the uniform ice and then falls as more water (indicated by black area) is present in the radiometer footprint. The scatterometer footprint is narrower and less water is present to affect the return.

Figure A7.20 and Table A7.11 give further details of event E32501.137.

A7.6 Second-year Ice

Only a few examples of second-year ice were positively identified from the Beaufort Sea imagery. The transition from rough first-year to rough second-year ice in the Beaufort Sea is illustrated in Figure A7.21. There is a clear delineation between the two ice classes in the time history of each sensor. The scatterometer records ~10 dB contrast in backscattering coefficient for each polarization and the radiometer brightness temperature falls by ~20 K. The scene is crossed by ridges indicated by A, B, C, D, and E, with the floe boundary marked by the ridge at B. This ridge is ~ 9 m wide where the flight line crosses it and its height is only 1.5 m*.

Ridge contrast is almost equal for the first-year and second-year examples in this illustration; however, it is clear from the RC-10 images that the second-year ridges are much lower and wider, implying that ridge height is unimportant in determining ridge contrast. Because the second-year ridges are sufficiently broad (90 m at D), a brightness temperature contrast of ~5 K is seen in the radiometer time history.

Figure A7.22 and Table A7.12 give further details of event E30803.173.

A7.7 Multi-year Ice

All the multi-year ice recorded in the Active-Passive Experiment was from the Beaufort Sea deployment under cold conditions. Rough (heavily ridged) and smooth (fewer hummocks and ridges) ice subclasses were separated subjectively from the visual interpretation of the RC-10 imagery. The separation of these two subclasses is much less distinct than is the case for younger ice forms because of the joint effect of weathering and snow cover.

A7.7.1 Smooth multi-year ice

Figure A7.23 shows a segment of a large multi-year floe from the N/S line of March 16. The sharp edges of the ridge features are clearly

---

* In this instance, the sun elevation angle is ~12.13°.

Figure A7.20.

WAVE-BROKEN FIRST-YEAR ICE
EVENT E 32501 (137)
DAVIS STRAIT
10 APRIL 1979, LINE I
16:56:58.3 TO 16:57:15.0 GMT

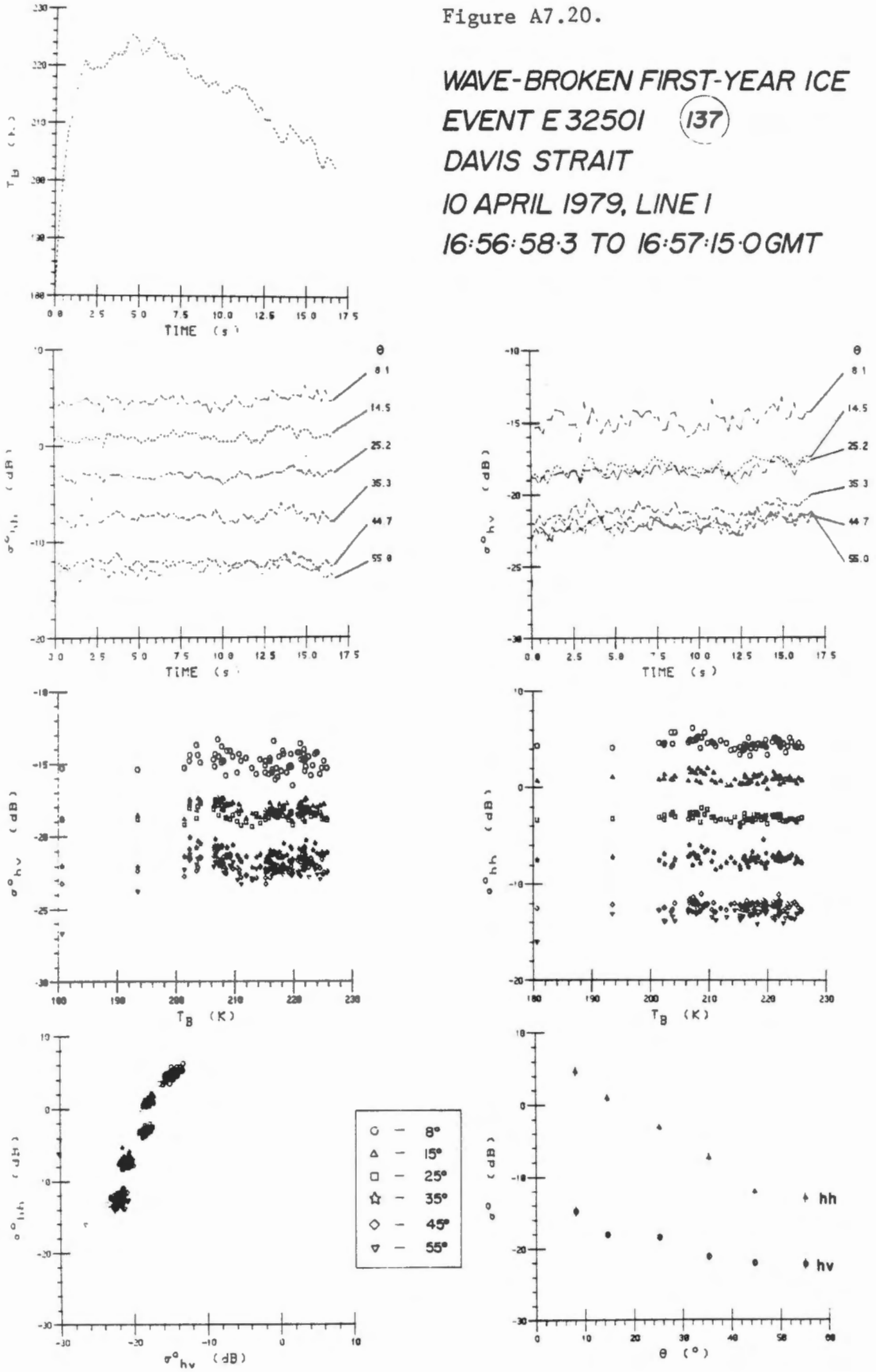

Table A7.11 SUMMARY OF EVENT E32501.137: WAVE-BROKEN FIRST-YEAR ICE

EVENT DESCRIPTION:

DANISH E/W 032501 (FK/G/R)

ASSOCIATED FILES

SCA2:EA2501.L31[64,400]
SCA2:EA2501.C31[64,400]
SCA3:032501.SMO[64,400]
SCAT:032501.INC[64,400]
SCAT:032501.RAD[64,400]
SCA3:D32501.137[64,400]

EVENT TIME

FROM: 100 16:56:58.3000
TO: 100 16:57:15.2000

NAV PARAMETERS	Alt (ft)	Vg (knots)	Lat.	Long.	Pitch	Roll	Drift
	1401.471	159.23	68.3861	-54.9073	2.42	-0.03	3.99
+/-	0.275	0.03	0.0000	0.0027	0.01	0.03	0.01

ANGLES †

	8.070	14.540	25.222	35.260	44.661	55.022

SCATTEROMETER STATISTICS

LMEAN	4.584	0.911	-3.127	-7.339	-12.143	-13.051
XMEAN	-14.851	-18.109	-18.472	-21.160	-22.039	-22.255
LSTD	0.540	0.457	0.363	0.543	0.386	0.613
XSTD	0.660	0.433	0.412	0.458	0.482	0.737
CORREL COEF	0.733	0.630	0.504	0.225	0.355	0.560

BRIGHTNESS TEMPERATURE STD 8.2 MEAN 214.6

CORRELATION COEFFICIENTS FOR RADIOMETER AND SCATTEROMETER

TB VS LPOL	-0.250	-0.201	-0.183	0.033	0.186	0.313
TB VS XPOL	-0.109	-0.073	-0.173	0.012	0.151	0.289

† In this table, the columns of statistics below refer to the six scatterometer angles indicated here. LMEAN, XMEAN, XSTD, and LSTD are the averages and standard deviations of the like- and cross-polarized backscattering coefficients. TB refers to the microwave brightness temperature.

Figure A7.21.

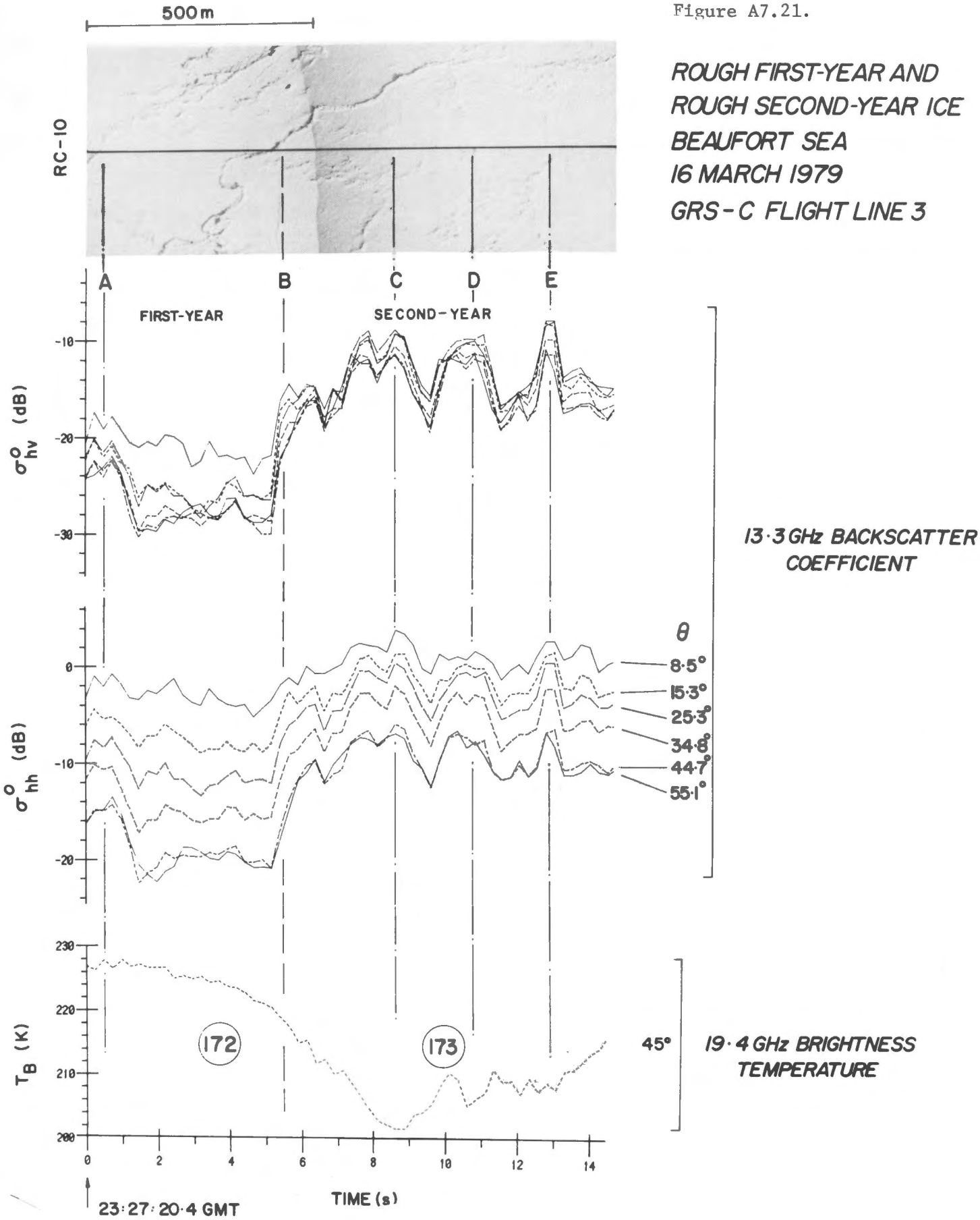
500 m
RC-10
ROUGH FIRST-YEAR AND
ROUGH SECOND-YEAR ICE
BEAUFORT SEA
16 MARCH 1979
GRS-C FLIGHT LINE 3
A
B
C
D
E
FIRST-YEAR
SECOND-YEAR
σ^o_{hv} (dB)
-10
-20
-30
13·3 GHz BACKSCATTER COEFFICIENT
σ^o_{hh} (dB)
0
-10
-20
θ
8·5°
15·3°
25·3°
34·8°
44·7°
55·1°
T_B (K)
230
220
210
200
172
173
45°
19·4 GHz BRIGHTNESS TEMPERATURE
0
2
4
6
8
10
12
14
TIME (s)
23:27:20·4 GMT

Figure A7.22.

ROUGH SECOND-YEAR ICE
EVENT E30803 (173)
BEAUFORT SEA
16 MARCH 1979, LINE 3
23:27:25.9 TO 23:27:35.7 GMT

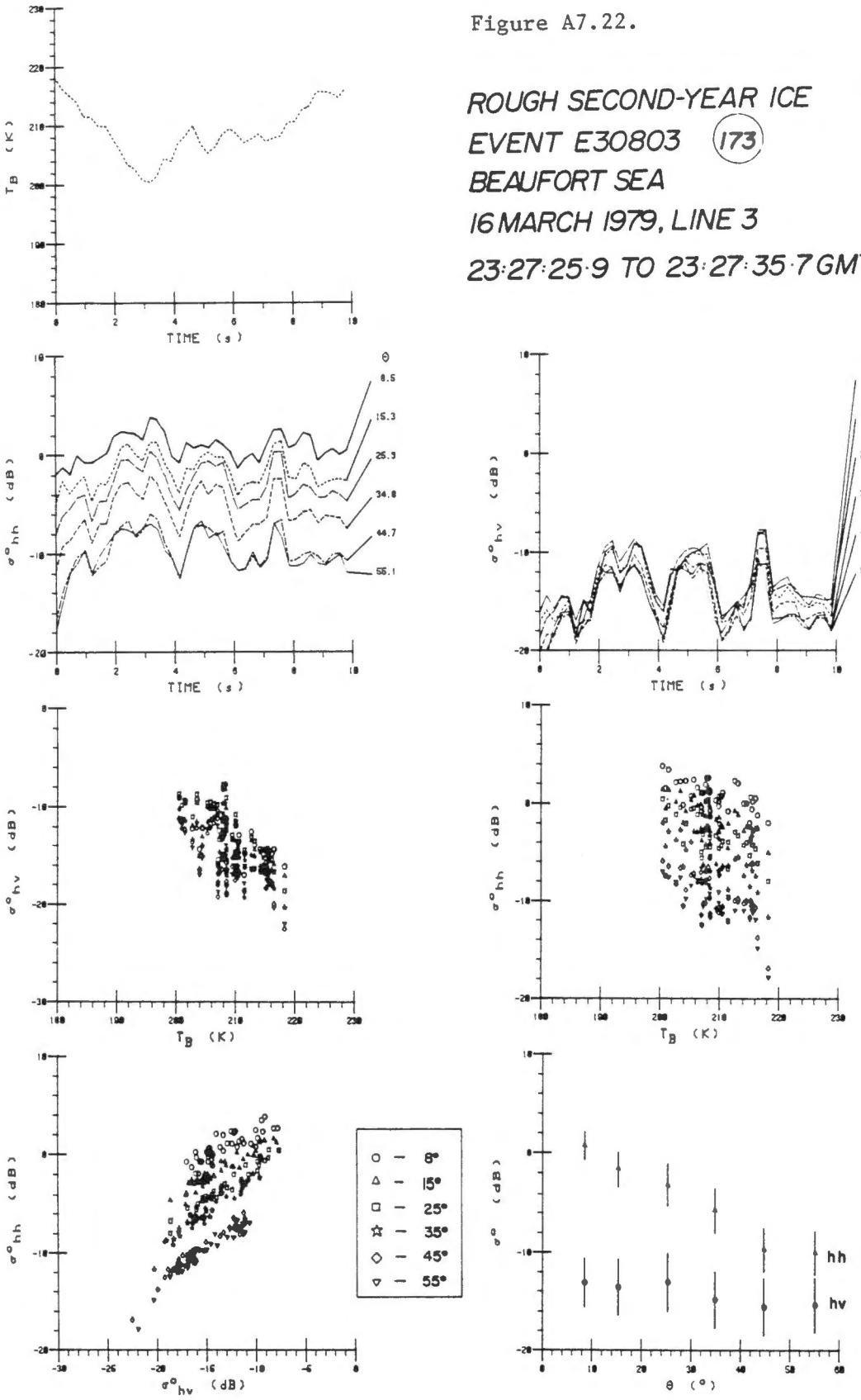

Table A7.12 SUMMARY OF EVENT E30803.173: ROUGH SECOND-YEAR ICE

EVENT DESCRIPTION:

BEAUFORT 030803 N/S (S)

ASSOCIATED FILES

SCA2:BA0803.L19[64,400]
SCA2:BA0803.C19[64,400]
SCA3:030803.SMO[64,400]
SCAT:030803.INC[64,400]
SCAT:030803.RAD[64,400]
SCA3:D30803.173[64,400]

EVENT TIME

FROM: 75 23:27:25.9000
TO: 75 23:27:35.9000

NAV PARAMETERS	Alt (ft)	Vg (knots)	Lat.	Long.	Pitch	Roll	Drift
	1303.800	156.15	72.3505	-131.9891	2.14	0.46	-0.91
+/-	0.247	0.01	0.0000	0.0000	0.01	0.07	0.01

ANGLES †

	8.490	15.268	25.250	34.778	44.727	55.069

SCATTEROMETER STATISTICS

LMEAN	0.707	-1.642	-3.213	-5.767	-9.720	-10.021
XMEAN	-13.088	-13.583	-13.070	-14.811	-15.586	-15.378
LSTD	1.397	1.702	2.066	2.229	2.222	2.210
XSTD	2.455	2.776	2.928	2.865	2.853	2.740
CORREL COEF	0.831	0.955	0.982	0.971	0.968	0.951

BRIGHTNESS TEMPERATURE STD 4.5 MEAN 209.2

CORRELATION COEFFICIENTS FOR RADIOMETER AND SCATTEROMETER

TB VS LPOL	-0.693	-0.750	-0.735	-0.720	-0.726	-0.742
TB VS XPOL	-0.670	-0.716	-0.719	-0.725	-0.748	-0.749

† In this table, the columns of statistics below refer to the six scatterometer angles indicated here. LMEAN, XMEAN, XSTD, and LSTD are the averages and standard deviations of the like- and cross-polarized backscattering coefficients. TB refers to the microwave brightness temperature.

Figure A7.23.

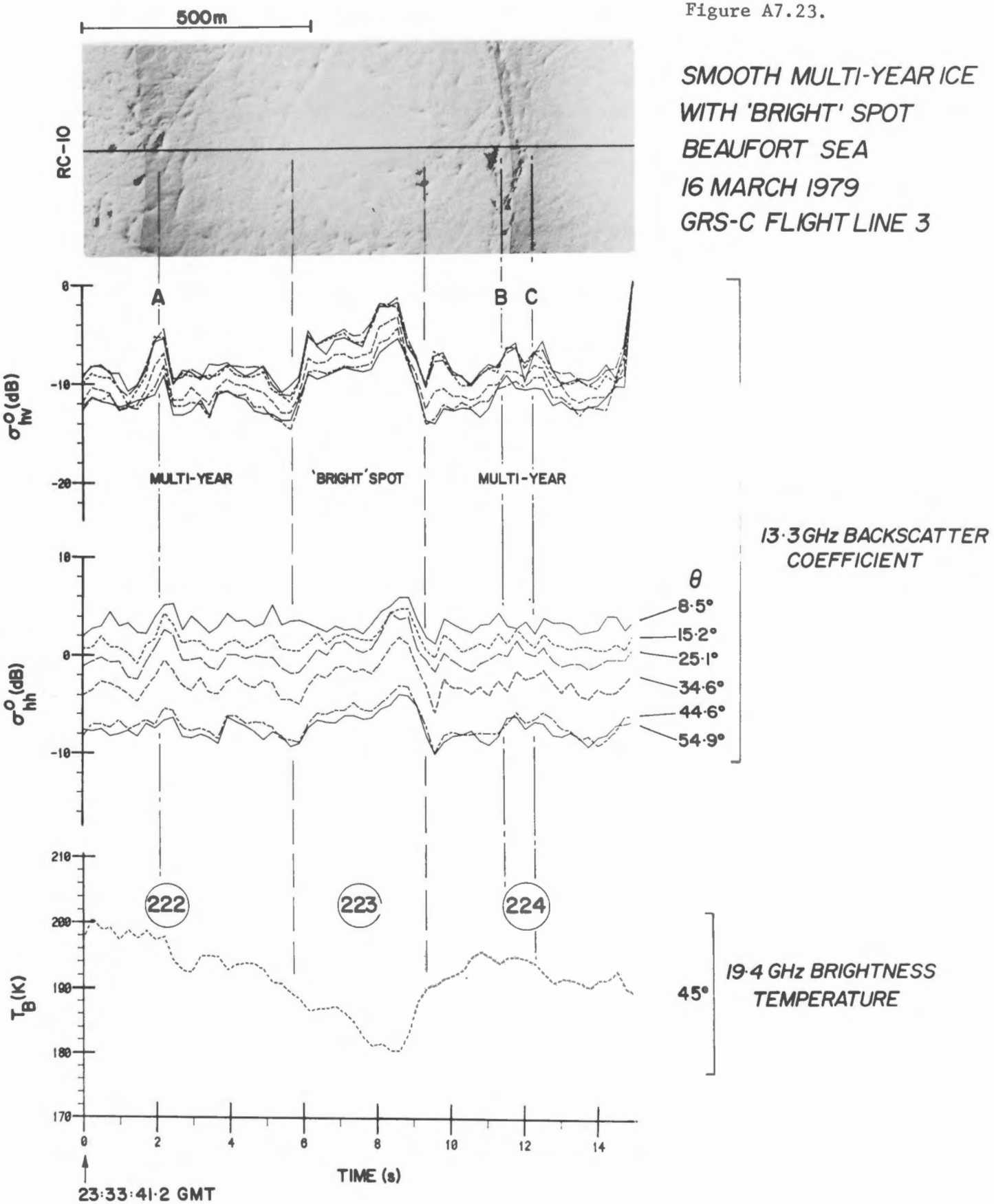
500m
RC-10
SMOOTH MULTI-YEAR ICE
WITH 'BRIGHT' SPOT
BEAUFORT SEA
16 MARCH 1979
GRS-C FLIGHT LINE 3
A
B
C
MULTI-YEAR
'BRIGHT' SPOT
MULTI-YEAR
σ^o_{hv}(dB)
0
-10
-20
13·3 GHz BACKSCATTER COEFFICIENT
θ
8·5°
15·2°
25·1°
34·6°
44·6°
54·9°
σ^o_{hh}(dB)
10
0
-10
222
223
224
T_B(K)
210
200
190
180
170
45°
19·4 GHz BRIGHTNESS TEMPERATURE
0
2
4
6
8
10
12
14
TIME (s)
23:33:41·2 GMT

weathered and the surface is packed with snow but the surface is not smooth in the sense of Figure A7.11 and has a uniformly textured appearance. More distinct ridging may be seen as features A, B, and C in the multi-year floe events 222 and 224. Here again cross-polarized radar returns are superior in distinguishing the surface relief as a contrast.

Figure A7.23 is particularly interesting because it contains a 'bright spot'. This 'bright spot' was first seen in the cross-polarized X-band radar imagery, and is designated as event E30803.223. A backscattering contrast of ~ 8 dB above the surrounding multi-year ice is apparent and a corresponding drop of 8 K is seen in the brightness temperature. Several theories have been projected for this 300 x 200 m feature; a tentative explanation is that it could be an ice island fragment within a multi-year floe. This explanation is supported by the similarity of the microwave signatures for event E30603.066, T3 ice island, discussed in Section A7.8. It is also supported by evidence of ridging along the perimeter of the bright spot, suggesting that it was once a separate floe interacting with adjacent ice. Event E30803.223 is further discussed in Figure A7.24 and Table A7.13.

A7.7.2 Rough multi-year ice

Figure A7.25 shows a section of rough multi-year ice from the 030803 line in the Beaufort Sea. The floe is weathered and snow-packed and is typical of the multi-year ice seen in this line.

Ridges clearly evident in the RC-10 imagery are virtually lost in the scatterometer profile, as is the hummock demarked at B. The long ridge, marked A, which crosses the flight line appears (anomalously) specular as indicated by the enhanced return in the two smaller incidence angle returns for σ^{o}_{hh}, with no corresponding enhancement in the cross-polarized returns. No clear physical explanation can be made for this behaviour.

The details of this event are given in Figure A7.26 and in Table A7.14.

A7.8 Ice Island

Figure A7.27 shows part of the March 13 low-altitude line over T3 ice island, event E30603.066. Probably all of the ice shown in the RC-10 image has a thick layer of packed snow obscuring features which affect the microwave signatures. This is especially true of T3, where it is speculated that features C and D of the microwave time history are related to summer drainage activity, both during the formation of the iceshelf from which T3 originated (Helk and Dunbar, 1953) and in the 30 or more years of its Beaufort Sea circumnavigations. Major ridges can be seen along the boundary at A, between the very old and newer multi-year ice, with greater contrast (~ 2 dB) noted at all incidence angles in the cross-polarized data. The angular dependence of the ridge contrast is marginal.

 Figure A7.24.

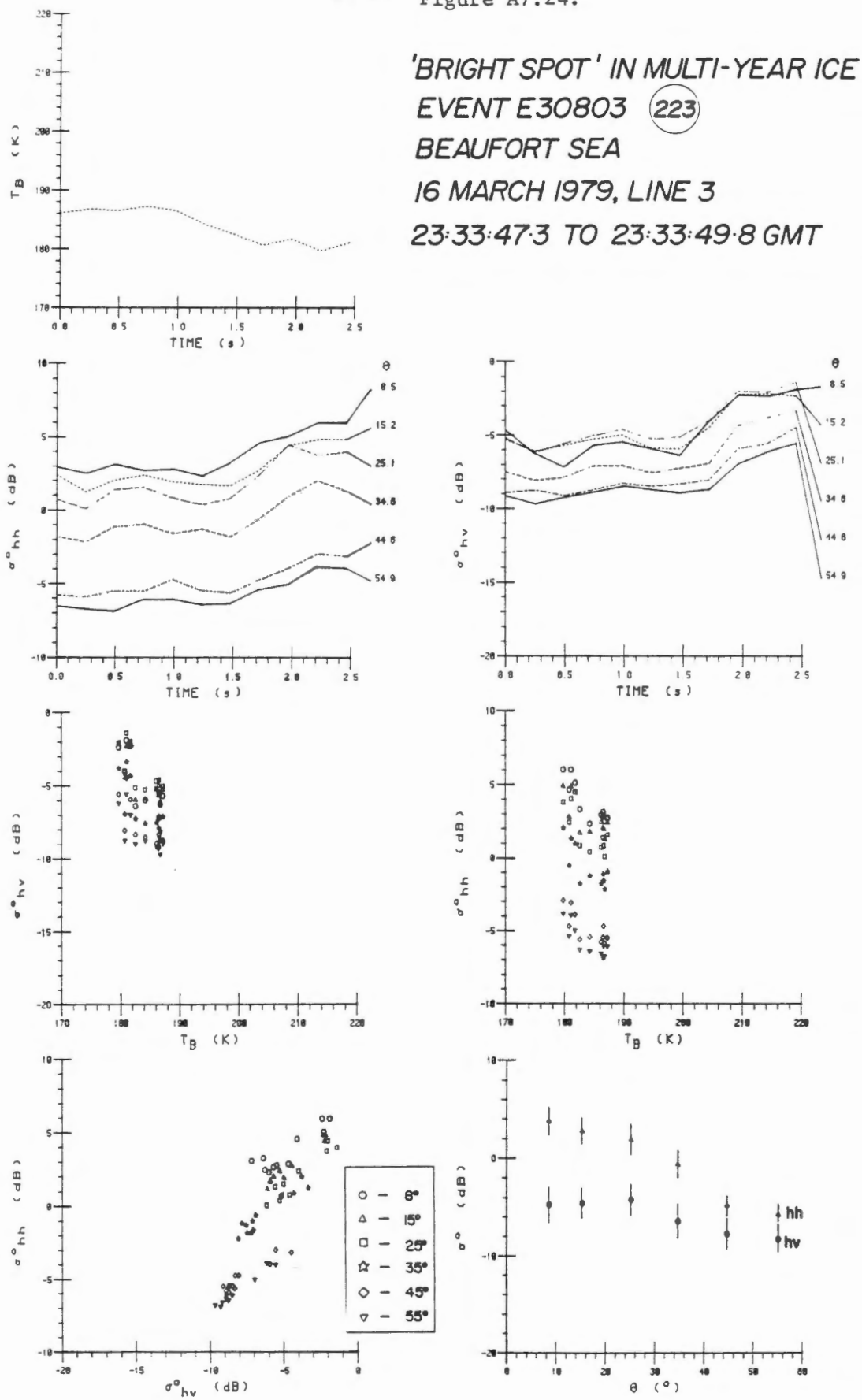
'BRIGHT SPOT' IN MULTI-YEAR ICE
EVENT E30803 223
BEAUFORT SEA
16 MARCH 1979, LINE 3
23:33:47.3 TO 23:33:49.8 GMT
TIME (s)
T_B (K)
σ^o_{hh} (dB)
σ^o_{hv} (dB)
θ
8.5
15.2
25.1
34.8
44.8
54.9
σ^o (dB)
hh
hv
θ (°)
○ – 8°
△ – 15°
□ – 25°
☆ – 35°
◇ – 45°
▽ – 55°

Table A7.13 SUMMARY OF EVENT E30803.223: MULTI-YEAR ICE WITH SAR 'BRIGHT SPOT'

EVENT DESCRIPTION:

BEAUFORT N/S 030803 (M BRIGHT SPOT)

ASSOCIATED FILES

SCA2:BA0803.L27[64,400]
SCA2:BA0803.C27[64,400]
SCA3:030803.SMO[64,400]
SCA3:030803.INC[64,400]
SCA3:030803.RAD[64,400]
SCA3:D30803.223[64,400]

EVENT TIME

FROM: 75 23:33:47.3000
TO: 75 23:33:50. 0

NAV PARAMETERS	Alt (ft)	Vg (knots)	Lat.	Long.	Pitch	Roll	Drift
	1315.667	156.57	72.0785	-132.0134	2.01	0.49	-1.56
+/-	0.323	0.02	0.0000	0.0000	0.00	0.02	0.02

ANGLES †

	8.450	15.195	25.138	34.642	44.580	54.933

SCATTEROMETER STATISTICS

LMEAN	3.755	2.759	1.859	-0.633	-4.831	-5.745
XMEAN	-4.773	-4.602	-4.245	-6.458	-7.718	-8.258
LSTD	1.338	1.263	1.491	1.350	1.019	1.023
XSTD	1.764	1.499	1.563	1.649	1.513	1.301
CORREL COEF	0.898	0.984	0.953	0.951	0.944	0.957

BRIGHTNESS TEMPERATURE STD 2.7 MEAN 183.9

CORRELATION COEFFICIENTS FOR RADIOMETER AND SCATTEROMETER

TB VS LPOL	-0.877	-0.794	-0.847	-0.809	-0.812	-0.847
TB VS XPOL	-0.829	-0.816	-0.867	-0.831	-0.851	-0.811

† In this table, the columns of statistics below refer to the six scatterometer angles indicated here. LMEAN, XMEAN, XSTD, and LSTD are the averages and standard deviations of the like- and cross-polarized backscattering coefficients. TB refers to the microwave brightness temperature.

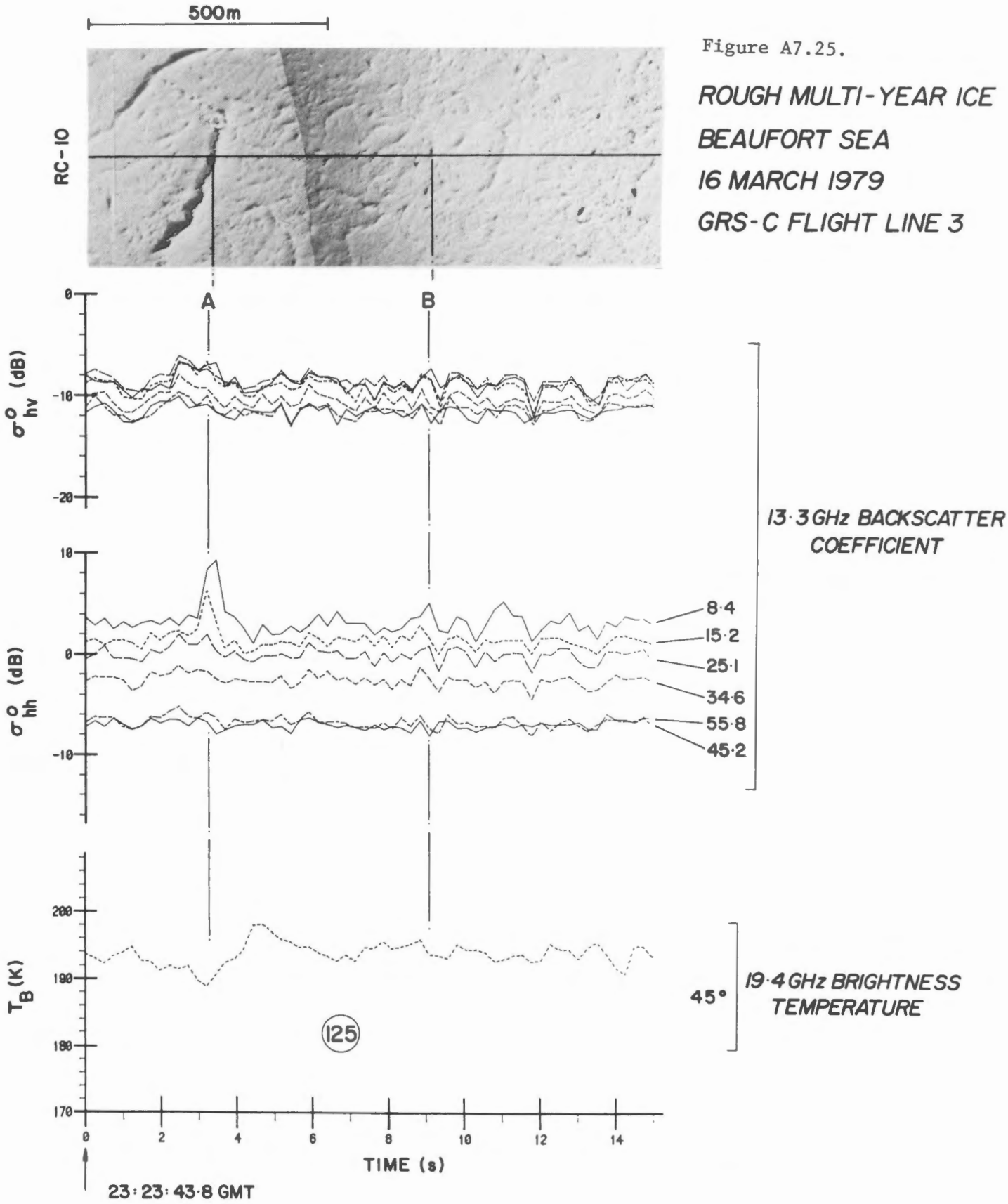

Figure A7.25.

ROUGH MULTI-YEAR ICE
BEAUFORT SEA
16 MARCH 1979
GRS-C FLIGHT LINE 3

Figure A7.26.

ROUGH MULTI-YEAR ICE
EVENT E30803 125
BEAUFORT SEA
16 MARCH 1979, LINE 3
23:23:43.8 TO 23:23:58.8 GMT

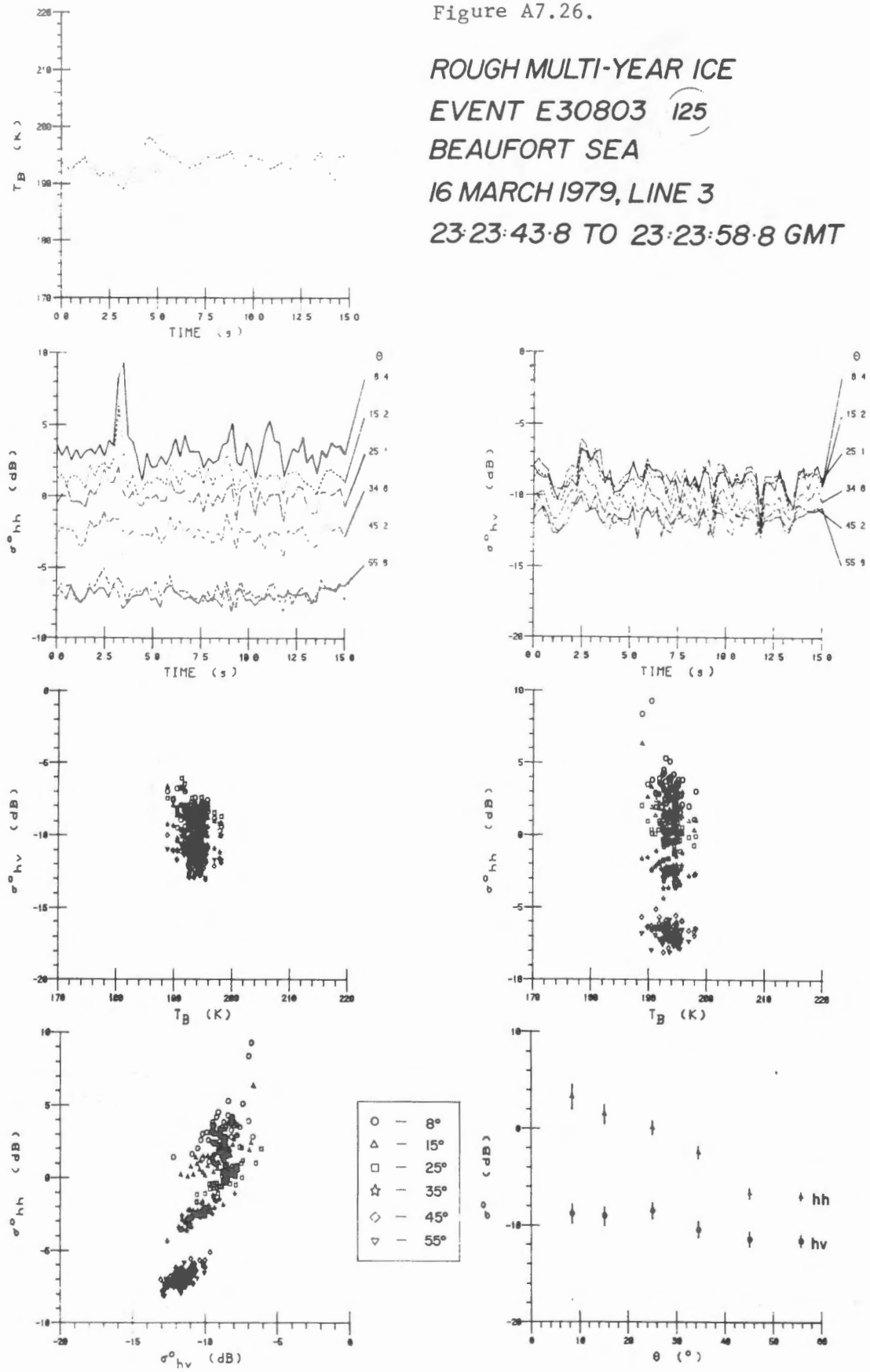

Table A7.14 SUMMARY OF EVENT E30803.125: ROUGH MULTI-YEAR ICE

EVENT DESCRIPTION:

BEAUFORT 030803 N/S (M)

ASSOCIATED FILES

SCA2:BA0803.L15[64,400]
SCA2:BA0803.C15[64,400]
SCA3:030803.SMO[64,400]
SCA3:030803.INC[64,400]
SCA3:030803.RAD[64,400]
SCA3:D30803.125[64,400]

EVENT TIME

FROM: 75 23:23:43.8000
TO: 75 23:23:59. 0

NAV PARAMETERS	Alt (ft)	Vg (knots)	Lat.	Long.	Pitch	Roll	Drift
	1301.000	155.40	72.5079	-131.9745	2.14	0.30	0.06
+/-	0.338	0.01	0.0000	0.0000	0.01	0.05	0.01

ANGLES †						
	8.440	15.175	25.108	34.610	45.209	55.814

SCATTEROMETER STATISTICS

LMEAN	3.276	1.462	0.021	-2.536	-6.682	-6.984
XMEAN	-8.835	-9.050	-8.536	-10.431	-11.437	-11.590
LSTD	1.312	0.904	0.730	0.612	0.572	0.458
XSTD	0.982	0.957	0.839	0.827	0.751	0.631
CORREL COEF	0.573	0.693	0.832	0.844	0.747	0.590

BRIGHTNESS TEMPERATURE STD 1.7 MEAN 193.7

CORRELATION COEFFICIENTS FOR RADIOMETER AND SCATTEROMETER

TB VS LPOL	-0.628	-0.631	-0.518	-0.426	-0.328	-0.195
TB VS XPOL	-0.422	-0.480	-0.437	-0.395	-0.410	-0.331

† In this table, the columns of statistics below refer to the six scatterometer angles indicated here. LMEAN, XMEAN, XSTD, and LSTD are the averages and standard deviations of the like- and cross-polarized backscattering coefficients. TB refers to the microwave brightness temperature.

Figure A7.27.

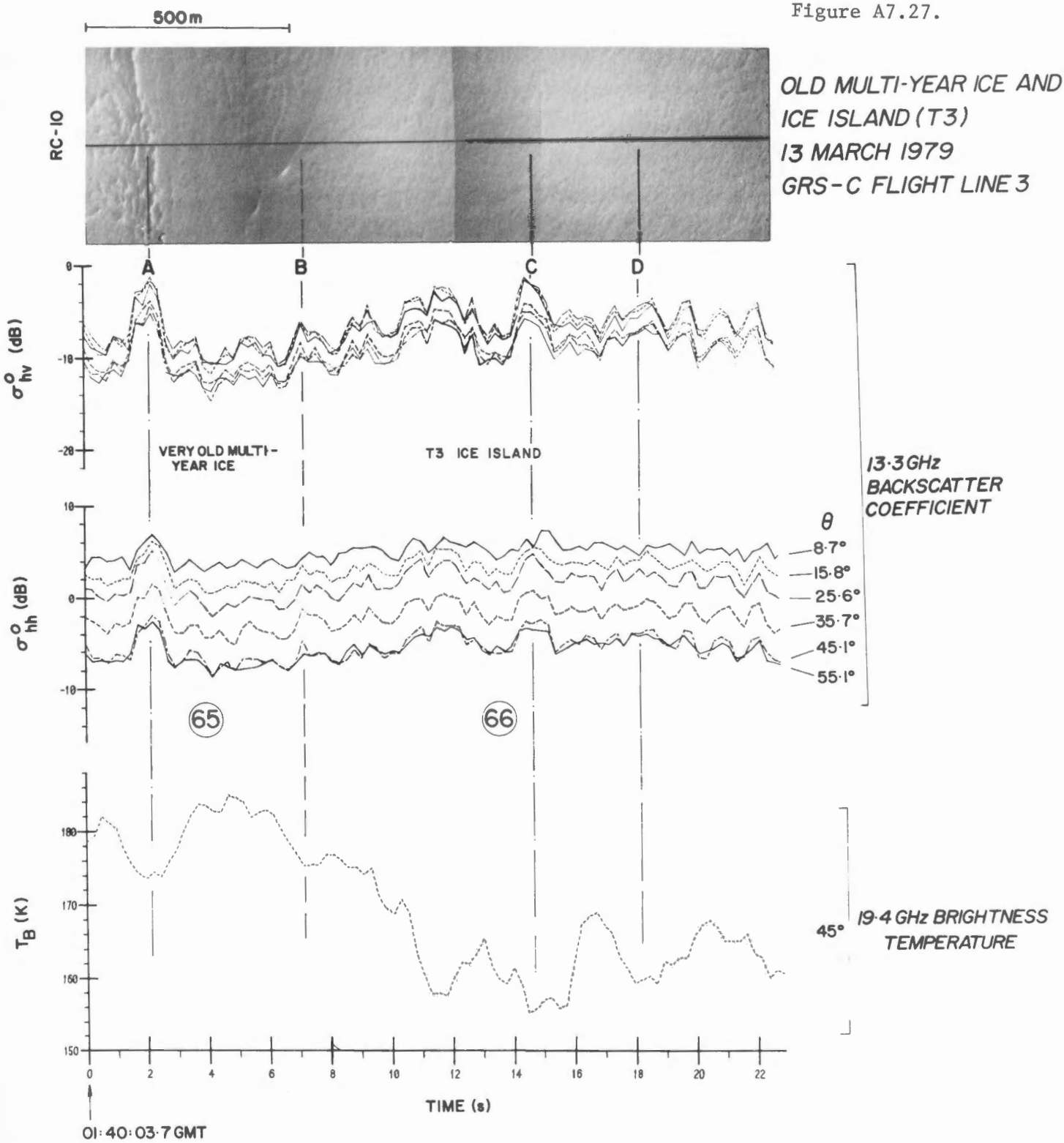
500m
RC-10
OLD MULTI-YEAR ICE AND
ICE ISLAND (T3)
13 MARCH 1979
GRS-C FLIGHT LINE 3
A
B
C
D
σ^o_{hv} (dB)
VERY OLD MULTI-YEAR ICE
T3 ICE ISLAND
13·3 GHz BACKSCATTER COEFFICIENT
θ
8·7°
15·8°
25·6°
35·7°
45·1°
55·1°
σ^o_{hh} (dB)
65
66
T_B (K)
45°
19·4 GHz BRIGHTNESS TEMPERATURE
TIME (s)
01:40:03·7 GMT

The transition from the old multi-year floe to T3 is not dramatic, either from the aerial photography or the scattering coefficient (which rises 2-3 dB); however, the radiometer shows a marked contrast, falling from an average of 182 K over the old floe to 163 K over T3. The large variance of ~ 2 dB RMS in the radar backscatter of T3 emphasized in the cross-polarized return, is seen as a strong textural variation in the radar imagery. This variation would, however, be more evident in a radiometric image of T3 where ~5 K RMS variation in brightness temperature is observed.

The details of these features are given in Figures A7.28 and A7.29 and Tables A7.15 and A7.16 where the analysis of the complete events are given.

A7.9 Icebergs

Figure A7.30 shows a large, grounded tabular iceberg, surrounded by bergy bits, frozen in a matrix of first-year ice. The Melville Bay scene on April 11 is heavily snow-drifted, obscuring details in the sculptured surface of the berg and the surrounding ice. The berg projects above the surrounding ice by ~ 53 feet (16 m), as indicated by the radar altimeter reading, and measures 530 x 280m. It is one of the largest bergs profiled during the mission.

The radar contrast between the berg and surrounding ice is ~14 dB for σ^o_{hv} and ~6 dB for σ^o_{hh} with an accompanying 20 K drop in brightness temperature. Comparison of backscattering properties with ice island T3, shown in Figure 12, demonstrates that this berg is similar, however, it has a much higher brightness temperature. The emissivity of this berg and T3 are 0.77 and 0.65 respectively.

A bergy bit is responsible for the feature at B, but the drop in the radar return at A requires explanation. It has been observed that about 30% of the icebergs show a feature similar to this, on the same side of the berg. It is possible that very smooth ice formed on a refrozen lead on one side of the berg as the ice pack moved away from the grounded berg, and subsequent snowfall obscured the feature. This would qualitatively account for both the rise in brightness temperature and fall in backscattering; however, it requires more than a transition from rough to smooth ice to achieve the required change in T_B and σ^o. Deep, wet snow accumulation could also be responsible for the backscattering behaviour and enhancement of the brightness temperature, as observed by Hall et al., 1979. This explanation, however, requires that the snow is wet only in the region around A. The ice immediately adjacent to the berg is scoured and bare of snow.

Figure A7.28.

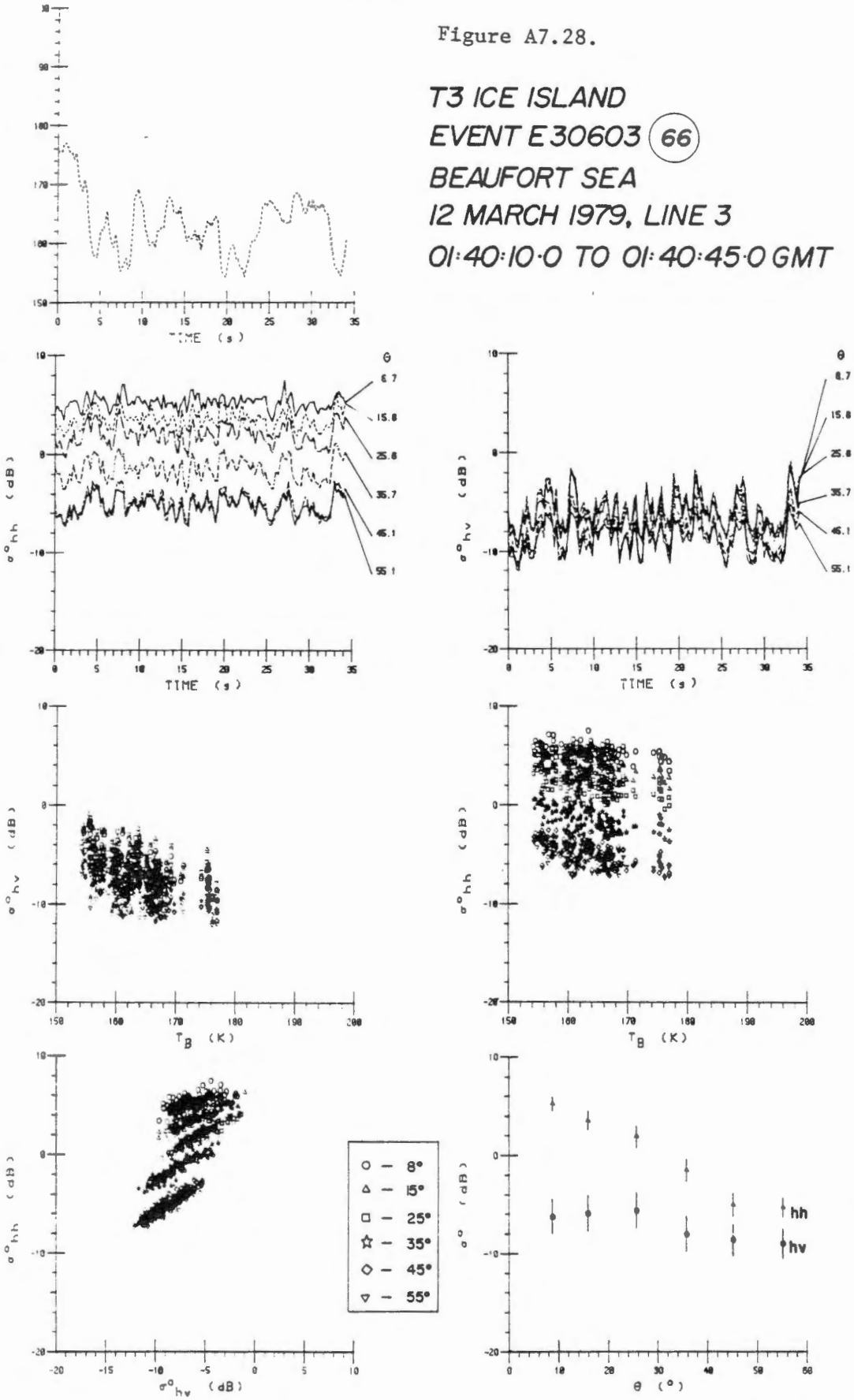
T3 ICE ISLAND
EVENT E30603 66
BEAUFORT SEA
12 MARCH 1979, LINE 3
01:40:10.0 TO 01:40:45.0 GMT
TIME (s)
θ
8.7
15.8
25.8
35.7
45.1
55.1
σ°hh (dB)
σ°hv (dB)
TB (K)
σ° (dB)
θ (°)
hh
hv
○ — 8°
△ — 15°
□ — 25°
☆ — 35°
◇ — 45°
▽ — 55°

Table A7.15 SUMMARY OF EVENT E30603.066: T3 ICE ISLAND

EVENT DESCRIPTION:
BEAUFORT 030603 XLINE (T3 ICE ISLAND)

ASSOCIATED FILES
SCAT:BA0603.L07[64,400]
SCAT:BA0603.C07[64,400]
SCA3:030603.SMO[64,400]
SCAT:030603.INC[64,400]
SCAT:030603.RAD[64,400]
SCA3:D30603.066[64,400]

EVENT TIME
FROM: 71 1:40:10.8000
TO: 71 1:40:45. 0

NAV PARAMETERS	Alt (ft)	Vg (knots)	Lat.	Long.	Pitch	Roll	Drift
	1375.882	145.27	72.6956	-131.4556	3.51	-0.67	-0.42
+/-	0.218	0.01	0.0000	0.0000	0.01	0.03	0.03

ANGLES †

	8.700	15.838	25.622	35.717	45.063	55.052

SCATTEROMETER STATISTICS

LMEAN	5.236	3.554	1.947	-1.486	-4.985	-5.229
XMEAN	-6.258	-5.926	-5.606	-7.984	-8.595	-8.936
LSTD	0.714	0.947	1.106	1.137	1.197	1.006
XSTD	1.736	1.867	1.809	1.780	1.643	1.518
CORREL COEF	0.594	0.901	0.927	0.936	0.921	0.921

BRIGHTNESS TEMPERATURE STD 5.3 MEAN 163.4

CORRELATION COEFFICIENTS FOR RADIOMETER AND SCATTEROMETER

TB VS LPOL	-0.520	-0.654	-0.620	-0.629	-0.650	-0.671
TB VS XPOL	-0.667	-0.650	-0.659	-0.650	-0.691	-0.689

† In this table, the columns of statistics below refer to the six scatterometer angles indicated here. LMEAN, XMEAN, XSTD, and LSTD are the averages and standard deviations of the like- and cross-polarized backscattering coefficients. TB refers to the microwave brightness temperature.

Figure A7.29.

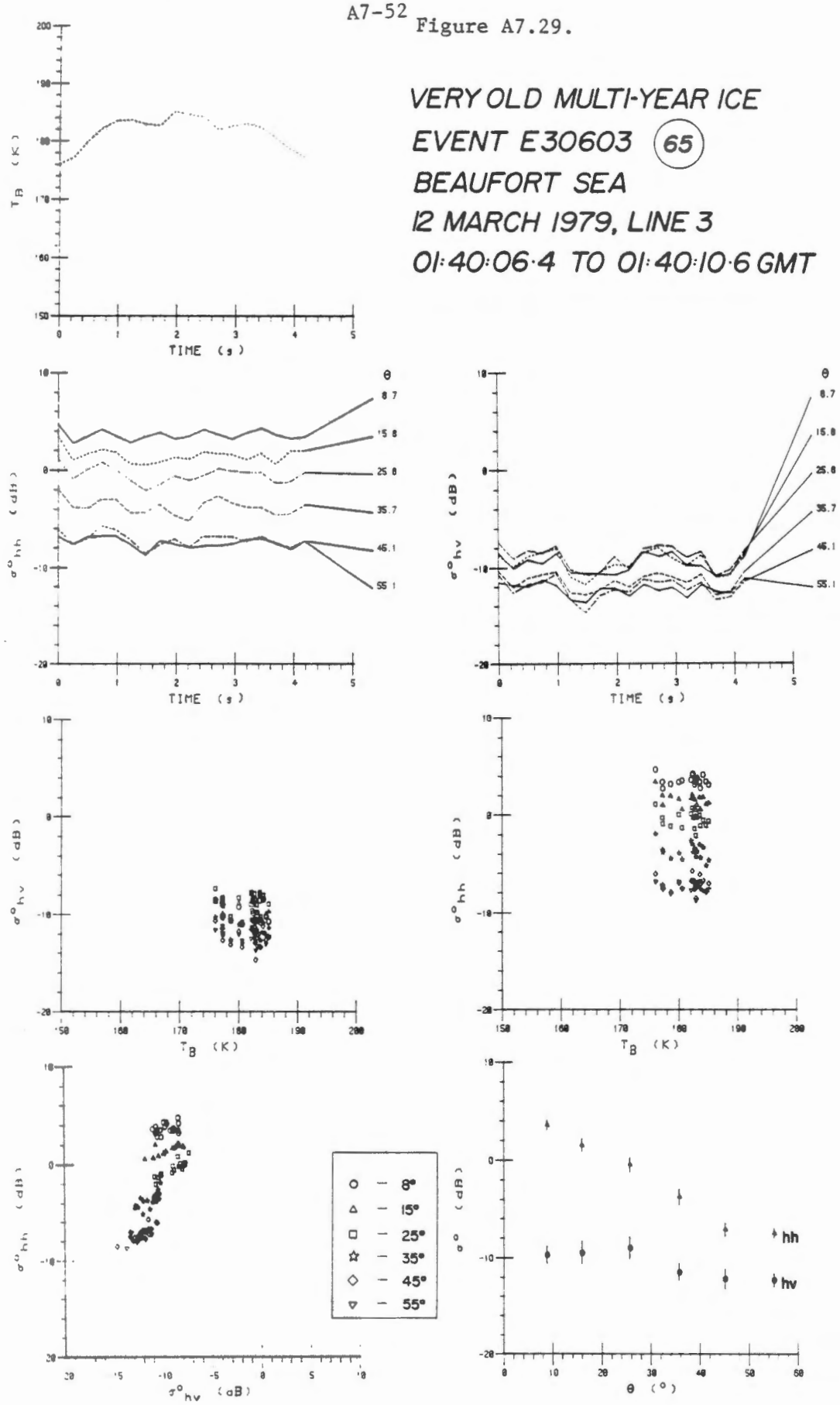
VERY OLD MULTI-YEAR ICE
EVENT E30603 (65)
BEAUFORT SEA
12 MARCH 1979, LINE 3
01:40:06.4 TO 01:40:10.6 GMT
TIME (s)
θ
8.7
15.8
25.8
35.7
45.1
55.1
σ°hh (dB)
σ°hv (dB)
TB (K)
σ° (dB)
θ (°)
hh
hv
○ — 8°
△ — 15°
□ — 25°
☆ — 35°
◇ — 45°
▽ — 55°

Table A7.16 SUMMARY OF EVENT E30603.065: OLD MULTI-YEAR ICE

EVENT DESCRIPTION:

BEAUFORT 030603 XLINE (M [OLD ICE ON T3 EDGE])

ASSOCIATED FILES

SCAT:BA0603.L07[64,400]
SCAT:BA0603.C07[64,400]
SCA3:030603.SM0[64,400]
SCAT:030603.INC[64,400]
SCAT:030603.RAD[64,400]
SCA3:D30603.065[64,400]

EVENT TIME

FROM: 71 1:40: 6.4000
TO: 71 1:40:10.6000

NAV PARAMETERS		Alt (ft)	Vg (knots)	Lat.	Long.	Pitch	Roll	Drift
		1382.750	145.51	72.7069	-131.4333	3.56	-1.14	-0.47
	+/-	0.479	0.02	0.0000	0.0000	0.00	0.03	0.02

ANGLES †

	8.700	15.838	25.622	35.717	45.063	55.052

SCATTEROMETER STATISTICS

LMEAN	3.581	1.497	-0.512	-3.747	-7.113	-7.461
XMEAN	-9.708	-9.500	-9.002	-11.473	-12.175	-12.297
LSTD	0.496	0.683	0.773	0.771	0.693	0.509
XSTD	0.905	1.125	1.128	0.898	1.029	0.680
CORREL COEF	0.365	0.712	0.876	0.731	0.853	0.645

BRIGHTNESS TEMPERATURE STD 2.6 MEAN 181.6

CORRELATION COEFFICIENTS FOR RADIOMETER AND SCATTEROMETER

TB VS LPOL	-0.349	-0.714	-0.449	-0.483	-0.194	-0.378
TB VS XPOL	-0.273	-0.155	-0.319	-0.295	-0.306	-0.649

† In this table, the columns of statistics below refer to the six scatterometer angles indicated here. LMEAN, XMEAN, XSTD, and LSTD are the averages and standard deviations of the like- and cross-polarized backscattering coefficients. TB refers to the microwave brightness temperature.

Figure A7.30

TABULAR ICEBERG
MELVILLE BAY
11 APRIL 1979
GRS-C FLIGHT LINE 2